Technical Report

TR-13-07

EBS TF – THM modelling

BM 2 – Large scale field tests

Lennart Börgesson, Mattias Åkesson,
Ola Kristensson, Ann Dueck
Clay Technology AB

Jan Hernelind, 5T Engineering AB

November 2016

Svensk Kärnbränslehantering AB
Swedish Nuclear Fuel
and Waste Management Co

Box 250, SE-101 24 Stockholm
Phone +46 8 459 84 00

ISSN 1404-0344
SKB TR-13-07
ID 1385780
November 2016

EBS TF – THM modelling

BM 2 – Large scale field tests

Lennart Börgesson, Mattias Åkesson,
Ola Kristensson, Ann Dueck
Clay Technology AB

Jan Hernelind, 5T Engineering AB

Abstract

Phase 1 of the EBS Task Force on modelling THM processes in buffer and backfill materials for nuclear waste disposal has been running between the years 2005 and 2010. This phase included a number of THM (thermo-hydro-mechanical) tasks for modelling both well-defined laboratory tests and large scale field tests such as the two Canadian URL tests ITT and BCE and the Swedish ÄHRL test CRT.

This report deals with the modelling results of the large scale field tests (Benchmark 2) from the two teams granted by SKB. The large scale laboratory tests (Benchmark 1) are reported in another report (Börgesson et al. 2016).

The following tasks are included in BM 2:

Task 2.1 – ITT and BCE

The experiments were performed by Atomic Energy of Canada Limited (AECL) in its Underground Research Laboratory between 1991 and 1999. Both tests were installed in full-scale, 1.24 m diameter by 5 m deep boreholes.

In the Isothermal Test (ITT), the lowermost two meters of the borehole were filled with buffer material and sealed with a 1.25 m–thick cap of high performance concrete and was left undisturbed for 6.5 years. In the Buffer/Container Experiment (BCE), a full-size heater, representing a container of nuclear fuel waste, was placed in the buffer, which filled the remaining part of the 5 m hole. Power was provided to this heater for almost 900 days.

The buffer and the rock were instrumented for temperatures, total pressures, water pressures, suctions and displacements.

Task 2.2 – CRT

The full scale test the Canister Retrieval Test (CRT) that simulates a deposition hole with canister and buffer material according to the reference design of a KBS-3V deposition hole was performed by SKB in Äspö HRL. It was installed in 2000 and run for more than 5 years. It was excavated with extensive sampling and determination of the density and water ratio of the buffer material. A large number of transducers for measuring temperature, relative humidity, pore water pressure and total pressure in the buffer during the test time were installed as well as force and displacement transducers on the plug.

The test was equipped with a plug in the top of the deposition hole that simulated a compressible backfill by flexible anchors. When the test was interrupted the buffer material between the rock and the canister was completely saturated while the buffer material above the canister was not water saturated.

Task 2.1 was modelled by one team (SKB 1) while Task 2.2 was modelled by both teams. SKB1 used the finite element code Code Bright and team SKB2 used the code Abaqus for the modelling. The report describes the set-up of the tests, the tasks, the results of the modelling and analyses made by the two modelling teams.

Sammanfattning

Fas 1 av ”EBS Task Force” avseende modellering av THM-processer i buffert- och återfyllningsmaterial för slutförvaring av radioaktivt avfall har pågått mellan åren 2005 och 2010. Denna fas inkluderade ett flertal THM (termo-hydro-mekaniska) beräkningsuppgifter som innebar att modellera både väldefinierade småskaliga laboratorieförsök och storskaliga fältförsök såsom de två kanadensiska försöken ITT och BCE och det svenska försöket CRT i Äspö.

Denna rapport beskriver den modellering av de storskaliga fältförsöken (Benchmark 2) som utförts av de två svenska modelleringsgrupperna som finansierats av SKB. Modelleringen av de småskaliga laboratorieförsöken (Benchmark 1) beskrivs i en separat rapport (Börgesson et al. 2016).

Följande beräkningsuppgifter inkluderas i BM 2:

Task 2.1 – ITT and BCE

Dessa experiment utfördes av Atomic Energy of Canada Limited (AECL) i deras underjordiska laboratorium URL mellan 1991 och 1999. Båda försöken simulerade fullskaliga deponeringshål med diametern 1,24 m och djupen 5 m.

I ITT (Isothermal Test) var de två nedersta metrarna av borrhålet fyllda med buffertmaterial och avtätat uppåt med ett lock av högkvalitativ betong med tjockleken 1,25 m och lämnat ostört under 6,5 år. I BCE (Buffer/Container experiment) placerades en fullskalig värmare, som representerar kapseln, i bufferten i det 5 m djupa deponeringshålet. Värmaren var påslagen i knappt 900 dagar.

Bufferten och berget var instrumenterade för att mäta temperatur, totaltryck, vattentryck, RH och förskjutningar.

Task 2.2 – CRT

CRT (Återtagsförsöket) är ett fullskaligt experiment som simulerar ett deponeringshål med kapsel och buffertmaterial enligt referensutformningen i KBS-3V, utfört av SKB i Äspö HRL. Försöket installerades år 2000 och löpte under drygt 5 år innan brytning och provtagning. Ett stort antal givare som mätte temperatur, RH, portryck och totaltryck installerades i bufferten. I pluggen installerades givare som mätte kraft och deformation.

Pluggen ovanför deponeringshålet simulerade en kompressibel återfyllning genom att ha flexibla stag som mothåll. När försöket bröts var hela buffereten mellan berget och kapseln vattenmättad men inte bufferten ovan och under kapseln.

Task 2.1 modellerades av en av SKB:s modelleringsgrupper (SKB1) medan Task 2.2 modellerades av båda grupperna. SKB1 använde finita elementkoden Code Bright och SKB2 använde koden Abaqus för modelleringarna. Denna rapport beskriver experimenten, modelleringsuppgifterna, resultaten av modelleringarna från de båda modelleringsgrupperna och efterföljande analyser.

Contents

1 Introduction

The Task Force on Engineered Barrier System (EBS) is an international project arranged by SKB with the purpose to verify and evaluate the capability to model THM-processes in unsaturated and saturated buffer materials and to further develop the codes.

Phase 1 of the EBS Task Force on modelling THM processes in buffer and backfill materials for nuclear waste disposal has been running between the years 2005 and 2010. This phase included a number of THM (thermo-hydro-mechanical) tasks for modelling both well-defined laboratory tests and large scale field tests such as the two Canadian URL tests IT and BCE and the Swedish ÄHRL test CRT.

The Task Force is initiated and managed by SKB under supervision by Anders Sjöland, SKB. Antonio Gens, UPC has been chairman and Lennart Börgesson, Clay Technology AB has been secretary.

All defined tasks are given in Table 1-1. Participating organisations besides SKB have for this phase been Andra (France), BMWi (Germany), CRIEPI (Japan), Nagra (Switzerland), Posiva (Finland), NWMO (Canada), ENRESA (Spain) and RAWRA (Czech Republic). All together 9 modelling teams have been participating in the work using 7 different codes.

Table 1-1. Modelled tests in the EBS Task Force, phase 1.

Benchmark 1 – Laboratory tests
Task 1 – THM tests
1.1.1 Two constant volume tests on MX-80 (CEA)
1.1.2 Two constant volume tests on Febex bentonite – one with thermal gradient and one isothermal (Ciemat)
1.1.3 Constant external total pressure test with temperature gradient on Febex bentonite (UPC)
Task 2 – Gas migration tests
1.2.1 Constant external total pressure (BGS)
1.2.2 Constant volume (BGS)
Benchmark 2 – Large scale field tests
Task 1 – URL tests (AECL)
2.1 Buffer/Container Experiment and Isothermal Test
Task 2 – Äspö HRL test (SKB)
2.2 Canister Retrieval Test

The present report deals with the tasks in Benchmark 2. The tasks in Benchmark 1 are reported separately (Börgesson et al. 2016). The tasks in BM 2 concern well-documented full-scale tests at repository depths in underground laboratories. These tests and the proposed tasks were described in so called task descriptions that were delivered in advance. Those task descriptions are included in the report.

Twice a year there has been a Task Force meeting for a couple of days where the tasks, the modelling results and comparison between results and measurements were presented and discussed.

This report only describes the tasks and the results of the modelling and analyses made by the two modelling teams granted by SKB. The contributions of the other teams are reported separately. A general analysis and comparison of results between different modelling groups will be made in a separate report by A. Gens (Gens 2016).

The two modelling teams (named SKB 1 and SKB 2) are the following for Benchmark 2:

- SKB 1: Mattias Åkesson, Ola Kristensson and Daniel Malmberg, Clay Technology AB.
- SKB 2: Lennart Börgesson and Ann Dueck, Clay Technology AB and Jan Hernelind, 5T Engineering AB.

Tasks 2.1 has been modelled and reported only by team SKB 1. Task 2.1 has been modelled and reported by both teams.

The motivation for having two teams is that different codes with different capabilities and advantages have been used by the two teams. SKB 1 has mainly used Code Bright while SKB 2 has used Abaqus. Both these codes have been used in the modelling for SR-Site.

2 BM 2.1 – BCE and ITT

2.1 General

The experiments used for BM 2.1 were performed by Atomic Energy of Canada Limited (AECL) in its Underground Research Laboratory, Lac du Bonnet MB, between 1991 and 1999. Both tests were installed in full-scale in boreholes with 1.24 m diameter and 5 m depth.

The task specifications were provided by David Dixon of AECL. Section 2.2 is taken directly from his text and thus not adapted to past tense.

2.2 Specifications

2.2.1 Background

The EBS-TF is provided with 2 databases that will allow for THM modelling exercises to be conducted using a variety of numerical codes and tools. These databases represent selected instrument and field measurements collected over the course of operating the Buffer/Container Experiment (BCE) and the Isothermal Test (ITT) at Atomic Energy of Canada's (AECL) Underground Research Laboratory (URL).

In order to conduct THM modelling data on the total pressure, suction within the buffer mass, porewater pressure in the surrounding rock mass, temperature within the buffer and in the surrounding rock has been provided as spreadsheet datafiles. This data together with the known start-of-test and detailed end-of-test physical measurements of buffer water content and density conditions will provide the information needed to conduct numerical simulations.

Two Ontario Power Generation technical memoranda that contain the materials properties parameters developed for the materials contained in the ITT and BCE are also available.

2.2.2 Isothermal Test

In the ITT water content data obtained at the time of decommissioning (end-of-test EOT), was provided for 8 vertical layers within the buffer mass. Eight levels within the ITT were also sampled to provide density profiles within the buffer at the time of decommissioning and these data provide a measure of some of the H-M interactions that occurred during system evolution. Evolution of the system with time was monitored via total suction sensors (water content), total pressure cells, and piezometers (pore pressure in rock).

Figures 2-1 through 2-4 show the locations of instruments and field samples provided in this database. It is proposed that the modelling teams consider conducting the following simulations:

Porewater Pressure

a. Compare porewater pressure distribution within the buffer and adjacent rock mass at EOT to that predicted.

b. Compare porewater pressure evolution with time at locations IRP2, IRP3 (Figure 2-2) and IRP4 (Figure 2-3c).

c. Compare buffer's mid-height porewater pressure radial distribution in the rock at two times (Before buffer installation and 2 350 days after buffer installation).

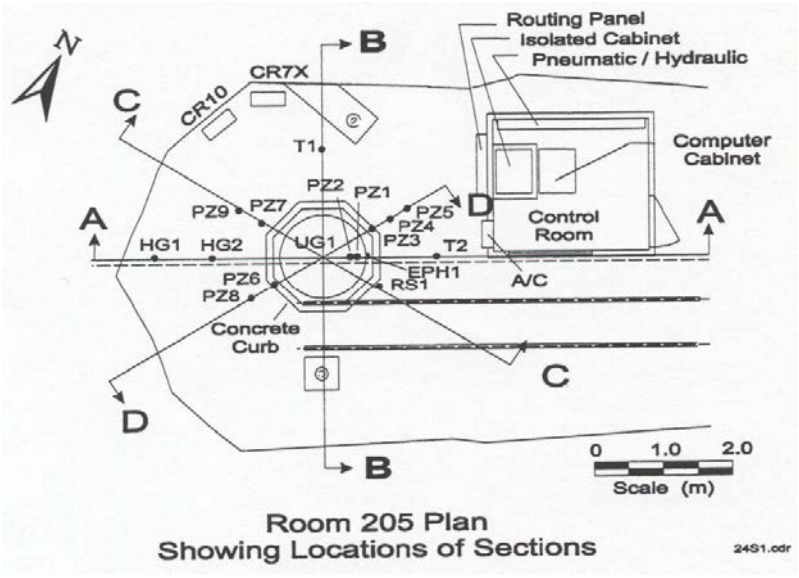

Figure 2-1. *Plan View of the Isothermal Test.*

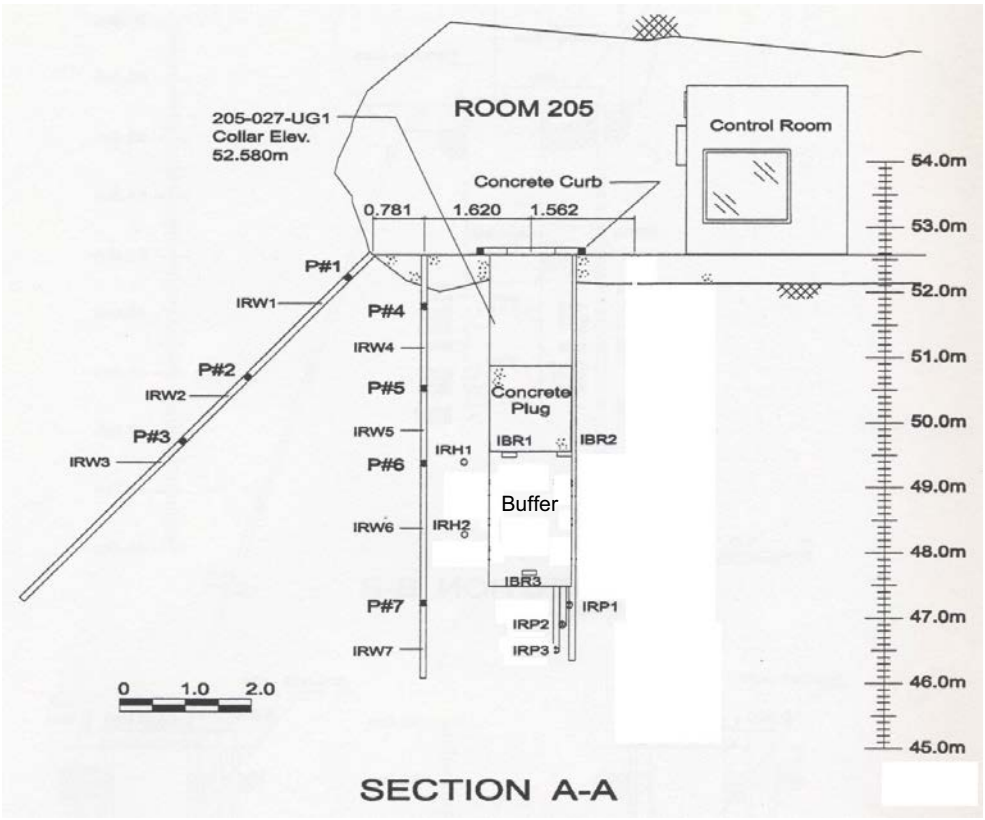

Figure 2-2. *Cross-Section A-A of the Isothermal Test.*

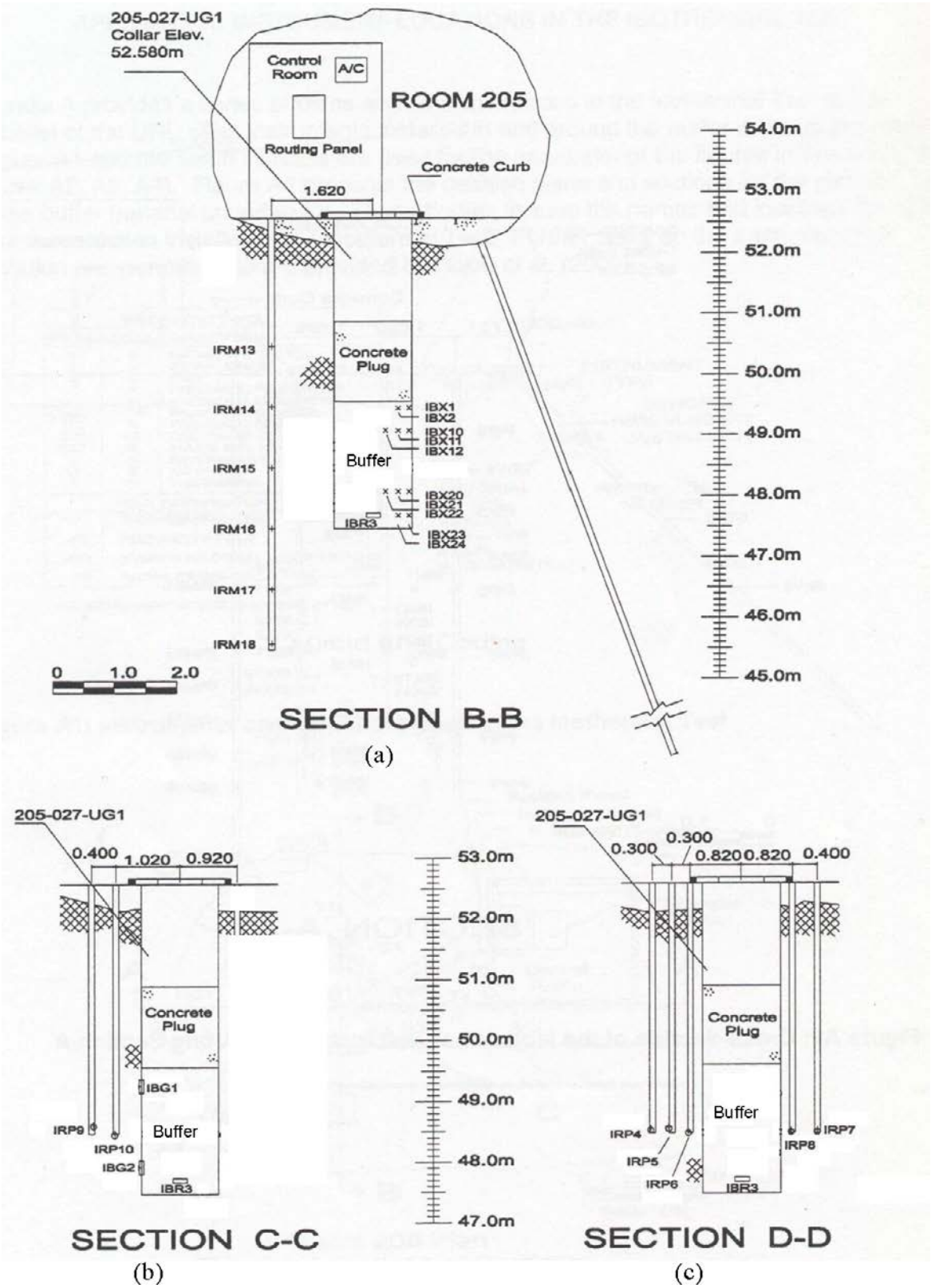

Figure 2-3. *Sections of Isothermal Test Showing Instrumentation Layers along Section (a) B-B; (b) C-C; and (c) D-D.*

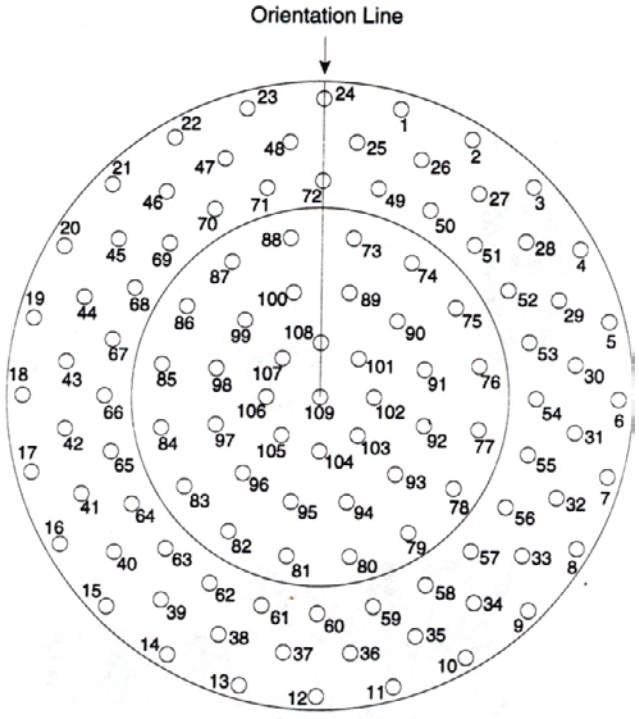

Figure 2-4. *Layout and Numbering System Using Template for Moisture Content Sampling.*

Suction (water content)

a. Suction (water content) predictions at elevations 0.5 m, buffer's mid-height, 1.5 m for 1-D suction conditions radially outwards from the borehole centreline with time. The bottom of the borehole is zero elevation. (Suction vs. distance at discrete times to be generated, t = 50, 400 days, 900 days and EOT).

b. Generate water content (suction) predictions for a 2-dimensional vertical cross-section of buffer at t = 50, 400, 900 and 1 500 days.

c. Comparison of suction radial profiles in the buffer on layers A through H at EOT.

Mechanical

a. Predict total pressure versus time at the buffer-rock interface along the vertical axis of the buffer and compare to measured data supplied.

b. Predict total pressure versus time radially outwards at the buffer-rock interface at mid-height of buffer and compare to measured data supplied.

Hydraulic

Compare the predicted water influx based on rock and porewater pressure conditions to those measured before the installation of the buffer.

2.2.3 The Buffer/Container Experiment

The BCE also operated at AECL's URL in a borehole of similar dimension to that of the ITT. The BCE however had a container-sized heater and a sand layer between the heater and the buffer-filled borehole. The BCE was monitored for total suction (water content), temperature, total pressure within the buffer and at the buffer-rock interface as well as the hydraulic pressure in the surrounding rock. At the completion of the BCE's operation the test was extensively sampled to capture the EOT density and water content conditions.

A series of 8 layers were selected from the EOT water content analyses to provide a measure of the conditions that ultimately developed. These data were accompanied with a series of block samples that captured the EOT density conditions within the BCE. The BCE was therefore a carefully monitored THM experiment. The locations of instruments and sampling are shown in Figures 2-5–2-13.

It is proposed that the following aspects be modelled as part of the EBS-TF activities:

Temperature

a. Temperature profile vertically along the vertical axis of the borehole from cell lid to the rock at 4 times (day 0, day 7, day 49 and EOT).

b. Temperature profile radially outwards from the heater at 4 times (day 1, day 10, day 50, and EOT) along the profile IBT61-67 (Figure 2-6) and outwards into the surrounding rock.

c. Develop vertical Temperature contour at 4 times (day 30, day 150, day 400 and EOT) in the Buffer along Section CC (Figure 2-6).

d. Develop vertical Temperature contour in the rock at 4 times (day 30, day 150, day 400 and EOT).

e. Comparison temperature profile vertically along boreholes 7 and 8 (Figure 2-8) at four different times (day 0, day 7, day 49 and EOT).

Porewater Pressure (PWP)

a. Develop a PWP profile radially outwards from the rock-clay boundary at 3 depths (1 m, 2.45 m and 4.6 m from the floor of Room 213) and at 4 times (day 26, day 154, day 400 and EOT) at the profile (HG6,7,8,9,10,11 in Figures 2-8 and 2-9).

b. Predict PWP evolution at IRH1 through IRH4 (Figure 2-10).

Suction (water content)

a. Develop a 2-D vertical profile through the buffer at the EOT.

b. Compare suction versus time for sensors IBX-1, IBX-6/7, IBX-12 and IBX-16/17 (Figure 11) to predictions generated using water influx data from rock.

Mechanical

a. Predict development of total pressure with time vertically along borehole axis and compare to sensor data (1BR1, 1BR3, 1BR4, 1BR5, 1BG13 in Figure 7).

b. Predict development of total pressure with time radially outwards within borehole at 0.75m, 1.5m, 3.1m, 4.6m below backfill-buffer interface at the rock-clay boundary and compare to pressure cell readings supplied.

c. Comparison of the simulated and measured vertical displacement profile along the EXT boreholes (Figures 5 and 8) on Day 110.

Hydraulic

Predict water supply based on PWP and rock properties and compare to measured data before the installation of the buffer and heater.

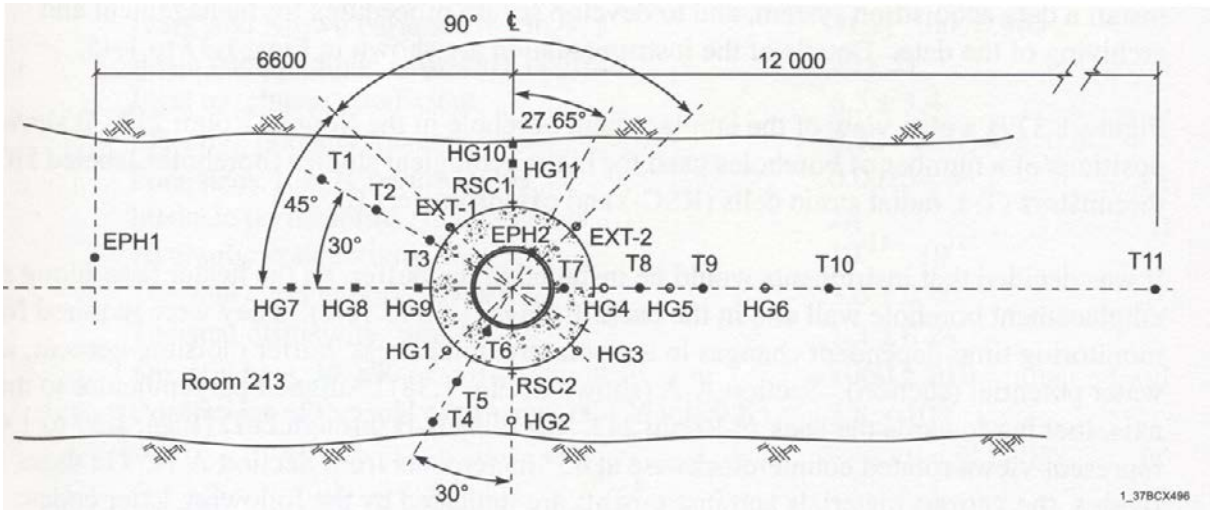

Figure 2-5. *Plan of Instrumentation.*

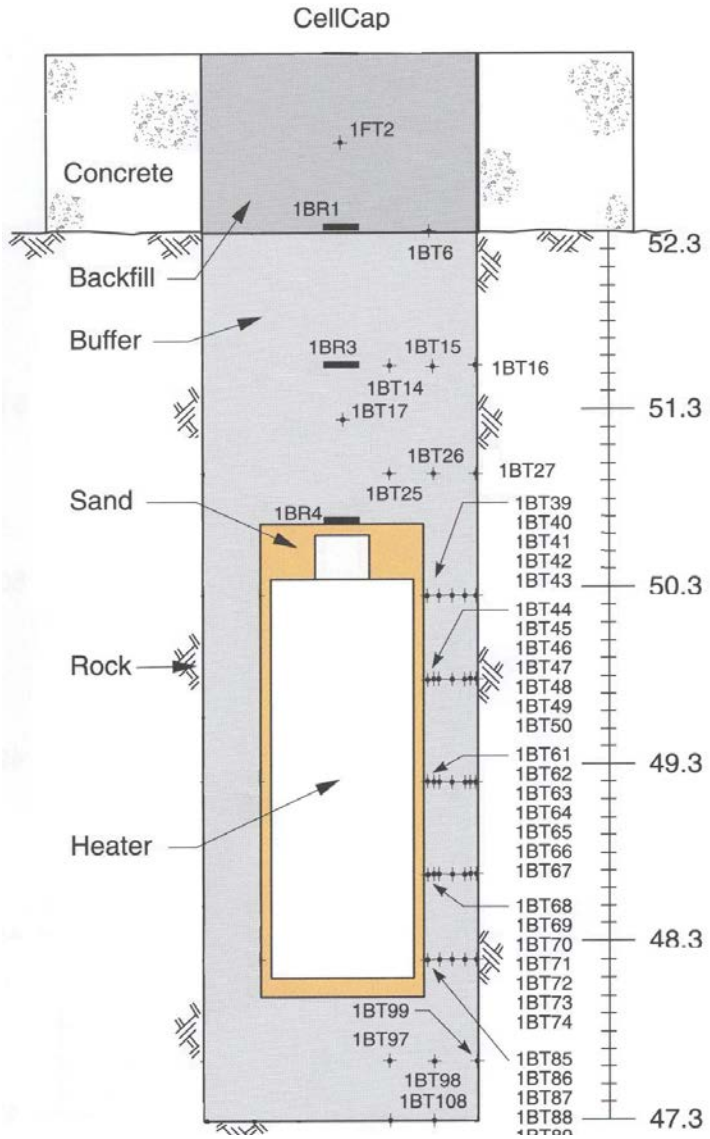

Figure 2-6. *Section C-C through the Buffer showing Thermocouples (BT, FT), and Earth Pressure Cells (BR).*

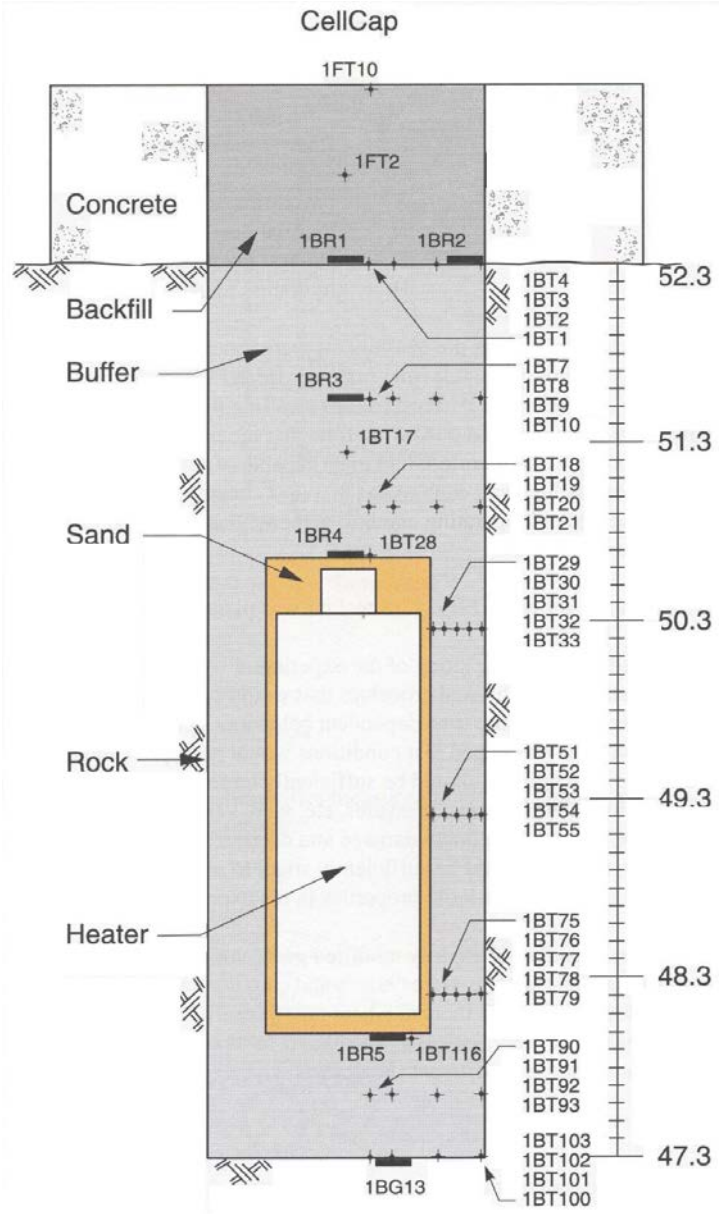

Figure 2-7. *Section AA showing Layout of Thermocouples (BT, FT) and some of the Total Pressure Cells (BR).*

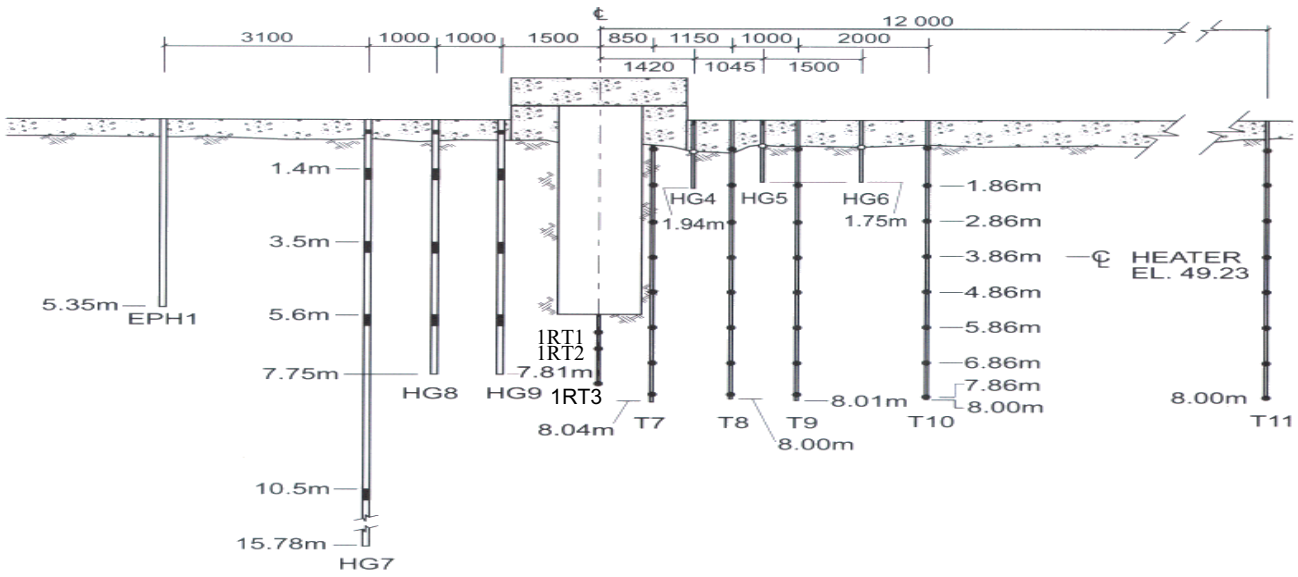

Figure 2-8. *Longitudinal Section of Room 213 showing Packer (HG) and Thermistor (T) Instrumentations in the Rock.*

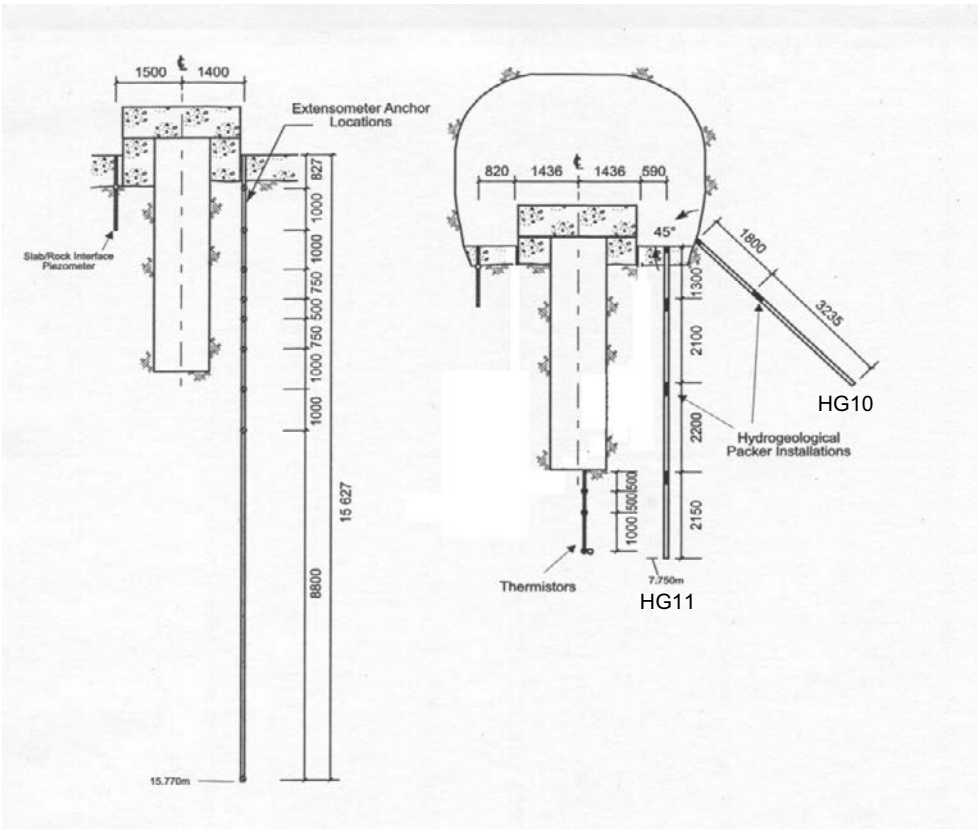

Figure 2-9. *Transverse Section of Room 213 showing Rock Strain and Packer Instrumentation.*

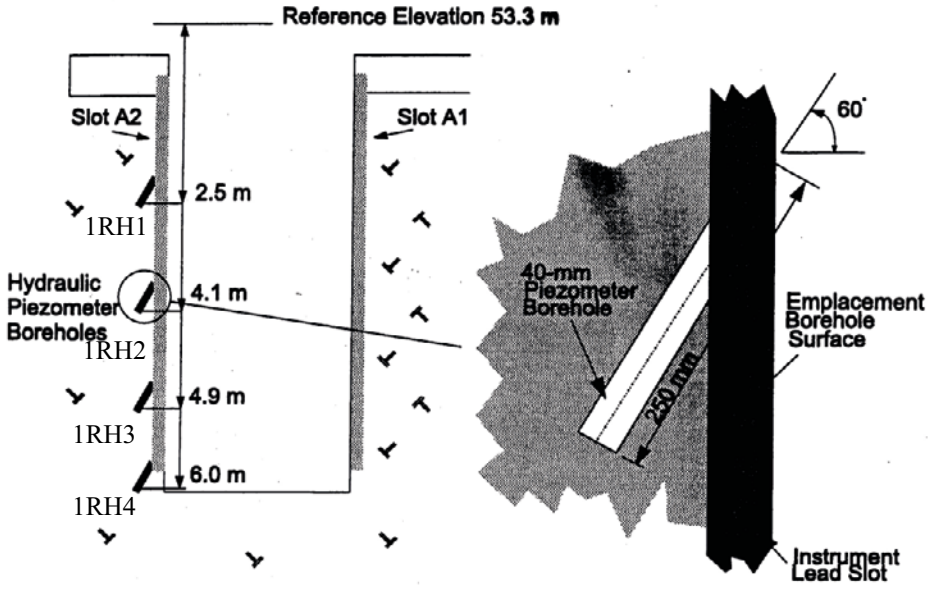

Figure 2-10. *Installation Geometry for Hydraulic Piezometers.*

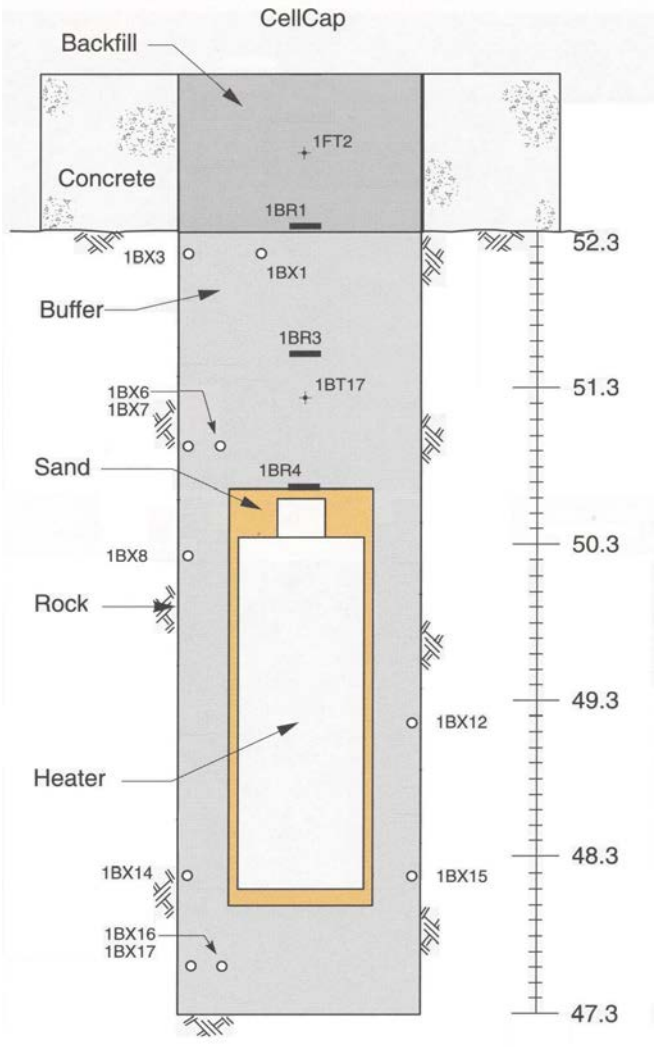

Figure 2-11. *Section DD showing Psychrometers (BX).*

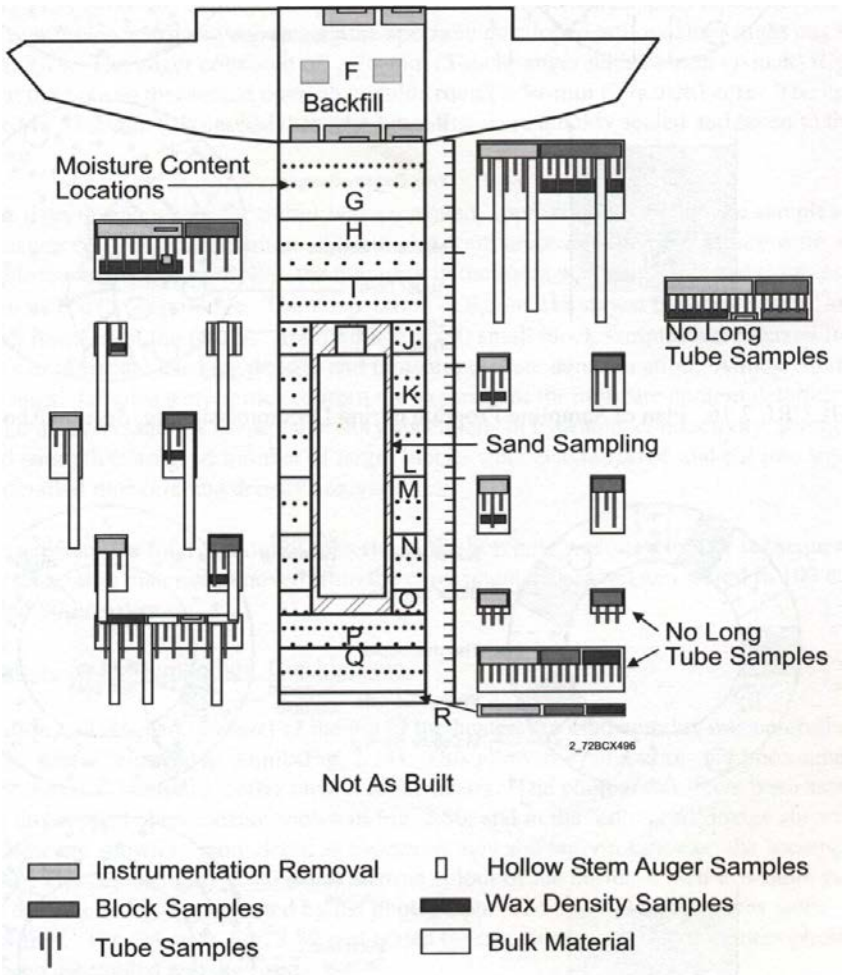

Figure 2-12. *Vertical Section Indicating Frequency and Type of Sampling Planned Decommissioning.*

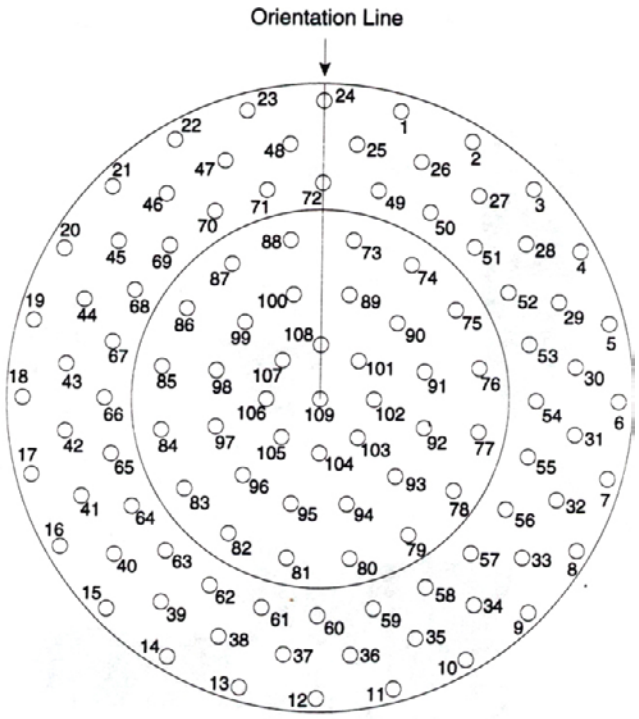

Figure 2-13. *Layout and Numbering System using Template for Moisture Content Sampling.*

2.3 Modelling results with Code Bright

2.3.1 General

The current section presents the benchmark calculations made by Team SKB 1 on benchmark system 2.1 which covers two Canadian large in-ground experiments: The Isothermal Test (ITT) and the Buffer/Container Experiment (BCE).

This section includes one appendix, Appendix 1 Progressing saturation front for 1D axis-symmetric geometry.

2.3.2 General considerations

Introduction

The hydration process of the ITT and the BCE tests are largely determined by the pore pressure conditions in the rock, and the water transport coefficients and the retention properties of the rock and the buffer material. In case of the BCE, there is also a significant effect of the heat load from the container. In order to simulate these experiments with precision, it is essential to have a relevant description of these conditions and properties.

The work on this benchmark has been focused on the hydrodynamic and thermo-hydrodynamic processes in the abovementioned experiments. No attempts to model the mechanical processes are reported here.

Geometries

For the ITT a 3D geometry with two symmetry planes was chosen. The reason for this was to enable a relevant draw-down from the tunnel with a considerable extension and not only a smaller representation. The ITT was located at the end of the tunnel and the drawdown should therefore display an azimutal variation. This test was modeled as a purely hydro-dynamical problem (although with the inclusion of thermal processes in some cases). The numerical complexity associated with a 3D geometry therefore appeared to be surmountable.

This approach was however avoided for the BCE in which the thermal processes had a much more prominent role. Moreover, since the experiment wasn't located at the tunnel ending, the azimutal variation was assessed to be less pronounced. Therefore an axis-symmetric 2D geometry was chosen for this case.

The distance from the boreholes to the outer boundaries were at least 30 m in both models.

The geometries of models are shown overlain the pore pressure isobars in Figure 2-14.

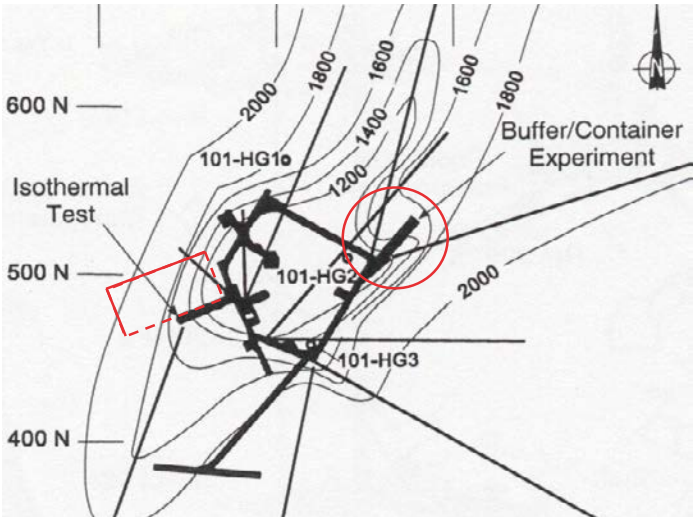

Figure 2-14. *Extensions of models overlain the groundwater pressure distribution at the 240 level (dashed lines are symmetry planes).*

Rock characteristics

In all models the gravity was included and hydrostatic pressure distribution was applied at the outer boundaries and for the initial conditions. Consideration had to made regarding the pressure at the tunnel level. Initially a pressure of 2.1 MPa was used for the outer boundaries at the tunnel level for both ITT and BCE. This was also stated in the modeling guidelines for ITT. Analyses of the pressure distribution around the BCE tunnel (Figure 2-14) led to a reduction of the boundary pressure to 1.5 MPa.

The porosity of the rock is 0.005 according to the modeling guidelines, and this value has been used for all models.

The hydraulic conductivity of the rock is a crucial parameter and is 10^{-12} to 10^{-13} m/s according to the guidelines. Analyses of the parameter showed that a value of 10^{-12} m/s is a relevant value for ITT, whereas the lower value of $5 \cdot 10^{-13}$ m/s gave a better representation for BCE. The cubic power law was used for the relative permeability in all models.

The applied retention curve (Figure 2-15) was adopted from Börgesson and Hernelind (1999).

Buffer material retention properties

A description of the retention properties was provided in the modeling guidelines:

$$\begin{cases} \log(\psi) = 2.729 - 0.142 \cdot w & 1 < w < 11 \\ \log(\psi) = 1.983 - 0.074 \cdot w & 11 < w < 25 \end{cases} \quad (2\text{-}1)$$

where ψ is the suction (in MPa) and w is the water content (in %). This curve was used for determination of the initial suction value and for adoption of parameters for van Genuchten expressions:

$$S_l = \left(1 + \left(\frac{\psi}{P_0}\right)^{\frac{1}{1-\lambda}}\right)^{-\lambda} \quad (2\text{-}2)$$

where S_l and ψ are the saturation degree and suction, respectively, and P_0 and λ are parameters.

The initial water content was 17.5 % and the porosity was 0.359. In the case of ITT (with no dehydration), this adoption was fairly straightforward (see Figure 2-17 and Table 2-1). For the BCE however, it was noticed that this line resulted in a too pronounced redistribution of water and an alternative was therefore sought.

This was done through evaluation of retention data for MX-80. Two paths were analyzed: one with zero initial water content and one with very high (64 %) initial water content (Dueck and Nilsson 2010). These paths represent the boundaries for hysteretic effects during hydration and dehydration (Figure 2-16, left).

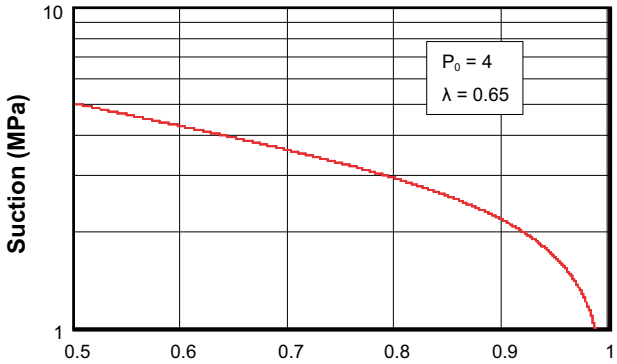

Figure 2-15. *Retention curve for rock material with used van Genuchten parameters.*

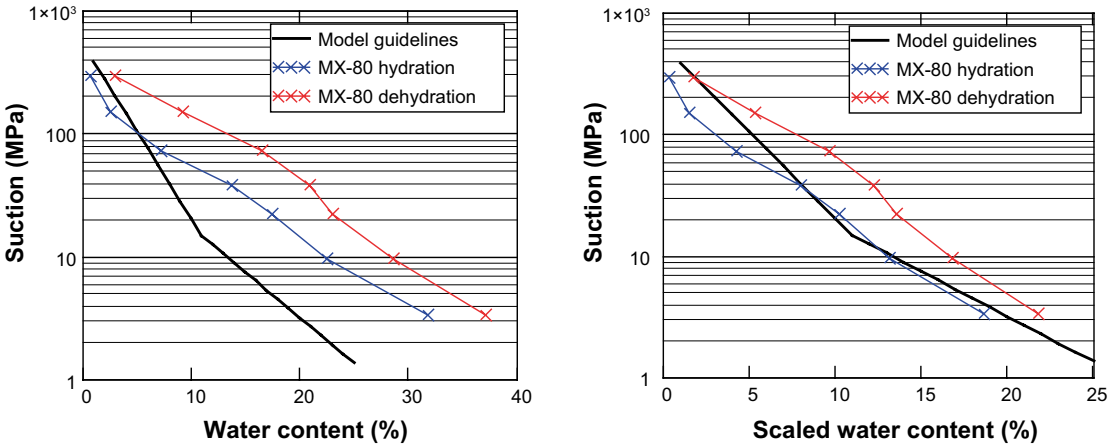

Figure 2-16. *Buffer material retention curve according to modeling guidelines and hydration and dehydration paths for MX-80. Measured data (left) and with scaled water contents for MX-80 (right).*

The second step was to relate the detailed information on MX-80 to the properties of the buffer material. For instance, with the blending of the bentonite with 50 % sand it could be expected that the water carrying capacity would be 50 % than for the pure material. More over, it was noticed that the Cation Exchange Capacity (CEC), and therefore probably also the montmorillonite content, for the Avonlea material was slightly higher than for MX-80: 88 meq/100 g for Avonlea (Graham 1997) as compared to 75 meq/100 g for MX-80 (e.g. Karnland et al. 2006).

Under the assumption that the water content is proportional to the CEC value for a given relative humidity is it possible to scale the retention data for MX-80 for the montmorillonite content in the buffer material. A condition for this is that both materials are sodium bentonites. Water contents (w) can be scaled according to:

$$w'_{MX-80} = \frac{CEC_{Buffer}}{CEC_{MX-80}} \cdot w_{MX-80} \qquad (2\text{-}3)$$

The scaling factor is in this case 0.6. Hydration and dehydration paths for MX-80 was scaled with this factor and is shown in Figure 2-16 (right). It can be noticed that the curve provided in the modeling guidelines coincide with the scaled hydration path.

The BCE is however characterized by significant dehydration, and it therefore appears to be justified to choose a retention curve that is steeper than the provided line. An alternative van Genuchten curve was therefore adopted (Table 2-1). This line intersects the provided curve at the initial condition, and approach the scaled dehydration path for higher suction values (Figure 2-17).

Table 2-1. Adopted retention curve parameters.

Experiment	P_0 (MPa)	I
ITT	7.2	0.42
BCE	4.66	0.24

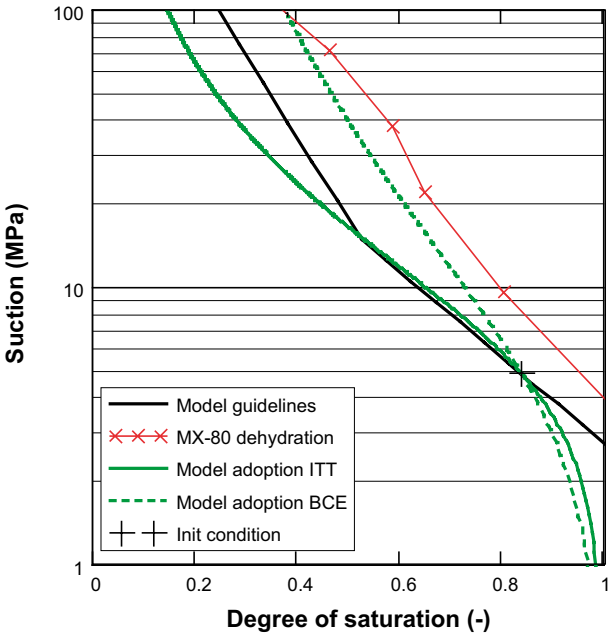

Figure 2-17. *Buffer material retention curve according to modeling guidelines, scaled dehydration paths for MX-80 and model adoptions for ITT and BCE. Red and black lines were based on experimental data for free swelling conditions and the water contents for these were divided with the water content at saturation (i.e. 20.8 %). Green lines are van Genuchten curves.*

Buffer moisture transport processes

In the course of the work, a slightly novel approach for the moisture transfer in the buffer material has been investigated. The basic assumption for this is that moisture is only transported in vapor form during unsaturated conditions. The motivation for this assumption is that vapor pressures tend to equilibrate during non-isothermal conditions (Åkesson 2008). The development of a progressing saturation front, governed by Darcy's law, was also sought. A motivation for this was provided by the laboratory tests, described in the next chapter, which fairly conclusively exhibited the characteristics of progressing fronts. The conceptual description is illustrated in Figure 2-18.

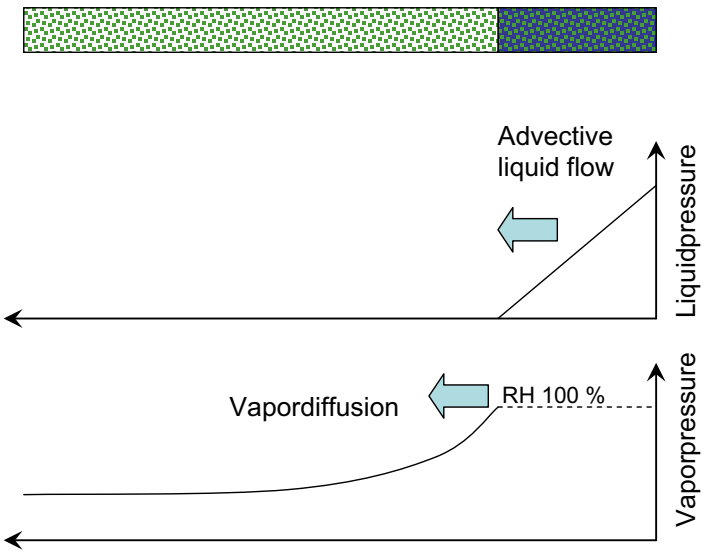

Figure 2-18. *Conceptual view of moisture transfer in buffer material: liquid advective flow through the saturated part, and vapor transport through the unsaturated part.*

The liquid flow is driven by the liquid pressure (P_l) gradient, and the volumetric flux (q) is calculated with Darcy's law:

$$\vec{q} = -\frac{k \cdot k_r}{\mu} \nabla P_l \tag{2-4}$$

where k and k_r is the intrinsic and relative permeability, respectively, and μ is the liquid viscosity.

The vapor diffusion is driven by gradient in the vapor mass fraction in the gas phase (ω_g^w), and the mass flux (i) is calculated with Fick's law:

$$\vec{i} = -n \cdot \tau \cdot (1 - S_l) \cdot \rho_g \cdot D \cdot \nabla \omega_g^w \tag{2-5}$$

where n, τ, S_l and ρ_g is the porosity, tortuosity, degree of liquid saturation, and gas density, respectively. The diffusion coefficient (D) is calculated as:

$$D = 5.9 \cdot 10^{-6} \frac{(273.15 + T)^{2.3}}{P_g} \tag{2-6}$$

where T and P_g, is the temperature and gas pressure, respectively.

The approach was implemented through application of a threshold in the relative permeability (k_r) law, through which k_r is set to zero below a certain high value, e.g. 0.95 (see Figure 2-19, left):

$$k_r = \begin{cases} A \cdot \left(\frac{S_l - S_{l0}}{1 - S_{l0}} \right)^{\lambda} & \text{if} \quad S_l \geq S_{l0} \\ 0 & \text{otherwise} \end{cases} \tag{2-7}$$

where S_l is the saturation degree, A and λ are parameters and S_{l0} is the threshold saturation degree.

In addition, the vapor tortuosity factor (τ) was allowed to have values higher than one. . The motive for this is analogous to the role of liquid islands discussed by Philip and de Vries (1957). A hydrated bentonite grain in a vapor pressure gradient field would not block the vapor transport like a grain of sand, but would rather absorb vapor on the front side and release it on the back side, each side in equilibrium with the local vapor pressure. This transfer should be related to the water contents, so that it would enhance the total flow at higher water contents, but reduce it at lower contents. The coefficient factor used in the constitutive laws, $\tau \cdot n \cdot (1 - S_l)$, has the opposite moisture dependence. The choice of the tortuosity factor value is therefore largely a compensation for this expression.

When ITT was modeled, τ was chosen under the assumption that $\tau \cdot n \cdot (1 - S_l)$ equals unity, and τ would in this case be approx. 30. Later when BCE was modeled, it was found that this value exaggerated the vapor transfer and instead a lower value was chosen (τ = 1). This approach is commented in the discussion at the end of Section 2.3.5.

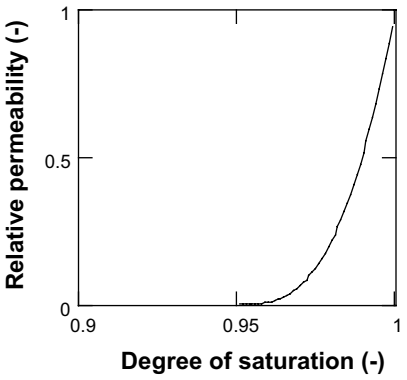

Figure 2-19. *Relative permeability law with a high threshold value.*

2.3.3 Laboratory tests

Introduction

Data from two water uptake tests has been provided together with the modeling guidelines. These tests were made through applying pressurized water on one side of an oedometer and the water uptake was quantified continuously (Figure 2-20, right). The pressure was increase stepwise from approx. 10 to 1 000 kPa. The evolution of the rate of water uptake is shown together with scheme of the applied pressures in Figure 2-20 (left).

The material in the tests had different properties. One test, denoted H-064-2, had a dry density of 1.7 kg/dm^3 and an initial saturation of 82.8 %. The other test, I-014-2, had a dry density of 1.56 kg/dm^3 and an initial water content of 19.8 %. The presentation below focuses on the H-064-2 test since this had properties similar to the material used in the field tests. It should nevertheless be noted that the results from the evaluation were basically the same in both tests.

Simple solution

A simple solution was first elaborated from this problem. This solution was based on the assumption that the water uptake takes place as a pure saturation front without any vapor transfer in the unsaturated part (Figure 2-21).

The calculation is performed iteratively in such a way the flow rate for each step is derived from the current pressure and the current distance to the front:

$$q = K \cdot \frac{P}{L} \tag{2-8}$$

This flow rate and the specified time step (Δt) are in turn used to calculate the increment in distance (ΔL):

$$q \cdot \Delta t = n \cdot (1 - S_r) \cdot \Delta L \tag{2-9}$$

where n is the porosity (= 0.358). Finally, the distance to the front was updated by adding the current distance with the length increment. The distance to the front was however not allowed to exceed the height of the sample (43.5 mm).

The result from such a calculation is shown in Figure 2-22. The hydraulic conductivity value was set to $5.3 \cdot 10^{-13}$ (m/s). The agreement between the measured and the calculated uptake rates are generally quite good and the tests therefore fairly conclusively exhibits the characteristics of a progressing front.

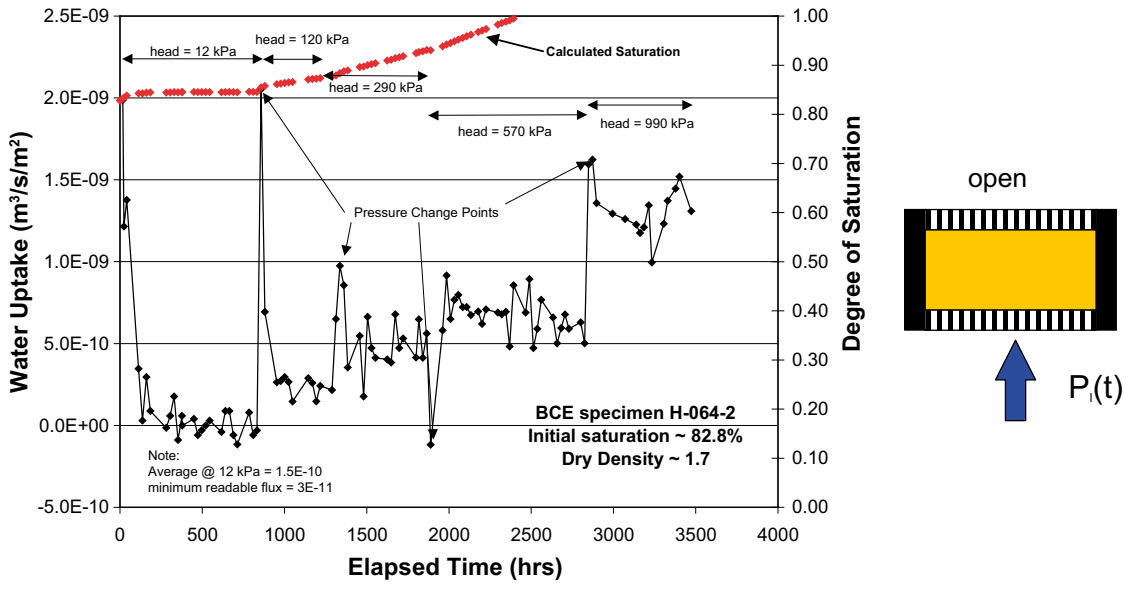

Figure 2-20. *Water uptake test. Evolution of uptake rate and pressure scheme (left). Schematic test geometry (right).*

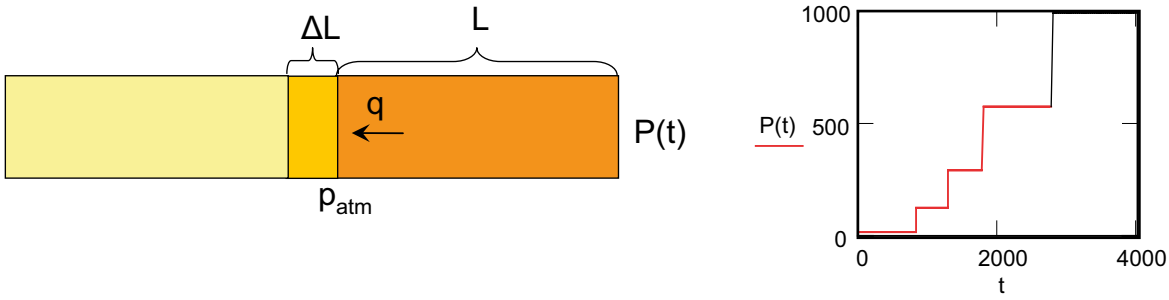

Figure 2-21. *Schematic representation of a progressing saturation front with marked increment in length (left). Applied pressure protocol (right).*

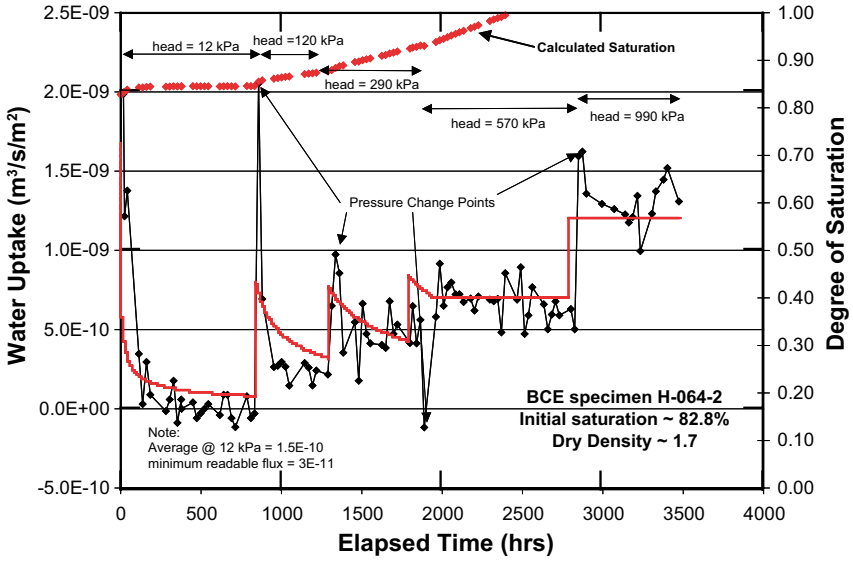

Figure 2-22. *Results from the simple solution overlain experimental data from water uptake test. Thin red line shows results from the simple solution.*

Numerical modeling

The same type of behavior that was found with the simple solution was sought through FEM numerical modeling. A 1D model with a prescribed protocol for the hydraulic boundary conditions was created. An atmospheric pressure was kept on the back side with a negative transition number so that only an outflow was allowed (Figure 2-23).

A number of modeling approaches were tried, including the one outlined in Section 2.3.3. However, the only approach found with which the results resembled the ones from the simple solution was through extreme lowering of the retention curve (Figure 2-24, left). This was modeled as a pure H problem (without vapor) and with the cubic relative permeability law. The used hydraulic conductivity and porosity were identical to the values used in the simple solution.

The results from this model are shown together with the simple solution in Figure 2-24 (right). It can be noted that the general evolutions are the same but that the numerical solution exhibits a variation which originates from the filling of each individual element.

This exercise indicates that a low slope of the retention curve (close to $S_l = 1$), rather than a detailed description of the moisture transfer at unsaturated conditions, is necessary to produce a saturation front. The notion of a low slope retention curve is further discussed at the end of Section 2.3.5 which includes an evaluation of psychrometer data from ITT. Unfortunately, both these results were obtained late in this modeling task and could therefore not be further analyzed.

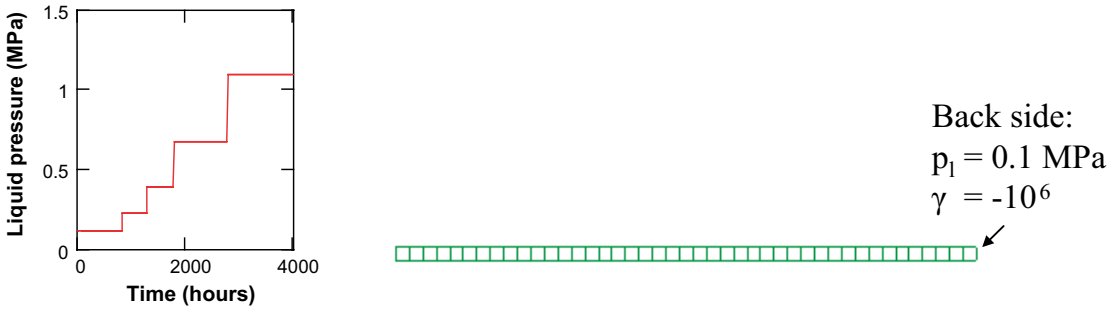

Figure 2-23. *Model geometry with 43 elements of 1x1 mm. Pressure protocol (left).*

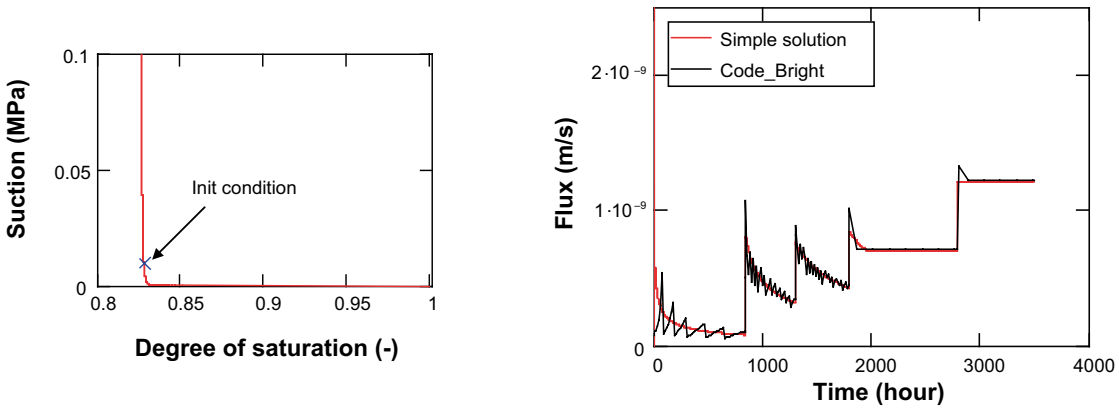

Figure 2-24. *Used retention curve for the water uptake test (left).Model results (right).*

2.3.4 Isothermal test

Introduction

The ITT was modeled with a 3D geometry with two symmetry planes. The modeling work was performed with the finite element program Code_Bright, version 2.2 (CIMNE 2002). The problem was modeled as a pure H problem, but in some also as a TH problem, although the conditions were basically isothermal. The reason for this was to allow vapor transport.

Two types of models were made: open borehole models and buffer hydration models. The purpose of the open borehole models was to enable a direct evaluation of the inflow into the borehole prior to the installation of the buffer, whereas the buffer hydration models were complete calculations.

Model description

Geometry and mesh

The dimensions of the geometry are shown in Figure 2-25. The tunnel, borehole, buffer and pump sump was modeled explicitly. No buffer was included in the open borehole models. The concrete plug was only treated as impermeable surfaces. The geometry was discretisized in 5 999 nodes and 26 200 tetrahedral elements (Figure 2-26).

Time line and boundary conditions

The time line which covered 3 683 days was divided in two main intervals: (i) open borehole and (ii) buffer hydration (see Figure 2-27). The intermediate installation was modeled as being done during one day (day 1 300–1 301). The seepage measurements were performed during the latter part of the open tunnel interval (day 1 100–1 153). This was taken into account through executing the open models up to day 1 153.

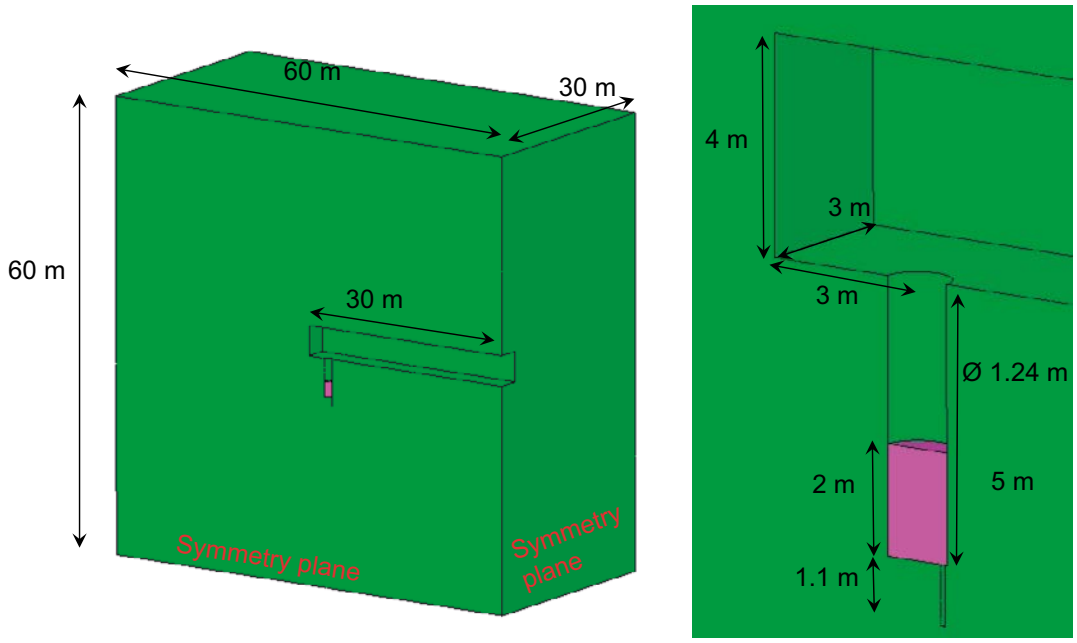

Figure 2-25. *Model geometry.*

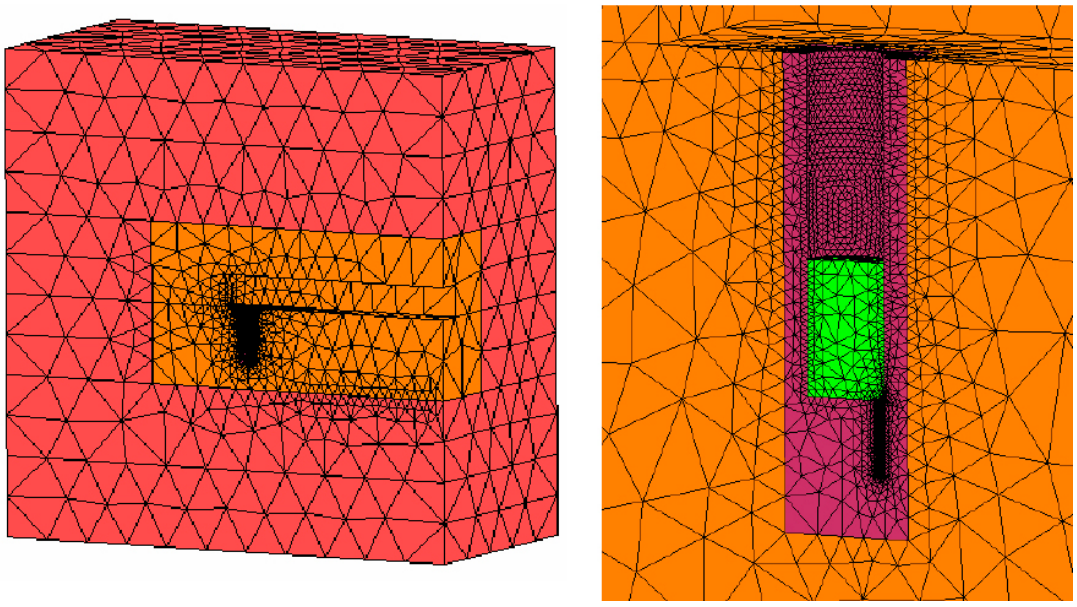

Figure 2-26. *Model mesh.*

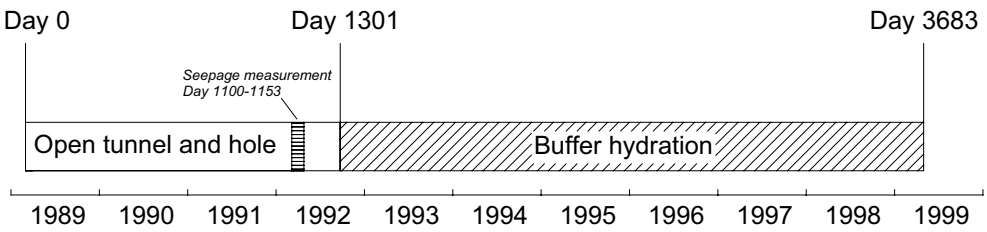

Figure 2-27. *Time line for ITT.*

The initial conditions were a homogenous temperature of 10 °C and a hydrostatic pressure distribution throughout the model, from 1.8 MPa at the top to 2.4 MPa at the bottom.

The outer boundary conditions are illustrated in Figure 2-28. These were, except the symmetry planes, kept at hydrostatic pressure, i.e. varying from 1.8 to 2.4 MPa. In the TH models, these outer boundaries were kept at 10 °C. The reason for this was that the inflowing water otherwise would cool the model.

The surface boundaries for the tunnel, borehole and pump sump were kept at atmospheric pressure in the open borehole models. In the buffer hydration models (with buffer material) all surface and volume boundaries were kept at atmospheric pressure during the initial period up to the installation event (Figure 2-29, left). After this, the surfaces corresponding to the concrete plug, the pump sump and the upper surface of the buffer were closed (Figure 2-29, right).

The buffer installation was implemented as a ramping of the liquid pressure volume boundary condition for the buffer: from 0.1 to –4.8 MPa. The liquid buffer pressure was set free once the ramping scheme reached the intended 4.8 MPa suction, i.e., that the buffer properties came into play at this point.

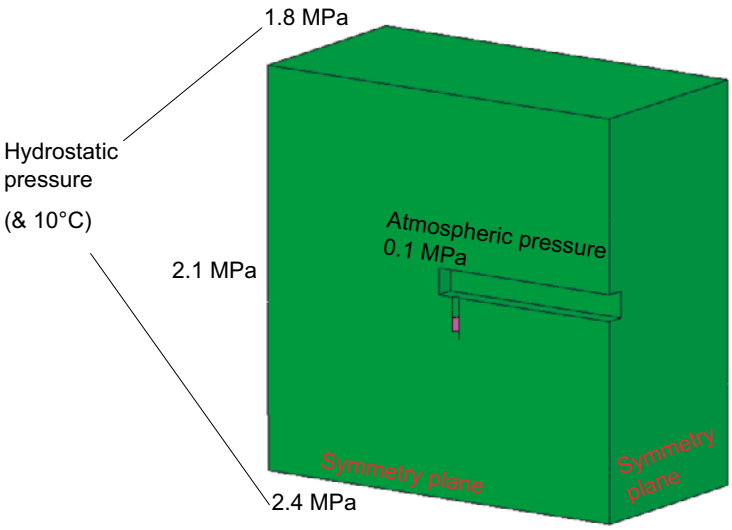

Figure 2-28. *Outer boundary conditions.*

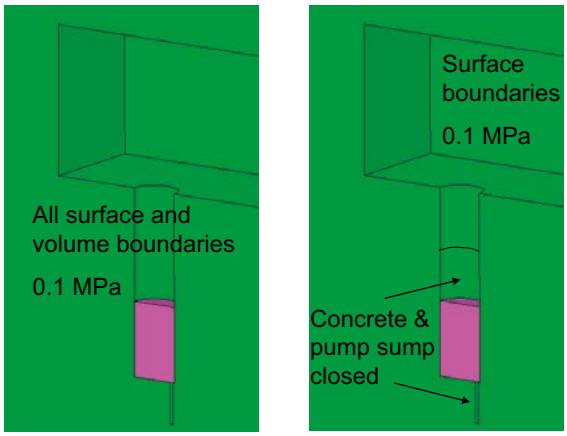

Figure 2-29. *Inner boundary conditions for buffer hydration models.*

Model versions and material parameter values

Three different open borehole models, with k-values ranging from 10^{-19} to 10^{-20} m^2, were tested (see Table 2-2). In all versions the cubic power law was applied for the relative permeability.

As will be evident from the results, the model with the highest permeability showed the best agreement with the measured inflow. This k-value was therefore subsequently used in the buffer hydration models. Three such models were investigated (see Table 2-3): One H-model with the cubic power law for the relative permeability; and two TH-models with high τ-values (30) and high thresholds in the relative permeability (0.999 and 0.95). This approach is commented in the discussion at the end of this section. In all three models the value of $5 \cdot 10^{-20}$ m^2 was used for the buffer intrinsic permeability. This value was first derived from a compilation of k-values presented by Dixon et al. (2002). Later on, this was also confirmed through evaluation of the water uptake tests (see Section 2.3.5). The porosity of the rock and the buffer was 0.005 and 0.359, respectively.

Table 2-2. Open borehole models – hydraulic transport parameters.

Version	Rock	
	k_r	k (m^2)
OB1		$1 \cdot 10^{-19}$
OB2	S_l^3	$5 \cdot 10^{-20}$
OB3		$1 \cdot 10^{-20}$

Table 2-3. Buffer hydration model – hydraulic transport parameters.

Version	Problem	Rock	Buffer		
		$k_r \cdot k$ (m^2)	k (m^2)	k_r	τ
BH1	H			S_l^3	–
BH2	TH	$S_l^3 \cdot 10^{-19}$	$5 \cdot 10^{-20}$	$S_{l0} = 0.999$	30
BH3	TH			$S_{l0} = 0.95$	30

Results

Water inflow

The open borehole models were run for 1 153 days, corresponding to end of the seepage measurement period. All models reached steady-state conditions before the end of that period. The inflow into the borehole was evaluated as horizontal flux along vertical surfaces and vertical flux along horizontal surfaces as shown in Figure 2-30 (middle). The pump sump was included in this evaluation. The volumetric inflow was calculated as the product of the flux and a representative area for each point. Finally, the contributions from the different areas were added in order to correspond to the four collection systems shown in Figure 2-30 (left).

The results for all three models are shown in Figure 2-30 (right) together with the measured values, and it can be noted that the model with the highest k-value gave the best agreement with the measured data.

Pore water pressure

The pore pressure distributions along two drilled holes with piezometers are shown in Figure 2-32. The location of the piezometers is shown in Figure 2-31. It can be noted that the modeled pressure were slightly higher than the measured values. This is especially apparent for the hole that was closer to the buffer borehole. It can also be noted that the model with advective flow (BH1) displayed the highest pressures for this hole. This is due to that this model reached total saturation before the end of the test.

Radial pore pressure distributions at buffer mid-height are shown in Figure 2-33. It can be noted that the initial distribution is fairly close to the measure profile. At the end of the test, the pressure at 6–7 m from the borehole axis was also quite close. At the rock wall, however, the modeled pressures exceeded the measured values significantly.

The pore pressure evolution at the three positions corresponding to the location of the piezometers IRP2, IRP3 and IRP4 is shown in Figure 2-34. In the case of BH1 with advective flow, it can be noted that the pressures reached their maxima around day 2 300 (model time). This was caused by the model reaching total saturation at this time.

The diffusive models both displayed a rapid pressure buildup to 0.5–1 MPa, after which the buildup was slower. In the case with a high permeability threshold (BH2) this buildup was smooth, whereas with the lower permeability threshold (BH3) the buildup was varying (see Figure 2-19). This is an effect of the progress of the saturation front in the buffer.

Finally a note about the experimental pore pressure data for ITT. These have been regarded as relative pressures. An atmospheric pressure of 0.1 MPa has therefore been added in those graphs showing absolute pressures.

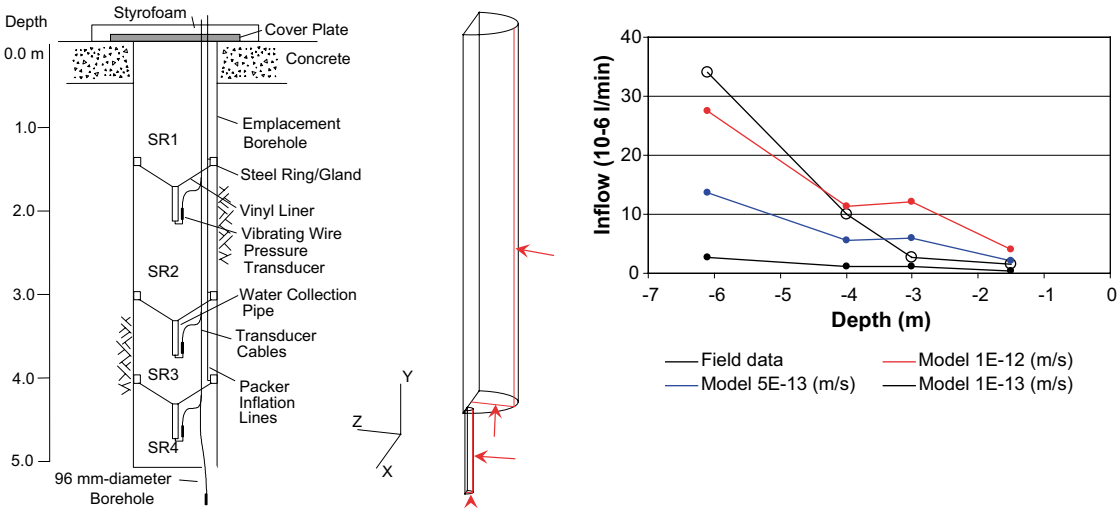

Figure 2-30. *Seepage collection system (left). Scan-lines for evaluation of inflow in models (middle). Inflow at different depths in bore hole; model and field data (right).*

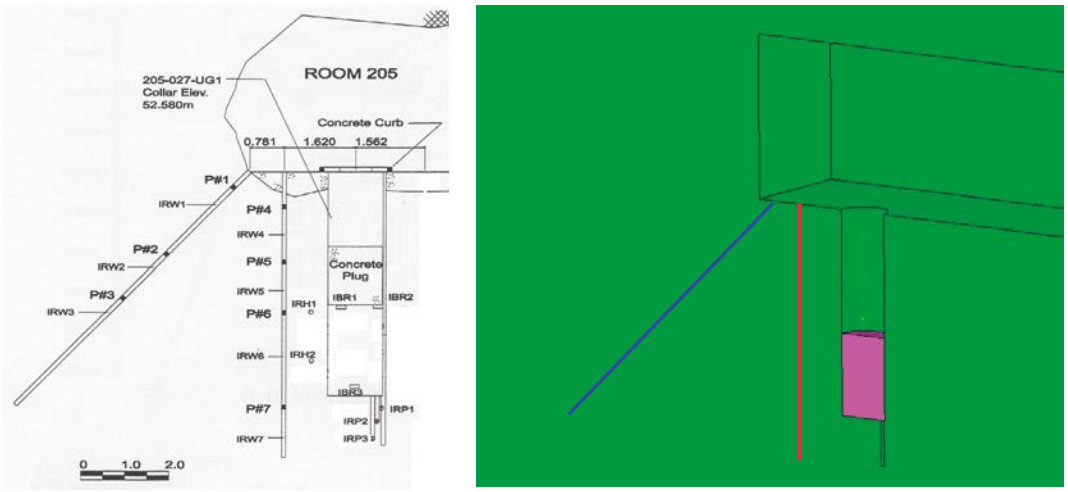

Figure 2-31. *Location of piezometers IRW1-7 (left) and corresponding scan-lines in models (right).*

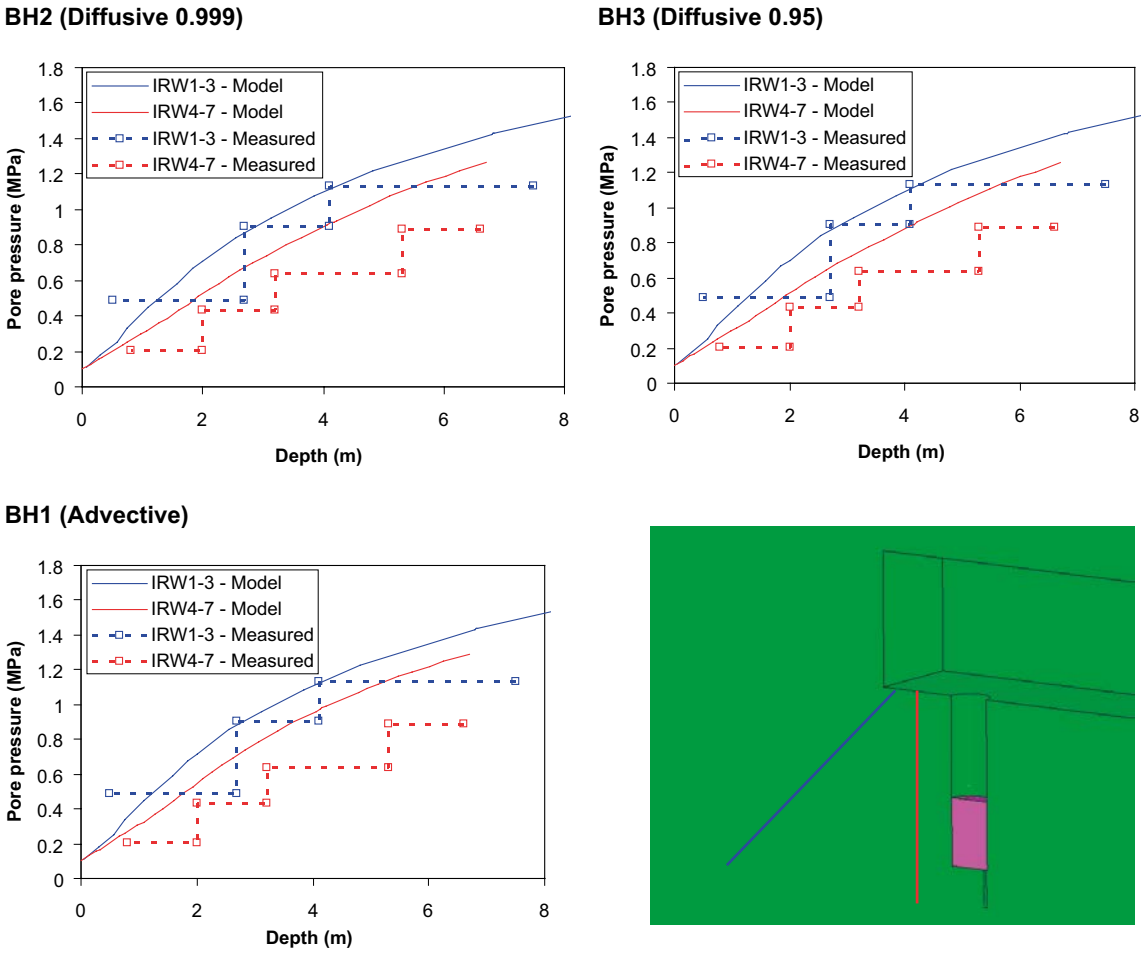

Figure 2-32. Pore pressure (absolute) profiles along holes with piezometers (IRW 1–7) at the end of the test.

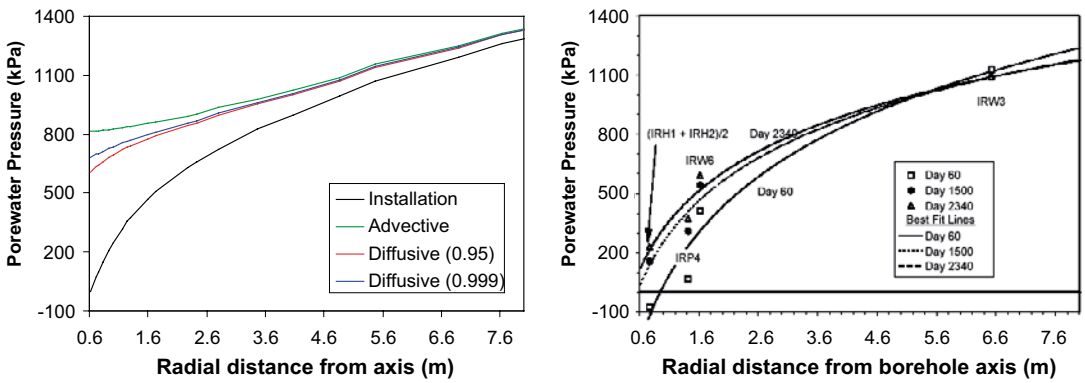

Figure 2-33. Radial pore pressure (relative) profiles at buffer mid-height. Model results toward the end of the tunnel at installation and at EOT for different versions (left); measured data (right) from Dixon et al. (2002).

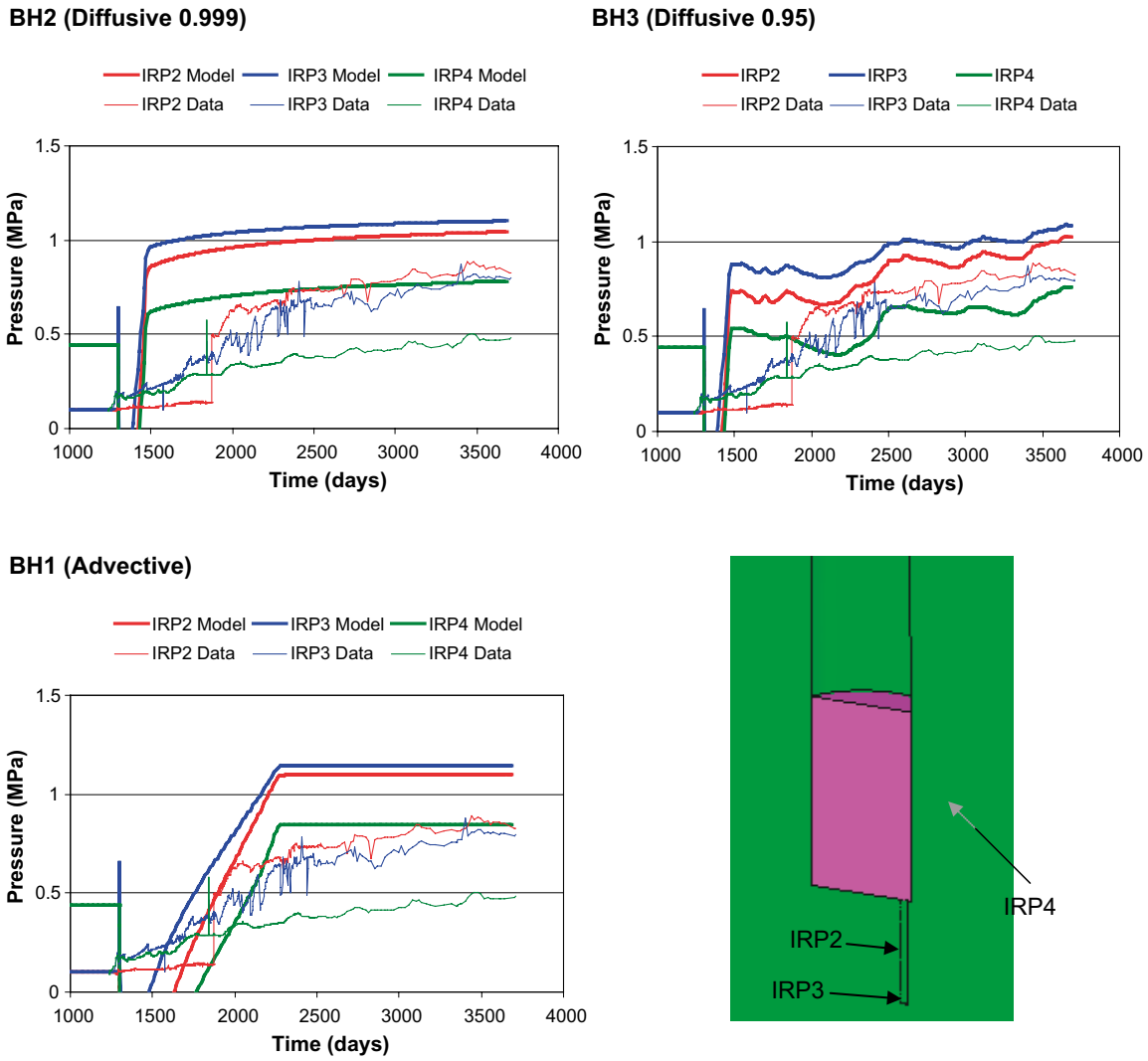

Figure 2-34. *Pore pressure (absolute) evolution at the positions of piezometers IRP2-4.*

Buffer hydration

Two types of experimental data are available for description of the buffer hydration: psychrometer data (see Figure 2-35) and EOT water contents. In the following section, results from the diffusive models (BH2 and BH3) are compared with experimental data. The advective model was disregarded since this reached total saturation prior to the end of the test.

Model results were evaluated along horizontal scan-lines in the symmetry plane. Each scan-line thereby provides two sets of data when these are related to the radius. The model suction values were evaluated as the atmospheric pressure (0.1 MPa) minus the model liquid pressure. The suction value was set to zero in cases when the liquid pressure exceeded the atmospheric pressure. The model water contents were evaluated as the product of the liquid saturation degree and the maximum water content (20.8 %).

Three scan-lines were evaluated with regard to suction (Figure 2-36). Two of these (0.5 and 1.5 m below the top of the buffer) correspond to levels instrumented with psychrometers (see Figure 2-35). Eight sensors were located at each of these levels. Eight scan-lines were evaluated with regard to water content (Figure 2-37).

The measured suction values were used for comparison, and not the values that were adjusted for the swelling pressure and included in the available spreadsheets. It was noted that all measured suction results increased significantly at the end April 1999. This appears to be a consequence of the dismantling procedure, and therefore the data for April 1 was used to represent the EOT conditions.

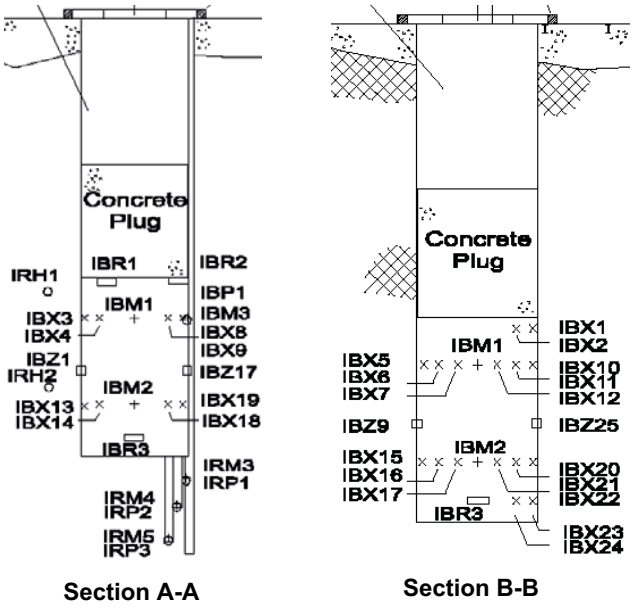

Figure 2-35. *Location of psychrometers (marked ×) in the buffer (Dixon et al. 2001). Section A-A was defined along the tunnel axis (corresponding to the symmetry plane of the model), while B-B was defined perpendicular to the tunnel axis.*

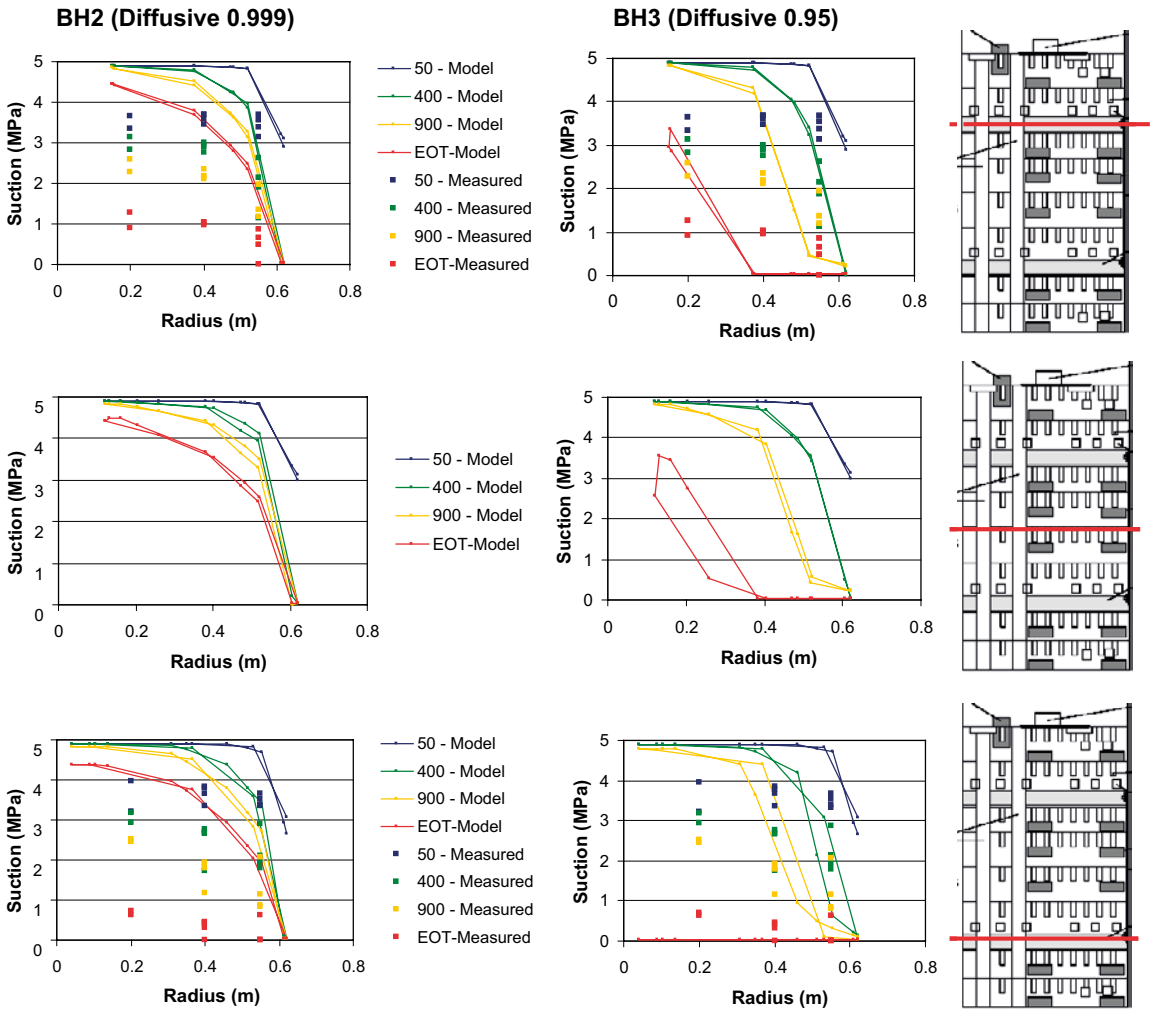

Figure 2-36. *Suction profiles at three different sections in the buffer (0.5 m, 1 m and 1.5 m below the top of the buffer).*

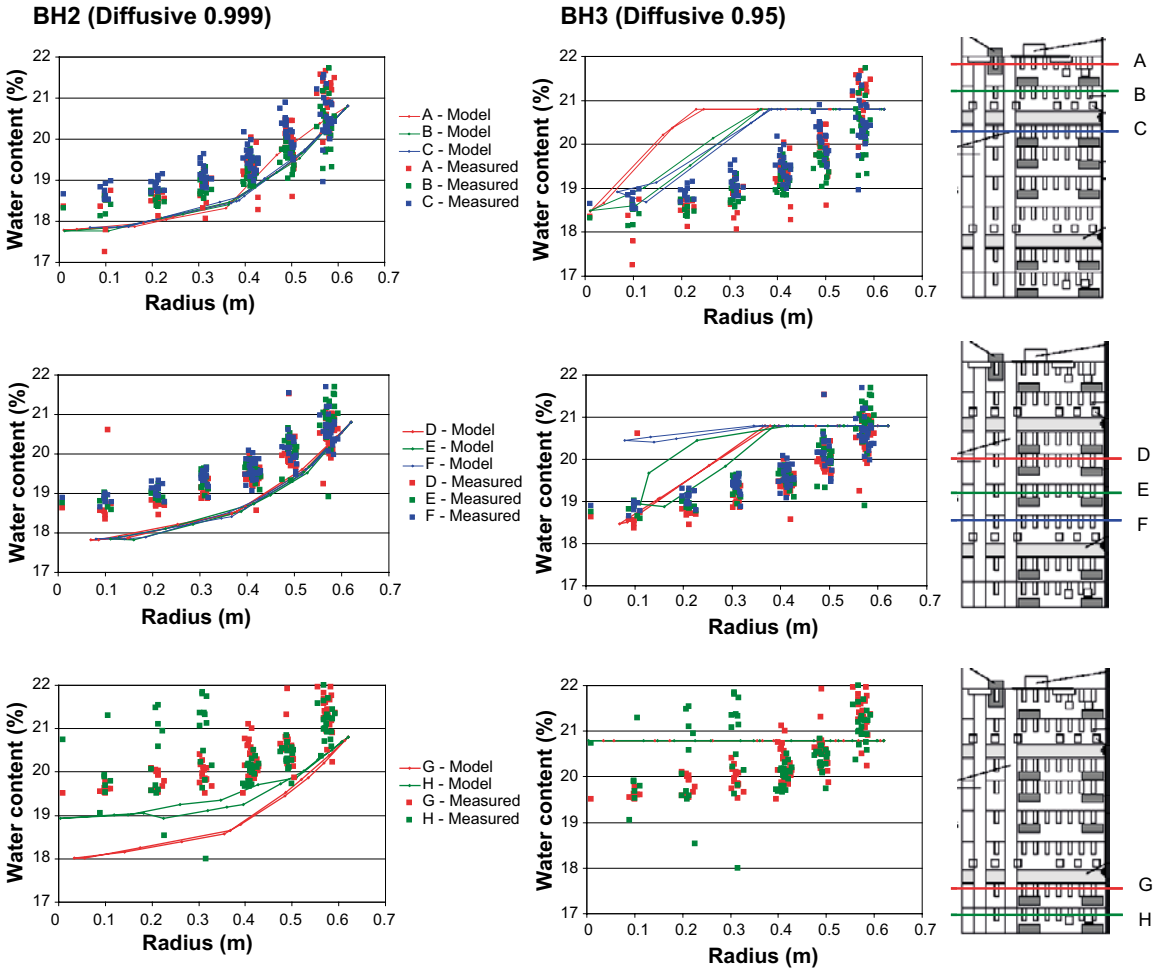

Figure 2-37. *Water content profiles at eight sections in the buffer at the end of the test.*

It was also noted that 7 sensors out of the 24 sensors (5 of the 16 sensors used for comparison in Figure 2-36) displayed results below zero at some period during the test period (Figure 2-38). These sensors were regarded to represent saturated conditions and were set to zero in the comparisons after these events.

In the suction comparisons in Figure 2-36 it can be noted that the initial modeled suction values were systematically higher than the measured values: 4.9 MPa in the models and slightly below 4 MPa as shown by the psychrometers. This may suggest that the actual water content was higher than the 17.5 % that was stated in the modeling guidelines or that the used retention curve was too high. This is discussed later.

The nodes at the wall boundary reached saturated conditions before day 400 in both models. Whereas this front progressed at least 0.2 m in the version with the lower threshold (BH3) it remained stationary in the version with the higher threshold (BH2). The notion of a progressing front is supported by the psychrometer data from the lower section.

In general, the model with the higher threshold (BH2) tends to underestimate the rate of hydration, whereas the model with the lower threshold (BH3) tends to overestimate the rate. The same observation can be made for the comparisons of the water content in Figure 2-37. The water contents measured close to the rock wall was fairly close to the maximum water content of 20.8 % considered in the model. This therefore supports the notion that the rock boundary was saturated.

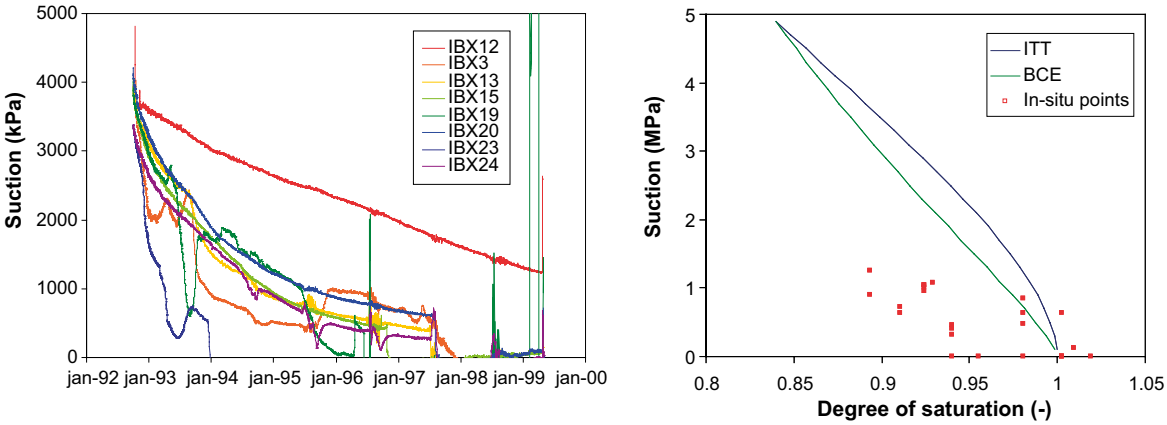

Figure 2-38. *Measured evolution of suction for selection of psychrometers, see text (left). Measured suction vs. final degree of saturation (right). Model retention curves are shown for comparison.*

Discussion

The following observations can be made for the three buffer hydration models: The conventional H model with only advective flow (BH1) exaggerated the rate of hydration significantly. The diffusive model with a high threshold (BH2) appears to have underestimated the rate of hydration and exaggerated the pore pressures close to the rock wall. The diffusive model with a lower threshold (BH3) appears to have overestimated the rate of hydration and also exaggerated the pore pressures, although to a lesser extent than in BH2.

The open borehole models indicate that 10^{-12} m/s is a representative value for the hydraulic conductivity of the rock. The buffer hydration models nevertheless displayed pore pressures close to the borehole that were significantly higher than the measured values. This may be a result of some type of connection or short-circuit along the rock wall, and this type of explanation was studied in the case of BCE. In ITT, however, it is more likely that the discrepancies between modeled and measured pore pressures are due to the difficulties associated with a progressing saturation front. This obstacle became apparent in the evaluation of the water uptake tests. The pressure conditions associated with the progress of a pure 1D axis-symmetric front is described in Appendix 1.

It is possible that the models could be improved by modification of the used retention curve. The experimental evolution of suction is illustrated by the left graph in Figure 2-38. This show the results from the sensor with the highest suction value at the end of the test (IBX12) together with the results from those sensors that reached zero suction at some point during the test period. All remaining sensor results can thus be found between these extremes. This graph shows the fairly well defined level at the start slightly below 4 MPa. This is clearly below the assumed initial value of 4.9 MPa, which was based on the provided retention curve (see Equation 2-1) and an initial water content of 17.5 % as stated in the modeling guidelines. In retrospect, this value of the water content actually underestimates the true value as shown by the compilations in Figure 2-39, although the deviation is minor. The true value, in ITT as well as in BCE, was rather 17.9 %. In addition, the provided retention curve also appears to contribute to the deviation. Figure 2-40 shows that the initial conditions, as shown by the analyses of water contents at installation (17.9 %) and the initial suction values for the psychrometers in ITT (slightly below 4 MPa), could only be modeled if the retention curve would be lower than the provided one. An overview of the experimental point on which the provided retention curve was based (Figure 2-40) do not appear to contradict this observation.

The right graph in Figure 2-38 shows a compilation of final suction values and corresponding saturation degrees. The latter values were derived as mean values for samples taken at approximately the same radius and level as the psychrometers. Saturation degrees were calculated as the ratio between these mean water contents and the maximum value of 20.8 %. The employed van Genuchten curves are shown for comparison. The experimental data indicate that the effective retention curve is significantly lower than expression used in the models.

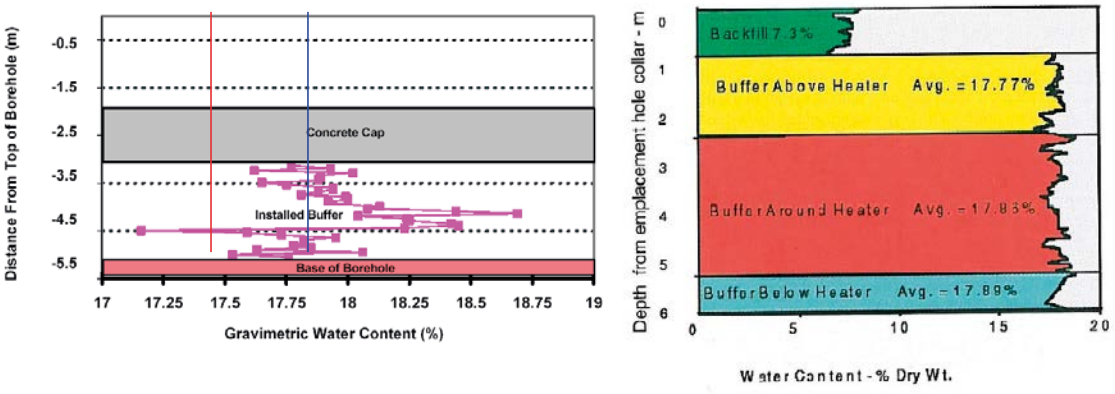

Figure 2-39. *Measured water content at installation of ITT (left, from Dixon et al. 2001) and BCE (right, from Graham 1997). Red line in left graph represents the initial water content stated in the modeling guidelines. Blue line is an approximated average at 17.9 %.*

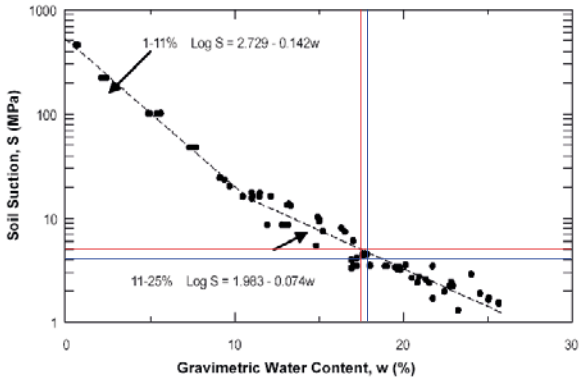

Figure 2-40. *Retention data and curve from modeling guidelines. Red lines represent the initial water content stated in the modeling guidelines and the suction value which follows from the stated curve. Blue lines represent the initial water content from measurements at installation and initial suction values from psychrometers in ITT.*

In retrospect it can also be noted that the chosen approach to model the moisture transfer as an exclusive vapor transport, with a high compensating tortuosity value, was unnecessarily imprecise, since it should be clear that the flow potential can be chosen freely for *isothermal conditions*, for instance the vapor pressure or the liquid pressure. If a flow coefficient, $D_{pl}(S_l)$, can be found that describes the hydration process in terms of gradients in liquid pressure, then the same results can be obtained in terms of gradients in vapor pressure for the flow coefficient $D_{pv} = dp_l/dp_v \cdot D_{pl}(S_l)$. In consequence, it could very well be sufficient to model the unsaturated moisture transfer with the standard relative permeability power law as long as the used retention curve does not exhibit the steep trend close to saturation as given by the van Genuchten expression. This was also noted in the evaluation of the water uptake tests, which showed that a progressing front could be modeled if the retention curve was extremely low. The approach to model the moisture transfer as an exclusive vapor transport should therefore be avoided unless it can be further justified and developed.

2.3.5 Buffer Container Experiment

Introduction

The BCE was modeled with an axis-symmetric 2D geometry. The modeling work was performed with the finite element program Code_Bright, version 2.3 (CIMNE 2002). The problem was modeled as a TH problem. The distinction between open borehole models and buffer hydration models made in the case of ITT was not made for BCE.

Model description

Geometry and mesh

The dimensions of the geometry are shown in Figure 2-41. The tunnel, borehole, buffer, heater, sand filling, backfill, concrete slab and an EDZ was modeled explicitly. The geometry was discretisized in 6 751 nodes and 6 540 quadrilateral elements (Figure 2-42).

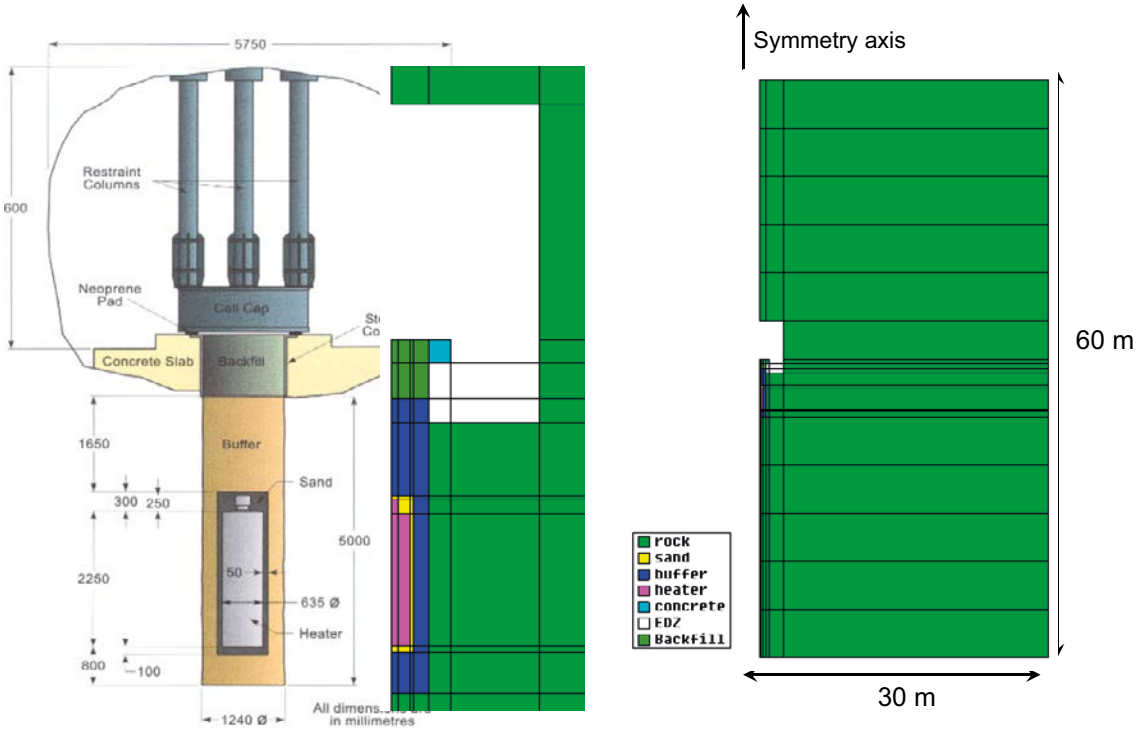

Figure 2-41. *Model geometry.*

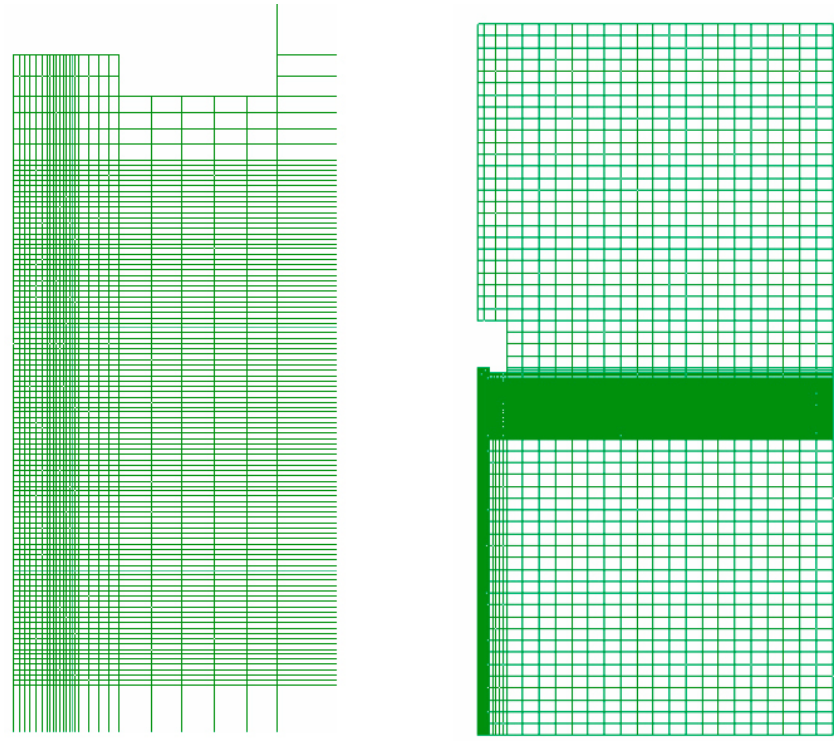

Figure 2-42. *Model mesh.*

Time line and boundary conditions

The time line which covered 1 451 days was divided in five intervals: (i) open borehole, (ii) buffer installation, (iii) buffer hydration without heating, (iv) hydration with 1 000 W heating, and (v) hydration with 1 200 W heating (see Figure 2-43). The seepage measurements were performed during the latter part of the open tunnel interval (around day 364).

The initial conditions were a homogenous temperature of 13 °C and a hydrostatic pressure distribution throughout the model, from 1.2 MPa at the top to 1.8 MPa at the bottom.

The boundary conditions are shown in Table 2-4 and Table 2-5. The outer hydraulic boundaries were kept at hydrostatic pressure, i.e. varying from 1.2 to 1.8 MPa, while the line boundaries in the tunnel were kept at atmospheric pressure, except for the line along the backfill and the concrete slab. The temperature in the tunnel and the outer boundary was kept at 13 °C, in the tunnel however with a low transition number.

During the initial period up to the installation event, all surface boundaries corresponding to fillings in the borehole (heater, sand, buffer and backfill) were kept at atmospheric pressure and 13 °C.

Table 2-4. Thermal boundary conditions.

Interval	Surface boundary		Line boundary		
	Hole filling*	Heater	Tunnel	Outer BC	Heater
1	13 °C	13 °C	13 °C	13 °C	
2			γ = 6	$\gamma = 10^6$	–
3		–			
4	–				1 000 W
5					1 200 W

* All surfaces in borehole except heater.

Table 2-5. Hydraulic boundary conditions.

Interval	Surface boundary			Line boundary	
	Buffer and sand	Heater	Backfill	Tunnel*	Outer BC
1	0.1 MPa			0.1 MPa	Hydrostatic
2	0.1–>–4.8 MPa	–	0.1–>–0.6 MPa		1.2 –> 1.8 MPa
3	–		–		
4					
5					

* All tunnel lines except along backfill and concrete.

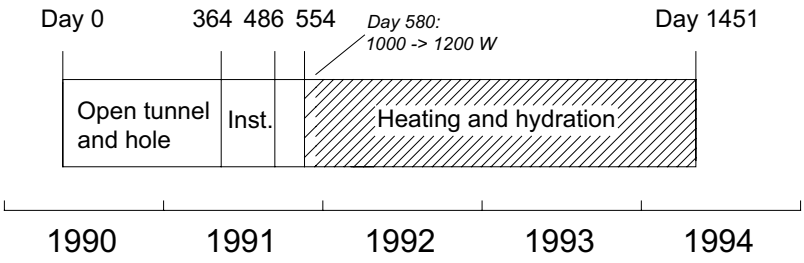

Figure 2-43. *Time line for BCE.*

The subsequent buffer installation was implemented as a ramping of the liquid pressure surface boundary condition for the buffer: from 0.1 to –4.8 MPa. The same condition was used for the sand. In the same way, the backfill installation was modeled by ramping the liquid pressure from 0.1 to –0.6 MPa. During these changes, the temperature was kept at 13 °C. No further change was however made for the heater.

No changes were made during the third interval. During the fourth and the fifth interval the heating was implemented as a line boundary along the symmetry axis of the heater.

Material parameter values and model versions

A number of materials and properties had to be described in the BCE. Compilations of parameter values are given together with their sources in Table 2-6 to Table 2-9. The hydraulic properties of the rock and the buffer were discussed in Section 2.3.3 (see Equation 2-2, 2-4 and 2-6) . It should be noted that the intrinsic permeability value used for the rock in BCE was fitted to give an acceptable agreement with the measured inflows. The EDZ material was treated in the same way as the rock material with one exception: the intrinsic permeability was set two orders of magnitude higher.

The backfill material had an initial water content of 7.2 % and a porosity of 21 % (Guo et al. 2006). The adopted retention curve was based of the retention function for the buffer material provided in the modeling guidelines. The water content was scaled with a factor of one fourth and a van Genuchten expression could by adapted to this scaled curve. An initial water content of 7.2 % thereby corresponds to an initial suction value of 0.7 MPa. A high permeability was chosen given the high content of gravel. The moisture transport was treated in the same way as for the buffer material, with a high vapor tortuosity and a high threshold in the relative permeability law.

The hydraulic properties of the heater and the concrete were chosen not to interfere with the adjacent materials, with a high retention curve and low permeability and vapor tortuosity. The sand was given a low retention curve, a fairly high permeability and a vapor tortuosity of one.

Table 2-6. Retention properties.

Material	P_0 (MPa)	λ
Rock/EDZ[1)]	4	0.65
Sand [3)]	0.002	0.7
Buffer[1)]	4.66	0.24
Backfill[2)]	0.22	0.2
Heater[3)]	500	0.3
Concrete[3)]	500	0.3

[1)] See Section 2.3.3.
[2)] See text.
[3)] Assumptions.

Table 2-7. Moisture transport properties.

Material	k (m^2)	k_r	Vapor τ
Rock[1)]	$5 \cdot 10^{-20}$	S_l^3	10^{-5}
EDZ[2)]	$5 \cdot 10^{-18}$	S_l^3	10^{-5}
Sand[4)]	$1 \cdot 10^{-18}$	S_l^3	1
Buffer[3)]	$5 \cdot 10^{-20}$	Eq. 2.2 $S_{lo} = 0.999$	1
Backfill[4)]	$1 \cdot 10^{-17}$	Eq. 2.2 $S_{lo} = 0.999$	1
Heater[4)]	$1 \cdot 10^{-30}$	S_l^3	10^{-5}
Concrete[4)]	$1 \cdot 10^{-30}$	S_l^3	10^{-5}

1) Tested with inflow measurements.
2) Two orders of magnitude higher than for rock.
3) See Chapter 3.
4) Assumptions.

Table 2-8. Thermal properties.

Material	λ_{dry} (W/mK)	λ_{sat} (W/mK)	C_s (J/kgK)
Rock/EDZ[1)]	3.6	3.6	1 060
Sand[1)]	0.44	1.7[5)]	757
Buffer[2)]	0.7	2	800[6)]
Backfill[3)]	0.7	2	800[6)]
Heater[4)]	220	220	900
Concrete[5)]	1.7	1.7	900

$\lambda = \lambda_{dry}(1-S_l) + \lambda_{sat}S_l$

[1)] Guo et al. (2006).
[2)] Graham (1997).
[3)] Assumed same as buffer material.
[4)] Ingelstam et al. (1982).
[5)] Fälth and Hökmark (2006).
[6)] Value for MX-80 Fälth and Hökmark (2006).

Table 2-9. Porosity and solid density.

Material	n (–)	ρ_s (kg/m^3)
Rock/EDZ[1)]	0.005	2 630
Sand[1)]	0.3	2 650[6)]
Buffer[1)]	0.359	2 680[2)]
Backfill[1)]	0.21	2 650[6)]
Heater[3)]	0.001[5)]	2 700
Concrete[4)]	0.001[5)]	2 800

[1)] Guo et al. (2006).
[2)] Back-calculated from Guo et al. (2006)
[3)] Ingelstam et al. (1982).
[4)] Fälth and Hökmark (2006).
[5)] Deliberately low values.
[6)] Standard value.

The thermal properties of the rock were provided by Guo et al. (2006). The thermal conductivity of the buffer material was derived from Graham (1997), and the same values were used for the backfill material. The specific heat for the buffer material and the backfill was given the value previously used for MX-80 (Fälth and Hökmark 2006). The thermal conductivity for dry sand for sand was provided by Guo et al. (2006). The value for water saturated sand was taken from Fälth and Hökmark (2006). The specific heat of the sand was calculated as the ratio between the volumetric heat capacity and the dry density provided by Guo et al. (2006). The heater was given thermal properties for aluminum (Ingelstam et al. 1982). The thermal properties for the concrete were taken from Fälth and Hökmark (2006).

The porosities for the rock, buffer, backfill and sand were taken from the guidelines (Guo et al. 2006). The porosities for the heater and concrete were set to low values.

The solid density of the rock was taken from the guidelines (Guo et al. 2006). The corresponding value for the buffer material was back-calculated from the data in the guidelines. A standard value was used in the case of the sand and the backfill. Data for aluminum and concrete was taken from Ingelstam et al. (1982) and Fälth and Hökmark (2006), respectively.

Five different model versions were investigated (see Table 2-10). The first version (the base case) was made according to the description above and all subsequent versions were based on this with minor modifications. Two changes were made in second version (the conventional case): the retention curve used for the buffer material in ITT and the cubic power law was used for the relative permeability of the buffer and the backfill. In the third version (the EDZ case), a zone around the borehole, with a thickness of 38 cm, was modeled as EDZ material (Figure 2-44). In the forth version (the Tau 30 case), the vapor tortuosity factor for the buffer and the backfill was set to 30. This was the same as for ITT. Finally, in the fifth version (the Cut 95 case) the threshold in the relative permeability law used for buffer and backfill was set to 0.95. This value was also investigated in ITT.

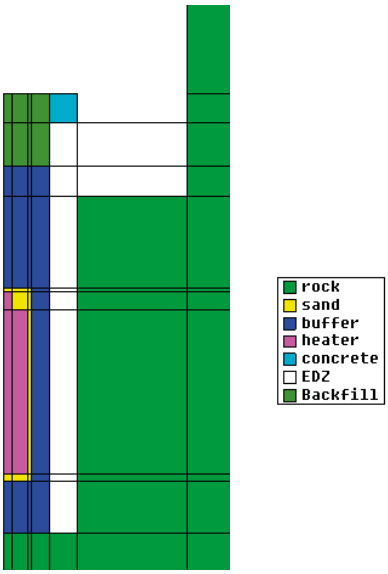

Figure 2-44. Materials in model version with EDZ along borehole.

Table 2-10. Model versions.

Base case:	As described above
Conv. Case:	Buffer retention as in ITT Buffer and backfill k_r: S_l^3
EDZ case:	EDZ along borehole
Tau 30 case:	Buffer and backfill τ: 30 (same as ITT)
Cut 95 case:	Buffer and backfill threshold in k_r: 0.95

Results

Water inflow

The inflow into the borehole was evaluated as the horizontal flux along the vertical line shown in Figure 2-45 (right). The variation of the flux along this line is shown in the left graph. The volumetric inflow was calculated as the product of the flux and a representative area for each point. Finally, the contributions from the different areas were added so that the sums corresponded to the five collection systems shown in the Figure 2-45 (middle). These sums are shown in Table 2-11 together with the measured inflow. It can be noted that the agreement is fairly good except for the upper collection system which was greatly underestimated.

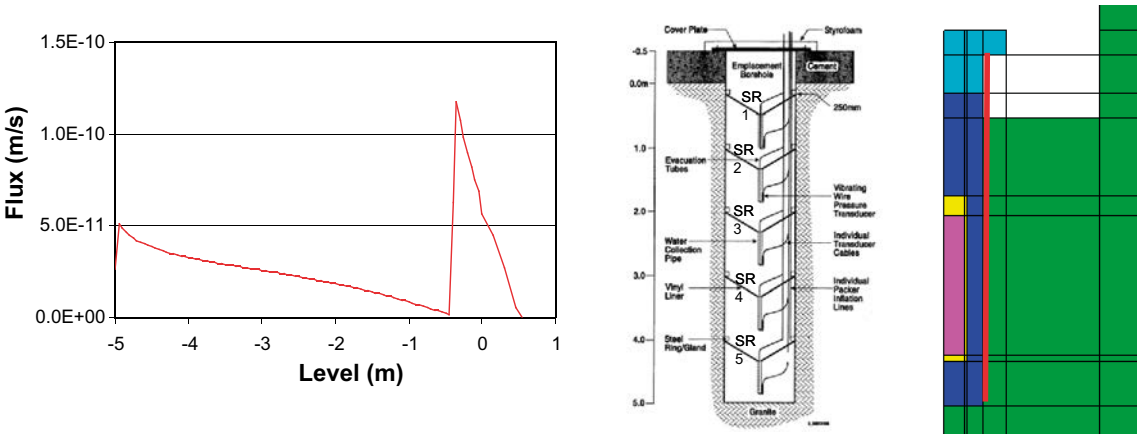

Figure 2-45. Model flux along rock wall (left). Seepage collection system (middle). Scan-line for evaluation of inflow in model; Base Case.

Table 2-11. Measured and modeled inflow at different collection sections; Base Case.

	Measured (10^{-11} m^3/s)	Modeled (10^{-11} m^3/s)
SR1	498	14
SR2	8.05	8
SR3	5.18	5
SR4	3.48	9
SR5	7.0	11

Temperature profiles and contours

Temperature profiles along three vertical and one horizontal scan-lines were evaluated for four points in time. The scan-lines are shown in Figure 2-46 and it can be noted that the innermost line (a) is actually a composite of three lines. The modeled profiles are shown in Figure 2-47 together with experimental results. It can be seen that the agreement is reasonable.

Plots of temperature contours in buffer and rock are shown in Figure 2-48 and Figure 2-49.

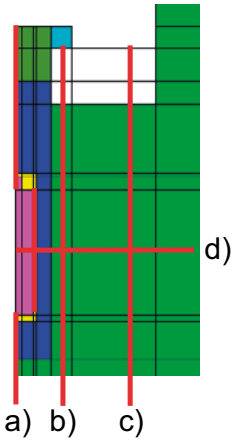

Figure 2-46. *Scan-lines in model for evaluation of temperature profiles.*

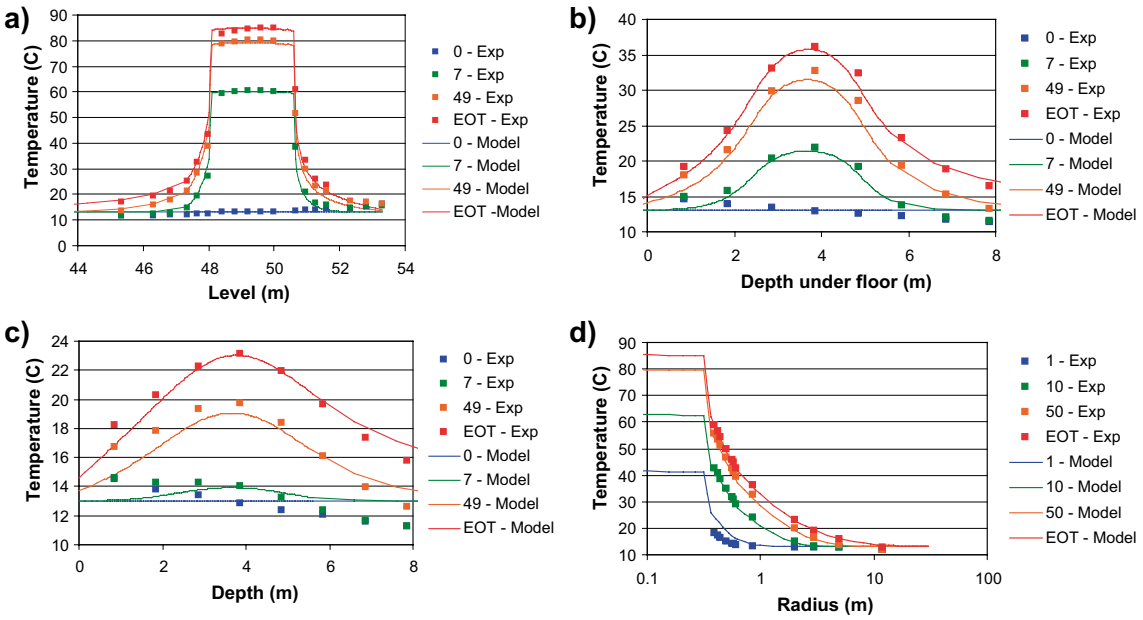

Figure 2-47. *Modeled and measured temperature profiles along scan-lines. Day 0 corresponds to day 554 model time; Base Case.*

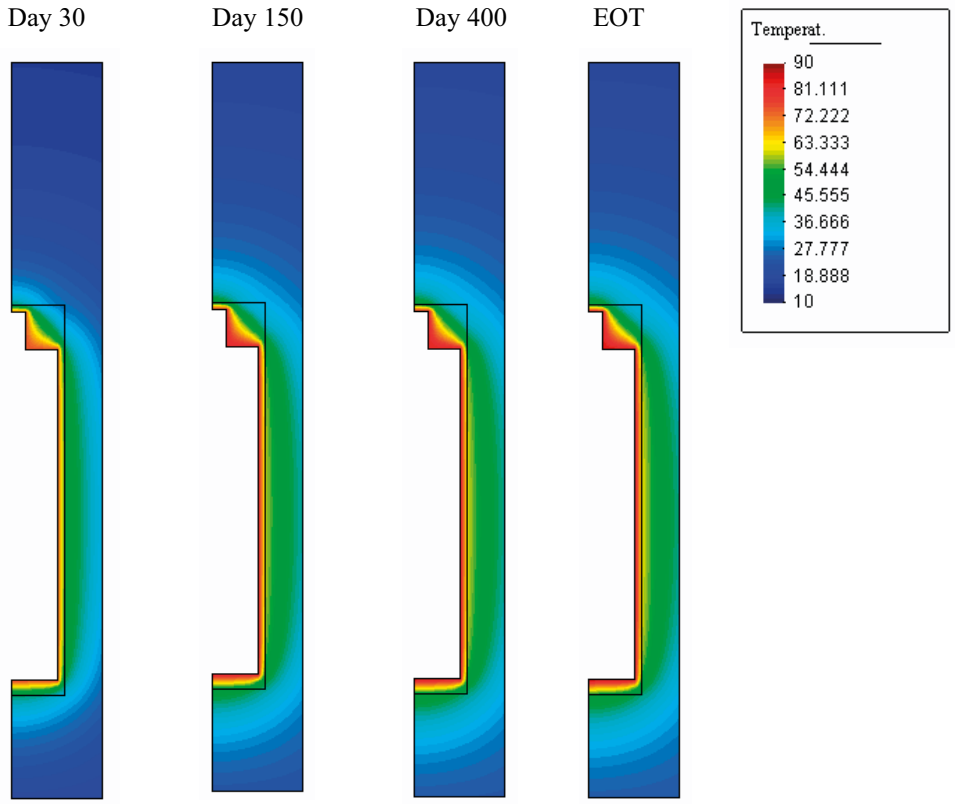

Figure 2-48. *Modeled temperature contours in buffer and sand filling; Base Case.*

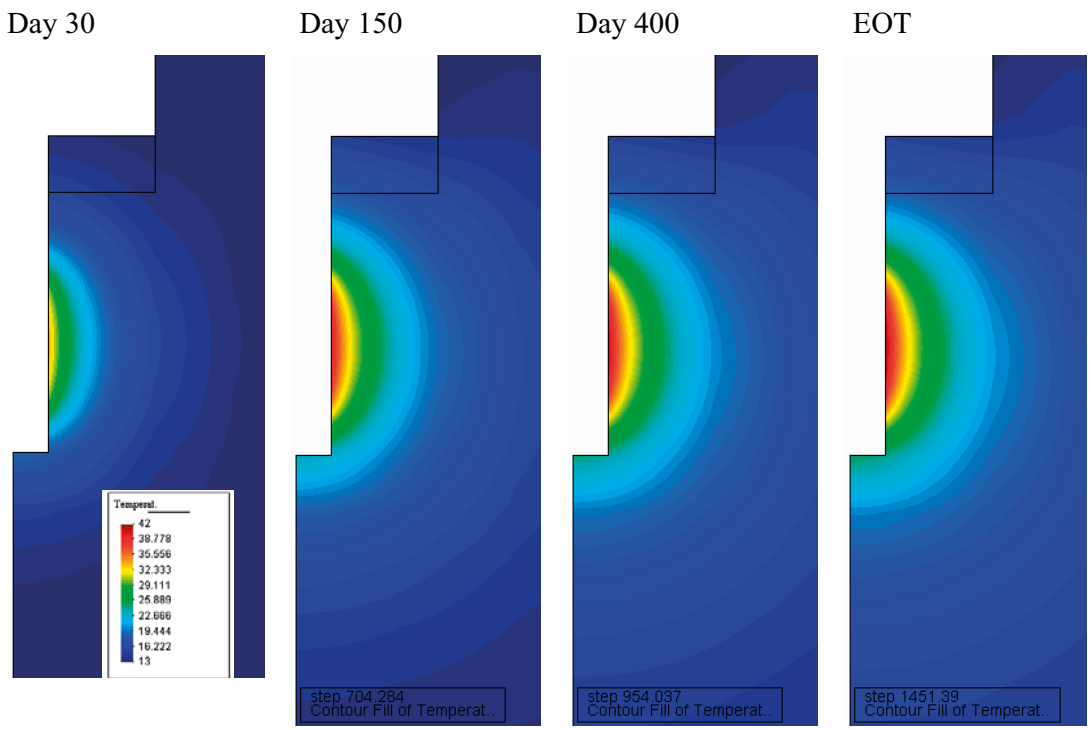

Figure 2-49. *Modeled temperature contours in rock; Base Case.*

Pore pressure profiles and contours

In the evaluation of the results, the experimental pore pressure data for BCE have been regarded as relative pressures except for the 1RH1-1RH4 sensors shown in Figure 2-52.

Pore pressure profiles along three horizontal scan-lines were evaluated for four points in time. The scan-lines are shown in Figure 2-50 (right) and modeled profiles are shown together with experimental results in the left graphs. It can be noted that the conditions along the upper scan-line is affected by the EDZ and that the pore-pressures therefore effectively is atmospheric. At the lower levels the agreement is also fairly good, at least at radii exceeding 2 m. At the interface between the rock and the buffer it can be noted that the model results in fairly high pressures.

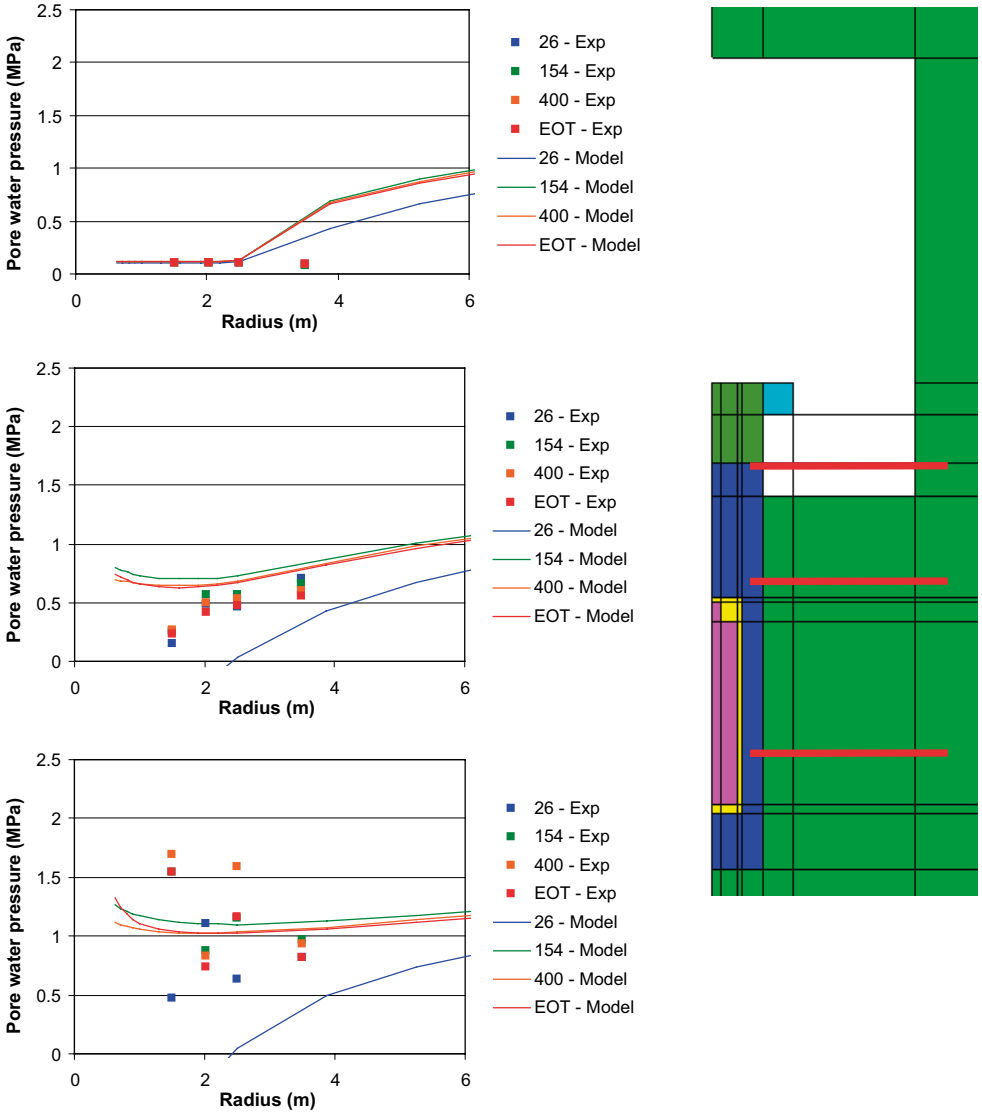

Figure 2-50. Modeled and measured pore pressure (absolute) profiles (left) along scan-lines in rock (right); Base Case.

The evolution of the pore pressures at the sensor positions along the middle and the lower scan-lines is shown in Figure 2-51. Results are shown for the Base case as well as the EDZ case. Again it can be noticed that the pressures from the Base case model are significantly higher than the measured values, with the exception for the pressure in the lower level in holes HG8 and HG9. The agreement is better in the EDZ case, although the high pressure in HG8 and HG9 is not mimicked in this case either. These high pressures could possibly reflect the occurrence of a thermal pulse, which is caused by the thermal expansion and the bulk modulus of the water together with a low hydraulic conductivity of the rock.

The modeled pore pressure evolution at the positions of the four different piezometers along the rock wall is shown together with experimental results in Figure 2-52. Here it can be clearly seen that the model overestimates the pore pressures significantly. The experimental data are quite unambiguous in showing atmospheric pressures along the rock wall. These data were the main reason for considering the possibility that some type of short-circuit was affecting the pressure conditions. The EDZ-case was therefore constructed. It should be noted however that the occurrence of EDZ along drilled holes is not generally accepted, and the approach should therefore be regarded as hypothetical. The effect of such a feature is show in Figure 2-53, where contour plots are shown for two points in time and for the base case as well as the EDZ case.

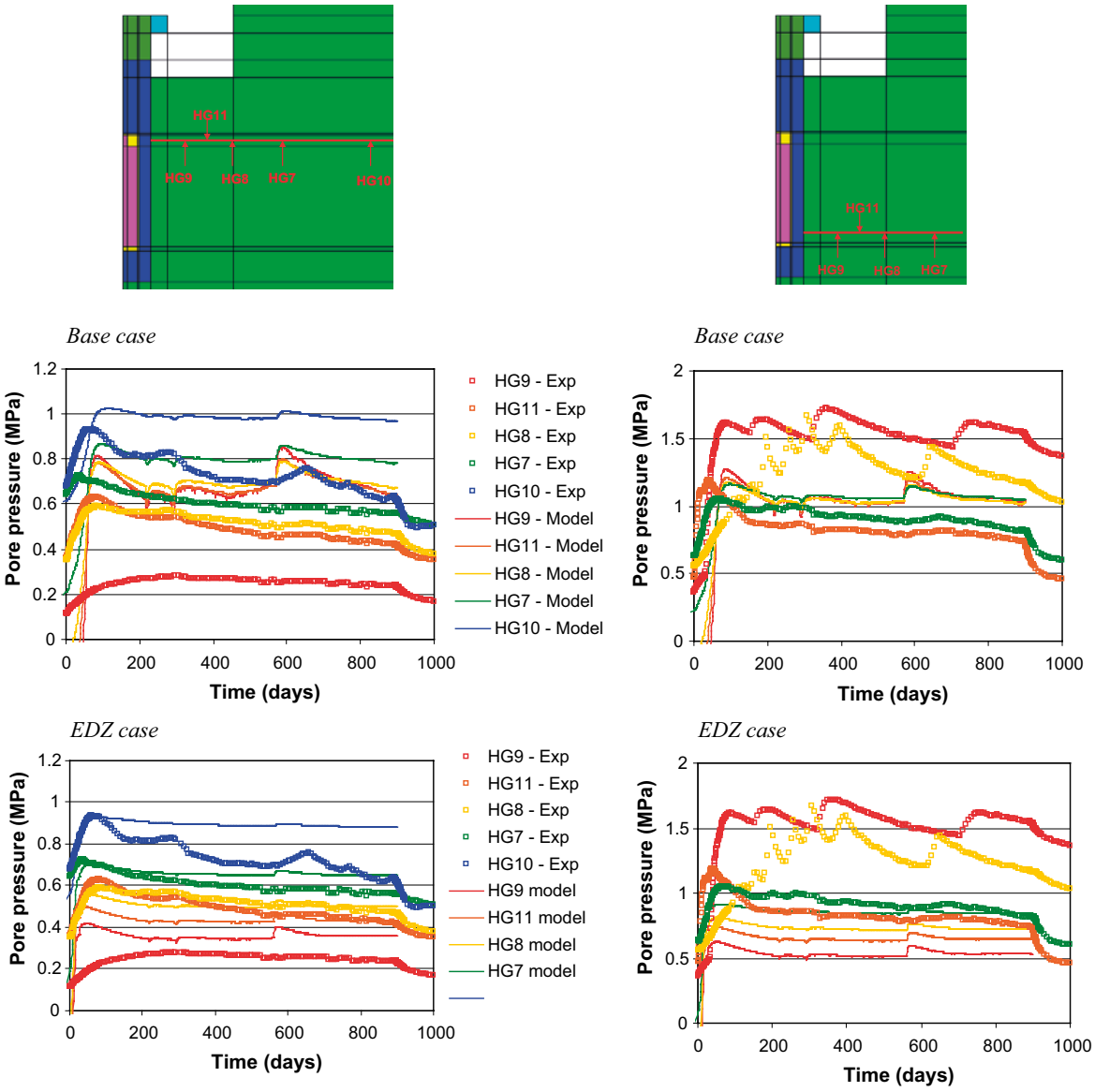

Figure 2-51. *Modeled and measured pore pressure (absolute) evolution. Left graphs: at 2.45 m depth below floor level; Right graphs: at 4.6 m depth below floor level. Base case and EDZ case.*

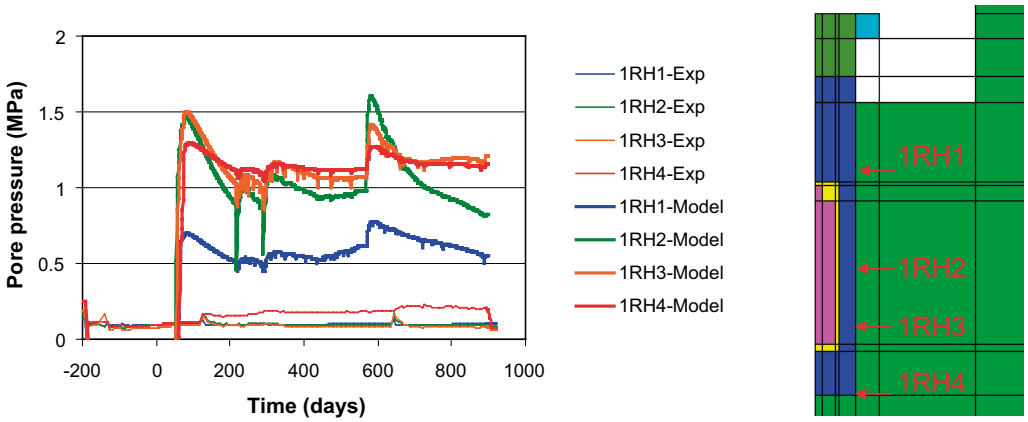

Figure 2-52. *Modeled and measured pore pressure (absolute) evolution at the sensor positions along the rock wall. Base case.*

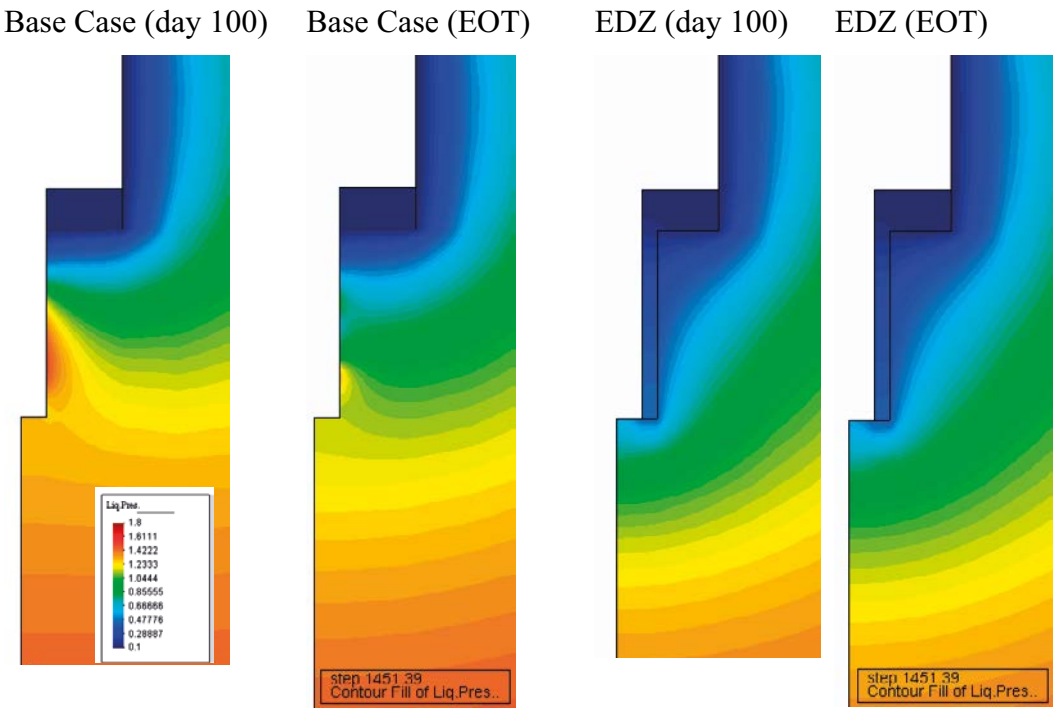

Figure 2-53. *Modeled pore pressure (absolute) contours in rock; Base case and EDZ case.*

Liquid saturation at EOT

The final distribution of liquid saturation in the buffer is shown in Figure 2-54 for all model versions except for the EDZ case. A contour plot of the experimental results is shown for comparison.

The Base case displayed a significant moisture redistribution along almost the entire length of the heater. In addition, significant dehydration was also apparent at the upper and the lower side of the heater. The Conv.-case, in contrast, was almost totally saturated at EOT and this version was therefore disregarded. The Tau30-case displayed a moisture redistribution more pronounced than the Base case. Moisture originally located in the middle section appears to have migrated into the upper and the lower part of the buffer. This redistribution is clearly exaggerated and therefore was also this version disregarded. The Cut95-case, on the other hand, displayed some interesting features. In this version a lower threshold was used for the relative permeability law for the buffer and the backfill, and water appears to have entered the buffer in this case to a higher extent than in the Base case. The extensive hydration at the corners of the heater package was similar to the experimental results. This version was therefore further evaluated along with the base case results.

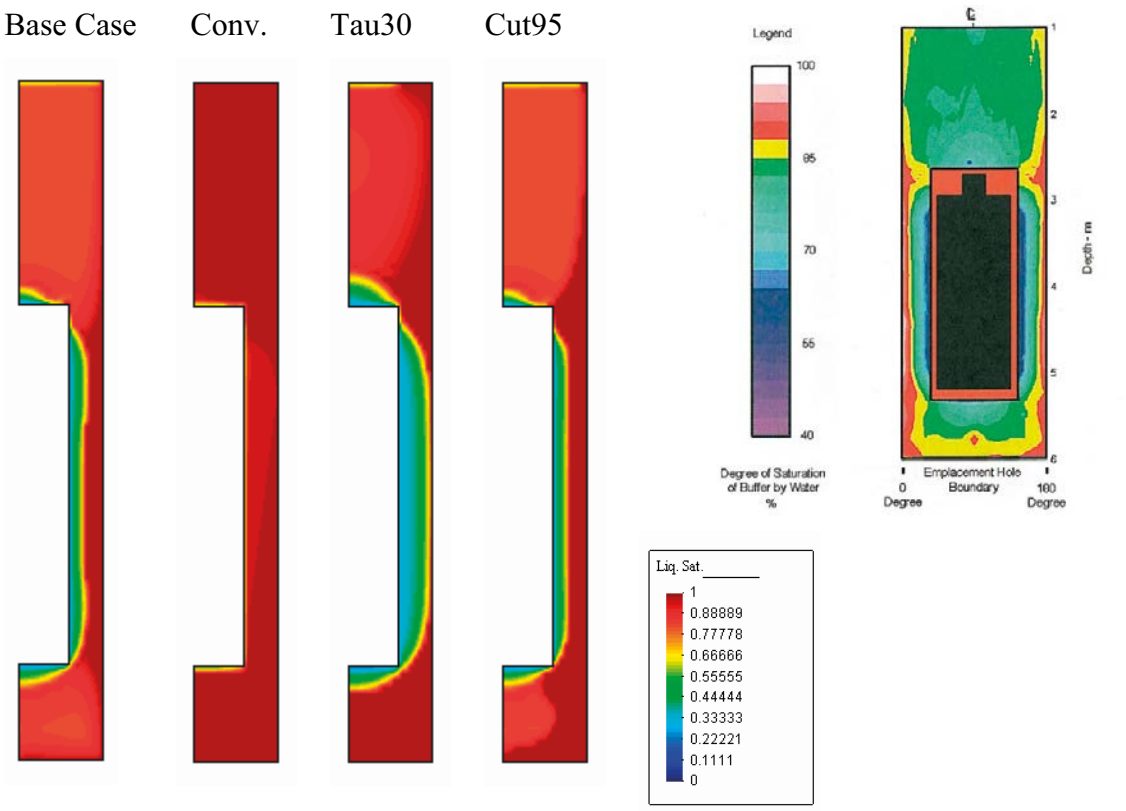

Figure 2-54. *Modeled contours of liquid saturation in buffer at EOT (left) and measured contours (Graham 1997) (right). Base case, Conv. case, Tau 30 case and Cut 95 case. The initial saturation degree was 0.84.*

Suction evolution in buffer

The modeled suction evolution at the positions of the six different psychrometers in the buffer is shown together with experimental results in Figure 2-55.

As in the case of ITT the initial modeled suction values were systematically higher than the measured values. The measured values generally also decreased more rapidly than the modeled trends. One exception is the location of the 1BX12 psychrometer which was totally water saturated in the model.

Water contents at EOT

The water content at the end of the test was evaluated for 14 horizontal scan-lines: 12 in the buffer and 2 in the backfill. The model water contents were derived as the product of the liquid saturation and the water content at full saturation (20.8 % for the buffer and 10 % for the backfill). Evaluated profiles are shown in Figure 2-56 to 2-58 together with experimental results. Model results for the Base-case as well as the Cut95-case are shown.

The experimental data for the backfill in the upper graphs in Figure 2-56 appears to indicate that the backfill was largely unaffected through the test. This is also the result from the models, although the lower part (F2 section) appears to have lost some water to the buffer. In the upper part of the buffer (G and H sections) the models underestimated the rate of hydration. Closer to the heater package (I section), on the other hand, the experimental results were lower than the modeled results, which actually were higher than the initial value. This is due to that the modeled I section intersects the zone immediately above the region with dehydration (compare Figure 2-54). The model results were fairly similar to the experimental results in the middle part of buffer (Figure 2-57; sections J–O). The most significant deviation was that the models exaggerated the dehydration close to the heater (sections K–N). In the lower part of the buffer, the model results were fairly close to the experimental results (Figure 2-58). This is especially apparent for the Cut95 case.

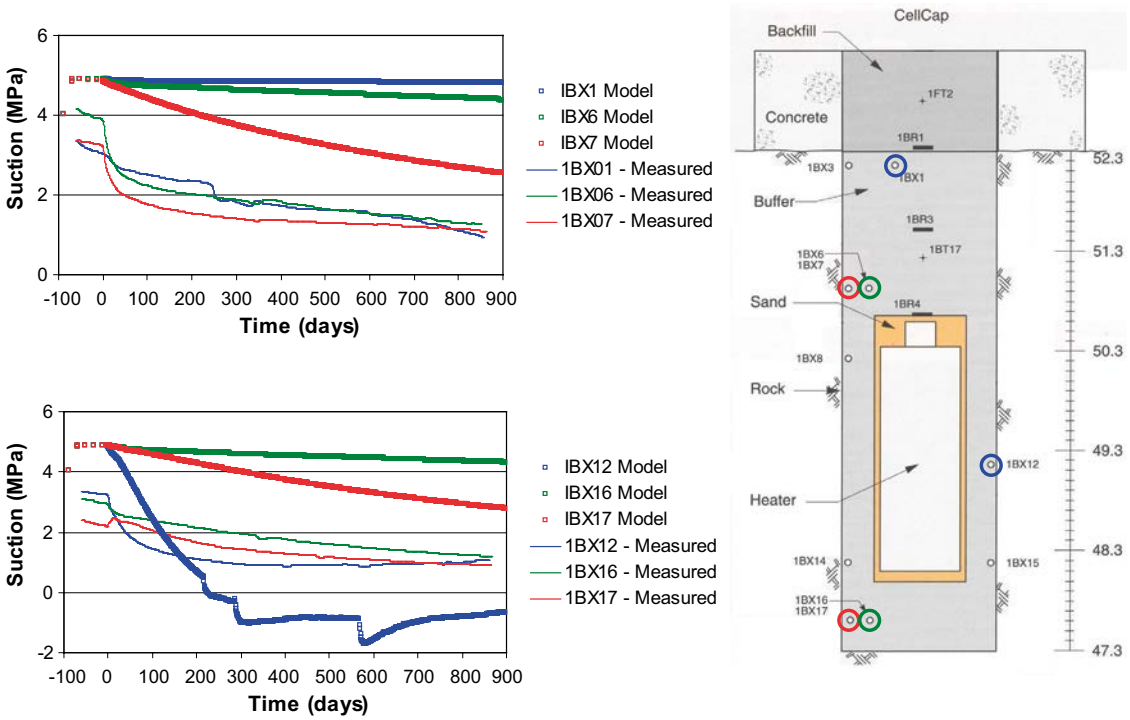

Figure 2-55. *Modeled and measured suction evolution (left) at the psychrometer positions in buffer (right). Base case.*

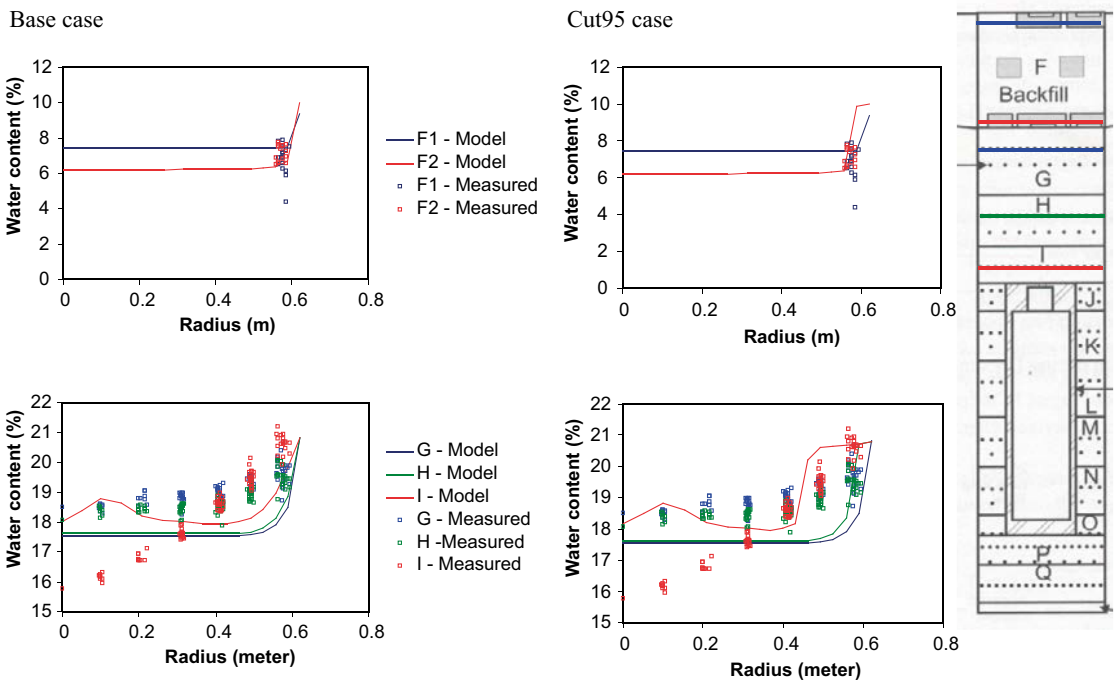

Figure 2-56. *Modeled and measured water content profiles (left) along scan-lines in upper part of test (right). Base case and Cut 95 case.*

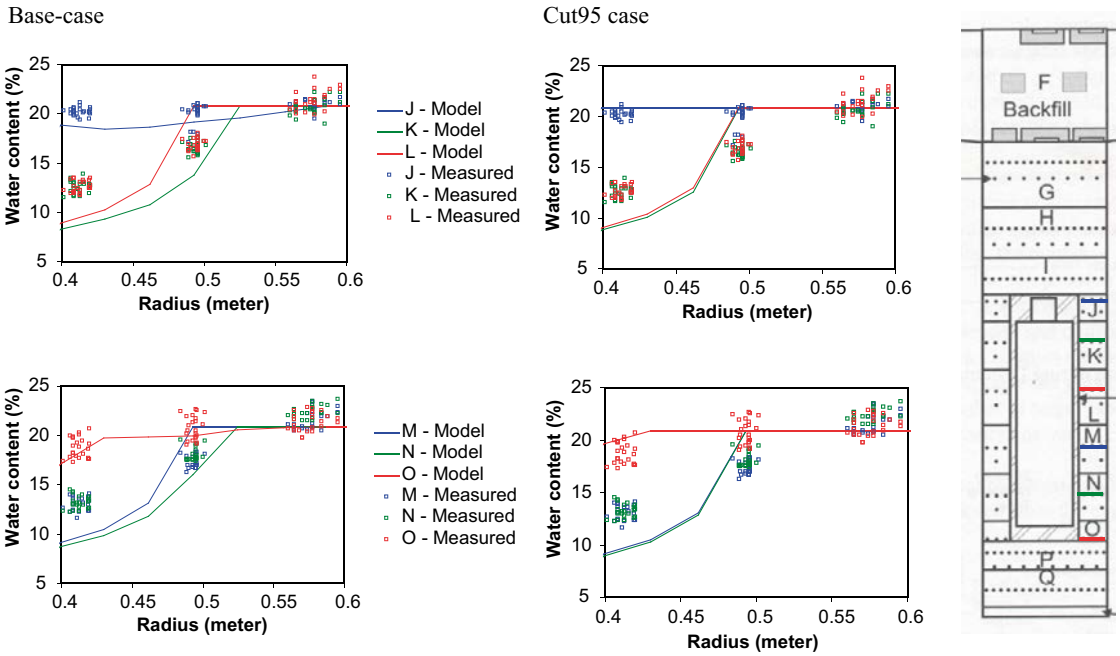

Figure 2-57. *Modeled and measured water content profiles (left) along scan-lines in middle part of test (right). Base case and Cut 95 case.*

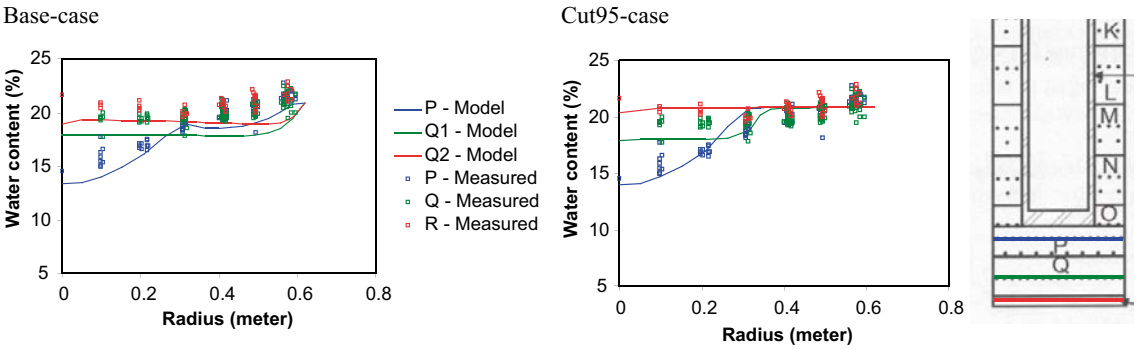

Figure 2-58. *Modeled and measured water content profiles (left) along scan-lines in lower part of test (right). Base case and Cut 95 case.*

Discussion

First of all, it can be noted that the model is able reproduce the thermal conditions in the buffer and the rock with fairly good accuracy.

Measured pore pressures in the rock and along the interface between the rock and the buffer indicate some kind of leakage along the bore hole. This suggests that the problem can be regarded as two separate problems – rock and buffer. The pore pressure evolution in the rock is fairly well captured with the models – especially if a short-circuit (EDZ) is included along the borehole. The nature of such a short-circuit is however unknown. The results from two pore pressure sensors indicate the occurrence of a thermal pulse with significantly higher pressures (see Figure 2-51). This was not reproduced by the models.

The approach with exclusive vapor transport implies strong moisture redistribution. The agreement with sample data is fairly good although the extent of dehydration close to the heater appears to be exaggerated in the models. The version with lower permeability threshold (0.95) exhibits better agreement than the base case (threshold 0.999). The reason for this is that more water entered the buffer in the Cut-95 case. By comparison, the conventional case resulted is almost total saturation at the time corresponding to EOT.

In the Base case model and the Cut-95 model there was no hydration in the upper and inner part of the buffer (see sections G–H in Figure 2–55). This has some support in the experimental results which shows that the final water content in the inner part of these sections was approx. 18–19 % and thereby only marginally higher than the initial value (see discussion at the end of Section 2.3.5 for a discussion concerning the initial water content).

2.3.6 Concluding remarks

The rock was in all the models assigned a fairly high retention curve making the rock effectively water saturated. The rock was thereby not allowed to choke the inflow into the borehole. An explanation for the fairly low extent of hydration found in both experiments has thus been sought in the properties of the buffer material, and not in the surrounding rock.

The development of a saturation front has been sought in this work. The pore-pressure evolution and profiles found in ITT supports the notion of a progressing front. So does the experimental results from the water uptake tests. In BCE however, the apparent atmospheric pressures along rock wall indicate the presence of a short-circuit. The results indicate that in order to reproduce a progressing front it appears to be more important to reduce the slope of the retention curve close to saturation than to modify the moisture flow coefficients.

The approach to model the buffer moisture transfer as an exclusive vapor transfer with a high tortuosity value and with a relative permeability law with a high threshold is a description with limited precision. The modeled moisture redistribution profiles in BCE at the end of the test are nevertheless quite similar to the measured profiles and therefore support the notion that the vapor pressure is the dominating potential. Still, the approach should be avoided unless it can be further justified and developed.

If the studied experiments would be the subject for further investigations, then two adjustments could be proposed. The first issue should be to modify the initial water content and the retention properties in order to match the experimental results more closely. Secondly, an alternative formulation of the retention curve, with a low slope close to saturation, should be implemented and tested. This would require a modification of the source code and this was the main reason why this path was not pursued. Such a modification may very well be sufficient to improve the agreement with experimental results, even with a conventional treatment of the moisture flow coefficients.

3 BM 2.2 CRT

3.1 General

The Canister Retrieval Test (CRT) was performed by SKB in Äspö HRL at the depth 420 m. The test was originally intended to be an exercise in canister retrieval after buffer saturation, but has been used for following the THM-processes with intensive supervision by a dense instrumentation and careful sampling after termination.

The specifications were provided by Ola Kristensson on behalf of SKB.

Below in Section 3.2 (“Specifications”) follow a description of the CRT experiment, the corresponding EBS Task Force assignment, information regarding the materials used in the experiment, and some additional information about issues discussed during EBS Task Force meetings. The two following sections contain modeling performed using the FE-solvers CodeBright and Abaqus, in Section 3.3 (“Modelling results with Code Bright”) and 3.4 (“Modelling results with Abaqus”), respectively.

3.2 Specifications

Here follows a description of the CRT experiment and the task as suggested to the EBS Task Force members. Much of the information has been gathered from CRT-reports and notes provided to the Task Force. As a result, the tense in the text might be inconsistent and somewhat confusing. Also, references might be given to Appendices or files that were included/attached to the handout but not to this report. The author hopes that this will not offend the reader too much.

3.2.1 Introduction

As one of the tasks within the EBS Task Force the Canister Retrieval Test (CRT) experiment is to be simulated. This document first gives a brief introduction to the experiment installation and operational phase. Then the tasks are defined and the experimental data are presented.

In this section the experimental geometry is first presented, after this follows a recapitulation of the summary in Thorsager et al. (2002). Then the test schedule is shown and some comments about the installation and operating phase of the experiment are given with data obtained from Goudarzi et al. (2006).

In the following sections the tasks are defined and in Appendix 2 the properties of the materials and the experimental data are shown.

Geometry

A schematic view of the experimental geometry is given in Figure 3-1. More detailed drawings of the geometry of the CRT experiment are given by Figure 3-2 to Figure 3-6 below. Also the geometry of the TBT experiment is given in Figure 3-7.

The tunnel-profile has the approximate dimensions 6 × 6 m with a horse shoe shaped profile. The experiments, CRT and TBT, are placed approximately at the tunnel center-line. The center of the TBT experiment is located 6 m from the center of CRT.

In the hole, 16 filter mats with a width of 10 cm are installed with uniform spacing, 0.15 m from the hole bottom up to 6.25 m height.

Ring-shaped or cylindrical bentonite blocks are placed in the hole. At the top of the canister bentonite bricks are filling up the volume between the canister top surface and the top surface of the upper most ring (R10). The height difference between the two surfaces was 220–230 mm. The volume between the bentonite blocks and the hole wall is filled with bentonite pellets and water.

An impermeable rubber mat was installed between C4 and the concrete plug. On top of the plug a steel lid was installed. The plug and lid can move vertically and are attached to the rock by nine rock anchors.

Each of the nine rock anchors has a total length of 10 m, 5 m fixed in the rock and 5 m free. The anchors consists of 19 steel wires with a nominal area of 98.7 mm^2. The inclination of the anchors is 2.5:1 or ≈ 22 °.

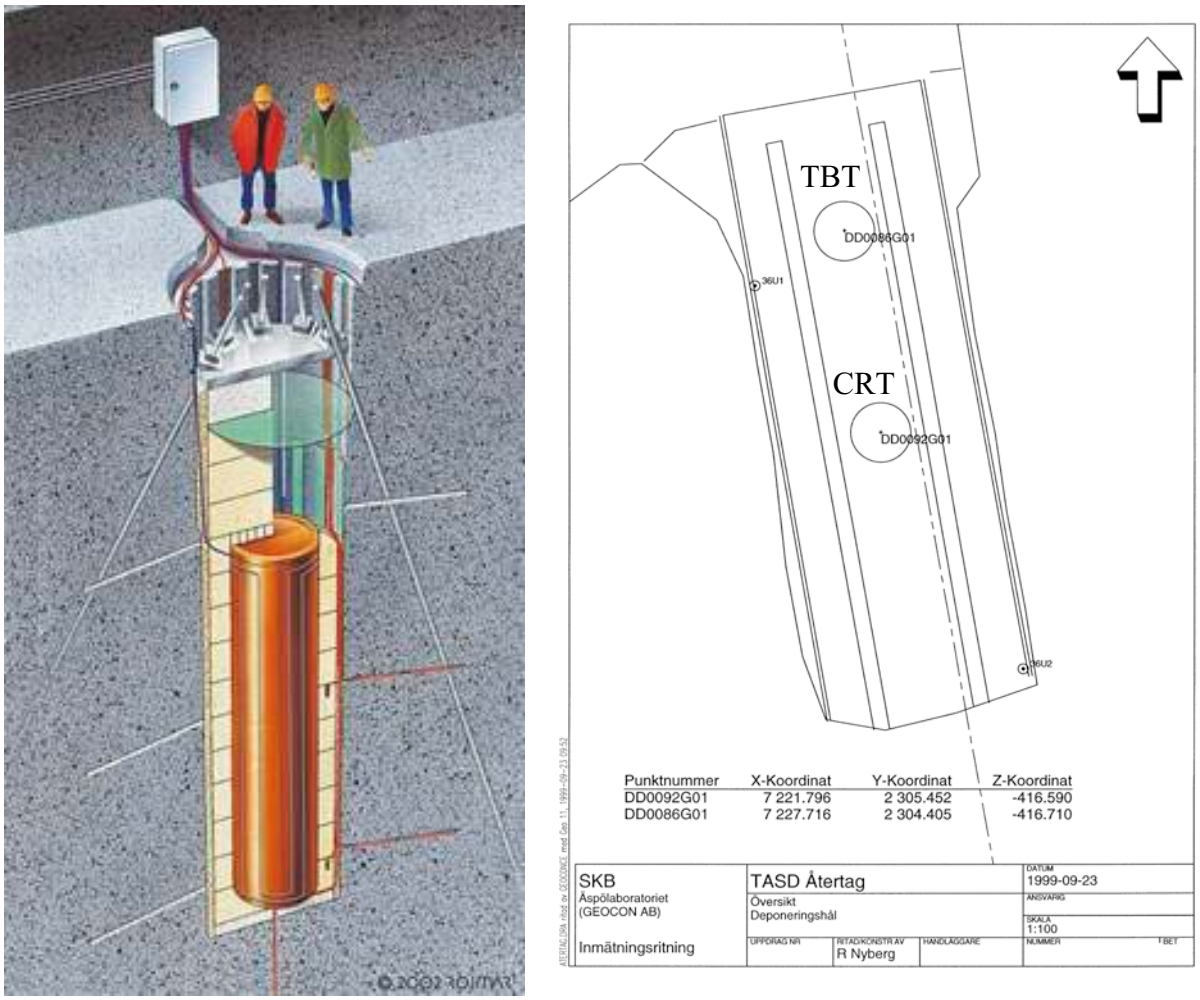

Figure 3-1. *Illustration of the experimental set-up of the Canister Retrieval Test and the location in the TASD tunnel.*

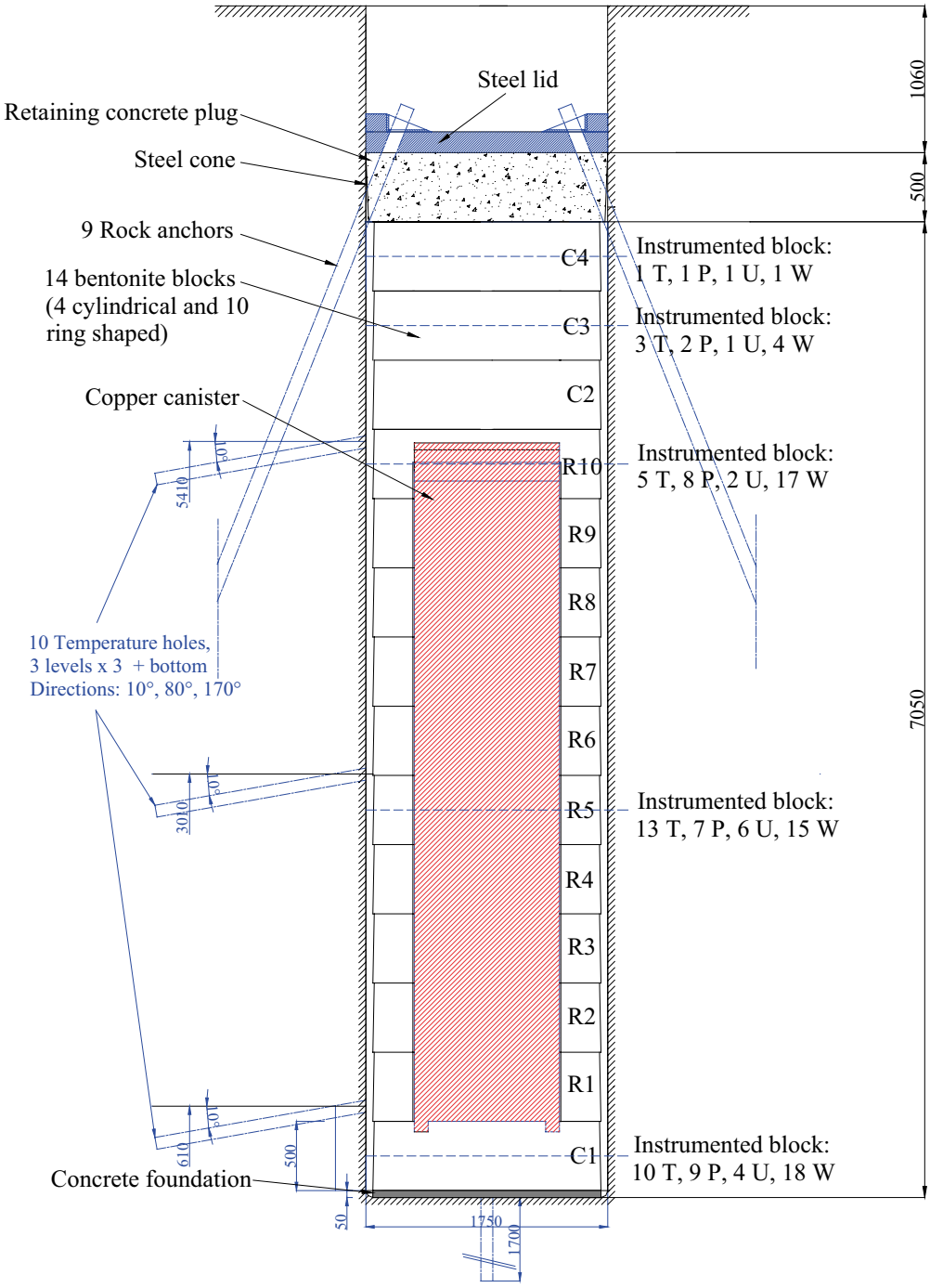

Figure 3-2. *Schematic view showing the experiment layout. Sensors have been placed in five of the bentonite blocks. For each block the number of each sensor type is described. (T = temperature, P = total pressure cell, U = pore pressure cell and W = relative humidity sensor).*

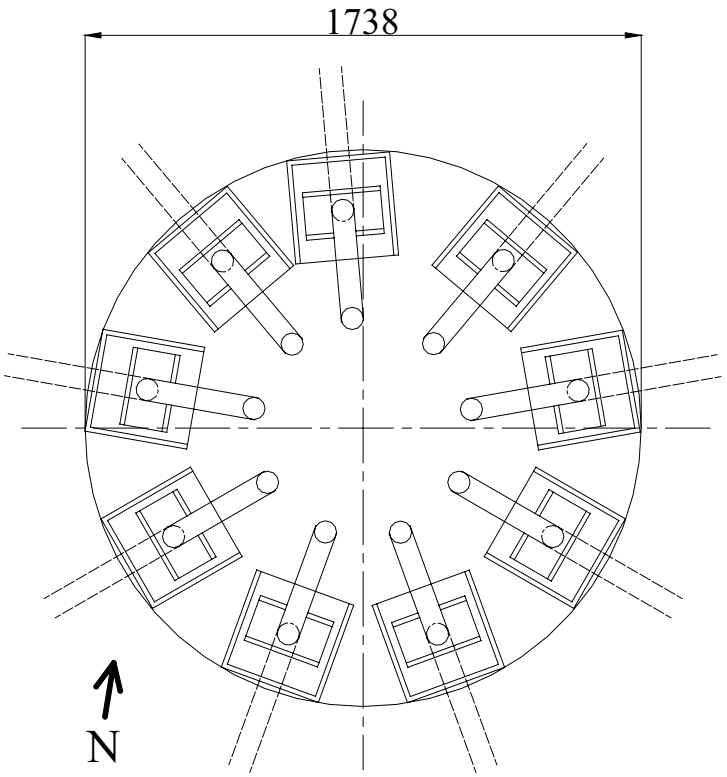

Figure 3-3. *Plan of the retaining plug with rock anchors.*

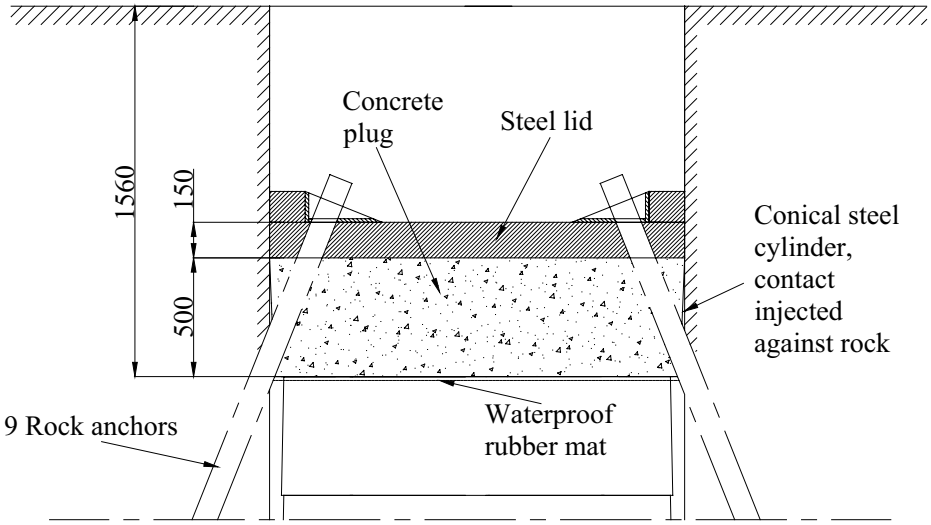

Figure 3-4. *Section of retaining plug with rock anchors.*

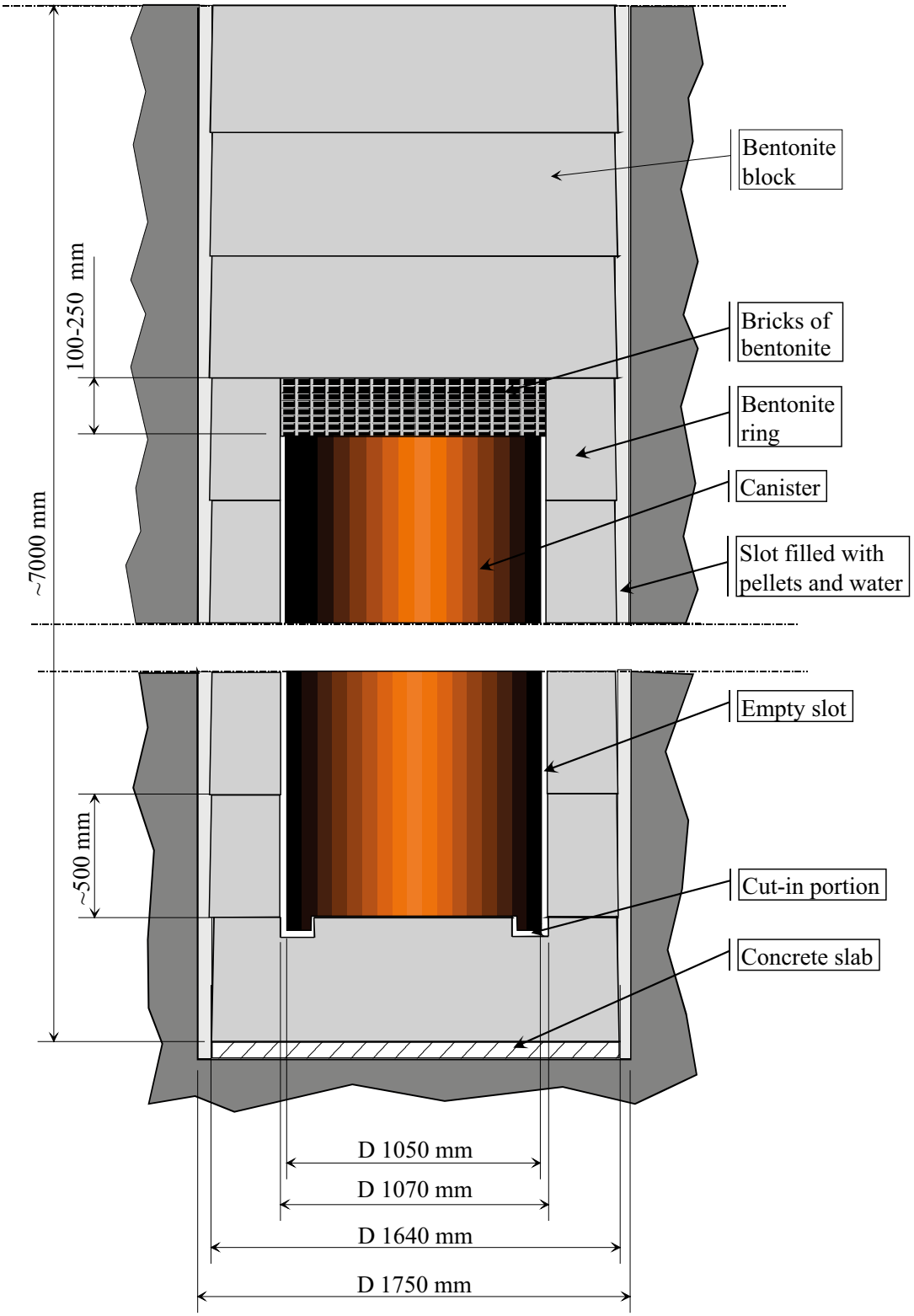

Figure 3-5. *Schematic drawing of the canister hole with bentonite blocks with dimensions in mm.*

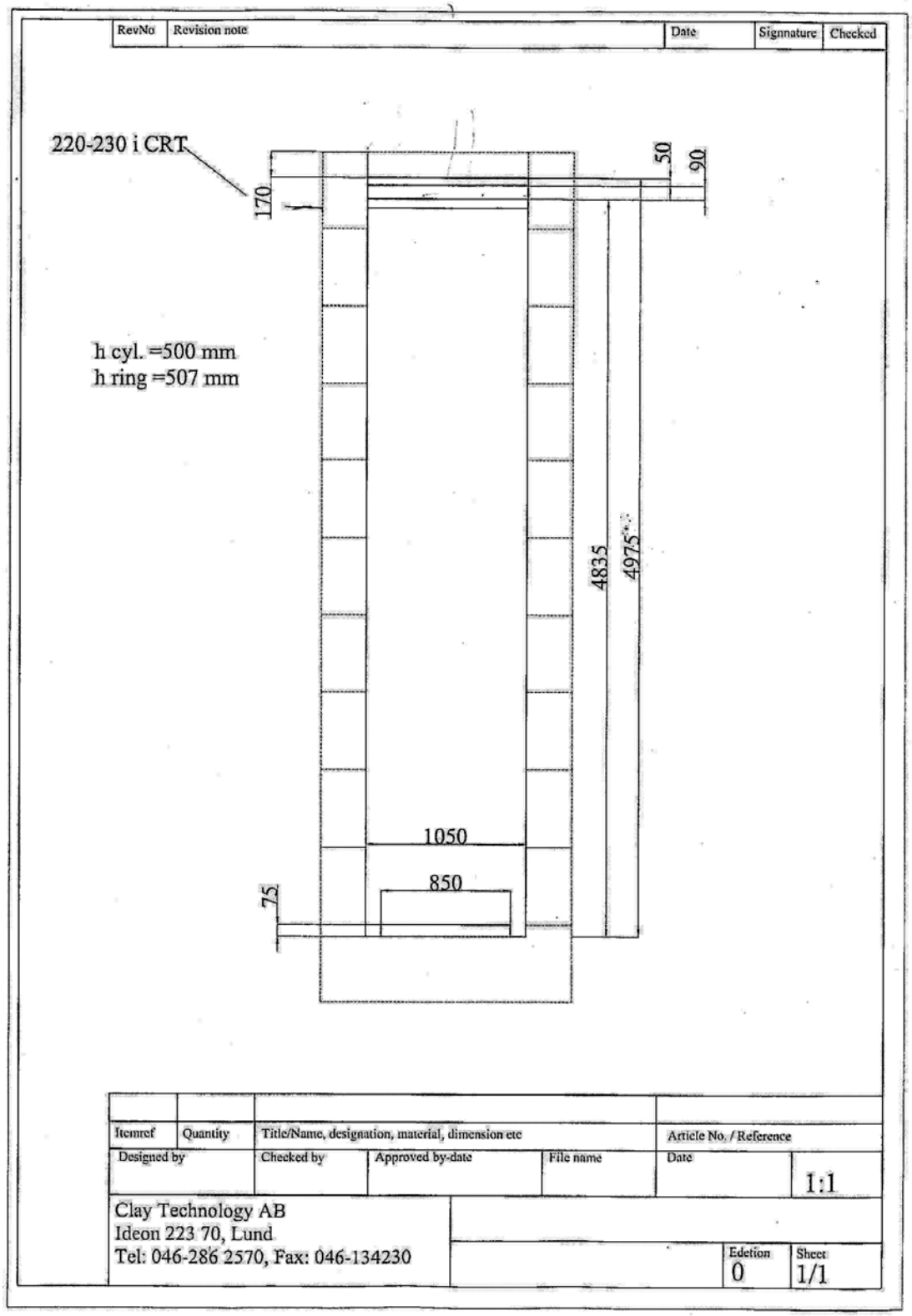

Figure 3-6. *Canister geometry.*

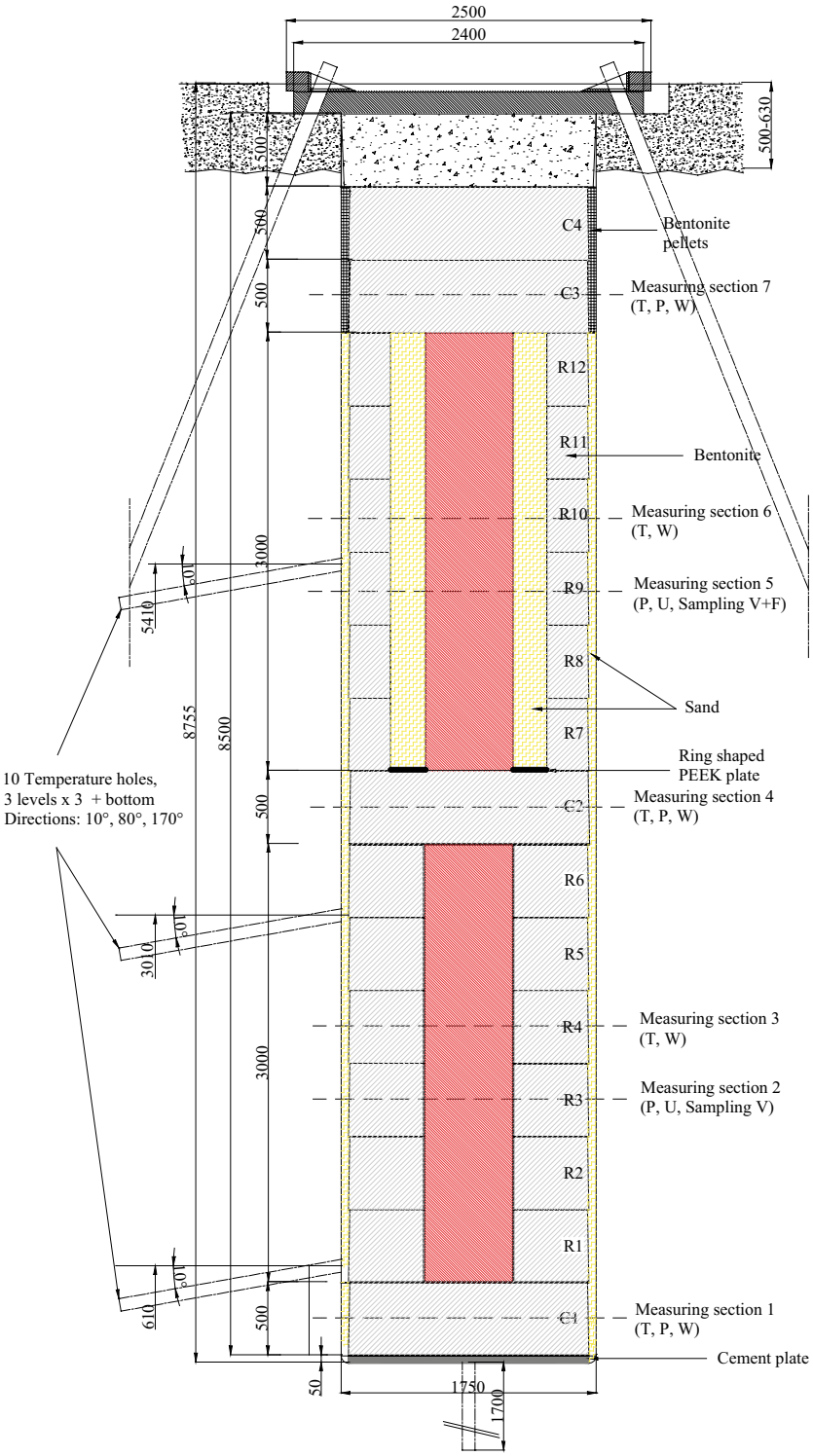

Figure 3-7. *TBT geometry.*

Summary from installation report

The Canister Retrieval Test was started to demonstrate the capability to retrieve deposited nuclear waste if a better disposal solution is found. The overall objective of the Canister Retrieval Test was to demonstrate to specialists and to the public that retrieval of canisters is technically feasible at any stage of the operating phase.

The CRT experiment has also been used to carefully record the THM processes in the Swedish KBS-3V deposit technique besides proving the possibility for retrieval of the canisters. This makes it very suitable for modelers to investigate theories, used in their simulations, since the calculated results can be checked against experimental data.

The test was installed in autumn 2000. This report *(the installation report that is, authors comment)* describes the test layout and the installation procedure. The deposition tunnel for the experiment is located on the 420-metre level and is excavated by conventional drill and blast. The centre-to-centre distance between the two deposition holes is 6 metres, which is the spacing being considered for the deep repository, but only one of the holes has been used for this test, see Figure 3-1. A maximum temperature of 100 °C on the surface of the canister is aimed at for the Canister Retrieval Test.

The bentonite buffer was installed in form of blocks and rings of bentonite, see Figure 3-2. The blocks have a diameter of 1.65 m and a height of 0.5 m. When the stack of blocks was 6 m high, the canister, equipped with electrical heaters, was lowered down in the centre of the hole and the cables to the heaters and instruments were connected. Additional blocks were emplaced until the hole was filled to a distance of one metre from the tunnel floor. The top of the hole was sealed with a retaining plug made of concrete and a steel plate, see Figure 3-3 and Figure 3-4. The plug was secured against heave caused by the swelling clay with nine cables anchored in the rock. Water was supplied artificially for saturation around the bentonite blocks.

Saturation is predicted to take two-three years in the buffer alongside the canister and 5–10 years in the buffer below and above the canister. The decision on when to start retrieval is dependent on the degree of saturation.

A pilot test, Test of Deposition Process, was performed as a preparatory exercise prior to the Canister Retrieval Test and the Prototype Repository Test. The purpose of the test was to try out and practice with equipment, technique and methods developed for the installation of buffer and canisters.

The deposition hole for the Canister Retrieval Test was bored with a full-face tunnel boring machine modified for boring vertical holes. The deposition hole is 8.55 metres deep and has a diameter of 1.76 metres. The surrounding rock at the upper part of the hole consists mainly of greenstone and the lower part of Äspö diorite.

A 0.15 metre high concrete foundation was built to prevent water leaking from the rock from reaching the bentonite blocks and to reduce the risk of tilting the stack of bentonite rings.

Slots were cut in the rock wall for cables to prevent them from being damaged.

A canister obtained from SKB's Encapsulation Project was used for the Canister Retrieval Test, see Figure 3-6. The outside diameter of the canister is 1 050 mm. The height of the canister is 4.83 m and the weight 21.4 tonnes.

The bentonite used as buffer material is SKB's reference material, named MX-80. The buffer consists of highly compacted bentonite blocks and rings with an initial density of 1 710 and 1 790 kg/m^3, respectively. The initial water content of the bentonite was 17 %.

An artificial pressurised saturation system was built because the supply of water from the rock was judged to be insufficient for saturating the buffer in a time consistent with the planning of the test. At the end of the test period, a high water pressure will speed up the saturation process. It will also provide a defined hydraulic boundary. The water is evenly distributed through a number of filter mats attached to the wall of the deposition hole.

A climate control system was used during installation to prevent the bentonite from being damaged by excessively high or low relative humidity.

A retaining structure is used to simulate a real storage situation. The aim of the structure is to prevent the blocks of bentonite from swelling uncontrollably. It consists of a concrete cone plug placed on top of the buffer and a steel lid which is pre-stressed by rock ties.

A large number of instruments are installed to monitor the test (see Figure 3-2) as follows:

- Canister – temperature and strain.
- Rock mass – temperature and stress.
- Retaining system – force and displacement.
- Buffer – temperature, relative humidity, pore pressure and total pressure.

The data acquisition system consists of a measurement computer and dataloggers. The monitored values are transferred via a serial link from the dataloggers to the measurement computer. The computer is connected to Äspö data network.

Test installation was carried out in the following sequence:

1. Preparations on site – concrete foundation, cutting of slots in the rock wall, drilling for rock anchors and instruments, installation of rock anchors, filter mats for saturation, installation of formwork for plug.
2. Emplacement of bentonite blocks and rings including installation of instruments.
3. Deposition of canister.
4. Continuation of 2.
5. Filling of void between rock and bentonite rings with bentonite pellets and water.
6. Casting of concrete plug and placement of steel lid.
7. Pre-stressing of retaining system.

Heating was started with an initially applied constant power of 700 W on October 27, 2000, one day after casting the plug. The displacements and forces on the plug were carefully checked and followed during the initial phase when the plug was only fixed by three anchors. When the total force exceeded 1 500 kN, the remaining anchors were fixed in the prescribed manner. This took place December 12–14 that is 46–48 days after test start.

3.2.2 Test schedule

The text in **Test start** and **End of the experiment** is copied directly from the installation report and the dismantling report respectively. Information added to the original text is given in italics.

The following sections: **Heater power and filter pressure** and **Rock anchors and heave of the lid**, are compilations of information found in reports concerning the CRT experiment.

Test start

Since pellet filling marks the start of the test, the best description of the launching of the test is a step-by-step description of the procedures from that point in time.

1. Before the pellets were blown into the gap, all preparations described in Chapter 5 (instruments, heaters and wetting system installed) were finished and the tubes for the drainage (pumping) system were removed along with the tubes and transducers for the ventilation system.
2. Data collection was started immediately before pellet filling.
3. The gap was filled with pellets on October 26 (2000), which thus can be considered the starting date.
4. Water was pumped into the gap and the filter mats, and the *(four)* water supply tubes were withdrawn immediately after *(during the)* pellet filling.
5. Measurement of water inflow into the filters started immediately after water filling.

6. The rubber mat was placed on top of the upper block.
7. The cable slots behind the conical ring were sealed with cement.
8. The plug was cast when all preparations had been finished. Not more than 12 hours were allowed to pass between water filling and casting.
9. Heating was started with an initially applied constant power of 700 W on October 27, i.e. one day after test start.
10. Three prescribed rods were locked on October 31 and the force and displacement transducers installed. *(At the installation the force in the anchors were prescribed to 20 kN /anchor.)*
11. Between test start and locking of the rods (5 days) the plug rose 13 mm due to swelling of the bentonite.
12. The displacements and forces on the plug were carefully monitored.
13. When the total force exceeded 1 500 kN, the remaining rods were fixed in a prescribed manner. This procedure took place 12–14 December, i.e. 46–48 days after test start. *(When the average force in the three anchors exceeded 500 kN, the six remaining anchors were attached to the lid. The total force where distributed equally between all anchors, i.e. the force was ≈ 170 kN/anchor when all nine anchors were installed.)*
14. The canister heating power was raised twice: to 1 700 W on November 13 and to 2 600 W on February 13.

End of the experiment

Table 3-1. Events during dismantling of the upper part of the buffer in the Canister Retrieval Test.

Activity	Date	Day	Comments
The power to the canister was switched of.	2005-10-11	1 811	The power was switched of about 3 month before the first samples of the buffer were taken
The plug was removed	2006-01-16–01-18	1 908–1 910	The rock anchors were removed and the steel lid and concrete plug was lifted up from the deposition hole
Samples were taken from block C4	2006-01-18–01-23	1 910–1 915	
Samples were taken from block C3	2006-01-24–01-30	1 916–1 922	
Samples were taken from block C2	2006-01-30–02-02	1 922–1 925	
Samples were taken from block R10	2006-02-06–02-10	1 929–1 933	Samples were taken on both the ring shaped block and the bricks placed on top of the canister lid. The thickness of the filling of bricks was about 220 mm.
Removal of the upper lid of the canister	2006-02-13–02-14	1 936–1 937	The upper lid of the canister was removed. Samples were taken on the filling between the lids of the canister. The power cables were removed from the deposition hole
Samples were taken from block R9	2006-02-14–02-20	1 937–1 943	
Samples were taken from block R8	2006-02-22–03-01	1 945–1 952	
Samples were taken from block R7	2006-03-02–03-09	1 953–1 960	
Samples were taken from block R6	2006-03-13–03-21	1 964–1 972	

Heater power and filter pressure protocols

Table 3-2. CRT heater power protocol.

Date	Day	Heater power [kW]	Comment
00-10-26	0	0	
00-10-27	1	0.7	
00-11-13	18	1.7	
01-02-13	110	2.6	
01-11-05	375	0	
01-11-06	376	2.6	
02-03-04	494	0	
02-03-11	501	2.6	
02-09-10	684	2.1	
03-12-04	1 134	1.6	
05-03-10	1 596	1.15	
05-10-11	1 811	0	
06-03-28	1 979	2	Testing the heaters
06-04-20	2 002	0	

Table 3-3. TBT heater power protocol.

Date	Day	Heater power [kW]
00-10-26	0	0
03-03-26	881	0.9
03-04-03	889	1.2
03-04-10	896	1.5
06-06-09	2 052	1.6

Table 3-4. CRT filter water pressure protocol.

Date	Day	Water pressure [MPa]	Comment
00-10-26	0	0	
02-09-05	679	0	Started to increase the water pressure gradually.
02-10-10	714	0.8	
02-12-05	770	0.1	
03-01-09	805	0.4	
03-01-23	819	0.8	
05-03-12	1 598	0	
05-12-16	1 877	0	Air flushed

Rock anchors and heave of the lid

Table 3-5. Overview of rock anchor history.

Date	Day	Comment
2000-10-31	5	Three pre-stressed anchors were attached to the lid. The initial force in each anchor was 20 kN.
2002-12-12–2002-12-14	46–48	The remaining six anchors were attached to the lid when the total force exceeded 1.5 MN. The total force was distributed evenly between the anchors, which gives ≈ 170 kN/anchor. The force in three of the anchors has been measured.
2006-01-16–2006-01-18	1 908–1 910	The rock anchors were removed and the steel lid and concrete plug was lifted up from the deposition hole

Table 3-6. Overview of plug displacement.

Date	Day	Comment
00-10-31	5	13 mm heave before attaching the three rock anchors according to late estimate.
00-10-31–	5–	See measurement called “displacement2”. 20.5 mm at the final reading (2006-01-03). Note that 13 mm should be added to “displacement2” in order to obtain the total heave.

Back calculations of the displacement using the average dry density in each block gives that the total vertical displacement should be ≈ 40 mm.

Comments about the installation and operating phase

When water filling the pellet-filled outer slot, the estimated amount of water to fill up the voids between the pellets, 800 l, was exceeded by approximately 150 l. The water is thought to have penetrated through at the interfaces between the bentonite blocks into the inner gap and thereby got access to an additional volume to fill. A calculation of the available volume between the canister and bentonite rings gives 160 l which strengthens the assumption that the inner slot had been water filled.

The analysis above is quite uncertain. Both the estimation of the added water volume and the available slot volume are uncertain. Sensor data is however also indicating that the inner slot was filled. The total pressure at the inner surface of R5 shows a peak at the start of the experiment. Both Vaisala sensors (RH) and Wescor sensors (suction) also indicate that there is something happening in the section close to the canister.

The initial conditions of the different sections of the CRT experiment are shown in Table 3-7, where a bentonite solid density of 2 780 kg/m^3 was used when the conditions were calculated. Pellets I denotes the state of the pellet filled outer slot before the water filling at installation and Pellets II after the water filling.

The start date of the experiment (taken as the date when the outer gap was filled with pellets) was 2000-10-26. Schematic protocols of the heater power of CRT and the heater power of TBT is given in Table 3-2 and Table 3-3. The TBT has two heaters with the power-history indicated in Table 3-3.

The TBT experiment has considerable thermal effect upon the CRT experiment since the hole-centers are located with 6 m between them. The thermal effect from the TBT experiment on CRT can clearly be seen in Figure 3-11 where rock temperatures at canister mid-height are shown. At approximately 900 days after the startup of CRT the rock temperatures increase suddenly due to the start of the TBT experiment.

The protocol of the water pressure in the filter is given in Table 3-4. Note that the pressure additional to the atmosphere pressure is shown. The measured inflow of water into the filter is given in Figure 3-12 below. In Figure 3-8 a graphical overview of the heater power and filter pressure protocols is given.

2000-10-31, five days after the test start, three pre-stressed rock anchors were attached to the lid. At this time the heave of the plug was 13 mm due to swelling of the bentonite, according to late estimates which are somewhat uncertain. Day 46–48 the remaining six, also pre-stressed, rock anchors were fixed since the total force had exceeded 1.5 MN. The forces in the rock anchors can be seen in Figure 3-9 and the displacement of the plug is shown in Figure 3-10.

In Figure 3-9 both the actual measurement and this multiplied with three are shown for anchor 3.6 and 9 since only these three of the anchors were instrumented. An estimate of the total force in all the anchors can thus be obtained by adding the × 3 values.

Table 3-7. Initial conditions of the CRT experiment.

Section	Density (kg/m^3)	Water ratio	Dry density (kg/m^3)	Void ratio	Degr. of saturation
Solid block	1 991	0.172	1 699	0.636	0.751
Ring shaped block	2 087	0.171	1 782	0.560	0.849
Bricks	1 883	0.165	1 616	0.720	0.637
Pellets I	1 101	0.100	1 001	1.778	0.156
Pellets II	1 574	0.572	1 001	1.778	0.895

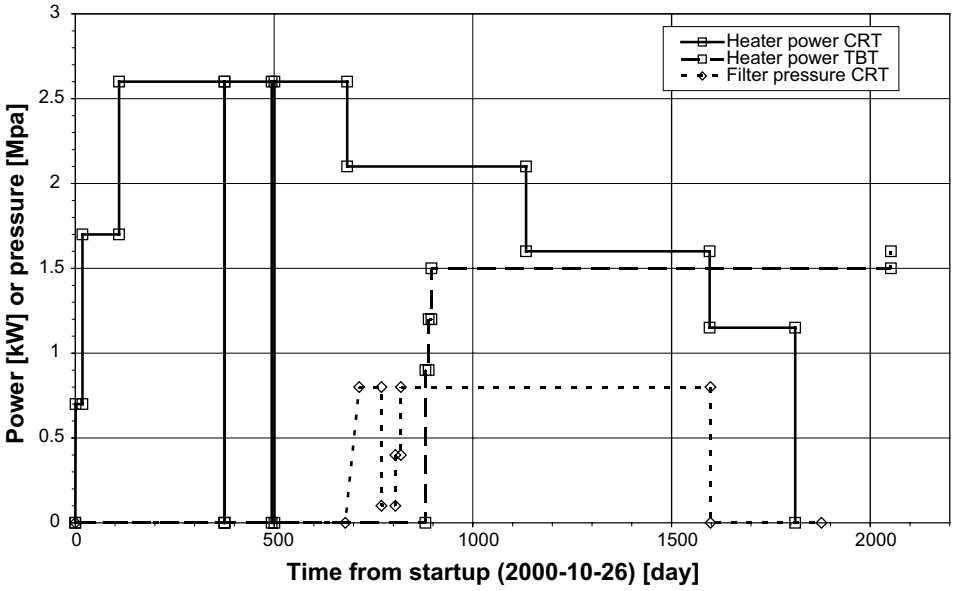

Figure 3-8. *Graph of the power protocols of CRT and TBT and the filter pressure of CRT.*

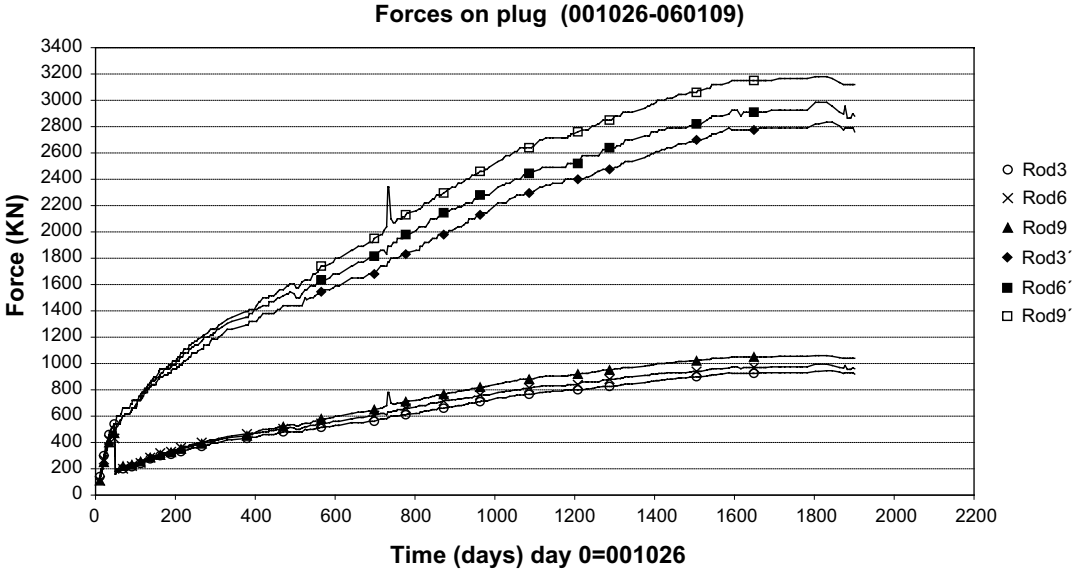

Figure 3-9. *The lower three curves show the force in rock anchors 3, 6 and 9. The upper curves show three times the force in the rock anchors.*

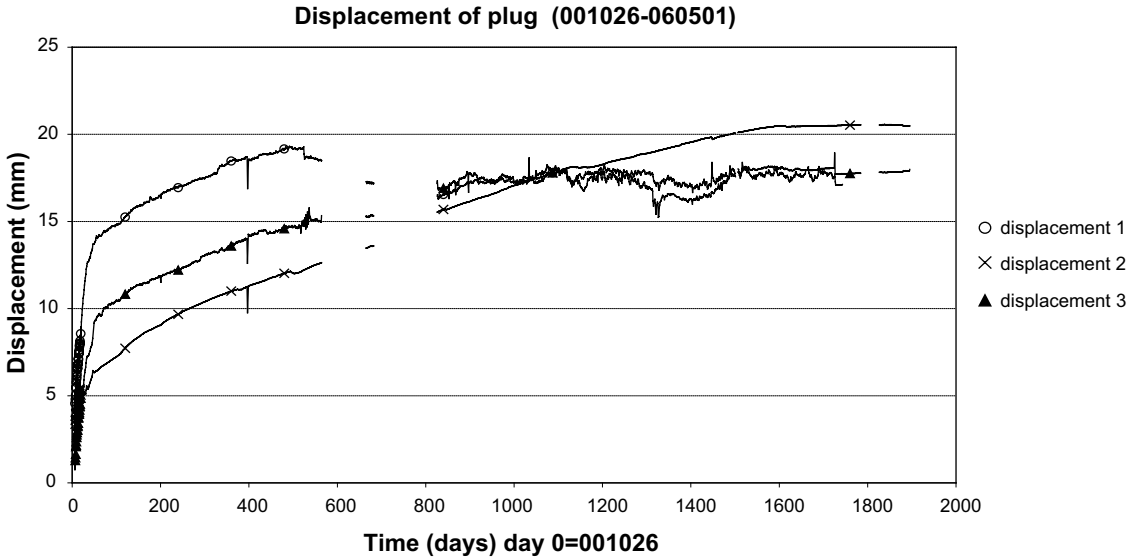

Figure 3-10. *Vertical displacement of the plug.*

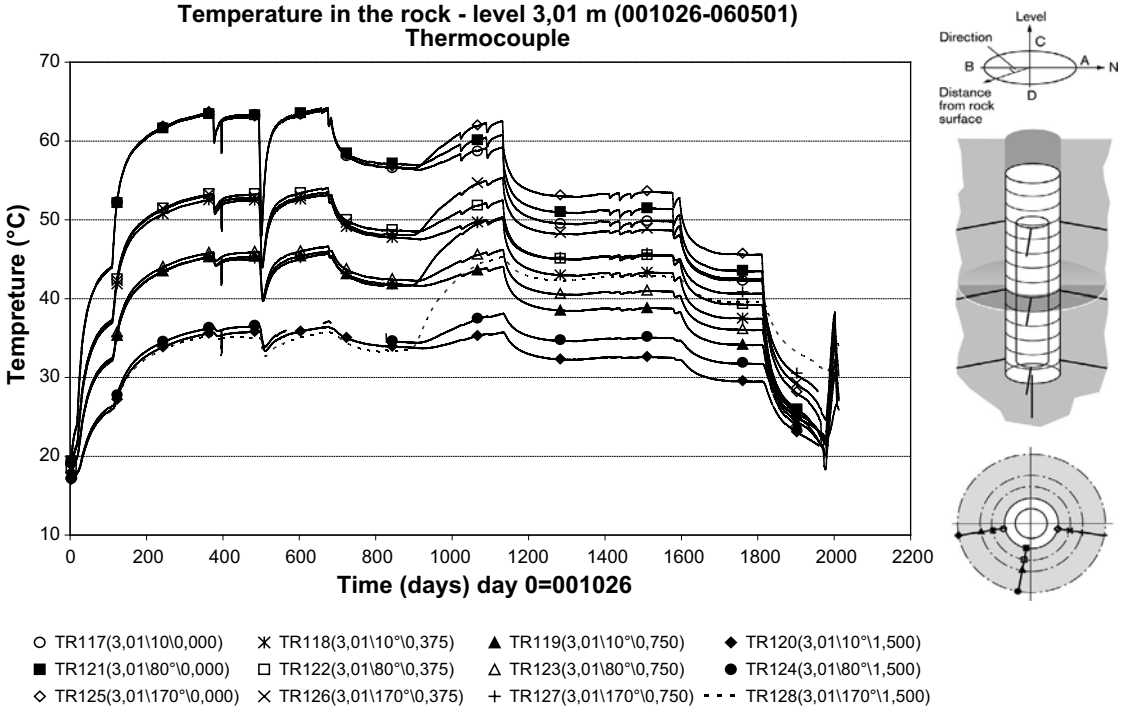

Figure 3-11. *Rock temperatures in the CRT experiment.*

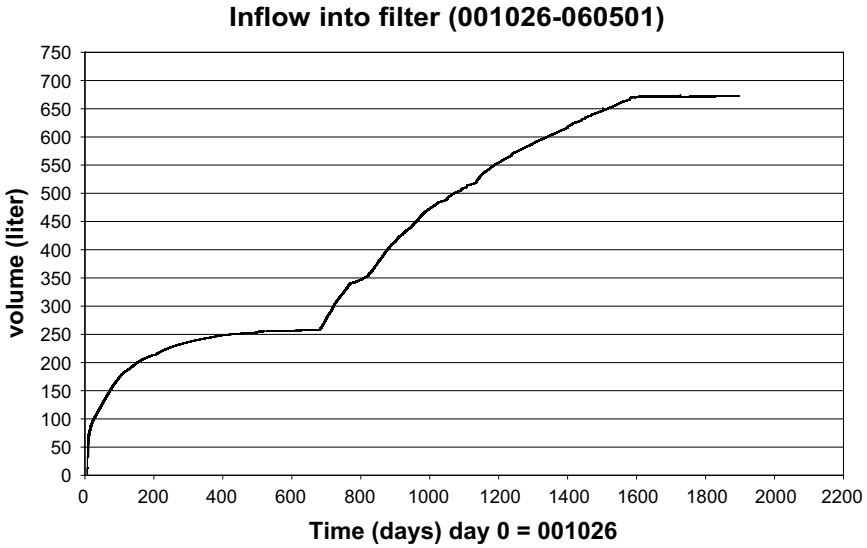

Figure 3-12. *Measured water inflow.*

The measured vertical displacement of the plug is not entirely reliable. The curve called "displacement2" in Figure 3-10 is considered to be the most accurate. Back calculations of the displacement by using the average dry density in each block yield that the total vertical displacement should be ≈ 40 mm instead of ≈ 20 mm, as the measurements show. In Figure 3-13 the calculated accumulated swelling is shown at different heights from the hole bottom and in Table 3-8 the average dry density at installation and dismantling, the calculated vertical swelling and the absorbed water are shown for each bentonite block section.

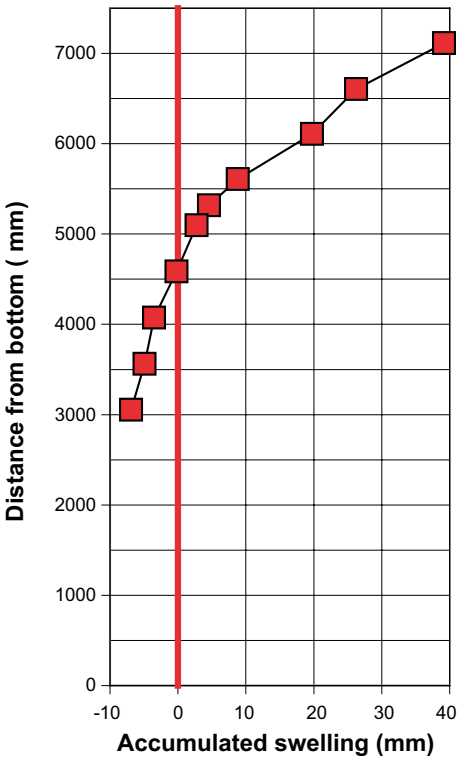

Figure 3-13. *Calculated accumulated swelling at different height from the hole bottom.*

Table 3-8. The average dry density at installation and at dismantling at different sections of the buffer together with the calculated vertical displacement and absorbed amount of water. The absorbed water for rings R5–R1 are assumed to be the average absorbed water of rings R6–R9, block C1 is assumed to be the same as block C2.

Block No	Average dry density at installation (kg/m³)	Average dry density at dismantling (kg/m³)	Calculated vertical swelling (mm)	Absorbed water (kg)
C4	1 598	1 558	12.9	79.7
C3	1 598	1 578	6.5	89.6
C2	1 598	1 563	10.9	83.6
R10*)	1 608	1 578	4.2	47.7
R10**)	1 569	1 559	1.8	35.7
R9	1 569	1 560	2.9	61.0
R8	1 569	1 580	–3.3	53.7
R7	1 569	1 574	–1.4	50.4
R6	1 569	1 575	–2.0	56.6
R5***)	1 569		0	55.4
R4***)	1 569		0	55.4
R3***)	1 569		0	55.4
R2***)	1 569		0	55.4
R1***)	1 569		0	55.4
C1***)	1 598		0	83.6
∑			39.1	918.2

*) Above the canister top.
**) Underneath the canister top.
***) Estimated.

If the displacement of 13 mm, reported during the first five days, is added to the measured displacements a total of 33 mm is obtained. The remaining displacement up to the back calculated estimate 40 mm could origin from elastic deformations in the buffer occurring after unloading when the experiment was dismantled. Note also that the 13 mm of vertical swelling at day 5 is only a late estimate.

3.2.3 Sensor positions

The simulated processes should be compared with the specified sensor data in the notes. Below in Table 3-9 to Table 3-14 the exact position of the sensors is described.

Strategy for describing the position of each device

Every instrument is named with a short unique name consisting of 1–2 letters describing the type of measurement and 3 figures numbering the device. Every instrument position in the buffer and rock is described with three coordinates according to Figure 3-14.

The r-coordinate is the horizontal distance from the center of the hole and the z-coordinate is the height from the bottom of the hole (the block height is set to 500 mm). The α-coordinate is the angle from the vertical direction B (almost south).

The short description of the positions in the diagrams differs between the buffer and the rock. Positions are identified by three “coordinates” as follows in Table 3-9:

The bentonite blocks are called cylinders and rings. The cylinders are numbered C1–C4 and the rings R1–R10 respectively (Figure 3-15).

Table 3-9. Position identification within the Buffer and Rock.

Buffer:	Ring/Cylinder no.	Direction A, B, C, or D	Radius from centre line [mm]
Rock:	Distance from the hole bottom [m]	α according to Figure 3-14 [°]	Distance from hole wall [m]

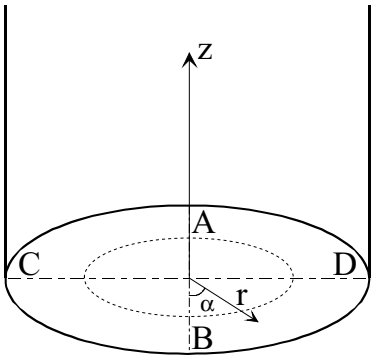

Figure 3-14. *The instrument planes (A–D) and the coordinate system used when describing the instrument positions.*

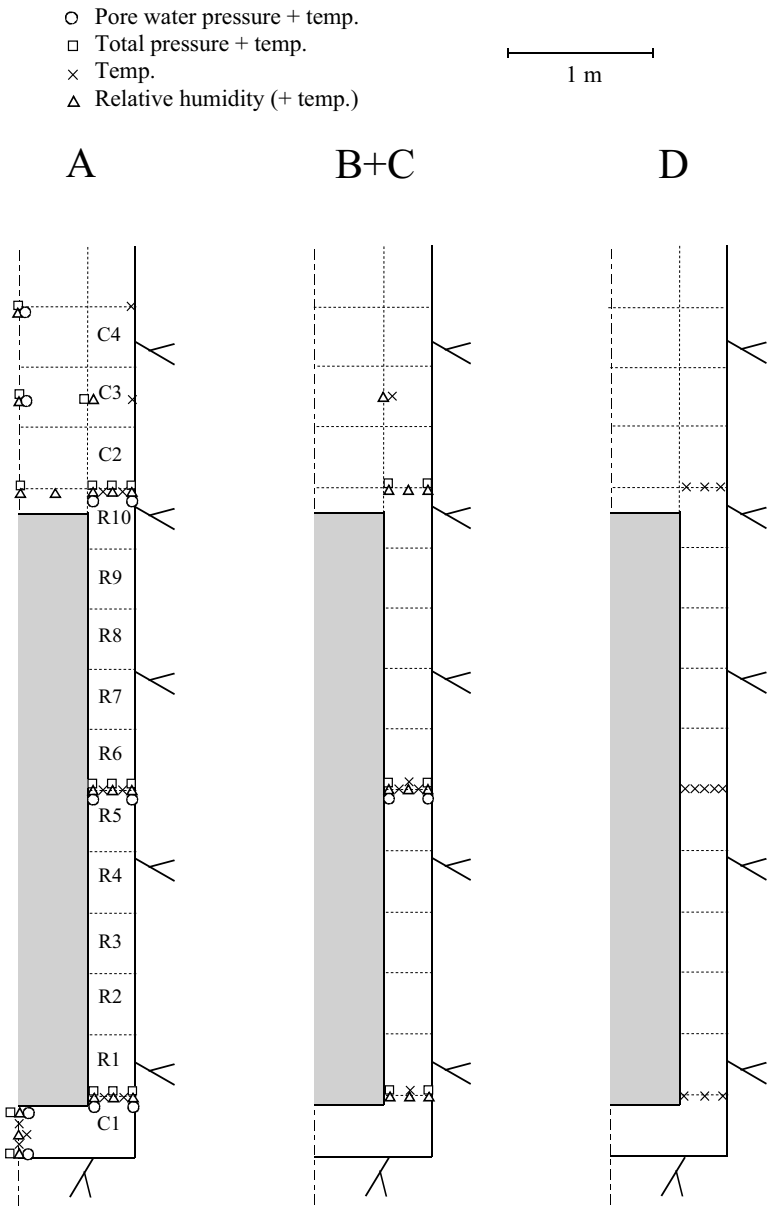

Figure 3-15. *Schematic view over the instruments in four vertical sections and the block designation.*

Position of each instrument in the bentonite

Measurements are done in four vertical sections A, B, C and D according to Figure 2-14. Direction A and B are placed in the tunnels axial direction.

An overview of the positions of the instruments is shown in Figure 3-15. Exact positions are described in Table 3-10 to 3-14.

The instruments are located in two main levels in the blocks, 50 mm and 160 mm, from the upper surface. The thermocouples have mostly placed in the 50mm level and the other gauges in the 160 mm level.

Table 3-10. Numbering and position of instruments for measuring temperature (T).

		Instrument position in block				Cable pos.		
Type and number	**Block**	**Direction**	**α**	**r**	**Z**	**α**	**Fabricate**	**Remark**
T101	Cyl. 1	Center	90	50	50	242	BICC	
T102	Cyl. 1	Center	90	50	250	238	BICC	
T103	Cyl. 1	Center	90	50	450	230	BICC	
T104	Cyl. 1	A	180	635	450	206	BICC	
T105	Cyl. 1	A	180	735	450	202	BICC	
T106	Cyl. 1	B	365	685	450	38	BICC	
T107	Cyl. 1	C	275	685	450	274	BICC	
T108	Cyl. 1	D	90	585	450	96	BICC	
T109	Cyl. 1	D	90	685	450	94	BICC	
T110	Cyl. 1	D	90	785	450	92	BICC	
T111	Ring 5	A	180	635	2950	224	BICC	
T112	Ring 5	A	180	735	2950	218	BICC	
T113	Ring 5	B	360	610	2950	318	BICC	
T114	Ring 5	B	360	685	2950	322	BICC	
T115	Ring 5	B	360	735	2950	324	BICC	
T116	Ring 5	C	270	610	2950	258	BICC	
T117	Ring 5	C	270	685	2950	260	BICC	
T118	Ring 5	C	270	735	2950	262	BICC	
T119	Ring 5	D	90	585	2950	44	BICC	
T120	Ring 5	D	90	635	2950	46	BICC	
T121	Ring 5	D	90	685	2950	48	BICC	
T122	Ring 5	D	90	735	2950	50	BICC	
T123	Ring 5	D	90	785	2950	52	BICC	
T124	Ring 10	A	180	635	5450	200	BICC	
T125	Ring 10	A	180	735	5450	194	BICC	
T126	Ring 10	D	90	585	5450	54	BICC	
T127	Ring 10	D	90	685	5450	56	BICC	
T128	Ring 10	D	90	785	5450	58	BICC	
T129	Cyl. 3	A	180	785	6250	166	BICC	
T130	Cyl. 3	B	365	585	6250	358	BICC	
T131	Cyl. 3	C	275	585	6250	280	BICC	
T132	Cyl. 4	A	180	785	6950	66	BICC	

Table 3-11. Numbering and position of instruments for measuring total pressure (P).

		Instrument position in block				Cable pos.		
Type and number	**Block**	**Direction**	**α**	**r (mm)**	**Z (mm)**	**α**	**Fabricate**	**Remark**
P101	Cyl. 1	Center	180	50	0	244	Kulite	
P102	Cyl. 1	Center	180	50	450	232	Kulite	
P103	Cyl. 1	A	185	585	340	208	Geokon	
P104	Cyl. 1	A	185	685	340	204	Geokon	
P105	Cyl. 1	A	185	785	340	186	Geokon	
P106	Cyl. 1	B	365	585	340	40	Geokon	
P107	Cyl. 1	B	365	785	340	2	Geokon	
P108	Cyl. 1	C	275	585	340	278	Geokon	
P109	Cyl. 1	C	275	785	340	270	Geokon	
P110	Ring 5	A	185	585	2840	228	Geokon	
P111	Ring 5	A	185	685	2840	222	Geokon	
P112	Ring 5	A	185	785	2840	188	Geokon	
P113	Ring 5	B	365	535	2840	36	Geokon	
P114	Ring 5	B	365	825	2840	16	Geokon	
P115	Ring 5	C	275	585	2840	296	Geokon	
P116	Ring 5	C	275	785	2840	290	Geokon	
P117	Ring 10	Center	180	50	5340	24	Kulite	
P118	Ring 10	A	180	585	5340	216	Geokon	
P119	Ring 10	A	180	685	5340	198	Geokon	
P120	Ring 10	A	180	785	5340	192	Geokon	
P121	Ring 10	B	365	585	5340	20	Kulite	
P122	Ring 10	B	365	785	5340	18	Kulite	
P123	Ring 10	C	275	585	5340	286	Kulite	
P124	Ring 10	C	275	785	5340	284	Kulite	
P125	Cyl. 3	Center	180	50	6250	158	Geokon	
P126	Cyl. 3	A	180	585	6250	162	Geokon	
P127	Cyl. 4	Center	180	50	6840	64	Kulite	

Table 3-12. Numbering and position of instruments for measuring pore water pressure (U).

		Instrument position in block				Cable pos.		
Type and number	**Block**	**Direction**	**α**	**r (mm)**	**Z (mm)**	**α**	**Fabricate**	**Remark**
U101	Cyl. 1	Center	270	50	50	246	Geokon	
U102	Cyl. 1	Center	270	50	450	236	Geokon	Horizontal
U103	Cyl. 1	A	175	585	340	126	Geokon	
U104	Cyl. 1	A	175	785	340	178	Geokon	
U105	Ring 5	A	175	585	2840	138	Geokon	
U106	Ring 5	A	175	785	2840	180	Geokon	
U107	Ring 5	B	355	535	2840	314	Geokon	In the slot
U108	Ring 5	B	355	825	2840	348	Geokon	In the slot
U109	Ring 5	C	265	585	2840	256	Geokon	
U110	Ring 5	C	265	825	2840	264	Geokon	In the slot
U111	Ring 10	A	175	585	5340	146	Geokon	
U112	Ring 10	A	175	785	5340	152	Geokon	
U113	Cyl. 3	Center	270	50	6250	156	Geokon	
U114	Cyl. 4	Center	270	50	6950	62	Kulite	

Table 3-13. Numbering and position of instruments for measuring water content (W).

		Instrument position in block				Cable pos.		
Type and number	**Block**	**Direction**	**α**	**r**	**Z**	**α**	**Fabricate**	**Remark**
W101	Cyl. 1	Center	360	50	50	248	Vaisala	
W102	Cyl. 1	Center	360	400	160	240	Vaisala	
W103	Cyl. 1	Center	360	50	450	234	Vaisala	Horizontal
W104	Cyl. 1	A	180	585	340	128	Vaisala	
W105	Cyl. 1	A	180	685	340	132	Vaisala	
W106	Cyl. 1	A	180	785	340	184	Vaisala	
W107	Cyl. 1	A	170	585	340	124	Wescor	
W108	Cyl. 1	A	170	685	340	130	Wescor	
W109	Cyl. 1	A	170	785	340	134	Wescor	
W110	Cyl. 1	B	360	585	340	304	Vaisala	
W111	Cyl. 1	B	360	785	340	360	Vaisala	
W112	Cyl. 1	B	360	685	340	308	Vaisala	
W113	Cyl. 1	B	355	585	340	302	Wescor	
W114	Cyl. 1	B	355	685	340	306	Wescor	
W115	Cyl. 1	B	355	785	340	310	Wescor	
W116	Cyl. 1	C	270	585	340	250	Wescor	
W117	Cyl. 1	C	270	685	340	252	Wescor	
W118	Cyl. 1	C	270	785	340	254	Vaisala	
W119	Ring 5	A	180	585	2840	226	Vaisala	
W120	Ring 5	A	180	685	2840	220	Vaisala	
W121	Ring 5	A	180	785	2840	182	Vaisala	
W122	Ring 5	A	170	585	2840	136	Wescor	
W123	Ring 5	A	170	685	2840	140	Wescor	
W124	Ring 5	A	170	785	2840	142	Wescor	
W125	Ring 5	B	360	535	2840	316	Vaisala	In the slot
W126	Ring 5	B	360	685	2840	34	Vaisala	
W127	Ring 5	B	360	785	2840	350	Vaisala	
W128	Ring 5	B	350	535	2840	312	Wescor	In the slot
W129	Ring 5	B	350	685	2840	320	Wescor	
W130	Ring 5	B	350	785	2840	346	Wescor	
W131	Ring 5	C	270	585	2840	294	Wescor	In the slot
W132	Ring 5	C	275	685	2840	292	Wescor	
W133	Ring 5	C	270	785	2840	288	Wescor	
W134	Ring 10	Center	360	50	5340	22	Vaisala	
W135	Ring 10	A	180	262	5340	26	Vaisala	
W136	Ring 10	A	180	585	5340	214	Vaisala	
W137	Ring 10	A	180	685	5340	196	Vaisala	
W138	Ring 10	A	180	785	5340	190	Vaisala	
W139	Ring 10	A	170	585	5340	144	Wescor	
W140	Ring 10	A	170	685	5340	148	Wescor	
W141	Ring 10	A	170	785	5340	150	Wescor	
W142	Ring 10	B	360	585	5340	328	Vaisala	
W143	Ring 10	B	360	685	5340	332	Vaisala	
W144	Ring 10	B	360	785	5340	336	Vaisala	
W145	Ring 10	B	355	585	5340	326	Wescor	
W146	Ring 10	B	355	685	5340	330	Wescor	
W147	Ring 10	B	355	785	5340	334	Wescor	
W148	Ring 10	C	270	585	5340	266	Wescor	
W149	Ring 10	C	270	685	5340	268	Wescor	
W150	Ring 10	C	270	785	5340	272	Vaisala	
W151	Cyl. 3	Center	360	50	6250	154	Vaisala	
W152	Cyl. 3	A	180	585	6250	160	Vaisala	
W153	Cyl. 3	B	360	585	6250	356	Vaisala	
W154	Cyl. 3	C	270	585	6250	276	Wescor	
W155	Cyl. 4	Center	360	50	6840	60	Vaisala	

Position of each instruments in the rock

The position of the thermocouples in the rock is shown in Table 3-14.

Table 3-14. Numbering and positions of thermocouples in the rock.

				Cable pos.		
Type and number	**Level**	**Direction**	**Distance from rock surface**	**α**	**Fabricate**	**Remark**
TR101	0	Center	0.000	70°–90°	BICC	
TR102	0	Center	0.375	70°–90°	BICC	
TR103	0	Center	0.750	70°–90°	BICC	
TR104	0	Center	1 500	70°–90°	BICC	
TR105	0.61	10°	0.000	4°–14°	BICC	
TR106	0.61	10°	0.375	4°–14°	BICC	
TR107	0.61	10°	0.750	4°–14°	BICC	
TR108	0.61	10°	1 500	4°–14°	BICC	
TR109	0.61	80°	0.000	70°–90°	BICC	
TR110	0.61	80°	0.375	70°–90°	BICC	
TR111	0.61	80°	0.750	70°–90°	BICC	
TR112	0.61	80°	1 500	70°–90°	BICC	
TR113	0.61	170°	0.000	168°–176°	BICC	
TR114	0.61	170°	0.375	168°–176°	BICC	
TR115	0.61	170°	0.750	168°–176°	BICC	
TR116	0.61	170°	1 500	168°–176°	BICC	
TR117	3.01	10°	0.000	4°–14°	BICC	
TR118	3.01	10°	0.375	4°–14°	BICC	
TR119	3.01	10°	0.750	4°–14°	BICC	
TR120	3.01	10°	1 500	4°–14°	BICC	
TR121	3.01	80°	0.000	70°–90°	BICC	
TR122	3.01	80°	0.375	70°–90°	BICC	
TR123	3.01	80°	0.750	70°–90°	BICC	
TR124	3.01	80°	1 500	70°–90°	BICC	
TR125	3.01	170°	0.000	168°–176°	BICC	
TR126	3.01	170°	0.375	168°–176°	BICC	
TR127	3.01	170°	0.750	168°–176°	BICC	
TR128	3.01	170°	1 500	168°–176°	BICC	
TR129	5.41	10°	0.000	4°–14°	BICC	
TR130	5.41	10°	0.375	4°–14°	BICC	
TR131	5.41	10°	0.750	4°–14°	BICC	
TR132	5.41	10°	1 500	4°–14°	BICC	
TR133	5.41	80°	0.000	70°–90°	BICC	
TR134	5.41	80°	0.375	70°–90°	BICC	
TR135	5.41	80°	0.750	70°–90°	BICC	
TR136	5.41	80°	1 500	70°–90°	BICC	
TR137	5.41	170°	0.000	168°–176°	BICC	
TR138	5.41	170°	0.375	168°–176°	BICC	
TR139	5.41	170°	0.750	168°–176°	BICC	
TR140	5.41	170°	1 500	168°–176°	BICC	

3.2.4 Overview of CRT tasks as suggested to the EBS Task Force members

Three possible tasks are listed below, where the first one should be considered as optional and the two following are considered as more important in the context of EBS Task Force.

The first task is a pure thermal problem where the temperature field in the surroundings of the CRT and TBT experiments is simulated without consideration to couplings with hydrological and mechanical processes. This task is not that challenging from a simulation point of view since it only considers the thermal process, and it is also rather time consuming developing the 3D model of the entire surrounding geometry which is needed. (Therefore results from a simulation with such a model are given in an attached file.) *(This was the case for the handout provided to the Task Force, authors comment.)*

In the two following tasks the THM processes in the CRT experiment are studied. In the first task the buffer at canister mid-height is modeled in detail. Here the geometry considered and conditions are specified rather precise since the main reason for this assignment is to evaluate how well the material models in the codes are able to capture the THM processes in the buffer. The Task Force teams may obviously adopt the specified conditions so that their code capabilities are met. An interesting subject in this task is how well the mechanical homogenization process is simulated. In this smaller problem the model can easily be "tuned" and controlled.

Thereafter the entire experiment is considered. Here the Task Force teams may freely design their own model. The object of interest is to compare how the teams choose to model the problem and how the overall behavior of the models compares to the experimental data. A schematic example of conditions that may be used for a model is given.

The thermal boundary conditions of the THM models can be obtained either from the results of the thermal 3D simulation or from experimental data.

Besides the suggested tasks, other additional studies initiated by the Task Force groups are encouraged!

Thermal simulation of the rock mass surrounding the CRT and TBT experiments (optional)

In this task the temperature field in the rock mass surrounding the CRT and TBT experiments is to be simulated. Since the TBT experiment is located close to the CRT experiment (6 m) the thermal influence from TBT has to be considered.

1. Compare the simulated temperature field in the surrounding rock mass with the given sensor data.
2. Record temperatures at the hole wall which can be used as boundary conditions in the following two tasks.
3. Record canister heat flux at canister mid-height which can be used as boundary conditions for the task where the canister mid-height section is simulated.

The results from calculations performed by Ola Kristensson are described in Sector 3.3.2.

Thermo-hydro-mechanical simulation of the engineered buffer at canister mid-height

In this task a disk of the engineered buffer, consisting of a gap close to the canister, a ring-shaped bentonite block and a pellet filled outer gap, at canister mid-height is to be simulated considering thermal, hydraulic and mechanical processes.

Here it is suitable to begin with a TH model, where the hydraulic laws and parameters can be tested, and later on the mechanical laws are incorporated in a THM model, which can be developed from the previously developed TH model.

In these smaller models, as compared to the one needed for the last task where the entire experiment is to be simulated, different constitutive laws and parameters can easily be tested. The influence of the mechanical processes can also be investigated since a TH and a THM model are available if the sequence of first using a TH and thereafter a THM model are used.

1. Compare the results obtained from the TH model with the given experimental data. Temperature and RH.
2. Compare the results obtained from the THM model with the given experimental data. Temperature, RH, void ratio profile and stress.
3. What differences can be found between the TH and THM models, and if there are differences why do they occur?

This task is described in detail in Section 3.2.6.

Thermo-hydro-mechanical simulation of the entire CRT experiment

Here the entire experiment is considered in a THM simulation. The canister, inner gap, ring- and cylinder-shaped bentonite blocks, (bentonite bricks at the top of the canister), pellet filled outer gap, concrete plug, steel lid, rock and a representation of the rock anchors may be considered in the model. As in the previous task thermal boundary conditions at the hole wall or here also in the rock can be obtained from the thermal 3D simulation or experimental data. The constitutive parameters calibrated in the previous task can be used in this model.

Also here a TH model is suitable to begin with and later on a THM model, derived from the TH model, can be developed. The validity of the parameters obtained in the small model can here be investigated on a larger scale as well as the mechanical influence.

1. Compare the results at canister mid-height with the results obtained with the small model for the TH and THM models.
2. Compare the results obtained from the model with the given experimental data. Temperature, RH and void ratio profiles and stress for the THM model.
3. Study the heave of and the force on the steel lid. Compare with given experimental data.

This task is described in detail in Section 3.2.7.

3.2.5 Thermal simulation of the rock mass surrounding the CRT and TBT experiments

The description of this task can be found in a later section (3.3.2) describing an example of a simulation.

3.2.6 Thermo-hydro-mechanical simulation of the engineered buffer at canister mid-height

Geometry

This task is focused on the mid-section of the buffer. A disc of the engineered buffer is to be modeled, rotational symmetry can be assumed, see Figure 3-16.

A radially symmetric model can be used, where the model should contain:

A. the inner gap (0.01 m width).

B. the ring shaped bentonite block.

C. the outer gap filled with bentonite pellets (0.055 m width).

Figure 3-17 shows the geometry of the considered mid-section.

Boundary conditions and initial conditions

Boundary conditions

Suggested boundary conditions of the selected disk of the engineered buffer are given in Table 3-16. When present, the names of the sensors, providing data for input as boundary conditions, are given.

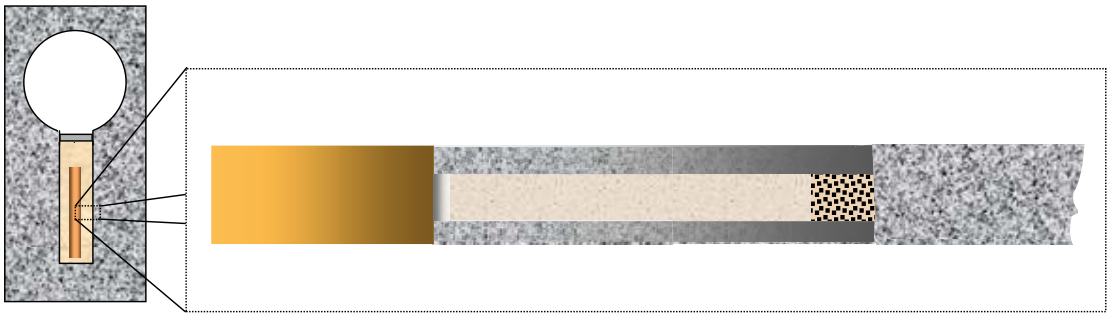

Figure 3-16. A schematic drawing of the CRT geometry and a blow up of a disc at the mid-section.

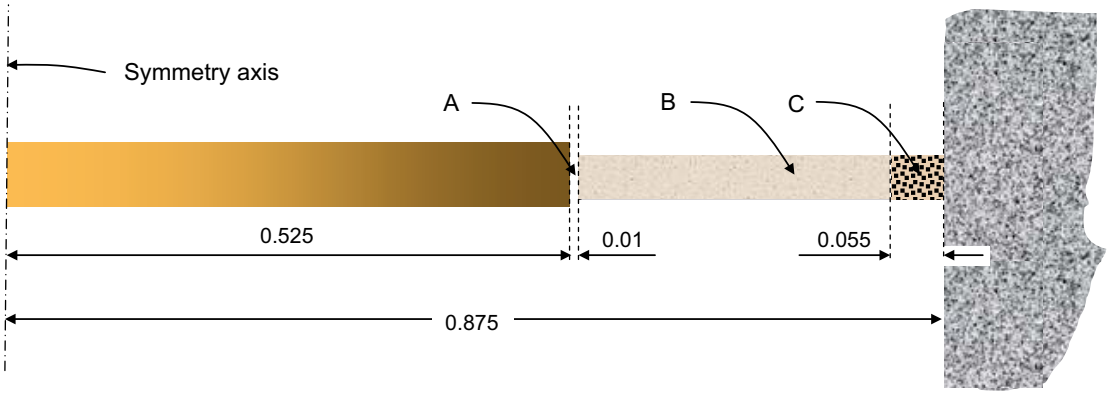

Figure 3-17. Geometry of the mid-section.

Table 3-16. Suggested boundary conditions.

	Type of process		
Boundary	**Thermal**	**Hydraulic**	**Mechanical**
Canister	Mid-height heat flux (only suitable if your model has a small radial dimension as compared to the canister height) or temperature from 3D simulation or temperature from experimental data. Sensor P12	Zero water flux	Roller conditions
Horizontal	Zero thermal flux	Zero water flux	Roller conditions
Hole wall	Temperature from 3D simulation or experimental data. Sensor TR125	Water pressure from filter pressure protocol.	Roller conditions

Initial conditions

The initial conditions are given in terms of the temperature, T, the water saturation, S_r, the total stress tensor, $\boldsymbol{\sigma}$, and the porosity, n. The water saturation is defined as $S_r = dV_w/dV_p$ and the porosity $n = dV_p/dV$.

In both the definitions given above we make use of an additive split of a volume element, dV, in a solid volume element, dV_s, and a pore volume element, dV_p. Furthermore the pore volume element is additively split into a water volume element, dV_w, and an air volume element, dV_a.

The initial conditions are given in Table 3-17. The estimation of the initial values of the S_r and n parameters is based on the values given in Johannesson (2007). The pellet-filled slot has here been considered as a homogenized material, i.e. the individual pellets interaction with each other and with the surroundings is not considered in detail.

Material properties

The material characteristics are shown in Section 3.2.8.

Results to present

The results that the teams should present are 1) variable histories at specified points and 2) variable profiles at specified times. Some of the selected results can be compared with experimental measurements. The experimental data to compare with, provided in the form of excel-files, are listed in the next section "Sensor data to compare with". The sensor names, positions and issues of the sensors can also be found in the next section.

The entire set of points, defined as a position of a material particle in the initial (undeformed) configuration, that is selected is shown schematically in Figure 3-18 below. The point position will thus change according to the deformation of the material. Note that all variables should not be shown for all points. See the list below for the correct variable – point selection. In the list the points (radial position) where sensor data is available are indicated using a bold font.

Table 3-17. Initial conditions.

	Type of process		
Section	**Thermal**	**Hydraulic**	**Mechanical**
A. Inner gap	T = 20 °C	S_r= 0–1 ? (is it filled)	$\boldsymbol{\sigma}$ = **0** MPa, n = 1
B. Bentonite block	T = 20 °C	S_r= 0.859	$\boldsymbol{\sigma}$ = **0** MPa, n = 0.36
C. Pellet-filled gap	T = 20 °C	S_r= 0.895	$\boldsymbol{\sigma}$ = **0** MPa, n = 0.64

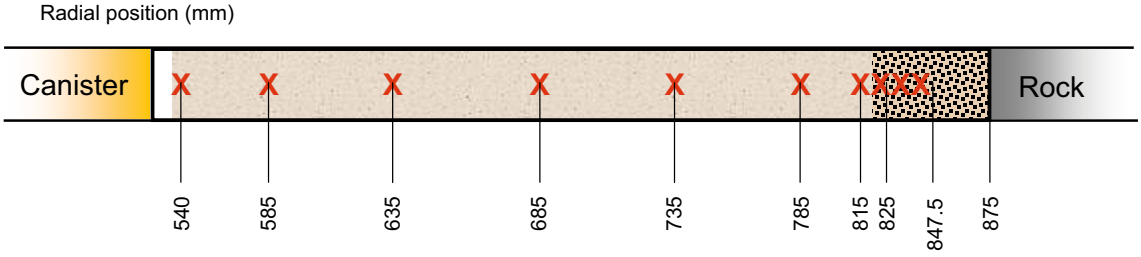

Figure 3-18. *Schematic drawing of the points where variable histories should be presented. The radial distances are given in the initial (undeformed) configuration.*

Temperature histories at the radial distances [mm] (in the initial configuration):

540, **585**, **635**, **685**, **735**, **785**, 815, 825, 847.5

Water saturation histories at the radial distances [mm]:

540, **585**, 635, **685**, 735, **785**, 815, 825, 847.5

Total vertical (axial) stress histories at the radial distances [mm]:

540, **585**, **685**, **785**, 815, 825, 847.5, 875

Total horizontal (radial) stress histories at the radial distances [mm]:

540, 585, 685, 785, 815, 825, 847.5, 875

Dry density histories at the radial distances [mm]:

540, 585, 635, 685, 735, 785, 815, 825, 847.5

Displacement histories at the radial distances [mm]:

540, 585, 635, 685, 735, 785, 815, 825, 847.5

Profiles of Temperature, Water saturation and Dry density in the buffer at day:

670, 1 400, 1 800, 1 910

Sensor data to compare with

This model is considered to mimic the behavior of the buffer at canister mid-height (ring 5) in the direction towards the TBT experiment (direction A or $\alpha = 180°$ in the nomenclature used in the sensors data report (Goudarzi et al. 2006).

The model can be compared with sensor data obtained during the experiment, see Goudarzi et al. (2006), and with data obtained after dismantling and sampling the buffer, see Johannesson (2007). The sensor names below are in some cases given together with the radial position given in mm (bracketed after the sensor name), e.g. T111(635) means sensor T111 at the radial position 635 mm from the hole center.

The results obtained from the simulation are to be presented together with the corresponding experimental data at least for the sensor names and profiles obtained by sampling after dismantling the experiment that are given below.

Thermal

Temperatures in the buffer can be checked against the temperatures measured by Vaisala sensors (which are RH sensors also able to measure temperature), but these broke down after ≈ 600 days. There are also thermocouples that can be used in this direction that worked during the entire experiment.

Vaisala: W119T(585), W120T(685), W121T(785)

Thermocouples: T111(635), T112(735)

Hydraulic

The wetting evolution can be checked comparing with RH-data and/or suction-data. The CRT-experiment has been equipped with two complementary sensors measuring the moisture in the buffer.

The Vaisala sensor measures relative humidity. These sensors functions well below ≈ 95 % RH, but give scattered results in the region above this limit. They also tend to break down when sudden drops in temperature occur (decrease in canister power) depending on the resulting peak in RH.

The Wescore psychrometer measures the suction. These sensors work well above ≈ 96 % RH, and give more steady measurements as compared to Vaisala in this region. Below ≈ 96 % RH they do not give correct measurements since they can only record suctions less then 5 MPa.

Dependent on the behavior of the hydraulic sensors described above, the best overview of the saturation evolution is probably obtained if the sensors are used as a complement of each other, using Vaisala to begin with, when RH < 95 %, and Wescore later on, when RH > 95 % or the suction < 5 MPa.

Vaisala: W119(585), W120(685), W121(785)

Wescore: W122(585), W123(685), W124(785)

From the samples taken in ring 6 and ring 7 (ring 5 was not sampled) after dismantling the experiment the corresponding water saturation profiles have been calculated. The profiles obtained at the end of the simulation can thus be compared with these experimental results.

Mechanical

Two different mechanical parameters, the axial stress and the dry density profile at the end of the test, are used as an indication of how well the model mimics the mechanical processes in the experiment.

In the experiment Geokon total pressure sensors were installed. The measured total pressure is in some cases found to be lower as compared to the expected total pressure at the given block density. The Geokon sensors have a cigar-shape where the pressure is measured at the tip of the sensor. When the sensors were installed, holes were drilled in the right position and the sensors were placed in the holes together with bentonite powder used to back fill the holes. At the tip where the pressure is measured there could therefore be a cavity, or lower density as compared to the block density, that might be responsible for the obtained low values of total pressure.

The total axial (vertical) stress σ_a in ring 5 is given by the selected sensors.

P110(585), P111(685), U106(785) (The sensor name U106 indicates that this sensor should measure pore pressure, but is was changed later on to measure total pressure.)

The dry density profile in ring 6 and ring 7 at end of test is also available. Comparison of the simulated profiles and the measured indicates whether the homogenization has been correctly captured or not.

3.2.7 Thermo-hydro-mechanical simulation of the entire engineered buffer in CRT

Loads, boundary conditions and initial conditions

Load

The thermal load (canister power) can be obtained from the protocol given in Table 3-2.

Boundary conditions

Table 3-18 is an attempt to structure the conditions that should be considered in the same manner as is done in the former task. The conditions are, however, defined in a more “fuzzy” fashion. The modelers are in this way given more freedom when it comes to designing the models in this task.

Initial conditions

Also here the initial conditions, shown in Table 3-19, have been obtained from Johannesson (2007).

Material properties

The properties of the materials are given in Appendix 2.

Table 3-18. Suggested conditions.

Type of process Thermal	Hydraulic	Mechanical
Tunnel air temperature. T = 15 °C.	Water pressure from filter protocol.	The effect from the rock anchors should be modeled. The steel lid and concrete plug are allowed to move in the vertical direction.

Table 3-19. Initial conditions.

Constituent	Type of process Thermal	Hydraulic	Mechanical
Bentonite blocks			
– Cylinder-shaped	T = 20 °C	S_r = 0.751	σ = 0 MPa, n = 0.39
– Ring-shaped	T = 20 °C	S_r = 0.859	σ = 0 MPa, n = 0.36
Pellet-filled gap	T = 20 °C	S_r = 0.895	σ = 0 MPa, n = 0.64
Bentonite bricks	T = 20 °C	S_r = 0.637	σ = 0 MPa, n = 0.42

Results to present

The results that the teams should present are 1) variable histories at specified points and 2) variable profiles at specified times. Some of the selected results can be compared with experimental measurements. The experimental data to compare with, provided in the form of excel-files, are listed in the next chapter “Sensor data to compare with”. The sensor names, positions and issues of the sensors can also be found in the next section.

For Ring 5 (at canister mid-height, 2.84 m from the hole bottom) all the results specified for the previous task should also be presented for this task, where the entire buffer is considered. In addition to this the history of variables belonging to points in Ring 10 (at the top of the canister, 5.34 m from the hole bottom) and Cylinder 3 (the second ring from the top, 6.25 m from the hole bottom) should be shown. Also profiles of variables at R10 and C3 should be presented at the specified times. Also iso-maps of variables at the given times should be shown. Finally the heave of the lid and the force on the plug also should be presented.

Below follows a list of the results that should be presented. As before the point position will change according to the deformation of the material, the definition is given in the undeformed configuration. In the list the points (radial position) where sensor data is available are indicated using a bold font.

C5: See the previous task.

Temperature histories at the radial distances [mm] (in the initial configuration):

- R10: 50, 585, **685**, 785, 847.5
- C3: 50, 585, 685, **785**, 847.5

Water saturation histories at the radial distances [mm]:

- R10: **50**, **585**, **685**, 785, 847.5
- C3: **50**, 585, **685**, 785, 847.5

Total vertical (axial) stress histories at the radial distances [mm]:

- R10: 50, 585, **685**, 785, 875
- C3: **50**, 585, 685, 785, 875

Total horizontal (radial) stress histories at the radial distances [mm]:

- R10: 50, 585, 685, 785, 875
- C3: 50, 585, 685, 785, 875

Dry density histories at the radial distances [mm]:

- R10: 50, 585, 685, 785, 847.5
- C3: 50, 585, 685, 785, 847.5

Profiles of Temperature, Water saturation and Dry density in the buffer at day:

- R10: 670, 1 400, 1 800, 1 910
- C3: 670, 1 400, 1 800, 1 910

Iso-maps (contour plots) of Temperature, Water saturation and Dry density in the buffer at day: 670, 1 400, 1 800, 1 910.

The history of the plug displacement.

The history of the force acting on the plug.

Sensor data to compare with

For R5 the sensors defined for the previous task should be used. The sensors that should be used for R10 and C3 are given below.

The sensors have been selected as consequent as possible with respect to position. The positions are given according to the definitions in Figure 3-19 where the direction A ($\alpha = 180°$) is closest to the north (located at $\alpha \approx 170°$).

For the indicated block (R10 or C3) the sensor names are followed by the radial position in mm and the direction name (A, B, C and D). The type (Wescor or Vaisala) of the "hydraulic" sensors is also indicated. The profile data is also indicated where available.

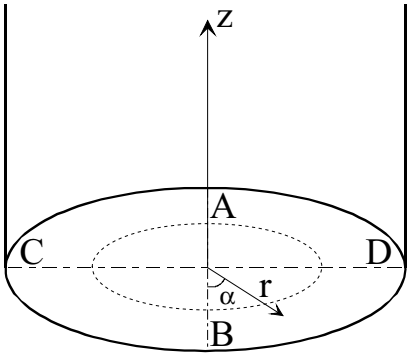

Figure 3-19. *The instrument planes (A–D) and the coordinate system used when describing the instrument positions.*

Thermal

R10:

T127(685) D.

C3:

T129(785) A.

Hydraulic

R10:

Vaisala: W134(50) center, W142(585) B, W137(685) A.

Wescor: W140(685) A.

S_r profile for R10.

C3:

Vaisala: W153(685) C, W151(50) center.

Wescor: W154(685) C.

S_r profile for C3.

Contour plot of the water saturation obtained after dismantling the test is available for the upper part (from C4 to R6) of the buffer.

Mechanical

R10:

P119(685) A.

Dry density profile for R10.

C3:

P125(50) center.

Dry density profile for C3.

Contour plot of the dry density obtained after dismantling the test is available for the upper part (from C4 to R6) of the buffer.

Here also the vertical displacement of the plug and the total force on the plug should be compared with experimental measurements.

3.2.8 Detailed description of the filling of the outer slot in CRT

The following indented text below is obtained from the CRT installation report where the filling of the outer slot with pellets and water is described. The text should be regarded as a source of information of how the process of filling the outer slot with pellets and water was carried out. *The estimations of densities in this text should however be considered as less reliable as compared to what is given in Table A2-1 in Appendix 2.*

Filling the gap with pellets and water

1) Pellets

In order to get a buffer with a sufficiently high density, the gap between the bentonite blocks and the rock surface was filled with bentonite pellets. The bentonite pellets had a width and length of about 16.3 mm and a maximum thickness of about 8.3 mm. The bulk density of an individual pellet varied between 1970 and 2 110 kg/m^3 and the water ratio of the pellets was $w \approx 10$ %. The expected bulk density of the pellet filling was between 1 100 and 1 300 kg/m^3.

The pellets were placed in the gap after all the bentonite blocks had been emplaced and the gap was drained before and during the filling procedure.

The filling sequence was:

1. The pellets were delivered in big bags. Three big bags were transported to the test site. The pellets left over after filling were also weighed.
2. Four tubes with an inner diameter of 10 mm and a length of 8.0 m were placed in the gap (for subsequent filling with water).
3. The pellet blowing machine was filled with pellets and the pellets were blown into the gap through a specially designed nozzle. This was done from the upper bentonite block (C4).
4. Filling worked very well, but dust was a major problem.

The total weight of pellets in the filled gap was 2 576 kg. Assuming a gap width of 0.055 m, an average hole diameter of 1.762 m (which was measured) and a height of 7.07 m, the average estimated dry density in the gap after filling is 1 020 kg/m^3, which is lower than expected (1 130 kg/m^3), probably due to the fact that all cables are located in the gap.

2) Water

The voids between the pellets in the gap were filled with water. To assure that all the voids between the pellets would be filled, the water was fed into the outer gap from the bottom of the deposition hole. Four tubes with an inner diameter of 10 mm and a length of 8 m (placed in the gap before it was filled with pellets) were used to fill the gap with water. The tubes were gradually withdrawn as water was added in order to prevent the swelling bentonite from sealing the water transport pathways. The total volume of water needed was estimated to be about 800 litres. Site water was used for this purpose. It was taken from hole HD0025 in the D-tunnel.

Filling of the voids with water was done as follows:

1. The four tubes were connected to a pump with tecalan tubes and connectors.
2. Water was added to the gap by pumping water from a reservoir at a flow rate of about 25 litres per minute.
3. When about 115 l had been filled with water (corresponding to 1.0 m in the pellet-filled gap), pumping was stopped and the tubes were pulled up 1.0 m). The procedure was then repeated and continued until the water table was visible at the top of the pellet filling. The degree of filling was also checked by measuring the water volume.

About 950 l of water was added to the gap.

3.2.9 Estimation of the water volume used in the initial wetting of the pellet slot in CRT

In this estimation of the added water volume in the pore space between the pellets at installation following data has been used.

1. The initial conditions given by Table 3-20 which have been obtained by a careful evaluation of the initial state.

Table 3-20. Initial conditions of the CRT experiment (identical to Table A1).

Section	Density (kg/m^3)	Water ratio	Dry density (kg/m^3)	Void ratio	Degr. of saturation
Solid block	1 991	0.172	1 699	0.636	0.751
Ring shaped block	2 087	0.171	1 782	0.560	0.849
Bricks	1 883	0.165	1 616	0.720	0.637
Pellets I (dry)	1 101	0.100	1 001	**1.778**	**0.156**
Pellets II (water-filled)	1 574	0.572	1 001	**1.778**	**0.895**

2. The measured geometry of the experiment, where:

   Average hole radius $R = 0.881$ m

   Average outer slot thickness $t = 0.061$ m

   $\Rightarrow$ Average outer block radius $r = R - t = 0.82$ m

Estimated height of the stack of bentonite blocks at installation $h = 7.112$ m

Using the following definitions,

$$S_l^{(I)} = \frac{V_w^{(I)}}{V_p},\ S_l^{(II)} = \frac{V_w^{(II)}}{V_p},\ n = \frac{e}{1+e} = \frac{V_p}{V} \tag{3-1}$$

we may express the water volume added when going from state I (dry pellet slot) to state II (water filled pellet slot) as,

$$\Delta V_w = V_w^{(II)} - V_w^{(I)} = V\frac{e}{1+e}(S_l^{(II)} - S_l^{(I)}). \tag{3-2}$$

The pellet slot volume $V = h\pi\,(R^2 - r^2) = 2.32$ m^3 together with $e = 1.778$, $S_l^{(I)} = 0.156$ and $S_l^{(II)} = 0.895$ gives that $\Delta V_w = 1.097$ m^3.

The water volume added at installation was measured (by registering the change in water level in the water tank from which the water was supplied) to 0.95 m^3 which does not match the estimation above.

Thus, there is a mismatch between the estimation and the measurement if the total available additional volume between the pellets was totally water filled. Either there has not been total water filling of the pellet slot or there are some errors in the data available.

As mentioned in the notes describing EBS assignment 2.2, sensors close to the inner slot (between the canister and the bentonite block) indicate that swelling occurs and that parts of the slot has been filled with water. The suggestion is to use the values described in Table 3-20.

3.2.10 Test of the total pressure transducers

A test of the total pressure transducers used in the CRT experiment has been performed by Ulf Nilsson. This was done since the measured total pressures obtained in the CRT experiment are lower than what was expected for the dry density that the excavated samples showed.

The test setup (Figure 3-20) measured the axial total stress, by using one of the transducers that was used in the CRT experiment (installed using the same technique as in CRT), and also the radial stress, by using two load cells, in a confined sample fed with water. The installation of the pressure sensor was performed using the same technique as in CRT, where a hole was drilled in the block and thereafter bentonite powder was compacted in the bottom of the hole and last the sensor was inserted into the hole and the hole was backfilled with bentonite powder. The bentonite powder compacted at the bottom of the drilled hole was used to fill the coned bottom caused by the drilling equipment and to obtain a good contact between the block material and the sensor tip.

The sample used in the sensor test setup was taken from a ring shaped block that was manufactured for the Prototype Repository experiment but not used. The ring shaped blocks used in the Prototype Repository had an initial density of 2 075 kg/m^3 and an initial water ratio of 17.3 %. The sample was cut so that it fitted very nicely into the steel cylinder, obtaining at most a 1 mm gap between the cylinder wall and the sample surface. The experimental setup is shown in Figure 3-20.

The obtained pressure response are shown in Figure 3-21, where the blue curve corresponds to the lower load cell, the green curve corresponds to the upper load cell and the red curve corresponds to the pressure sensor. The curves level out at approximately 15 MPa, 13 MPa and 9 MPa, for the blue, green and red curve respectively. The sudden step in pressure at 2007-10-10 comes from that a 1 MPa water pressure was imposed on the system at this time.

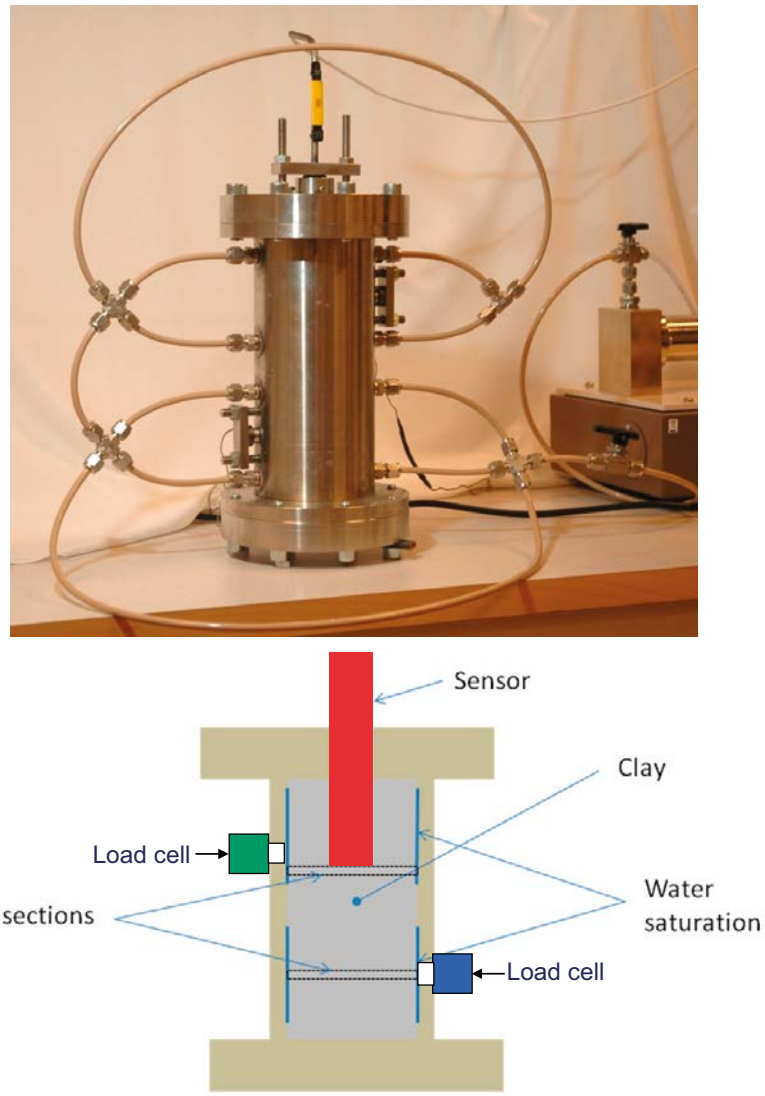

Figure 3-20. *Setup for investigation of the load cells used in the field.*

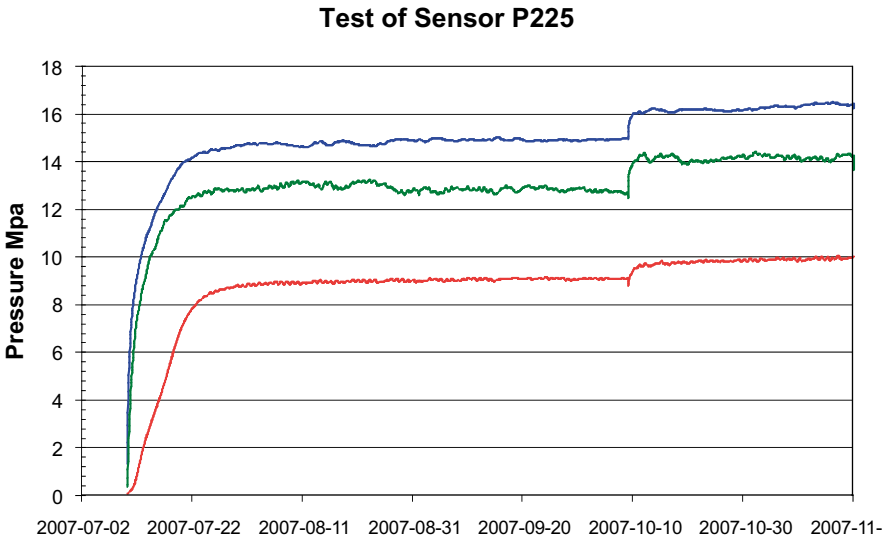

Figure 3-21. *Test results.*

After dismantling the experiment, the water ratio w and the density ρ was evaluated for samples of 1 cm length in the test sections indicated in the figure above. From these parameters the void ratio and water saturation can be calculated according to,

$$S_l = \frac{\rho_s}{\rho_w}\frac{w}{e}$$
$$e = \frac{\rho_s(w+1)}{\rho} - 1 \qquad (3\text{-}3)$$

The profile of water saturation is shown in Figure 3-22, where it can be seen that the samples are not totally water saturated when the experiment was sampled. If this was the case when the experiment was ongoing is hard to be certain about. The density might change somewhat if the bentonite block underwent elastic deformation when released from the tube. Loss of mass of water between the confined state and the state when the samples where measured might also be an error-source.

The obtained void ratios are averaged over the two test sections (excluding the outermost samples) and the result gives two void ratios that are thought to be representative for the two test sections in an overall sense.

Below, the obtained void ratios and swelling pressures are shown for the three different measured points.

Position	*e*	p_s [MPa]
Lower load cell	0.687	15
Upper load cell	0.706	13
Pressure sensor	0.706	9

The data in the table above is plotted in the graph shown in Figure 3-23, where also data from other swelling pressure experiments are shown. The data denoted Valuclay is quite old and the significance of these measurements should probably be regarded somewhat lower as compared to the other data.

It can be seen that the pressure measured by the two load cells and the evaluated void ratios correspond well with other measurements but that the pressure sensor measures lower pressures as compared with the other data for the same void ratio.

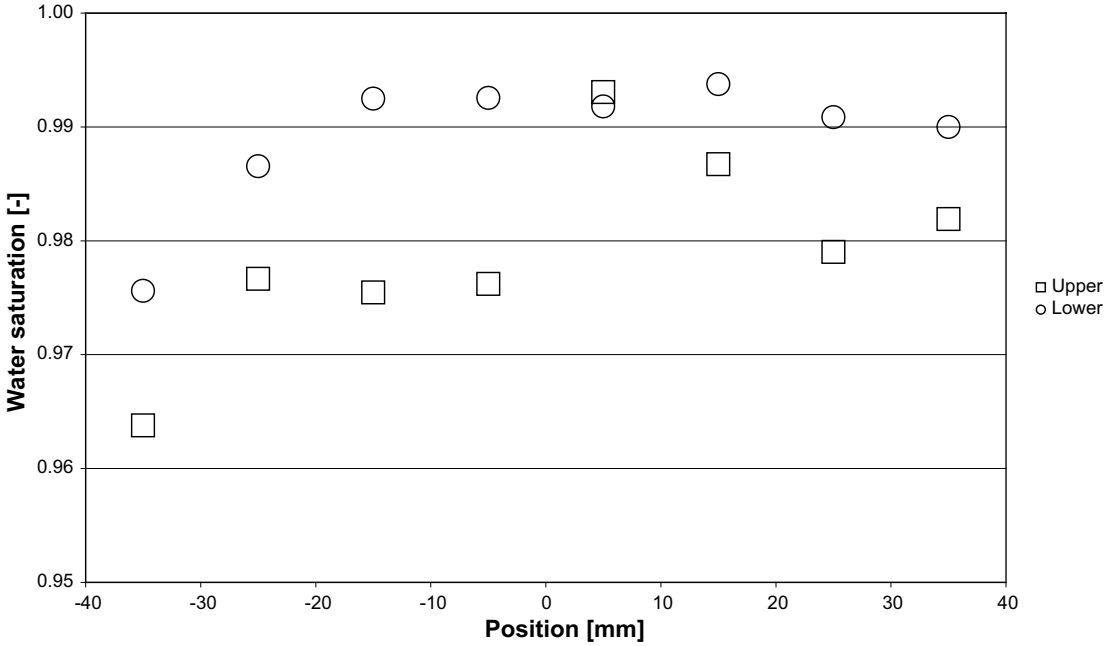

Figure 3-22. *Measured degree of saturation as a function of the distance from the transducer.*

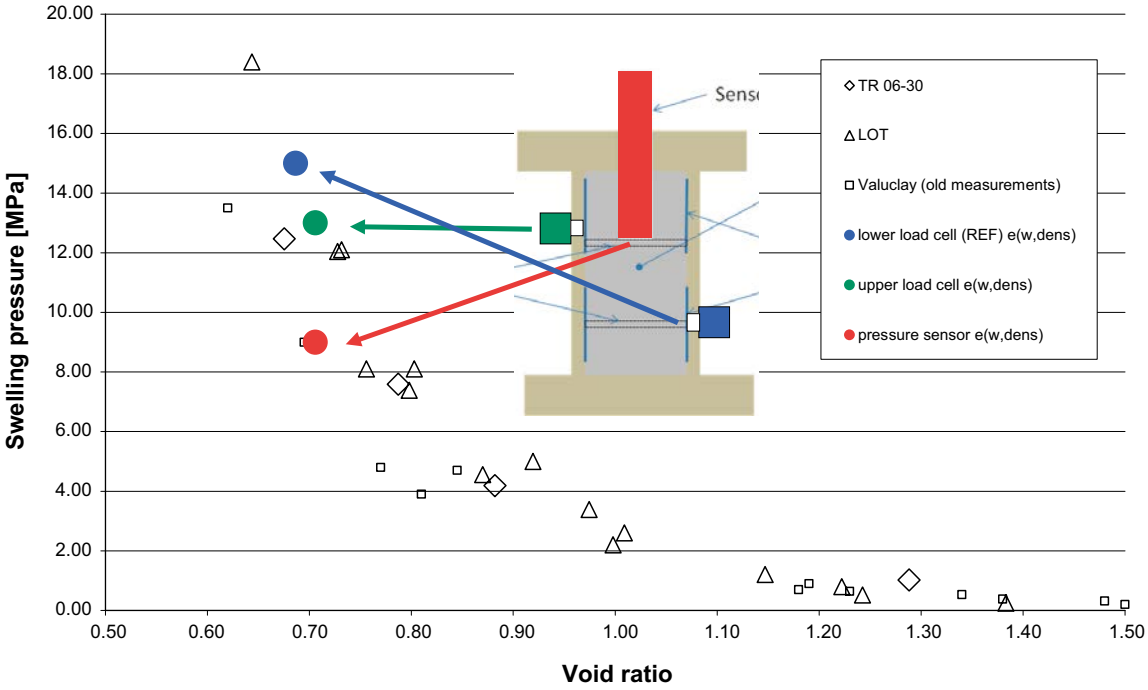

Figure 3-23. *Measured swelling pressure compared to other results.*

Some of this discrepancy is believed to stem from the locally lower average density around the pressure sensor, which occurs as a result from using the technique using bentonite powder backfill when installing the pressure sensor.

One other possible reason for the obtained low total pressures in the CRT experiment, which is not investigated using the present test setup, is that the sensor might not be installed "firmly enough" in the hole. When the sensor tip experiences a larger pressure as compared to the opposite end of the sensor the sensor might flex upwards in the installation-hole if the friction is overcome or the material close to the sensor is weak. In the present experiment such upward flex of the sensor is prevented by the small beam that can be seen in the picture showing the setup.

Generally it can be noted that the swelling pressure is very sensitive to changes in void ratio at the low void ratios that are considered here and small errors in the determination of the void ratio makes a large impact on the result.

The measurements in the test cell thus indicate that the pressure cells measure too low swelling pressure. It is suggested that the results from CRT are increased by 9/15 = 60 %.

3.2.11 New times where profiles of variables are to be shown for the 1D THM-model

Since the water saturation was more rapid at the canister mid-height then thought of when designing the 1D THM assignment, the old times given for which profiles of variables were asked to be shown are not very interesting.

The times 50, 100, 200, 1 000, and 2 052 are therefore suggested instead for which the profiles of: water saturation and dry density are to be shown in the 1D THM assignment. Profiles of temperature are not requested.

3.2.12 Small scale experiment

A small scale experiment suitable for validating the bentonite block material models has been performed. The setup is shown in Figure 3-24.

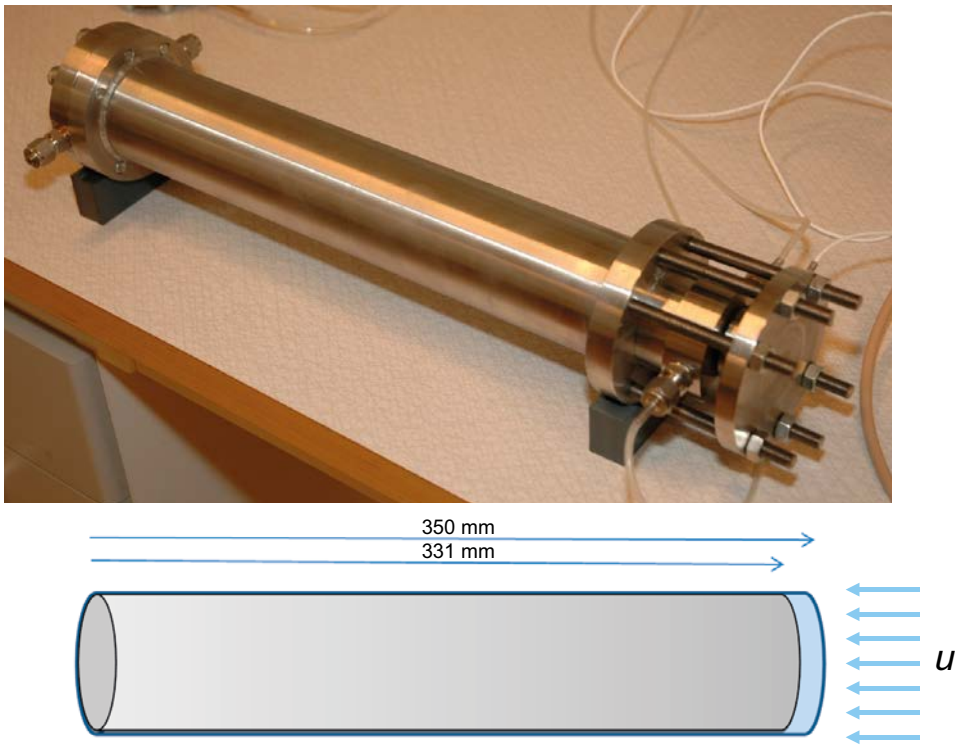

Figure 3-24. *Setup of experiment.*

The experimental setup consisted of a tube with inner diameter 50 mm and length 350 mm. Inside the tube were cylinders of compacted bentonite placed. The total length of the stack of bentonite cylinders was 331 mm. There was a 19 mm gap between the "last" bentonite cylinder and the end of the tube. The initial state of the bentonite had a water ratio of $w = 0.091$ and a void ratio of $e = 0.683$.

The experiment was started by water-filling the gap and thereafter providing access of water with the water pressure $u = 0$ MPa to this end of the test setup. The experiment was running for 33.99 days (815.67 hours) after which the experiment was dismantled and analyzed in terms of water ratio, water saturation, density and dry density. The resulting graphs, showing the variables as a function of the distance from the wet side, are shown in Figure 3-25.

3.2.13 Relative humidity and suction of Äspö-water

Water sample

Water from borehole HD0025A was taken 2007-10-09 for the purpose of saturating laboratory samples from the CRT project.

RH measurement

The relative humidity was measured above a surface of Äspö-solution. Psychrometers (Wescor) were installed in calibrators and measurements were made above Äspö solution and controlled above a saturated solution of K_2SO_4 ($RH = 97.6$ % at 20 °C). The results are shown in Figure 3-26. The suction was measured both by the psychrometer method (PS) and by the dew point method (DP). Two sensors were used represented by red and blue lines.

After approximately 150h RH = 99.5 % and RH = 99.6 % were measured in this limited investigation. The average of the measurements was $RH = 99.55$ %.

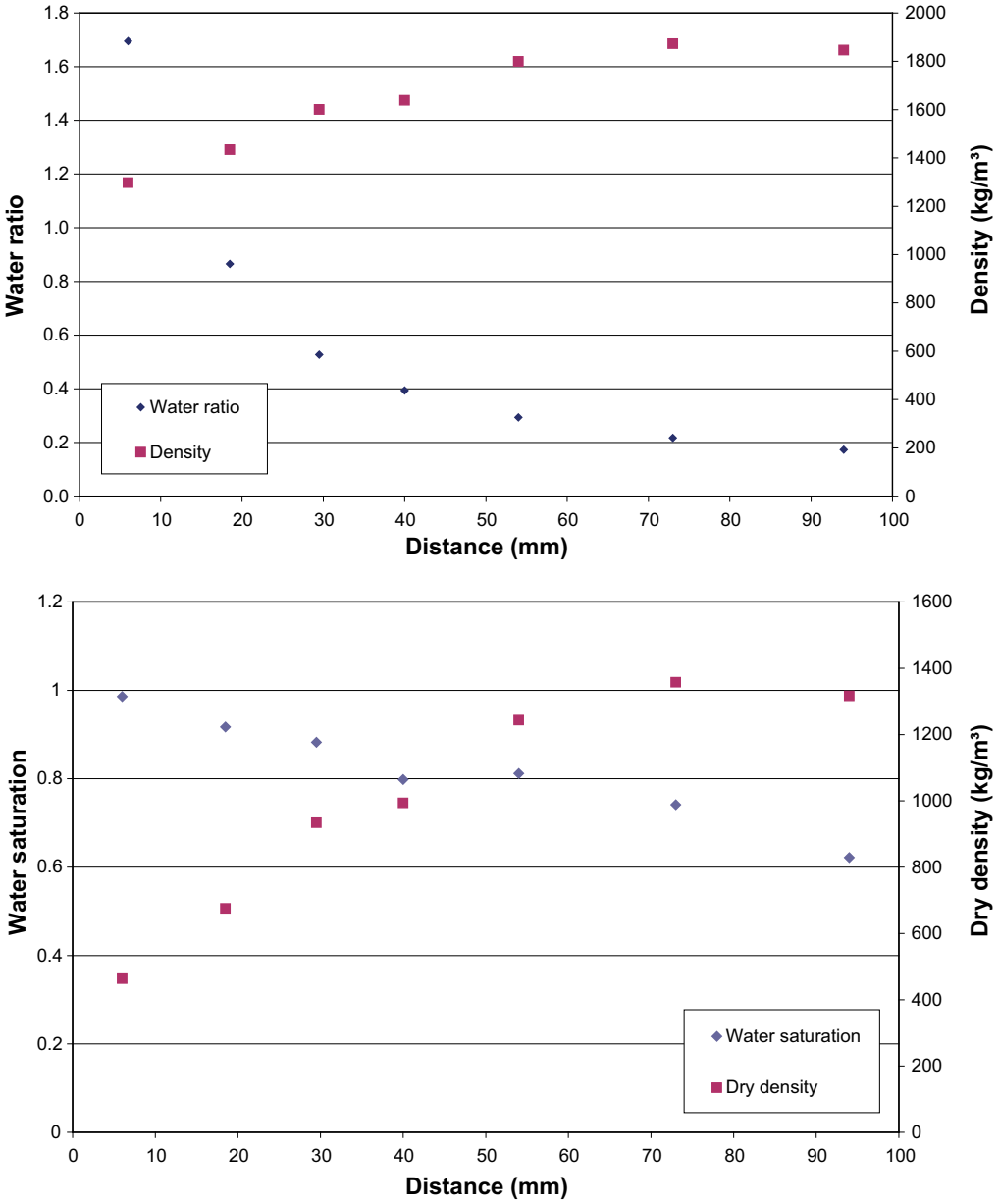

Figure 3-25. *Test results.*

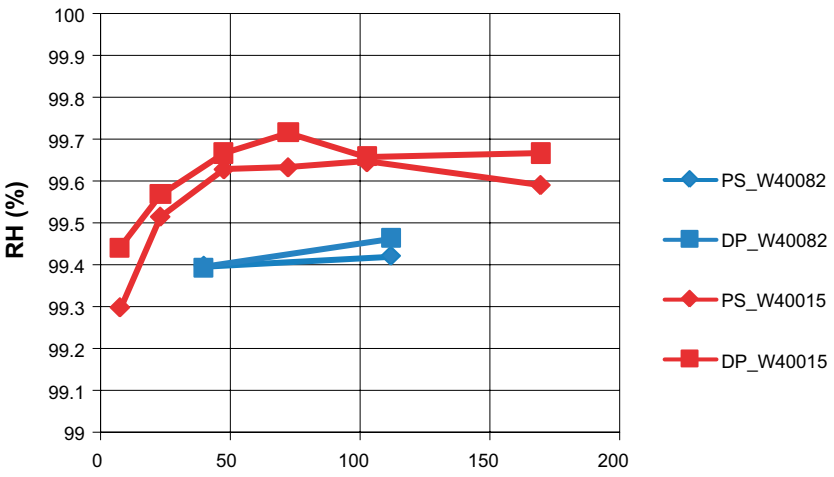

Figure 3-26. *Measurement of RH by two psychrometers.*

Calculations of activity from measured salt content

Data from the database SICADA gave the following contents (mg/l) of Na, Ca, Cl, K, Mg, HCO_3 and SO_4 (2003-04-02), Table 3-21. The contents of SO_4_S, BR, F, Si, Fe, Fe_{tot}, FeII, Mn, Li and Sr were not considered since the total weight was small.

From the concentrations (mmolar) of the elements in Table 3-21 a water activity of 99.5 % was calculated with the program PHREEQC by M. Birgersson. The corresponding salt content as weight-%, calculated from the data in Table 3-21, was 0.9 %. The measured data varies and the given data in Table 3-21 represents large contents of the elements (one extreme). Data representing lower contents (the other extreme) of the elements was also analysed and the resulting activity from this data was 99.7 % and the salt content 0.5 %. The actual variation is thus between these two values.

Table 3-21. Chemical data of Äspö water (SICADA) and calculated water activity.

Ion/element	mg/l[1]	molecular weight[1]	mmolar	Calculated activity[2]
Na	1 810	23	78.7	
Ca	1 310	40.1	32.7	
Cl	5 560.8	35.5	156.6	
K	15.90	39.10	0.4	99.50 %
Mg	71.5	24.3	2.9	
HCO_3	101.00	61.00	1.7	
SO_4	365.00	96.10	3.8	
Total	**9 234.20**			

[1] assumed to be mg per litre of the solution
[2] calculated with PHREEQC

The relative humidity measured above a surface of the solution should be the same as the activity in the solution, i.e. $RH = 100 \cdot p/p_s = 99.5\%$ or 99.7 %.

Conclusion

The relative humidity above Äspö water is between 99.5 % and 99.7 %. The corresponding suction calculated from Kelvins equation, Equation 3-4, is ψ = 404–678 kPa at 20 °C.

$$\psi = -\frac{R \cdot T}{\nu_{w0} \cdot \omega_v} \ln\left(\frac{p}{p_s}\right) \qquad (3\text{-}4)$$

where

ψ = suction (kPa).

T = absolute temperature (K).

R = universal gas constant (8.31432 J/(mol K)).

ν_{w0} = specific volume of water ($1/\rho_w$ m^3/kg).

ρ_w = density of water (kg/m^3).

ω_v = molecular mass of water vapour (18 kg/kmol).

p = partial pressure of pore-water vapour (kPa).

p_s = saturation pressure of water vapour over a flat surface of pure water of the same temperature (kPa).

3.3 Modelling results with Code Bright

3.3.1 Introduction

To the left in Figure 3-27 a schematic overview of the CRT experiment is shown.

According to Section 3.2 the CRT assignment consists of three sub-tasks:

- sub-task 1 Thermal-modeling of CRT and TBT.
- sub-task 2 THM modeling of a disc at canister mid height (see Figure 3-27).
- sub-task 3 THM modeling of the entire experiment.

In Section 3.4 only the modeling of sub-tasks 1 and 2 will be reported.

First, in Section 3.4.2, the thermal modeling of CRT and TBT (sub-task 1) is discussed. The work related to sub-task 2 is then presented in the three following Sections, 3.4.3, 3.4.4, and 3.4.5, respectively.

In 3.4.3 ("Sub-task 2: THM-modeling of a buffer disc at canister mid-height") the model setup and solution of the model considered most representative at the time of the writing of this report are presented. Section 3.4.3 contains the direct answers to what was asked for in the assignment description.

The following two Sections, 3.4.4 and 3.4.5, contain further analyses than asked for in the assignment description. Section 3.4.4 ("Sub-task 2: Investigating the homogenization process") contain an analysis of the homogenization process taking place in a KBS-3V buffer using both an analytical model and FE-models closely related to the one described in Section 3.4.3. In Section 3.4.5. ("Sub-task 2: Some investigations made during the model development") investigations performed during the development of the disc-model are briefly described. The investigations are: Comparison of suction responses for TH and THM, Effect from lowered retention curve (TH), Effect from porosity dependent retention (THM), Effect from increased intrinsic permeability (TH), and Effect from using different porosity dependency of the permeability (THM). The processes considered in the studies are indicated within the brackets.

After this follows appendices with subjects related to the modeling. The subjects are: Short review of BBM (including a derivation of a strain/suction/temperature driven format for BBM), Modifications made to BBM, and Notes on porosity update schemes using initial or updated coordinates.

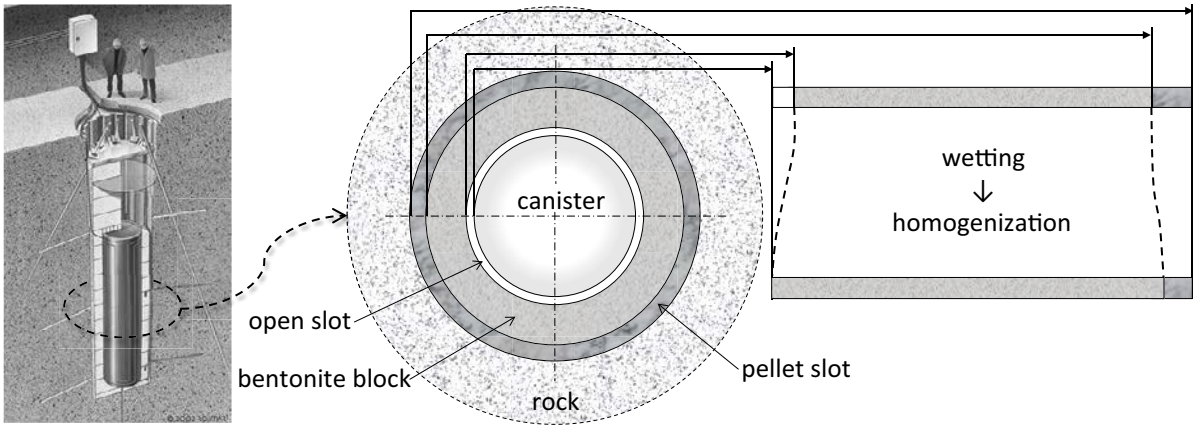

Figure 3-27. *Schematic description of sub-task 2 in the CRT assignment in which the homogenization due to wetting is an important process.*

3.3.2 Sub-task 1: 3D thermal model of CRT and TBT

Here follows a short presentation of the model used when simulating the thermal activity in the close surroundings of the CRT and TBT experiments. The obtained results are also given. These are used to formulate suitable boundary conditions of the following sub-task.

Geometry

Figure 3-28 shows the used geometry of the CRT and TBT experiments containing:

A. Surrounding rock.

B. Steel lid.

C. Concrete plug.

D. Engineered buffer (averaged properties of all constituents).

E. Canister/heaters.

As can be seen, a vertical symmetry plane aligned with the tunnel axis has been assumed.

Heat load, boundary conditions and initial condition

The canister powers of CRT and TBT, see (Figure 3-29), were applied to the model.

Convection conditions have been prescribed in the tunnel where a heat transfer coefficient of $\gamma = 10$ W/(°C·m^2) and a tunnel air temperature of 15 °C has been used. On the outer boundary surface, adiabatic conditions are used.

An initial temperature of 17 °C was imposed on the model.

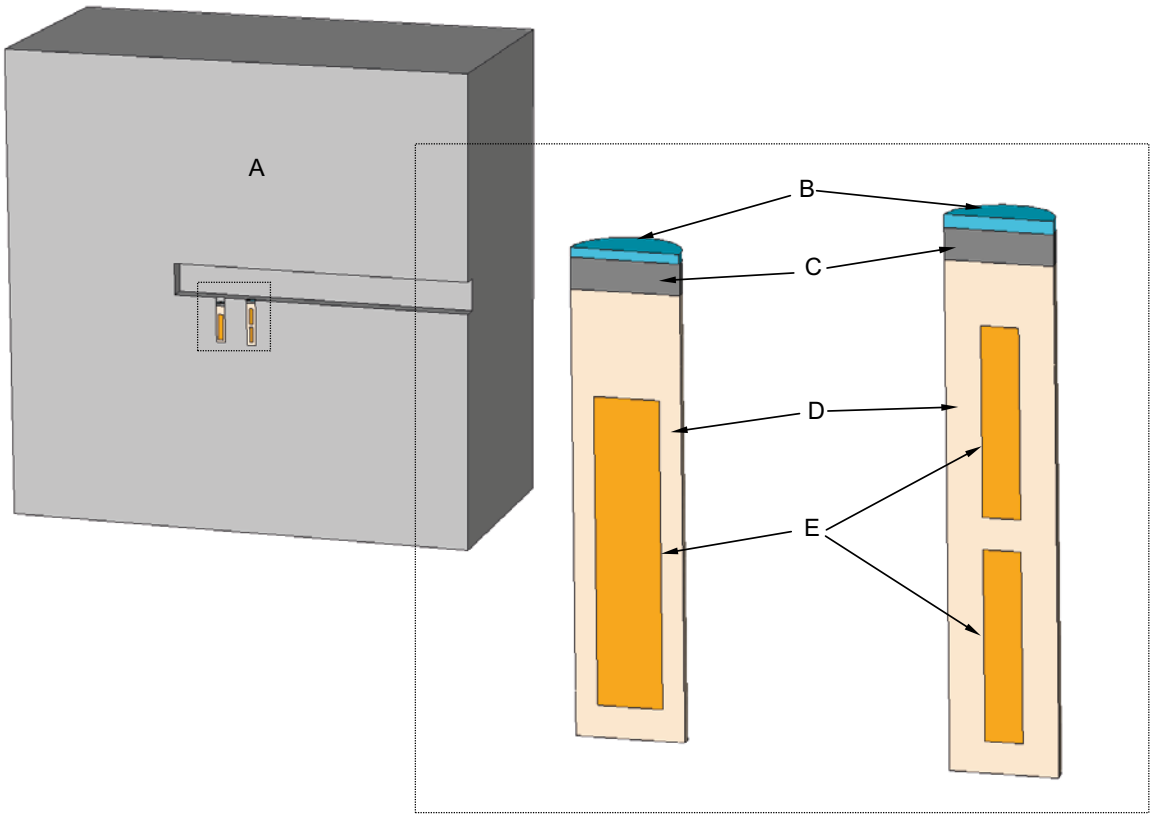

Figure 3-28. *The geometry used in the thermal simulation of the CRT and TBT environment.*

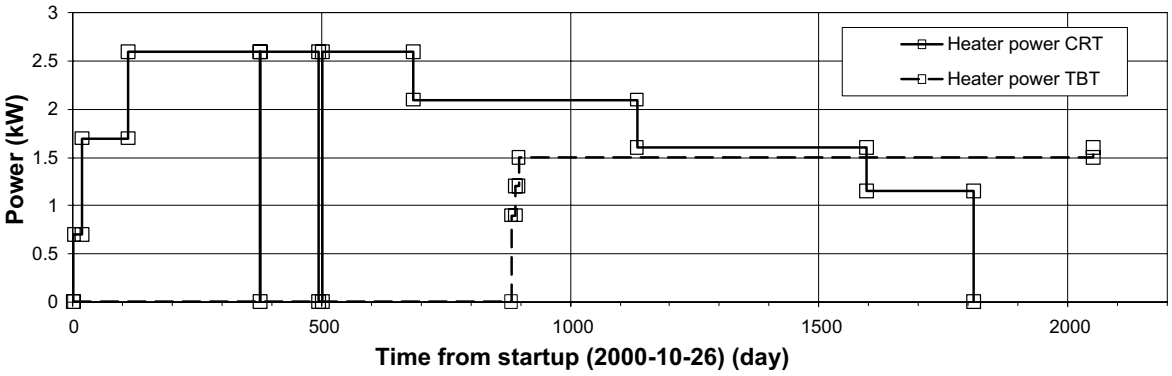

Figure 3-29. *Canister power in CRT and TBT.*

Material properties

Fourier's law was adopted for representing the conductive heat flow. In Table 3-1 the used material properties are shown, where ρ_s denotes the solid density, c_s the specific heat of the solid phase, λ the thermal conductivity and n the porosity.

Table 3-1 Material properties used in the model.

Material	ρ_s [kg/m^3]	c_s [J/(kg·K)]	λ W/(m·K)]	n [–]
Rock	2 770	770	2.6	0
Steele lid	7 840	460	47	0
Concrete plug	2 400	770	2.7	0
Buffer	2 780	800 (of solid)	1.2 (1.0)	0.4
Canisters	8 000	450	100	0

Spatial average estimates of the parameters have been used for representing the buffer and the canisters. For the buffer, the used value of conductivity is also an average in time in the sense that the conductivity is dependent on water saturation. In order to get an estimate of this effect an alternative value of conductivity has also been used for the buffer. The initial empty inner slot has, however, not been considered when estimating this alternative conductivity.

Results

Figure 3-30 shows the position and name of the sensors measuring the temperature in the rock and canister which the model results are verified against.

The comparison between the rock temperature measured by the chosen sensors and the temperature obtained by the simulation is given in Figure 3-31. In Figure 3-32 the experimental and simulated temperatures of the canister temperature are shown.

The buffer conductivity does not affect the temperature evolution in the rock significantly. Therefore the results in Figure 3-31 are obtained using the base case value of buffer thermal conductivity only. The simulated temperatures agree well with the measured.

When the canister surface temperatures were simulated, both base case and alternative buffer conductivity were used in order to evaluate the effect of the water saturation process in the buffer on the canister temperatures. The "true" simulated temperature evolution is considered to go from the temperature curve obtained from using the lower value of conductivity (= dry conditions) towards the curve obtained using the higher value of thermal conductivity (= wet conditions). Figure 3-32 shows that the simulated temperatures fit reasonable to the measured temperature evolution when "in thought" considering the water saturation process. Initially, the temperature is underestimated. This could be an effect from not considering the initially open inner slot in the model.

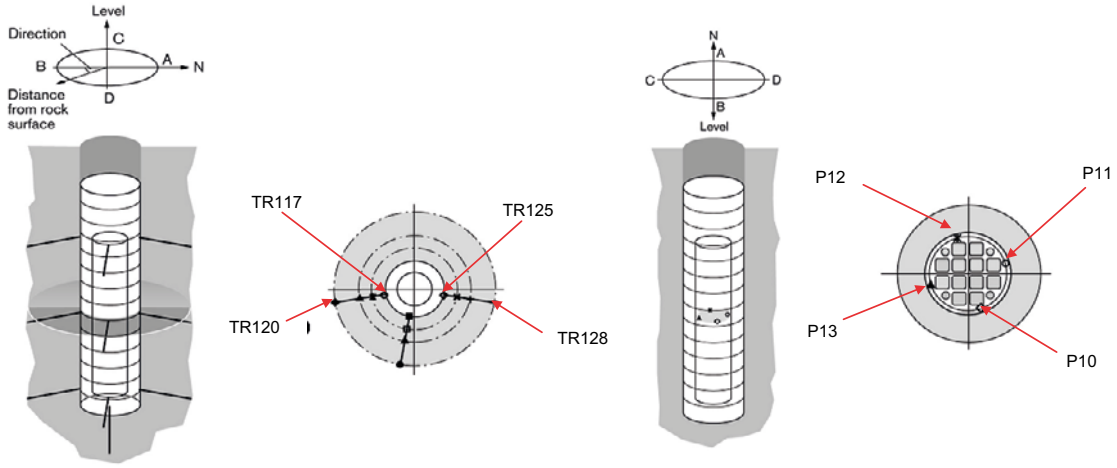

Figure 3-30. *Rock and canister temperature sensor positions and names.*

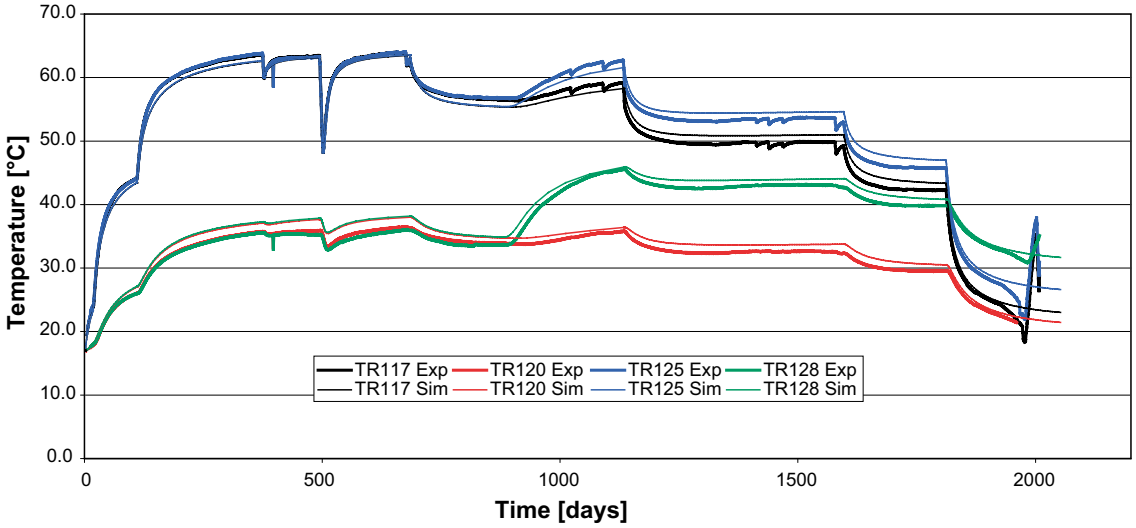

Figure 3-31. *Experimental and simulated rock temperatures at canister mid-height.*

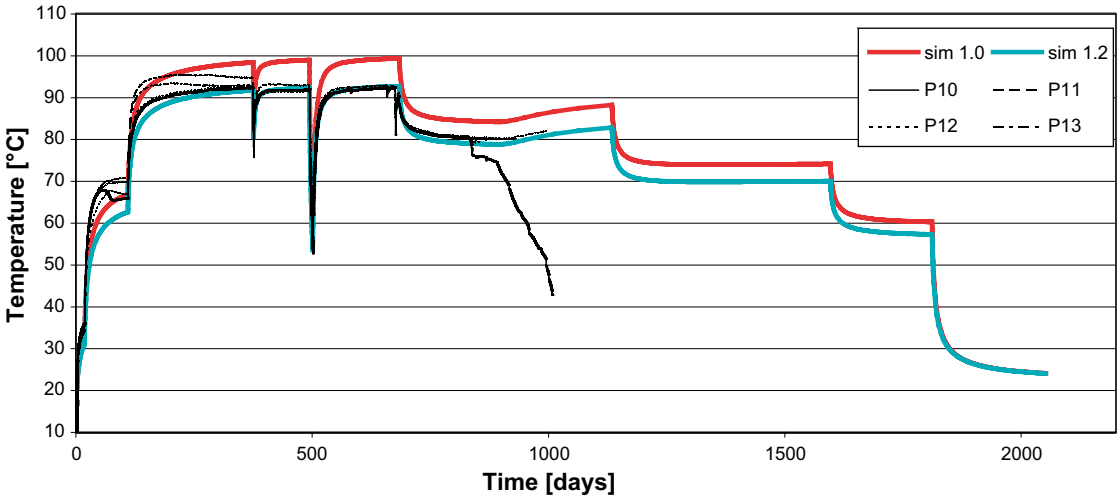

Figure 3-32. *Experimental and simulated canister surface temperatures at canister mid-height.*

The obtained horizontal component of the canister surface heat flux as a function of height at day 375 and day 1 063 is shown in Figure 3-33. The heat flux profile is shown for a vertical cut through the canister in the tunnel direction, i.e. the heat flux along the indicated canister boundary in Figure 3-33. The rugged appearance of the curves comes from the approximate representation of the field in the model. The difference in heat flux at the two different times is clear. The overall difference in magnitude comes from changes in canister power. The unsymmetrical appearance of the heat flux curves at the opposite sides of the canister at day 1 063 comes from that the TBT canisters are activated at this time and, as a consequence, the heat flux field around CRT therefore gains some in the opposite direction.

In the forthcoming an axially symmetric representation of the CRT experiment is used to simplify the models somewhat. In order to obtain a heat flux history at the canister mid-height which can be used in the axisymmetric representation, an average of the absolute value of horizontal heat flux at canister mid-height ± 0.5 m is calculated for flux histories. The result is shown in Figure 3-34.

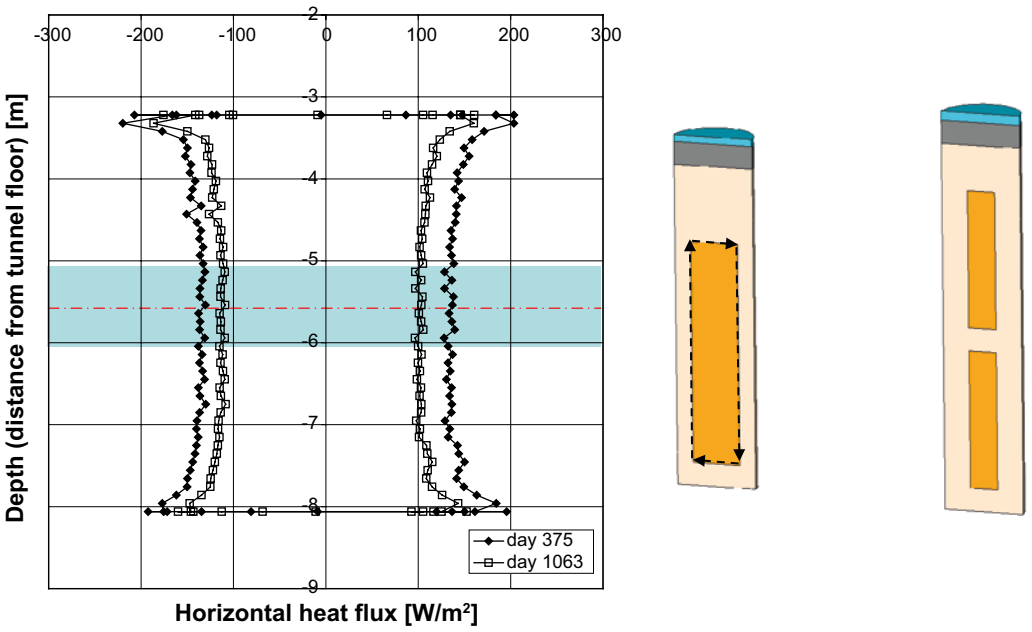

Figure 3-33. *The horizontal component of the canister surface heat flux profile at day 375 and 1 063 along the scan-line indicated with the dashed line. The mid-height is shown together with the interval where the heat flux is averaged.*

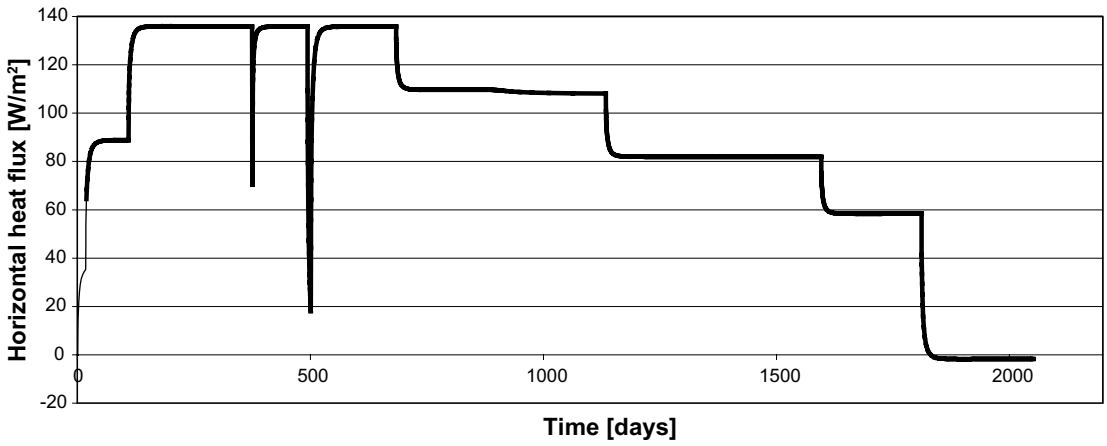

Figure 3-34. *Horizontal heat flux average formed at canister mid-height ± 0.5 m.*

Note that if the heat flux is to be used as a boundary condition together with adiabatic conditions at the horizontal boundaries, the radial dimension of the model has to be small as compared to the canister height. A suitable model could start at the canister surface and end at the hole wall.

3.3.3 Sub-task 2: THM-modeling of a buffer disc at canister mid-height

The model considered most representative for the CRT experiment, of those developed by SKB team 1, and its solution are here presented. The developing process began within EBS Task-Force and then continued when working with the Safety Report concerning THM modeling of buffer, backfill and other system components within the Swedish nuclear waste repository design KBS-3 (Åkesson et al. 2010a). The most current development was undertaken when working with a contribution to "*Clays in Natural & Engineered Barriers for Radioactive Waste Confinement*" held in Nantes 29th March to 1st April 2010, see Kristensson and Åkesson (2011).

First the model is described; General problem formulation, Geometry, Material properties, Initial conditions and Boundary conditions. Then the results as specified by the assignment description are given.

General problem formulation

In the poro-mechanical formulation CODE_BRIGHT is based on, an additive split of a material volume element, dv, in a solid volume element, dv_s, and a pore volume element, dv_p is used. Furthermore the pore volume element, dv_p, is additively split into a liquid volume element, dv^l, and a gas volume element, dv^g. The liquid volume element is divided into a liquid water volume element dv_w^l and a liquid air volume element dv_a^l (dissolved air into the liquid).

Using the defined volume elements above, or the corresponding mass elements, the following variables are defined: $w = dm_w^l/dm_s$, $S_l = dv_w^l/dv_p$, $e = dv_p/dv_s$, $n = dv_p/dv$.

In the THM model, balance laws of; solid mass (which gives the evolution of porosity n), water mass, energy for the system and momentum (here force balance since quasi static conditions are assumed) are considered. The gas pressure is held constant, $p_g = 0.1$ MPa, in the model. The psycrometric law,

$$\omega_g^w = (\omega_g^w)_0 \frac{RH}{100}$$

$$(\omega_g^w)_0 = f(T)$$

$$\frac{RH}{100} = \exp\left(\frac{-(p_g - p_l)\, M_w}{R(273.15+T)\rho_l}\right),$$

is used as an equilibrium constraint between the liquid phase and vapor phase of water.

Dependent variables; advective liquid flux $\boldsymbol{q}_l$, vapor flux $\boldsymbol{i}_g^w$, conductive heat flux $\boldsymbol{i}_c$ and liquid degree of saturation S_l are expressed in terms of material specific constitutive laws, functions of the adopted independent variables; porosity n, liquid pressure p_l, temperature T and displacements $\boldsymbol{u}$. Left to be specified, in order to obtain a full problem formulation, are the initial and boundary conditions.

Geometry

The model is axisymmetric and incorporates three constituents:

1. Empty inner slot (0.525 < r < 0.535)
2. Bentonite block (0.535 < r < 0.820)
3. Pellet filled outer slot (0.820 < r < 0.881)

as shown in Figure 3-35 below. This geometry differs in the outer radius compared with the suggested geometry given in the assignment description. The new geometry is motivated from calculating the volume average of the measured void ratios close to the canister mid-height, in block R6 and R7, and assuming no axial swelling.

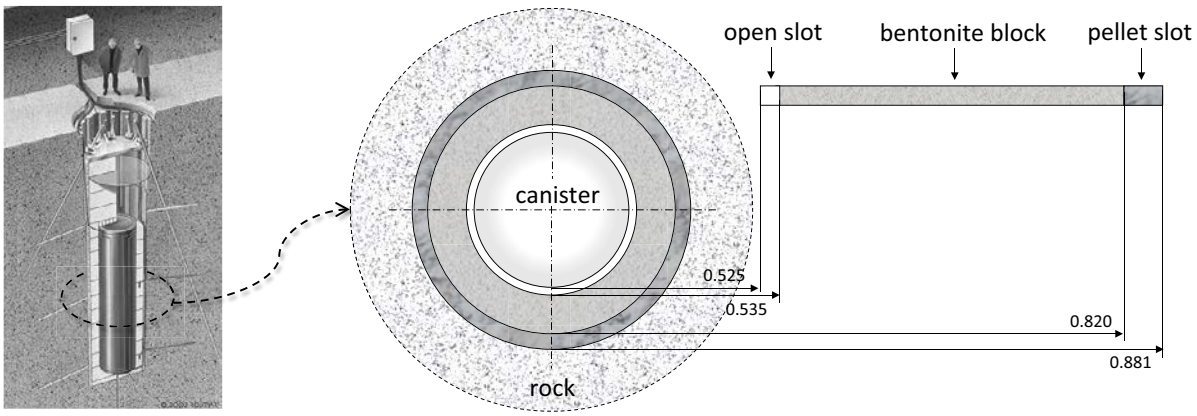

Figure 3-35. *Schematic CODE_BRIGHT model geometry and constituents.*

Focus is concentrated at modelling the homogenization in a disc at canister mid-height of the CRT experiment. A 2D axial symmetric model with the constituents and geometry shown in Figure 3-35 has been developed for this purpose. On the 2D model an axial plane deformation condition is prescribed, so that the model becomes 1D radial symmetric. The constituents are discretized using linear quadrilateral elements with four integration points and selective integration. The inner slot is represented by 1 element, the block by 30 elements and the pellet slot by 6 elements.

Material properties

In Table 3-2 to Table 3-6 the constitutive laws and parameter values used for representing the different materials are shown. The choices of material representation are made according to what is reported in Åkesson et al. (2010b). The thermal and hydraulic constitutive laws used, shown in Table 3-3, are on the standard format. When it comes to the mechanical constitutive laws, an elastoplastic model available in CODE_BRIGHT, shown in Table 3-4, has been used for representing the block and pellet slot materials. The open slot is modelled as a nonlinear elastic material as shown in Table 3-5.

The elastoplastic model, a derivative of Barcelona Basic Model (BBM), described in Appendix 3, has been equipped with two new features, also described in the mentioned section. This material model will be referred to as BBM in the forthcoming despite the differences to the "original" formulation of BBM. The first new feature concerns the "hydraulic" strain increment, where a modulus has been made dependent on void ratio through use of a swelling pressure curve. The second of the new features concerns the plastic strain increment, where the friction angle has been made variable through a dependence on the hardening parameter.

One of the mechanical parameters (κ_{i0}) of the pellet slot material, see Table 3-4, was calibrated so that the simulated void ratio profile became continuous over the block/pellet slot interface at full water saturation.

Table 3-2 Parameters.

	Parameter	Block	Pellets	Slot
Solid density	ρ_s [kg/m^3]	2 780	2 780	2 780
Heat capacitivity	c [J/(kg K)]	800	800	800

Table 3-3 Thermal and hydraulic laws and parameters.

		Parameter	Block	Pellets	Slot
Liquid advective flux	$\boldsymbol{q}_l = -\frac{kk_{rl}}{\mu_l}\boldsymbol{I}\nabla p_l$	k_0 [m^2]	$2.18\cdot10^{-21}$	$1.04\cdot10^{-18}$	$1\cdot10^{-10}$/$1\cdot10^{-30}$ (I)
		B	– Eq.1)(II)	21.3 Eq.2)	– Eq.1)
	Eq. 1) $k = k_0 \frac{n^3}{(1-n)^2}\frac{(1-n_0)^2}{n_0^3}$	λ	3	3	0
	Eq. 2) $k = k_0 \exp\left(B(n-n_0)\right)$				
	$k_{rl} = S_r^{\lambda}$				
Vapour non-advective flux	$\boldsymbol{i}_g^w = -(n\rho_g(1-S_r)D_m^w)\nabla\omega_g^w$	τ	1	1	1/0.001 (I)
	$D_m^w = \tau\cdot 5.9\cdot 10^{-6}\frac{(273.15+T)^{2.3}}{p_g}$				
Conductive heat flux	$\boldsymbol{i}_c = -\lambda\nabla T$	λ_{dry} [W/(m·K)]	0.7	0(IV)	0.04/1.0 (III)
	$\lambda = \lambda_{sat}S_l + \lambda_{dry}(1-S_l)$	λ_{sat} [W/(m·K)]	1.3	1.3	0.6/1.0 (III)
Retention curve	$S_l = \left(1+\left(\frac{p_g - p_l}{p_0}\right)^{\frac{1}{1-\lambda}}\right)^{-\lambda}$	p_0 [MPa]	37.273	0.558	0.558
		λ	0.2	0.26	0.26
Liquid density	$\rho_l = 1002.6\exp\left[4.5\cdot10^{-4}\left(P_l - P_{l0}\right) - 3.4\cdot10^{-4}T\right]$				
Gas density	ρ_g : *ideal gas law*				
Liquid viscosity	$\mu_l = 2\cdot10^{-12}\exp\left(\frac{1808.5}{273.15+T}\right)$				

(I) When the slot closed (became small enough) water transportation was prevented in the slot material.
(II) Convergence problems occurred when adopting 2) for the block material, therefore 1) was used instead.
(III) The higher value was used when the slot closed.
(IV) Using this unrepresentative value of λ_{dry} still gives a representative function of λ for $S_l > 0.2$ which prevails through the simulation.

Table 3-4 BBM and the parameters.

		Parameter	Block	Pellets
Elastic strain increment:	$d\varepsilon^e = -\frac{1}{3} d\varepsilon_v^e \mathbf{1} + d\mathbf{e}^e$ $d\varepsilon_v^e = \frac{dp'}{K},\ K = \max\left\{\frac{(1+e)p'}{\kappa_i(s)}, K_{\min}\right\}$ $\kappa_i = \kappa_{i0}[1+\alpha_i s]$ $d\mathbf{e}^e = \frac{d\mathbf{s}}{2G},\ G = \frac{3(1-2\nu)}{2(1+\nu)}K$	κ_{i0}	0.13	0.15
		α_i	–0.021	0
		v	0.2	0.2
		K_{min} [MPa]	20	2
Plastic strain increment:	$d\varepsilon^p = d\Lambda \frac{\partial g}{\partial \boldsymbol{\sigma}}$ $f = q^2 - M^2(p'+p_s)(p_0 - p')$ $g = \alpha q^2 - M^2(p'+p_s)(p_0 - p')$ (I) $M = 0.5\left(\frac{p_0 + p_s}{2}\right)^{-0.23}$ $p_0 = p^c\left(\frac{p_0^*}{p^c}\right)^{\frac{\lambda_0 - \kappa_{i0}}{\lambda(s) - \kappa_{i0}}}$ $dp_0^* = \frac{1+e}{\lambda_0 - \kappa_{i0}} p_0^* d\varepsilon_v^p$	α	0.5	0.5
		p_0^* [MPa]	16.9	0.242
		p_c [MPa]	1	1
		λ	0.184	0.243
		p_s [MPa]	2.5	0.05
Hydraulic strain increment:	$d\varepsilon^h = -\frac{1}{3} d\varepsilon_v^h \mathbf{1}$ $d\varepsilon_v^h = \frac{\kappa_s}{(1+e)(s+p_{atm})} ds$ $\kappa_s = \kappa_{s0} h(p', e)$ (I) $h(p',e) = \begin{cases} 1 & \text{if } p' < p_{ref} \\ 10^{-20} & \text{if } p' > p_{swell}(e) \\ 1 - \frac{\ln p' - \ln p_{ref}}{\ln(p_{swell}(e)) - \ln p_{ref}} & \text{otherwise} \end{cases}$ $p_{swell} = 10^{\left[-4.741 + 4.117\cdot 10^{-3}\frac{\rho_s}{1+e} - 3.94\cdot 10^{-7}\left(\frac{\rho_s}{1+e}\right)^2\right]}$	κ_{s0}	0.3	0.2
		p_{ref} [MPa]	1	0.1

(I) The functions $M(p_0)$ and $h(p',e)$ are features that are in-house developments of the code.

Table 3-5 Nonlinear elastic model and the parameters.

		Parameter	Slot
Elastic strain increment:	$d\varepsilon = -\frac{1}{3} d\varepsilon_v \mathbf{1} + d\mathbf{e}$ $d\varepsilon_v = \frac{1}{K} dp'\ K = \frac{p'}{-a_1}$ $d\mathbf{e} = \frac{d\mathbf{s}}{2G}, G = \frac{3(1-2\nu)}{2(1+\nu)}K$	$-a_1$	1
		v	0.2

Initial conditions

The initial conditions, shown in Table 3-6, are given in terms of the temperature, T, the water ratio, w, (or the corresponding water saturation, S_l), the void ratio, e, (or the corresponding porosity, n), and the total stress tensor, $\boldsymbol{\sigma}$.

The initial water ratio of the pellet slot was 0.1 in the experiment. Directly after installing the pellet filling in the outer slot the slot was water filled using hoses installed before the pellet filling. In the simulations, the initial water ratio is taken as 0.136, which give the same level of suction as the block material has initially. This makes the problem more suitable numerically and does not deviate significantly from the conditions in the experiment.

Sensors that measured the hydraulic conditions in the block close to the canister showed that water had penetrated trough the buffer when the outer slot was water filled initially. Therefore, the slot material is initially taken as fully water saturated.

Boundary conditions

The used boundary conditions are indicated in Figure 3-36. The thermal boundary conditions, $q = q(t)$ and $T = T(t)$ are obtained from analysing the thermal evolution of a 3D model of the tunnel where CRT and the Temperature Buffer Test experiment are located, see Section 3.3.2.

To mimic the water filling of the pellet slot at installation, the water pressure $p_l = p_l(t)$ is initially, ($t < t^*$ in Figure 3-36), prescribed in the entire pellet slot. After full water saturation, ($t > t^*$ in Figure 3-36), of the pellet slot the water pressure, as given by the filter protocol (in CRT the buffer was artificially fed with water through filter mats installed at the borehole wall) is prescribed at the outer boundary of the model.

To incorporate the closing of the inner slot in the model, the initial radial stress at the inner surface of the block is unaltered until the slot is closed. When the slot is closed, no displacement increment is permitted on the inner block boundary.

Thermal boundary conditions

The heat flux evolution, prescribed at the canister boundary, is taken from a thermal 3D FE model where both CRT and TBT are considered, see Figure 3-36. The heat flux boundary condition in the small THM model is obtained from evaluating the horizontal heat flux response of the 3D model at the canister surface at canister mid-height. As can be seen, the abrupt spikes in the heat flux (the heater elements were shut off) have not been incorporated in the boundary condition. This was done in order to simplify the numerical solution of the problem.

The temperature boundary condition at the rock wall boundary is obtained from fitting a function to relevant temperature sensor data, see Figure 3-38. Also here the spikes in the temperature have not been incorporated in the boundary condition.

Table 3-6 Initial conditions.

Material	T [°C]	w/S_l	e/n	p [MPa]
Block	15	0.171/0.849	0.56/0.359	–0.11
Pellets		0.136/0.212	1.78/0.64	
Slot		359/1	999/0.999	

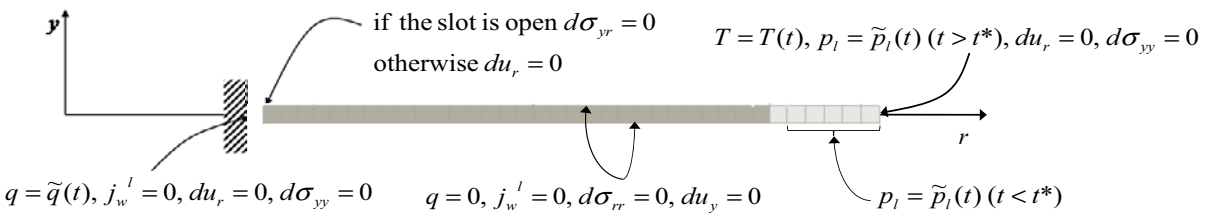

Figure 3-36. *Schematic picture of the boundary conditions used in the model.*

Hydraulic boundary conditions

The water pressure condition at the pellet slot side is first prescribed as a surface condition over the outer part of the pellet slot (0.835 < r <0.881) to mimic the fast water filling of the pellet slot when hoses were used. The water pressure is in this first step increased from –45.9 MPa to 0.1 MPa. After the initial water filling a water pressure boundary condition is prescribed at the rock wall side of the model. The prescribed water pressure follows the filter pressure protocol shown in Figure 3-39.

Mechanical boundary conditions

Since no contact elements are available in the current version of CODE_BRIGHT, the inner slot closure has been modeled by using a manual technique. The inner slot is modeled using a soft material. A first simulation is run where the displacement of the inner slot/block interface is studied for zero tangential traction (here equal to $d\sigma_{yr}$) prescribed at the nodes at the slot/block interface. The time where the inner slot is sufficiently small is identified. In the next simulation (the actual simulation) the node displacements are locked at the interface at the identified time.

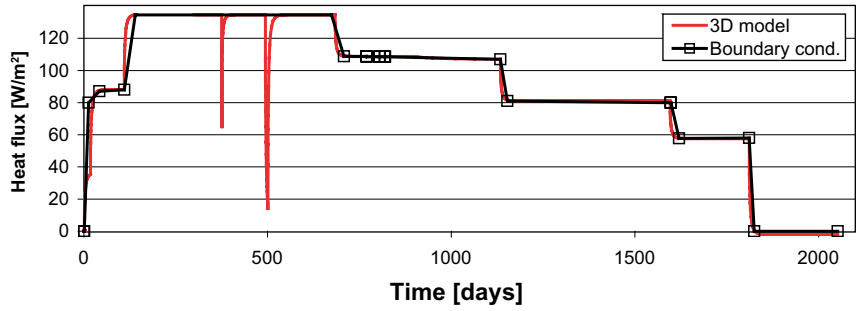

Figure 3-37. *Heat flux prescribed at the canister boundary.*

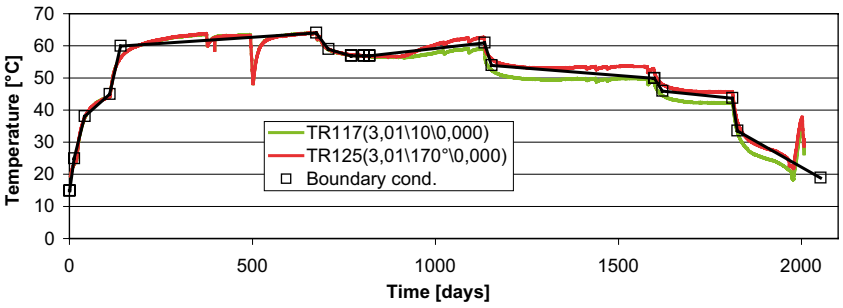

Figure 3-38. *Temperature prescribed at the rock wall boundary.*

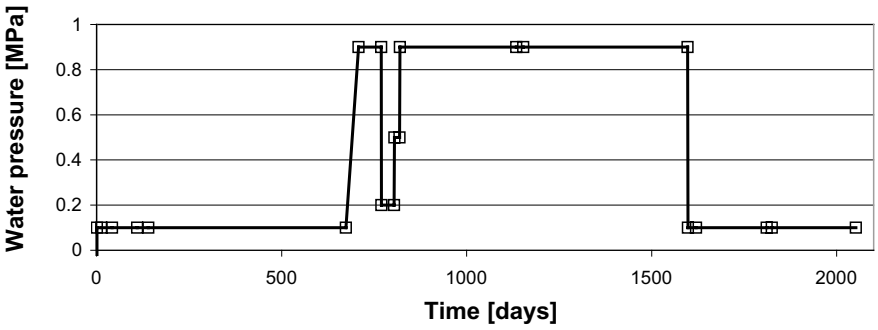

Figure 3-39. *Filter water pressure protocol.*

Results

The presented results are 1) variable histories at specified points and 2) variable profiles at specified times. Some of the selected results are compared with CRT data. Both suction and axial stress are compared at r = 585, 685 and 785 mm and the void ratio profile obtained at the end of the simulation is also compared with measured void ratios in block R6 and R7.

The entire set of points for which the variable evolutions are shown is indicated schematically in Figure 3-40 below. Note that the two largest radii are changed from the suggestion given in the assignment since the geometry (deposition hole radius) has been altered from the one suggested in the assignment. In the section below a compilation of the points where the variables are reported are given. Also, comments and references to the corresponding figure/figures are given.

Temperature evolutions at r = 540, 585, 635, 685, 735, 785, 815, 825, 850.5 are given in Figure 3-41.

Water saturation evolutions at r = 540, 585, 635, 685, 735, 785, 815, 825, 850.5 are given in Figure 3-42.

Suction evolutions at r = 585, 685 and 785 are given in Figure 3-43, Figure 3-44 and Figure 3-45, respectively. Both experimental and simulated suction evolutions are here shown for the first 1 000 days.

Total axial stress evolutions at r = 540, 585, 685, 785, 815, 825, 850.5, 881 is shown in Figure 3-46. In Figure 3-47 and Figure 3-48 experimental and simulated results are shown at r = 585, 685, 785. Based on the observation made concerning the "installation effect", discussed in Section 3.2.10, the results from the simulation should be compensated for not incorporating this effect in the model. Below in Figure 3-48 the calculated stresses have been multiplied by a factor of 0.6 = (9/15), which is motivated from the experiment data shown in Section 3.2.10. In all figures related to stress components, Figure 3-46 – Figure 3-49, compressive stress is shown as positive for convenience.

Total radial stress evolutions at r = 540, 585, 685, 785, 815, 825, 850.5, 881 are given in Figure 3-49

Dry density evolutions at r = 540, 585, 635, 685, 735, 785, 815, 825, 850.5 are given in Figure 3-50.

Displacement evolutions at r = 540, 585, 635, 685, 735, 785, 815, 825, 850.5 are given in Figure 3-51.

Water saturation profiles at day = 50, 100, 200, 1 000, and 2 052 are given in Figure 3-52.

Dry density profiles at day = 50, 100, 200, 1 000, and 2 052 are given in Figure 3-53.

Void ratio profiles at the end of the simulation are given in Figure 3-54, Figure 3-55 and Figure 3-56. Both experimental and simulated void ratios are presented. Figure 3-54 and Figure 3-55 show the unfiltered data from block R6 and R7, respectively. In Figure 3-56 the experimental data from R6 and R7 has been filtered by calculating volume averages for selected radial segments, i.e. every red and yellow marker indicate a calculated volume average of the void ratio at the centre of the selected radial segment. Also, the initial void ratio profile and homogenized initial values are shown.

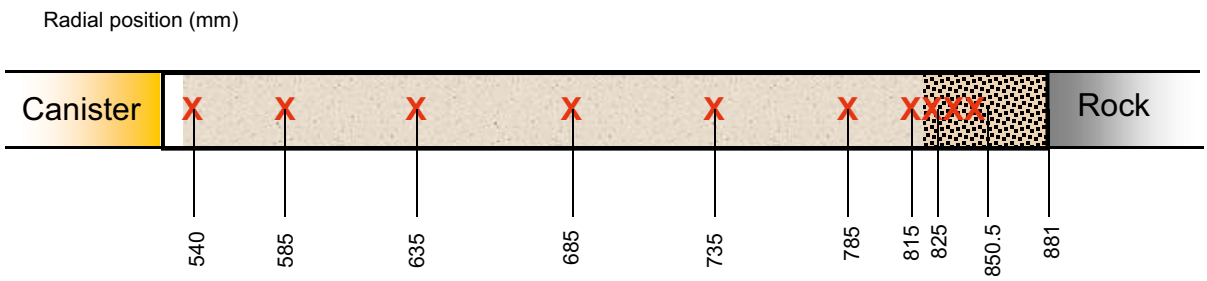

Figure 3-40. *Schematic drawing of the points where variable histories are presented. The radial distances are given in the initial (undeformed) configuration.*

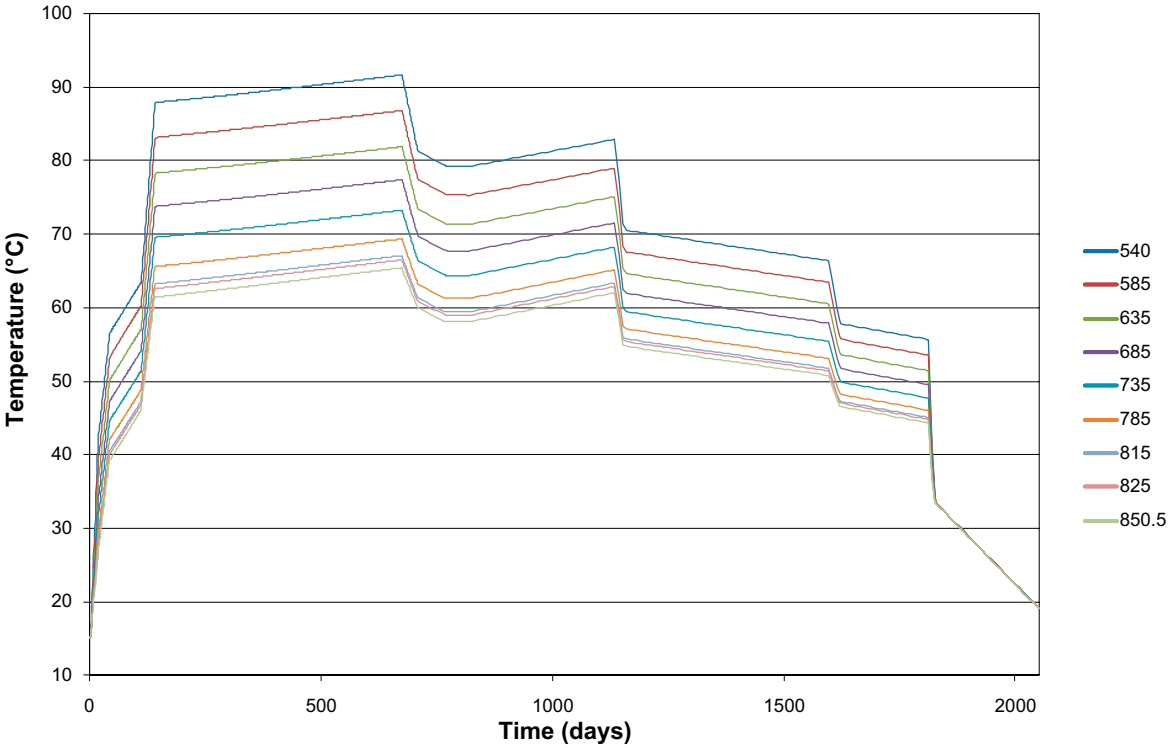

Figure 3-41. *Temperature evolutions.*

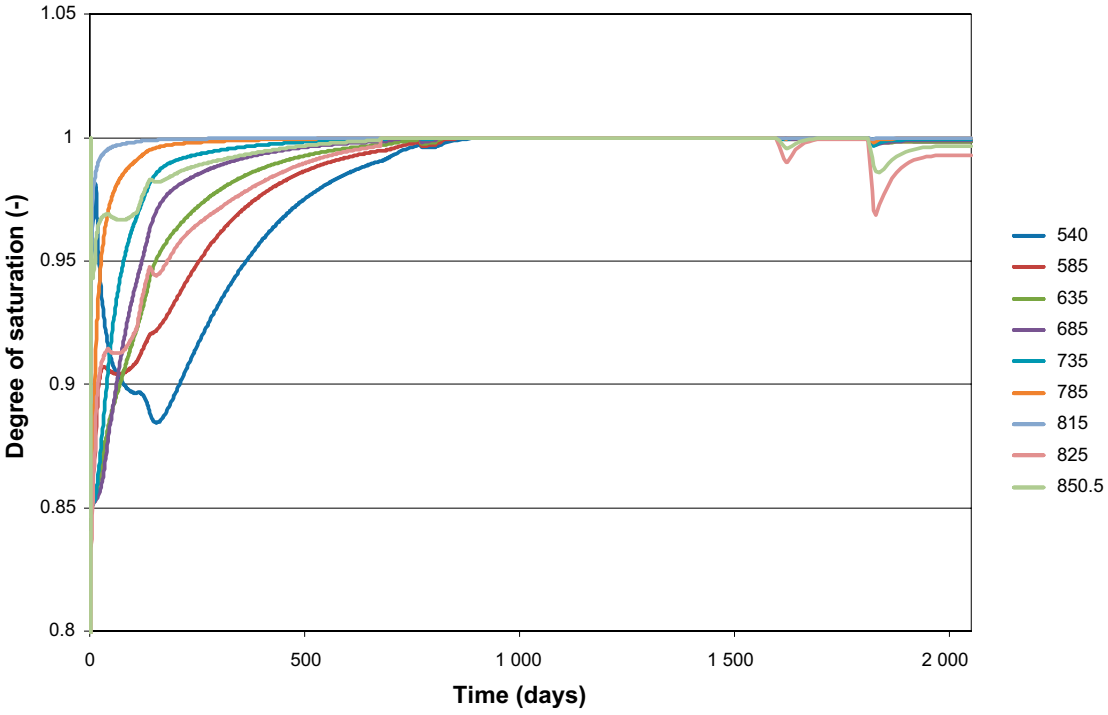

Figure 3-42. *Evolutions of degree of saturation.*

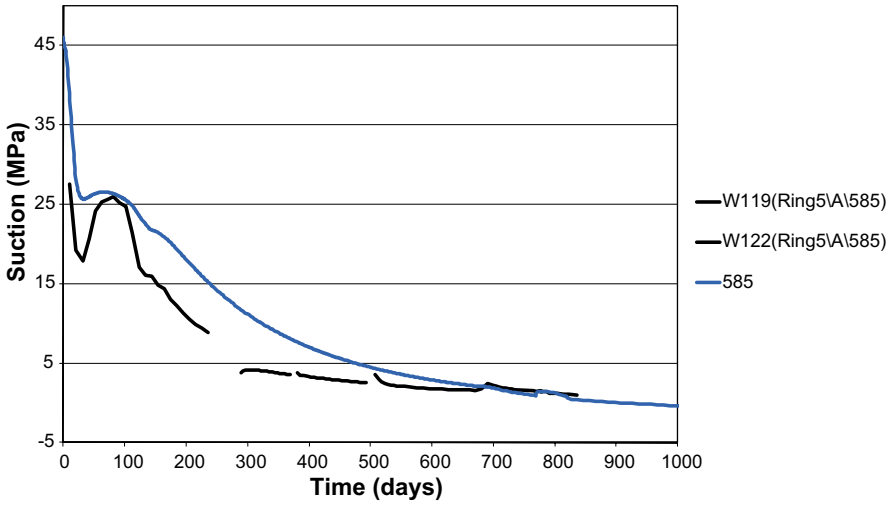

Figure 3-43. *Experimental and simulated suction evolution (first 1 000 days) at r = 585 mm.*

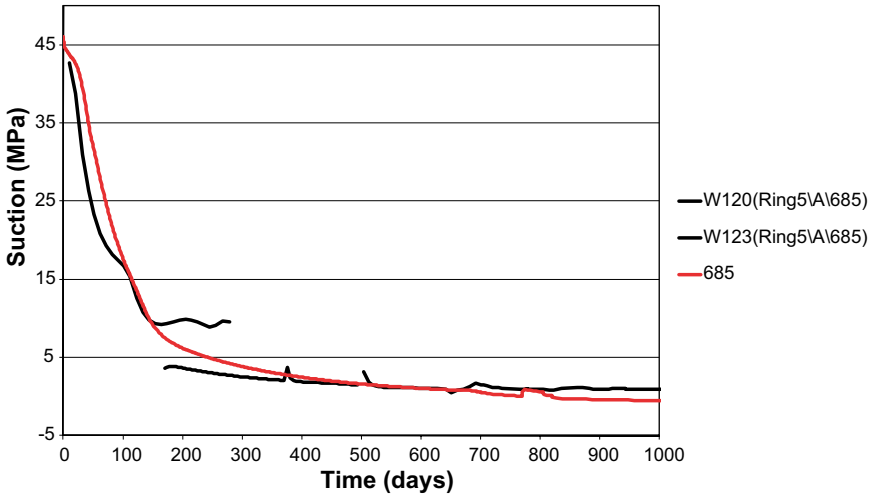

Figure 3-44. *Experimental and simulated suction evolution (first 1 000 days) at r = 685 mm.*

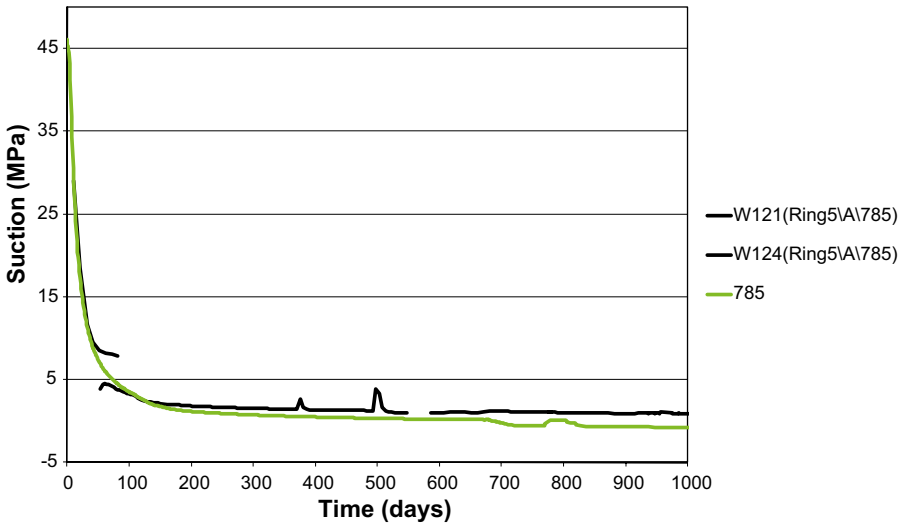

Figure 3-45. *Experimental and simulated suction evolution (first 1 000 days) at r = 785 mm.*

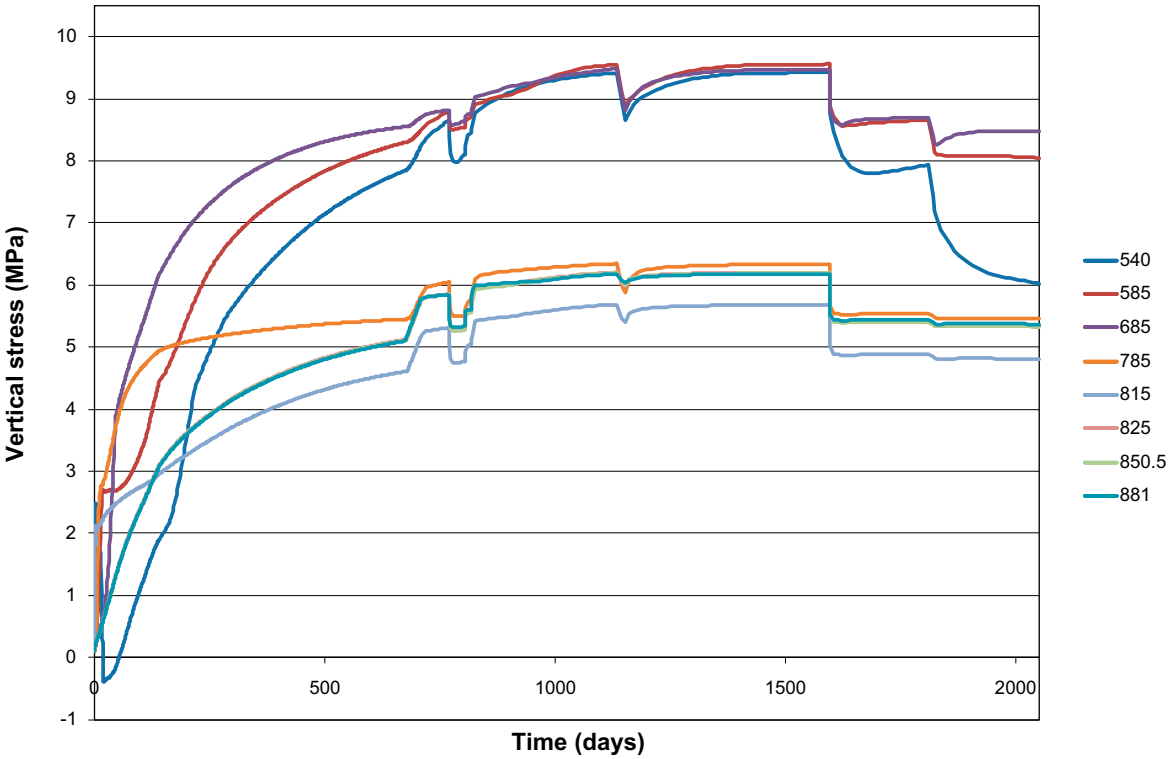

Figure 3-46. *Axial (vertical) stress component evolution.*

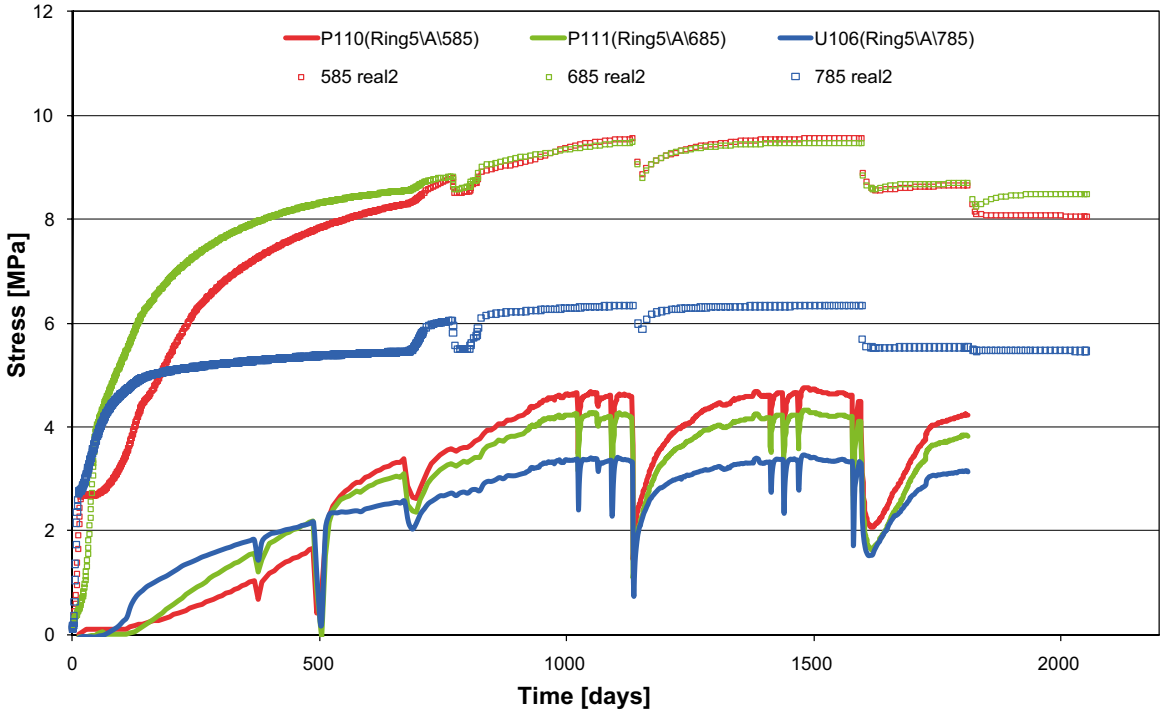

Figure 3-47. *Experimental and simulated axial (vertical) stress component evolution at r = 585, 685 and 785 mm.*

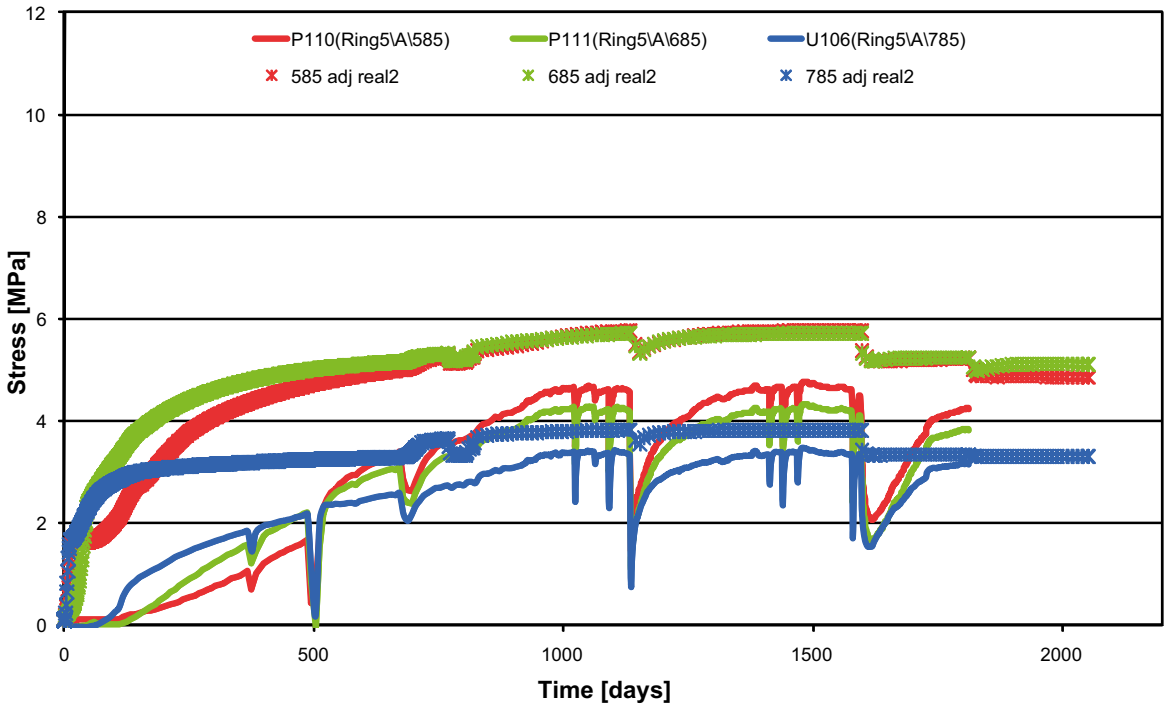

Figure 3-48. *Experimental and adjusted (× 0.6) simulated axial (vertical) stress component evolution at r = 585, 685 and 785 mm.*

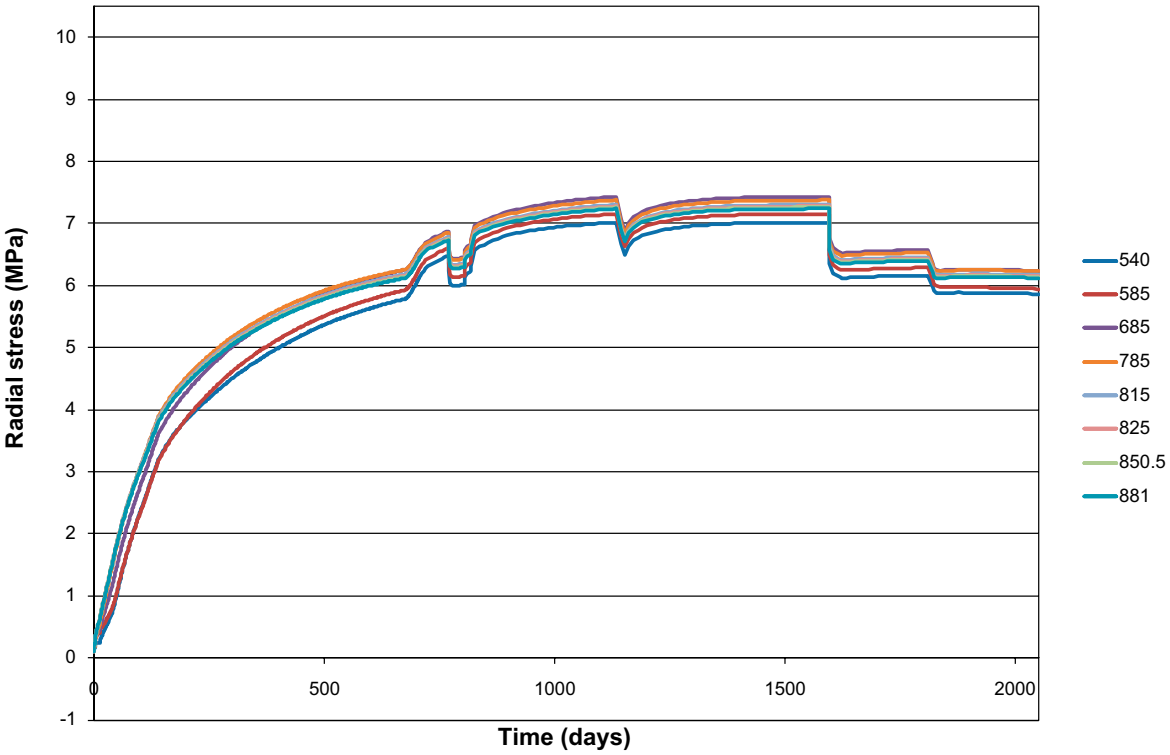

Figure 3-49. *Radial (horizontal) stress component evolution.*

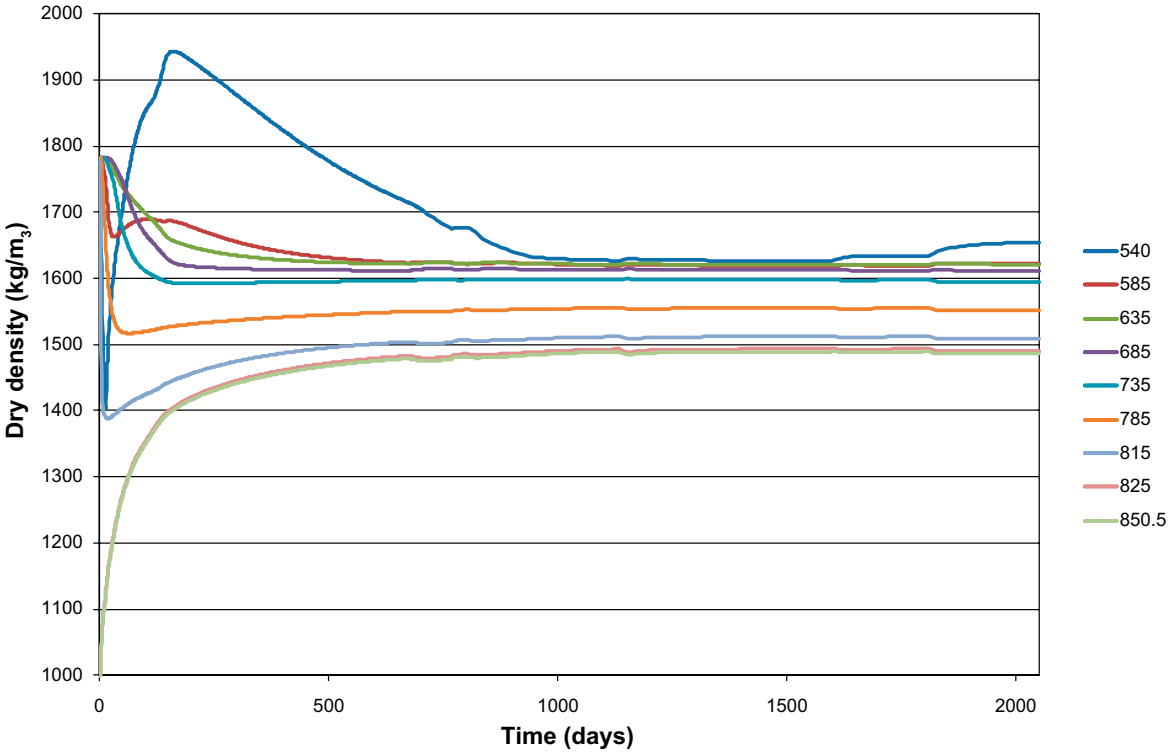

Figure 3-50. *Dry density evolution.*

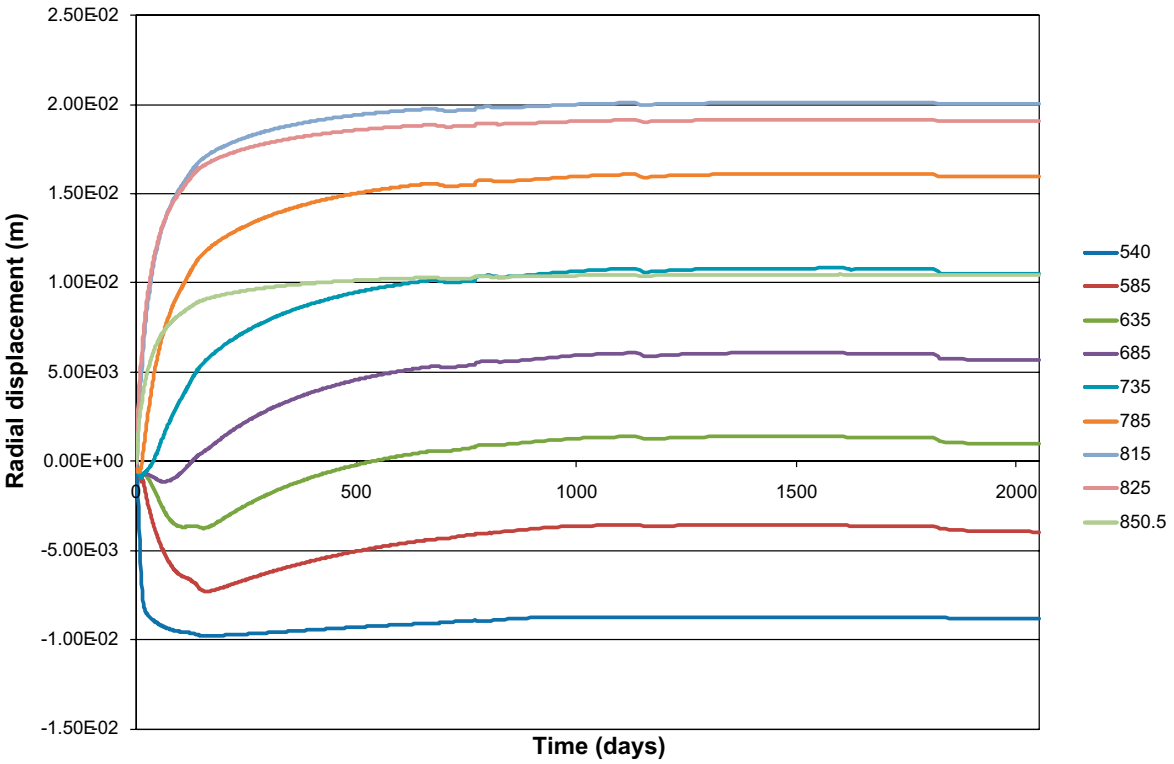

Figure 3-51. *Evolution of radial displacement.*

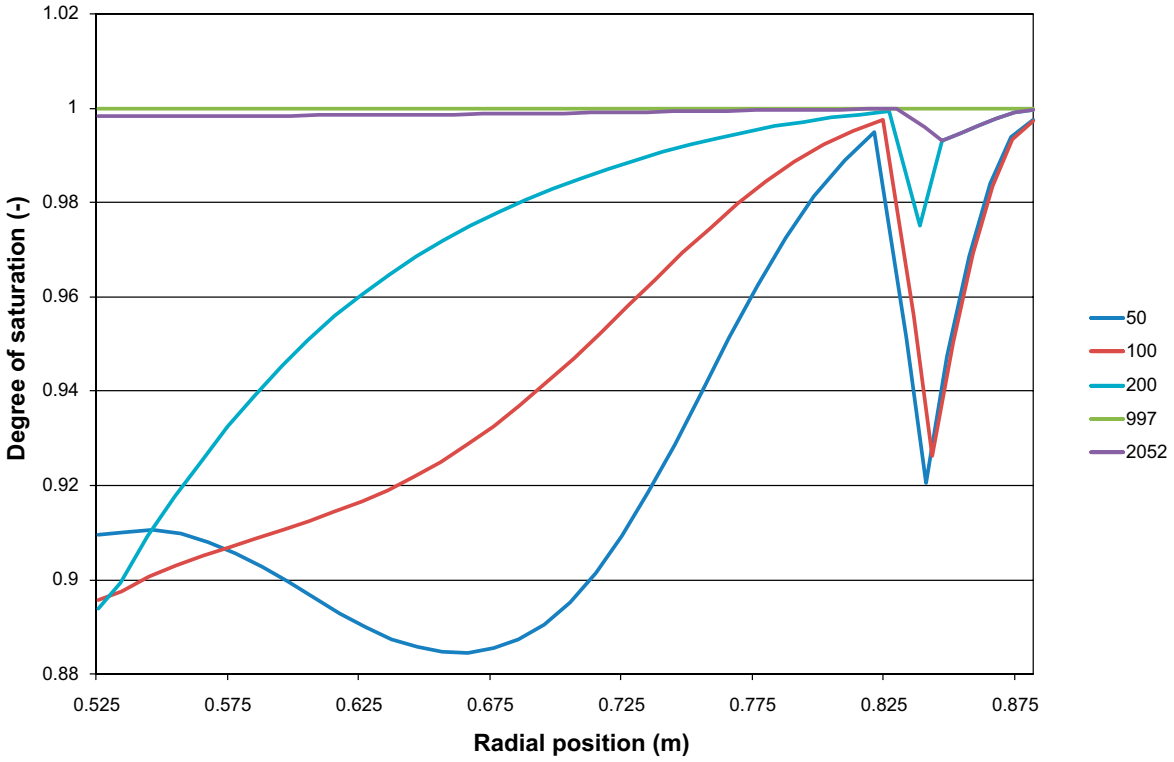

Figure 3-52. *Profiles of degree of saturation.*

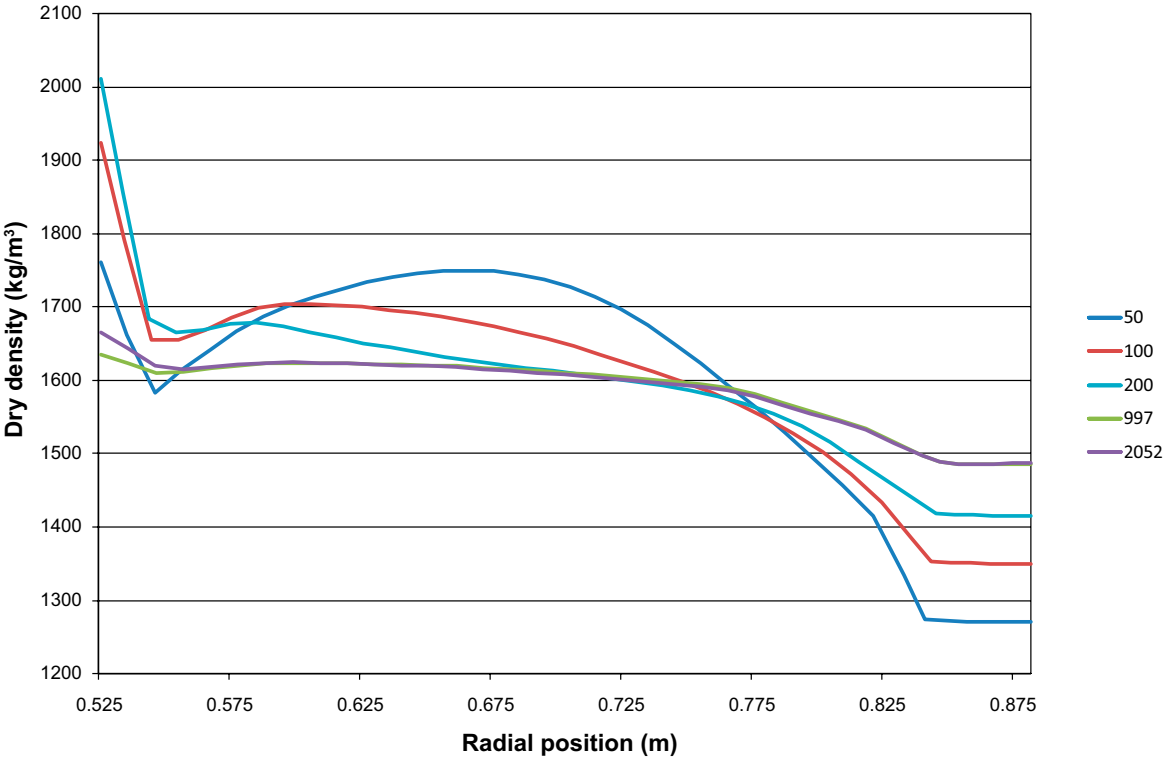

Figure 3-53. *Profiles of dry density.*

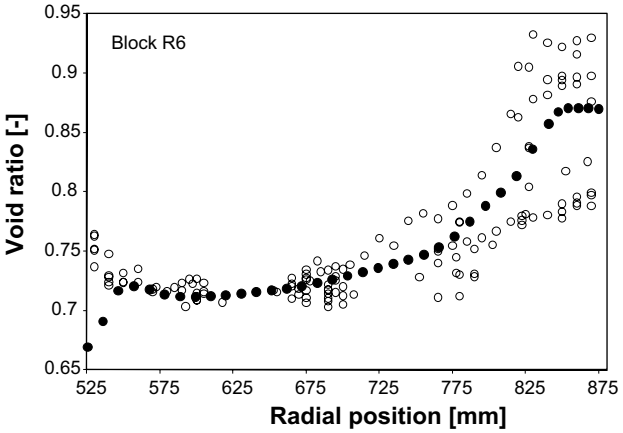

Figure 3-54. *Experimental void ratio data for R6 and void ratio profile at end of simulation.*

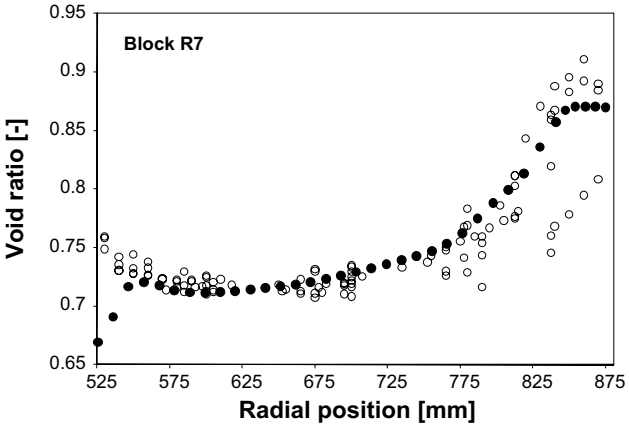

Figure 3-55. *Experimental void ratio data for R7 and void ratio profile at end of simulation.*

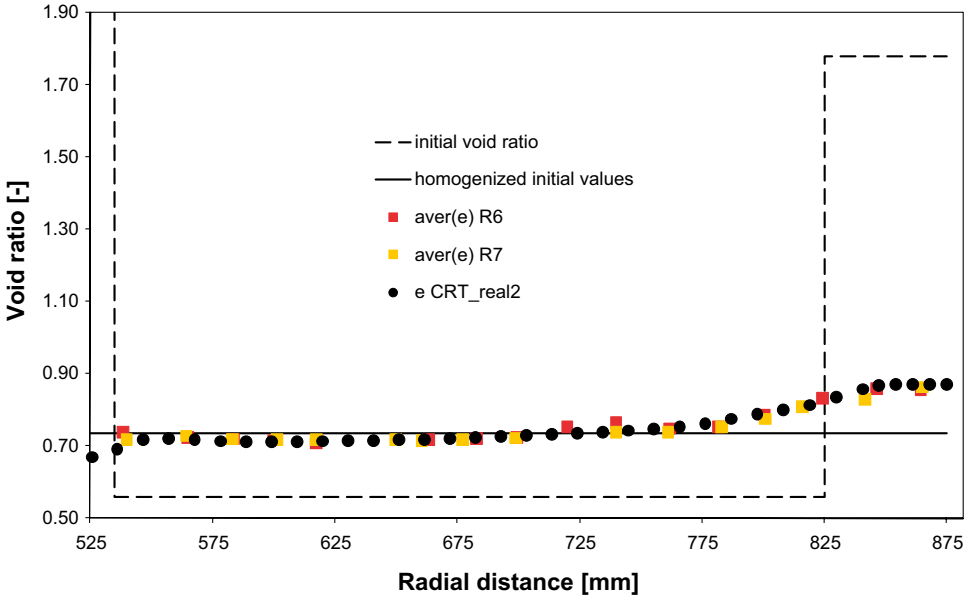

Figure 3-56. *Filtered experimental void ratio data for R6 and R7 and void ratio profile at end of simulation.*

3.3.4 Sub-task 2: Investigating the homogenization process

The work reported in this section was first conducted for the SR-Site report (Åkesson et al. 2010b). The analytical model was also presented for the EBS Task-Force and later on further developed and included in the contribution to "*Clays in Natural & Engineered Barriers for Radioactive Waste Confinement*" held in Nantes 29th March to 1st April 2010. A large part of the material presented here is also present in Kristensson and Åkesson (2011).

Introduction

The work is focused on buffer homogenization in the Swedish KBS-3 designed deposition holes, according to which the CRT was equipped. At installation of the buffer, the density is strongly heterogeneous due to presence of the different buffer constituents; compacted bentonite blocks, an outer slot filled with bentonite pellets and an inner open slot. When subjected to wetting from the host rock the bentonite clay swells and the buffer becomes more homogeneous,

When the density of a fully water saturated buffer is studied (in CRT the buffer was fully saturated at canister mid-height when excavated) it is found to be heterogeneous.

The objectives are to: (i) describe a developed analytical model predicting the buffer homogenization at canister mid-height, (ii) using the analytical model, discuss what governs the homogenization in the clay buffer and gives rise to the remaining heterogeneity, (iii) show modelling of the homogenization in CRT at canister mid-height where results from using CODE_BRIGHT and the analytical model are compared to CRT data and finally, (iv) investigate how CODE_BRIGHT models and the analytical model correspond for extreme wetting cases.

Description of the analytical model

The point of departure when developing the analytical model has been to utilize the thermodynamical formulation used when studying soil water characteristics (Low and Anderson 1958, Kahr et al. 1990, Birgersson et al. 2010). To arrive at the formulation, an isothermal closed system where pure water is connected to moist soil via a semi-permeable membrane can be considered (Low and Anderson 1958). Forming the difference in Gibbs energy between the pure water and soil water and using the definition of activity give,

$$-\frac{\rho_w R\theta}{m_w}\ln(RH) = p \tag{3-5}$$

where ρ_w is the water density, R the universal gas constant, θ the absolute temperature, m_w the molecular mass of water vapour, RH the relative humidity and p the swelling pressure.

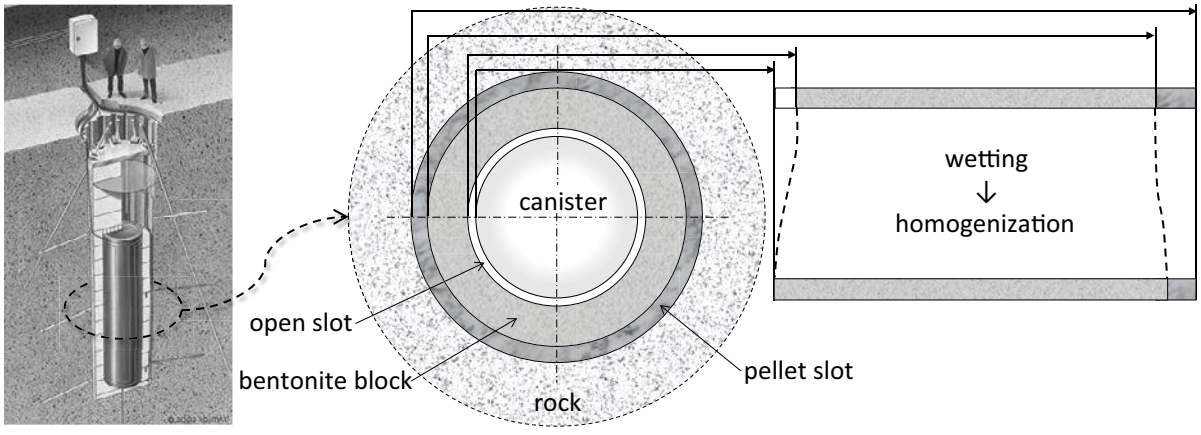

Figure 3-57. *Schematic figure of the CRT experiment and the buffer homogenization.*

When compared to the general theory of thermodynamics, applicable to solids, some simplifications have been made. The mechanical contribution to Gibbs energy should be expressed in terms of the scalar product of the stress tensor and strain tensor multiplied with initial specific volume. Here, for simplicity, this term is considered to be represented by the product of pressure and specific volume. For more information see Houlsby and Puzrin (2000).

The left hand side of Equation (3-5) equals the definition of suction under free swelling conditions, s_{free}, which gives the relation,

$$s_{free} = p \tag{3-6}$$

valid at isothermal and fully water saturated conditions. Thus, from considering basic thermodynamics, a relation between swelling pressure and suction under free swelling conditions is obtained.

The retention properties of the buffer material, which can be experimentally determined (e.g. Dueck 2004), is defined by the relation $RH = RH(w,w_{ref})$. (Note that the left hand side is a variable whereas the right hand side is a function. This notation where functions are indicated by the parenthesis is used in the following.) The relation gives the relative humidity for a water ratio, w, and a history variable, here denoted w_{ref}. The water ratio is defined as $w = dm_w^l/dm_s$, where dm_w^l is the mass element of liquid water and dm_s the mass element of compacted solid material in the volume element considered. The incorporation of the history variable, w_{ref}, is necessary due to the path dependency of the retention property. As a consequence of the appearance of the retention relation the "free suction" can be expressed $s_{free} = s_{free}(w,w_{ref})$.

In a fully water saturated KBS-3 buffer at canister mid-height there are a bentonite block volume, v^b, and a pellet slot volume, v^p. Taking the volume averages of Equation (3-6), over v^p and v^p, and using $s_{free} = s_{free}(w,w_{ref})$ produces the expressions,

$$\begin{aligned} \frac{1}{v^p}\int_{v^p} s_{free}(w,w_{ref})dv &= \frac{1}{v^p}\int_{v^p} p dv \\ \frac{1}{v^b}\int_{v^b} s_{free}(w,w_{ref})dv &= \frac{1}{v^b}\int_{v^b} p dv \end{aligned} \tag{3-7}$$

The w and w_{ref} may generally vary over v^p and v^p but in order to simplify the model some approximations are made.

The water ratio, w, and the history variable, w_{ref}, are approximated as being constant in v^p and v^b. Thus, $w = w^b$ and $w_{ref} = w_{ref}{}^b$ in the block and $w = w^b$ and $w_{ref} = w_{ref}{}^b$ in the pellet slot. The right hand sides of the relations above define the volume average of the pressure field in the pellet slot, p^p, and the bentonite block, p^b, respectively. Using the assumptions and definitions in Equation (3-7) give,

$$\begin{aligned} s_{free}(w^p, w_{ref}{}^p) &= p^p \\ s_{free}{}^b(w^b, w_{ref}{}^b) &= p^b \end{aligned} \tag{3-8}$$

The pressure averages at full water saturation are not likely to be equal since there are no conditions that constrain the axial and tangential stresses to be similar in the block and pellet slot (the radial stresses are expected to be similar due to force balance). Therefore, a pressure ratio, $\alpha = p^p/p^b$, is introduced.

The water ratios at full water saturation can be expressed in terms of: water density ρ_w (here taken as 1 000 kg/m^3), solid density ρ_s (here taken as 2 780 kg/m^3), and the void ratios e^p and e^b (being constant in v^p and v^b due to the assumption made for the water ratio).

$$\begin{aligned} w^p &= \frac{\rho_w}{\rho_s} e^p \\ w^b &= \frac{\rho_w}{\rho_s} e^b \end{aligned}$$

The void ratio, e, is defined and related to other variables according to,

$$e = \frac{dv_p}{dv_s} = \frac{\rho_s}{\rho_d} - 1 = \frac{n}{1-n}$$

where dv_p denotes the pore volume within a material volume element dv, dv_s denotes the volume of solid material within the material volume element, ρ_s is the solid mass density, ρ_d is the dry mass density and $n = dv_p / dv$ denotes the porosity.

Using the conditions that are assumed to prevail at full water saturation together with Equation (3-8) and the definition of the pressure ratio $\alpha = p^p / p^b$, give,

$$s_{free}\left(\frac{\rho_w}{\rho_s} e^p, {w_{ref}}^p\right) - \alpha\, s_{free}\left(\frac{\rho_w}{\rho_s} e^b, {w_{ref}}^b\right) = 0 \qquad (3\text{-}9)$$

which for example may be solved for the pellet slot void ratio if the block void ratio, the pressure ratio, α, the two history variables and the $s_{free}(w, w_{ref})$ functions are specified. From studying (3-9) it can be seen that the pressure ratio governs the homogenization as well as the history variables. The history variables will depend on the character of the wetting process the buffer has been subjected to, which reflects the path dependence of the retention.

The format of the function chosen to represent s_{free}, is developed from considering experimental measurements (similar format is used in Kahr et al. 1990) and reads,

$$s_{free}(w, w_{ref}) = \exp(a(w_{ref}) - b(w_{ref})w) \qquad (3\text{-}10)$$

where the parameters a and b is determined from calibrating the expression against experimental measurements. In Figure 3-58, experimental data of s_{free} is shown as a function of w for different initial water saturations, w_{init}, indicated in the legend. The initial water saturation is here identified with the referential water saturation (i.e. is chosen as the history variable).

If the parameters a and b are evaluated for the different curves between the high and low limits shown in Figure 3-58 and are plotted against the corresponding referential water saturation, the graphs in Figure 3-59 are obtained.

It can be seen that the values of the parameters for a referential degree of water saturation of 0.17 deviates significantly from the trend of the other results. An adjusted parameter set has therefore been developed for $w_{ref} = 0.17$ to match the trend of the other results. Piecewise linear relations corresponding to the adjusted graphs have been used when determining the variables, thus the functions $a = a(w_{ref})$ and $b = b(w_{ref})$ are determined.

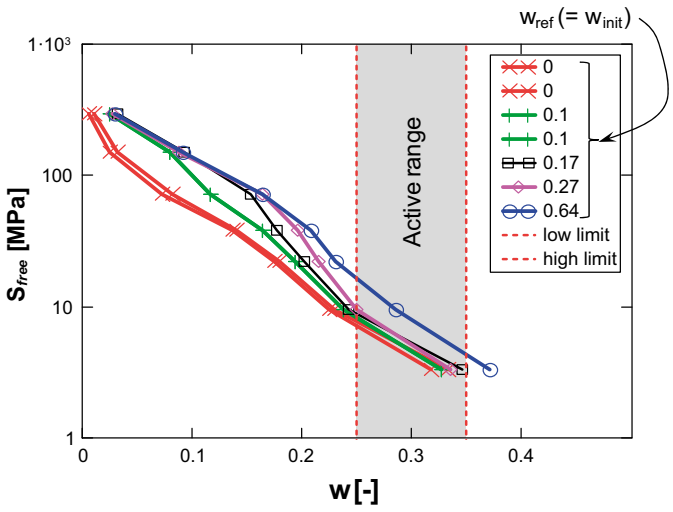

Figure 3-58. *Retention data for free swelling MX-80.*

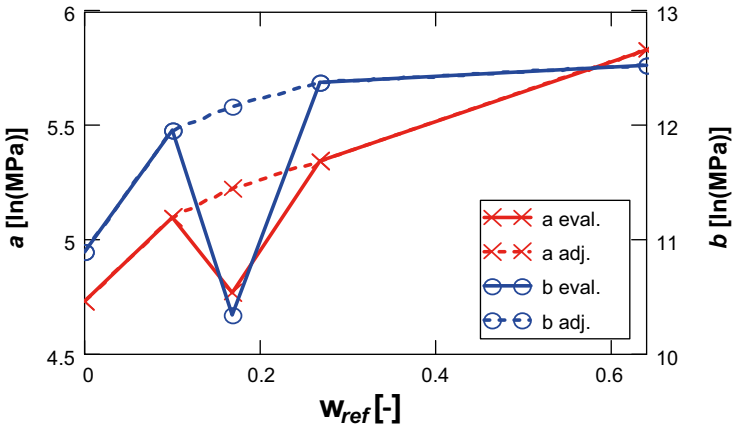

Figure 3-59. *Parameters in the expression of free retention as a function of the referential water ratio.*

With the expression of the free suction inserted in Equation (3-9) the resulting expression, valid at full water saturation under the assumptions made, reads,

$$e^p = \frac{\rho_s}{\rho_w}\frac{a(w_{ref}{}^p) - a(w_{ref}{}^b) - \ln(\alpha)}{b(w_{ref}{}^p)} + \frac{b(w_{ref}{}^b)}{b(w_{ref}{}^p)}e^b \qquad (3\text{-}11)$$

Using the relation above gives an opportunity to investigate how retention and pressure difference affects the heterogeneity in void ratio at full water saturation.

In the following, two extreme wetting scenarios are used to study the effect from the retention path dependency on homogenization. The *serial wetting scenario* is defined as wetting of the pellet slot (from 0 to1 in the left part of Figure 3-60) followed by wetting of the block material (from 1 to 2 in the left part of Figure 3-60). The left part of Figure 3-60 show how the paths of the pellet slot material and block material appear in S_{free}-w space using Equation (3-10) for the serial scenario. The *parallel wetting scenario* is defined as concurrent wetting of block and pellet slot (from 0 to1 in the right part of Figure 3-60) and the paths in S_{free}-w space using Equation (3-10) is shown in the right part of Figure 3-60.

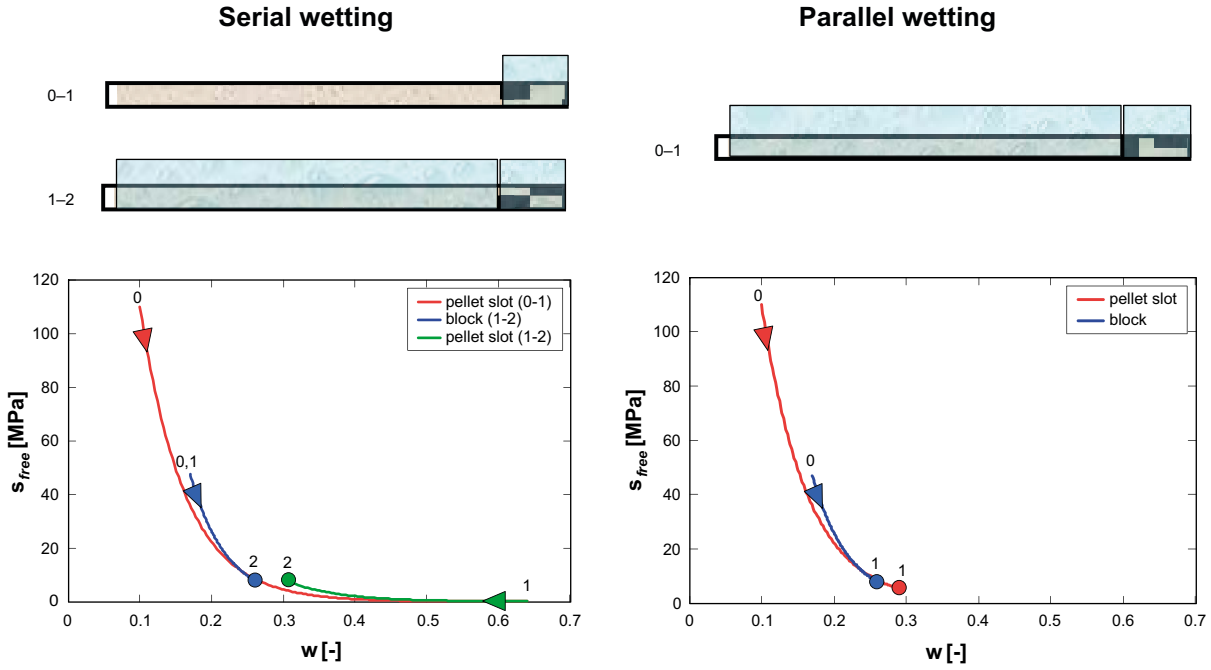

Figure 3-60. *Serial wetting 0–1–2 (to the left) and Parallel wetting 0–1 (to the right), paths in S_{free}-w space.*

The two wetting scenarios can be seen as representations of a saturation process going from the pellet-side to the block-side at different speed. *The serial wetting could represent an extremely rapid saturation process,* where water quickly transports from the rock wall towards the canister, and *the parallel wetting may represent an extremely slow wetting process*, where no gradient in suction occurs since before every "new" drop of water entering, the system is equilibrated.

Below in Figure 3-61 the relation (Equation 3-11) between the average void ratios of the pellet slot and block are plotted for serial and parallel wetting scenarios. The pressure ratio has been set to $\alpha = \{1, 0.9, 0.8, 0.7\}$ for both wetting scenarios. The average void ratio combination obtained from analyzing the data at canister mid-height of the CRT experiment is also indicated (red circle) for comparison. The relation obtained for an assumption of constant volume of pellets, blocks and initially open inner slot in CRT (as compared to the measured state in the CRT experiment) is also shown (solid thick black line).

Figure 3-61 shows possible void ratio states at full water saturation when different wetting processes and different pressure ratios are adopted. Examples of obtained "void ratio profiles" when assuming different combinations of wetting process and pressure ratio are shown to the right in the figure (the combinations are indicated with A, B, C and D along the constant volume assumption relation in the graph).

Results and discussion

The first comparison between experimental data and model data concerns the final void ratio profile with respect to radial distance, which is shown in Figure 3-62. The experimental data from blocks R6 and R7, close to the canister mid-height, has been filtered by calculating the volume average in some chosen radial intervals. This was done in order to make the data comparable with the results obtained from the axisymmetric model. The solution from the FE-model is given as well as two analytical solutions using Equation (3-11), where α = 0.84 has been adopted (obtained from evaluating the pressure in the pellet slot and block in the FE-solution) and a serial wetting or parallel wetting have been assumed, respectively.

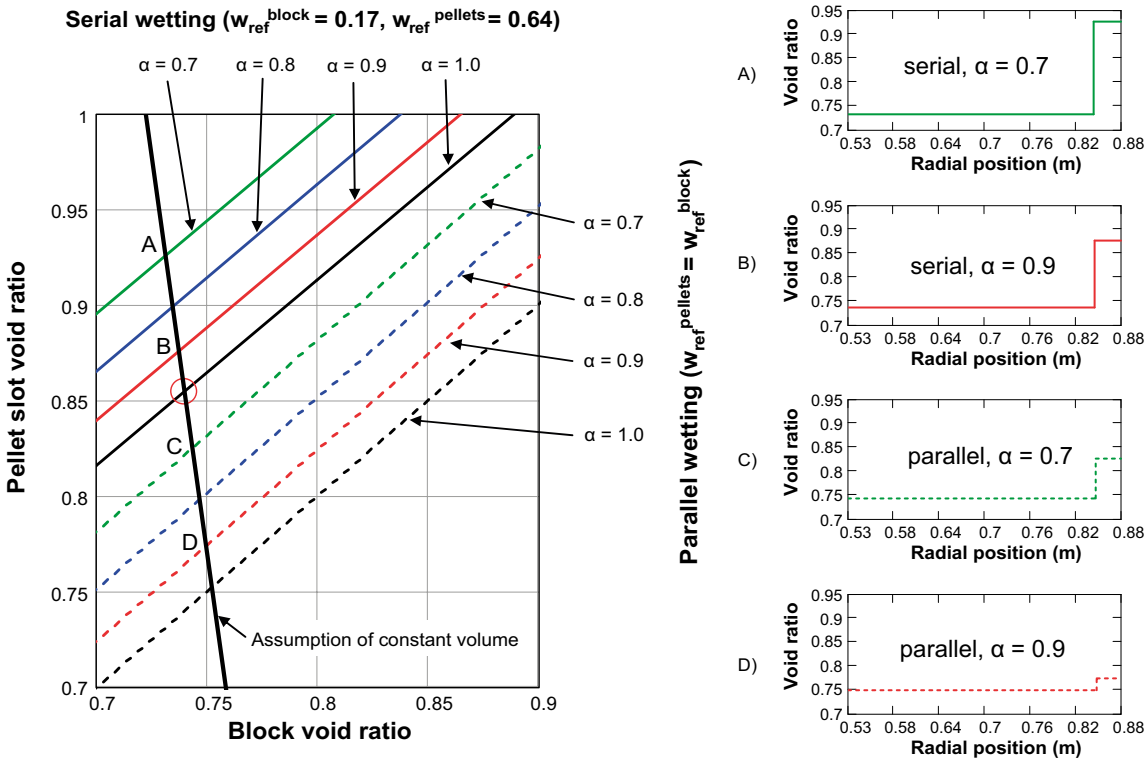

Figure 3-61. *Compilation of the analytical model results for serial (solid lines) and parallel wetting (hatched lines) assuming different pressure ratios. The thick black solid line indicates void ratio combinations obtained if constant volume is assumed with the CRT void ratio state at canister mid-height (red circle) taken as a reference. To the right the void ratios obtained when adopting four different combinations of wetting process and pressure ratio along the constant volume assumption are shown.*

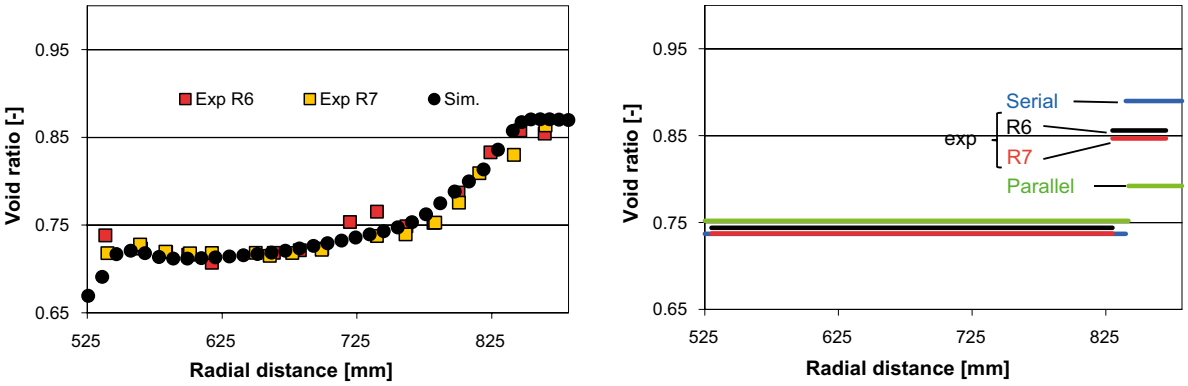

Figure 3-62. *Final void ratio profiles for CRT experiment and models.*

As can be seen, the FE-model void ratio profile agrees well with the filtered experimental data. The pellet slot mechanical parameter κ_{i0} in BBM, see Table 3-4, was calibrated so that the void ratio profile became continuous over the block/pellet slot interface. At the inner slot/block interface of the model there is an effect from the presence of the inner slot material and/or the boundary, that makes the simulated void ratio profile drop, can be seen.

To the right in Figure 3-62 two analytical solutions, for which serial or parallel wetting have been assumed, are shown. $\alpha = 0.84$ is adopted in accordance with the FE solution. The result from averaging the experimental data in R6 and R7 over the block and pellet slot volume are also shown. The analytical solutions agree well with the experimental data considering that the wetting scenario occurring in CRT should be something "in between" serial and parallel. It can be seen that the analytical solutions bound the experimental averages.

Modeling parallel and serial wetting processes

To study the capabilities of the FE-code the two extreme cases of serial and parallel wetting are modelled using the FE-model and the solutions are compared to the results obtained from using the analytical model.

Just to remind the reader what is meant by the two extreme wetting cases. A *serial wetting* scenario (wetting of the pellet slot followed by wetting of the block material) *may represent an extremely rapid saturation process,* where water quickly transports from the rock wall towards the canister. A *parallel wetting* scenario (concurrent wetting of block and pellet slot) *may represent an extremely slow wetting process*, where no gradient in suction occurs, since before every new drop of water entering the system, the system is equilibrated.

Pure serial and parallel wetting processes are here simulated using the FE-solver by prescribing the suction field evolution in the block and pellet slot. The serial wetting process is accomplished by first prescribing a suction decrease from the initial value (46 MPa) to 0.1 MPa in the pellet slot and thereafter prescribing an identical suction decrease in the block. The parallel wetting process is given by prescribing a simultaneous decrease in both pellet slot and block.

The traces in e-ln(p') space obtained from the FE-models are shown in Figure 3-63. Also, the selected point's position and the obtained volume average pressure ratios are shown.

The pellet slot evolution (point 1 and 2) has for the serial wetting case an initial increase in void ratio (actually not seen in the logarithmic plot above since the void ratio increase occurs at very low pressures) and at pressures between 0.1–0.2 MPa the slope is lower as compared to the evolution for parallel wetting. At higher pressures the slope of the $e - \ln(p')$ curve is determined by the value of the λ parameter only. This is seen in Figure 3-63 since the both wetting processes produce the same slope in $e - \ln(p')$ at high pressure levels.

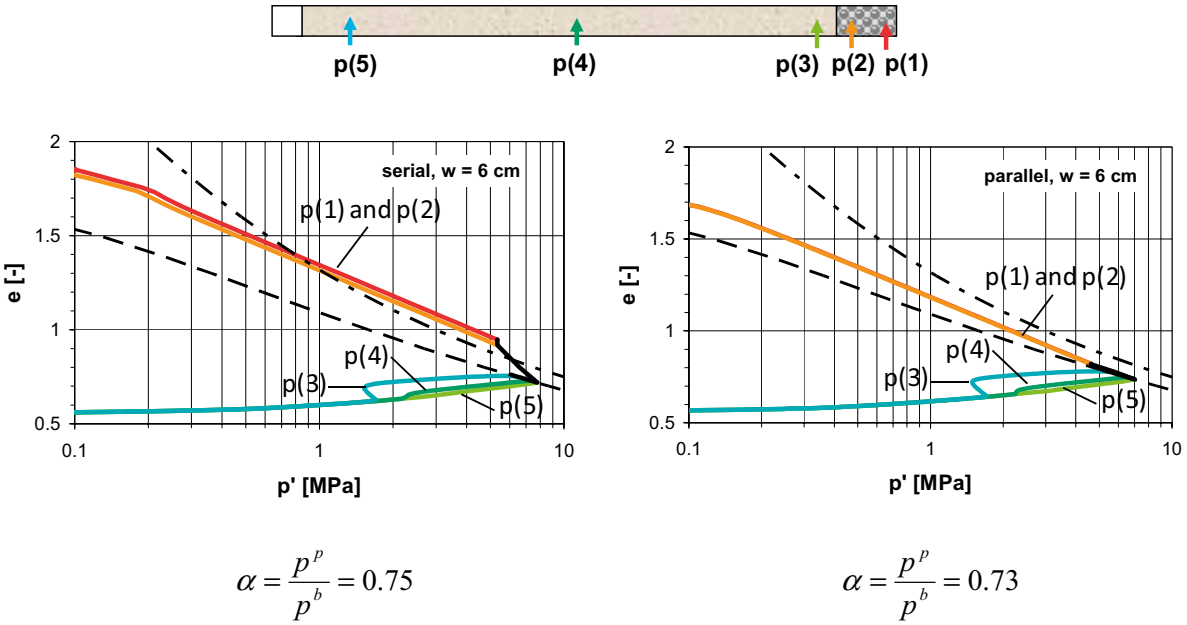

$$\alpha = \frac{p^p}{p^b} = 0.75 \qquad \alpha = \frac{p^p}{p^b} = 0.73$$

Figure 3-63. *Traces in e-ln(p') space for a serial and parallel wetting process. Indicated are also: (dash) the swelling pressure curve adopted in BBM, see Table 3-4, representative for swelling conditions and (dash dot) a swelling pressure curve representative for compressive conditions.*

As a result, the serial wetting process gives rise to a final state of the pellet slot that overshoots the adopted swelling pressure curve (dashed line) but is closer to the swelling pressure curve representing compressive conditions (dash-dotted line) and the parallel wetting process produces a final pellet slot state that coincides with the adopted swelling pressure curve (dashed line). The obtained final state in the FE simulations depends on the adopted swelling pressure curve and the adopted λ parameter value.

The final void ratios (at full water saturation) agree well between the FE-models and the corresponding analytical model for both wetting scenarios, as can be seen in Figure 3-64.

Conclusions

An analytical model capable of predicting the final (at full water saturation) state in terms of average void ratios in the block and pellet slot has been developed.

When developing the analytical model, with its foundation in soil water thermodynamics, it was concluded that a difference in pressures in the bentonite block and pellet slot as well as the character of the wetting process, through the path dependence of the retention, played governing roles.

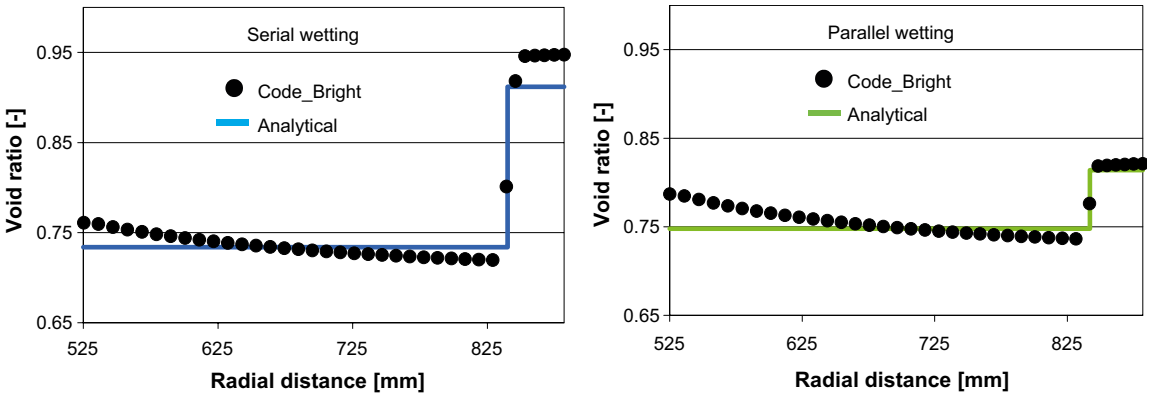

Figure 3-64. *Final void ratio profiles for the serial and parallel FE-models and analytical models.*

The homogenization of the buffer at canister mid-height in the Canister Retrieval Test experiment has been modelled by use of the finite element program CODE_BRIGHT and the analytical model. The obtained responses were found to agree well with experimental data.

Two extreme wetting scenarios (serial = fast or parallel = slow) have also been simulated using both CODE_BRIGHT and the analytical model and the solutions agree well.

3.3.5 Sub-task 2: Some investigations made during the model development

During the process developing the model presented in the former chapter the effect from using different constitutive laws and parameters were studied. These investigations are presented here. The models are not considered to be the most representative of the CRT experiment. They are considered to serve their purpose anyway; by allowing studies of differences between models where the processes are reasonable alike those which are considered to prevail during the CRT experiment.

It should thus be noted that the "Base Case" model used here is not the model presented in the former chapter which is considered more representative. There are of course similarities, but there are also large deviations. One significant difference is that the updated coordinate formulation was not used in these preliminary studies. The assumption that follows for this choice (deformations are close to zero) is clearly not valid for the problem investigated. This is discussed in Appendix 5. Also, the models presented here do not use the modifications made on the mechanical constitutive law, which were used in the formerly presented model.

The investigations reported are:

Comparison of suction responses for TH and THM: The effect from the mechanical process on the suction evolution was studied. It was found that the mechanical process slowed down the suction decrease. The mechanical coupling to the suction was found to be significant.Effect **from lowered retention curve (TH):** The lower retention curve initially gave a more rapid decrease in suction but at some point the decrease in suction became slower as compared to the responses obtained from using the old (higher) retention.

Effect from porosity dependent retention (THM): The porosity dependence gave slower decrease in suction.

Effect from increased intrinsic permeability (TH): The increased intrinsic permeability gave faster decrease in suction.

Effect from using different porosity dependency of the permeability (THM): The different porosity dependencies did not give significant differences in the suction evolution.

Model description

A radial-symmetric model is used, where the model contains: (A) an inner gap (0.01 m width), (B) a ring shaped bentonite block and (C) an outer gap filled with bentonite pellets (0.055 m width). Figure 3-65 shows the geometry.

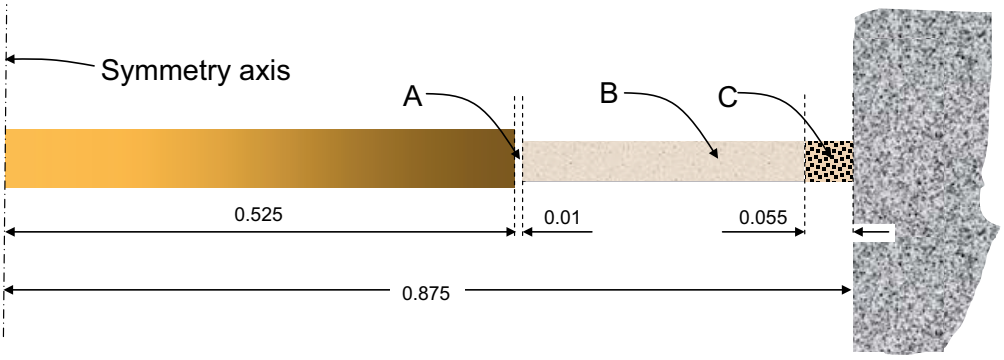

Figure 3-65. *Model geometry.*

Table 3-7 Initial conditions in the model.

Material	T [°C]	w/S_l	e/n	σ [MPa]
Block (ring shaped)	15	0.171/0.849	0.56/0.359	0
Pellets I		0.1/0.156	1.78/0.64	
Pellets II		0.572/0.895	1.78/0.64	
Slot		35.6/1.0	99/0.99	

The initial conditions are given in terms of the temperature, T, the water ratio, w, (or the corresponding water saturation, S_l), the void ratio, e, (or the corresponding porosity, n), and the total stress tensor, $\boldsymbol{\sigma}$.

Material properties

Here follows a compact compilation of the material properties, the used constitutive laws together with the ingoing parameter values for the different materials, Table 3-8 to Table 3-13.

Table 3-8. Material properties.

Parameter	Block	Pellets	Slot
ρ_s [kg/m^3]	2 780		
c_s (J/(kg·K))	800		

Table 3-9. Constitutive law of conductive flux of heat and the adopted parameter values.

Constitutive law	Parameter	Block	Pellets	Slot
Conductive heat flux $\boldsymbol{i}_c = -\lambda \nabla T$ $\lambda = \lambda_{sat} S_l + \lambda_{dry}(1 - S_l)$	λ_{dry} [Wm/K] λ_{sat} [Wm/K]	0.7 1.3	0 1.3	0.04 0.6

Table 3-10. Retention constitutive law and adopted parameter values.

Constitutive law	Parameter	Block	Pellets	Slot
Retention behavior, Van Genuchten $S_l = \left(1 + \left(\frac{S}{p_0}\right)^{1/(1-\lambda)}\right)^{-\lambda}$ $S = p_g - p_l$ $p_0(n) = p_0(n = n_0)\exp[A(n_0 - n)]$	p_0 [MPa]	69.398	0.266	0.5
	λ	0.4	0.235	0.6

Table 3-11. Constitutive model with parameter values for the flow through the porous medium.

Constitutive law	Parameter	Block	Pellets	Slot
Flow through porous medium $\boldsymbol{q}_l = -\frac{k k_{rl}}{\mu_l} \boldsymbol{I} \nabla p_l$ $k = k_0 \frac{n^3}{(1-n)^2} \frac{(1-n_0)^2}{n_0^3}$ $k_{rl} = A S_l^{\lambda}$ $\mu_l = a \exp\left(\frac{b}{273.15+T} \right)$	k_0 [m^2]	$2 \cdot 10^{-21}$	$1.4 \cdot 10^{-19}$	$1 \cdot 10^{-11}$/$1 \cdot 10^{-50}$
	A	1		
	λ	3		
	a [MPa·s]	$2 \cdot 10^{-12}$		
	b [K]	1 808.5		

Table 3-12. Constitutive model and parameter values for the vapor diffusion.

Constitutive law	Parameter	Block	Pellets	Slot
Vapor diffusion $\boldsymbol{i}_g^w = -(n \rho_g S_g D_m^w) \nabla \omega_g^w$ $S_g = 1 - S_l$ $D_m^w = \tau D \frac{(273.15+T)^a}{p_g}$	D [m^2·Pa/(s·K^n)]	$5.9 \cdot 10^{-6}$		
	a	2.3		
	τ	1	1	$1/1 \cdot 10^{-10}$

When it comes to the mechanical constitutive laws, BBM has been used to model the bentonite block and pellet slot. The block material is modeled using both elasticity and plasticity and for the pellet slot only the elastic part of BBM is used. The inner slot has been modeled using linear elasticity where Young's modulus is altered from very small when the slot is open, to high when the slot is closed.

The BBM parameters were calibrated using the experimentally validated relation,

$$p_{swell}(e) = 2e^{-1/0.24}, \tag{3-12}$$

between the swelling pressure p_{swell} and the void ratio e. The relation (3-12) was developed from studying confined swelling pressure experiments. (3-12) is of course not valid for all deformation processes arriving at the same void ratio, but it has been found very useful. Two different basic processes were considered when calibrating the BBM parameters:

1. Confined wetting until full saturation (no change in void ratio), which should give a swelling pressure according to (3-12).
2. Simultaneous wetting and swelling from the initial void ratio to an assumed final void ratio corresponding to what was found in CRT should also give a swelling pressure obtained by (3-12)

The results of the calibration calculations are shown below in Figure 3-66 and Figure 3-67 for block and pellet slot material, respectively.

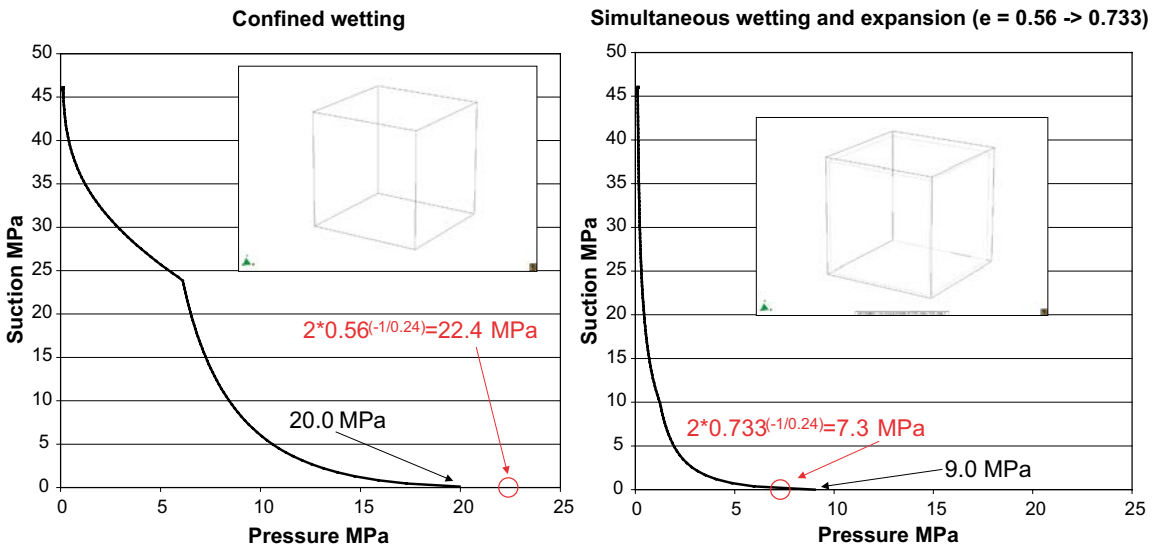

Figure 3-66. *Block material calibration calculation results.*

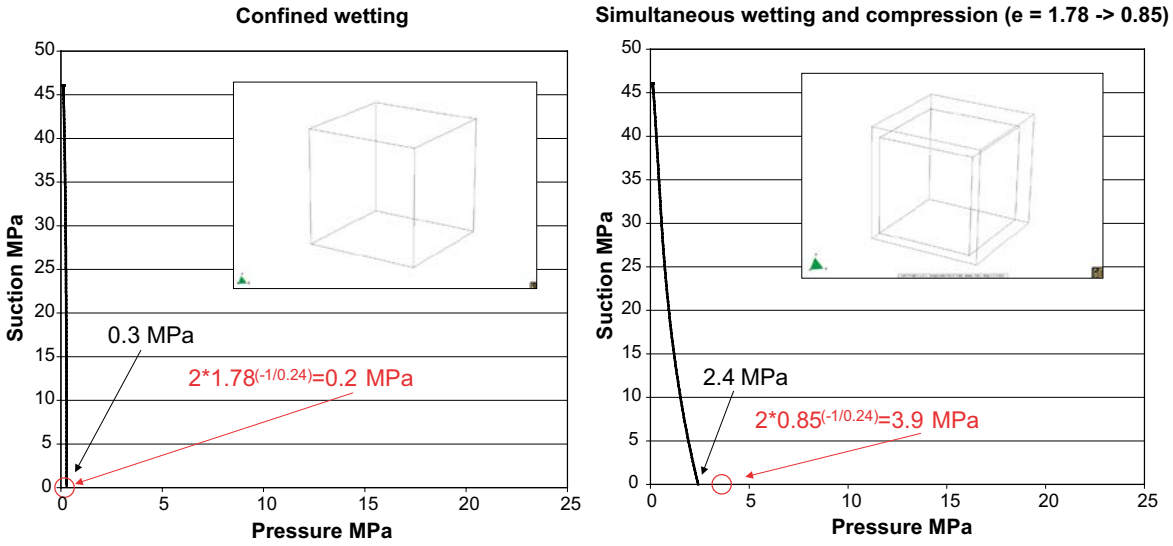

Figure 3-67. *Pellet slot material calibration calculation results.*

Table 3-13. "Elastic" part of BBM and parameter values.

Constitutive law	Parameter	Block	Pellets
"Elastic strain increment"	κ_{i0}	0.16	0.35
$d\boldsymbol{\varepsilon}^e = -1/3\, d\varepsilon_v^e \mathbf{1} + d\mathbf{e}^e$	α_i	0.001	0
$d\varepsilon_v^e = \frac{dp'}{K},\ K = \max\left\{\frac{(1+e)p'}{\kappa_i(s)}, K_{\min}\right\}$	α_{ils}	–0.164	0
	v	0.2	0.45
$\kappa_i(s) = \kappa_{i0}\left[1 + \alpha_i s + \alpha_{ils}\ln\left(\frac{s+0.1}{0.1}\right)\right]$	K_{min} [MPa]	10	3
$d\mathbf{e}^e = \frac{d\mathbf{s}}{2G},\ G = \frac{3(1-2\nu)}{2(1+\nu)}K$			

Table 3-14 “Plastic” part of BBM and parameter values.

Constitutive law	Parameter	Block	Pellets
“Plastic strain increment” $d\varepsilon^p = d\Lambda \frac{\partial g}{\partial \boldsymbol{\sigma}}$ $f = q^2 - M^2(p'+p_s)(p_0 - p') = 0$ $g = \alpha q^2 - M^2(p'+p_s)(p_0 - p')$ $p_s(s) = ks$ $p_0(s, p_0^*) = p^c \left(\frac{p_0^*}{p^c} \right)^{\frac{\lambda_0 - \kappa_{i0}}{\lambda(s) - \kappa_{i0}}}$ $\lambda(s) = \lambda_0((1-r)\exp(-\beta s) + r)$ $dp_0^* = \frac{1+e}{\lambda_0 - \kappa_{i0}} p_0^* d\varepsilon_v^p$	M	0.9	–
	α	0.5	–
	p_0^* [MPa]	0.8	–
	p_c	0.21	–
	λ_0	0.19	–
	r	0.05	–
	β	0.0036	–
	k	0.03	–

Table 3-15 “Hydraulic” part of BBM and parameter values.

Constitutive law	Parameter	Block	Pellets
“Hydraulic strain increment” $d\boldsymbol{\varepsilon}^h = -1/3\ d\varepsilon_v^h \boldsymbol{1}$ $d\varepsilon_v^h = \frac{\kappa_s(p')}{(1+e)(s+p_{atm})} ds$ $\kappa_s(p') = \max\left\{ \kappa_{s0}\left(1 + \alpha_{sp} \ln \frac{p'}{p_{ref}}\right), 0 \right\}$	κ_{s0}	0.16	0.2
	α_{sp}	–0.165	–1.622
	p_{ref} [MPa]	0.1	0.1

As mentioned before the inner slot is modeled using linear elasticity where the Young’s modulus is changed dependent on if the slot is open or closed. The constitutive law can be formulated as,

$\boldsymbol{\sigma} = \boldsymbol{D\varepsilon}$

where $\boldsymbol{D}$ is the elastic stiffness tensor, defined by

$$\boldsymbol{D} = \frac{E}{1+\nu}\left(\frac{1}{2}\boldsymbol{1} \otimes \boldsymbol{1} + \frac{\nu}{1-2\nu}\mathbf{I}\right) \tag{3-13}$$

where E is the Young’s modulus and ν is the Poisson’s ratio, $\boldsymbol{1}$ is the second order unit tensor and $\mathbf{I}$ the forth order unit tensor. The value $\nu = 0.2$ is used in the model and

$$E = \begin{cases} 1 \cdot 10^{-3} \\ 1.1 \quad \text{MPa} \\ 1 \cdot 10^{6} \end{cases} \tag{3-14}$$

The small value of E is used when the slot is open, the mid value is used to accomplish a total and the larger value is used when the slot is closed.

Boundary conditions

To complete the model description thermal, hydraulic and mechanical boundary conditions have to be specified. In Figure 3-68 a schematic graphical overview is given of the boundary conditions prescribed in the model.

In the following list the variables defining the boundary conditions are declared.

- Thermally: The evolutions of heat flux, q, and temperature, T, are obtained from studying the solution of sub-task 1.
- Hydraulically: The evolution of liquid pressure, p_l, is obtained from the filter pressure protocol. The leakage coefficient, γ, is set high to prescribe the liquid pressure.
- Mechanically: u_i is the displacement in the i-direction, where $i = x$ or y, and t_i is the traction component in the i-direction. If unit vectors $\boldsymbol{e}_n$ and $\boldsymbol{e}_t$ are introduced, denoting unit vectors in the normal and tangential direction of the boundary surface respectively, the boundary conditions can be expressed $\boldsymbol{e}_n \cdot \boldsymbol{u} = 0$ and $\boldsymbol{e}_t \cdot \boldsymbol{t} = 0$.

Investigations

Comparison of suction responses for TH and THM

Two identical models except for not including the mechanical part in one of them were used. Below in Figure 3-69, Figure 3-70 and Figure 3-71 the suction evolution at r = 585, 685 and 785 mm are shown. Excluding the mechanics results in a more rapid saturation process, most visible at r = 585 mm.

In Figure 3-72 the method used for studying the origin of the difference is described. The different contributions were identified by expanding an expression of the suction rate. Three terms were found for the THM model: a water mass rate term (the rate of which water is entering the volume element considered), a water density rate term (taken as dependent on water pressure and temperature in CODE_BRIGHT) and a void ratio rate term (which equals the rate of which the pore volume in the volume element considered is changing) of which the last term is not present for the TH model.

In Figure 3-73 the evolution of suction rate and the three contributing terms are given for the TH and THM model up to day 500.

The contribution from density rate term is very similar for the TH and THM model except for the spikes at day 375–400 which concur with the first heater shutdown. Thus, neglecting the effect from heater shutdown, the density rate contribution can be disregarded when searching for the origin of the difference in suction evolution.

On the other hand, when comparing the water mass rate, there is a significant difference in the evolution for the TH and THM model. It can therefore be concluded that the mechanics has a significant effect on the water saturation process. Including the mechanics does not only mean that another term is added to the suction rate as compared to the TH model. The water mass rate term has a strong coupling to the mechanics and its' evolution undergoes significant changes due to the presence of the mechanics. This comes from the change in available volume for the water due to swelling/compression of the considered volume element.

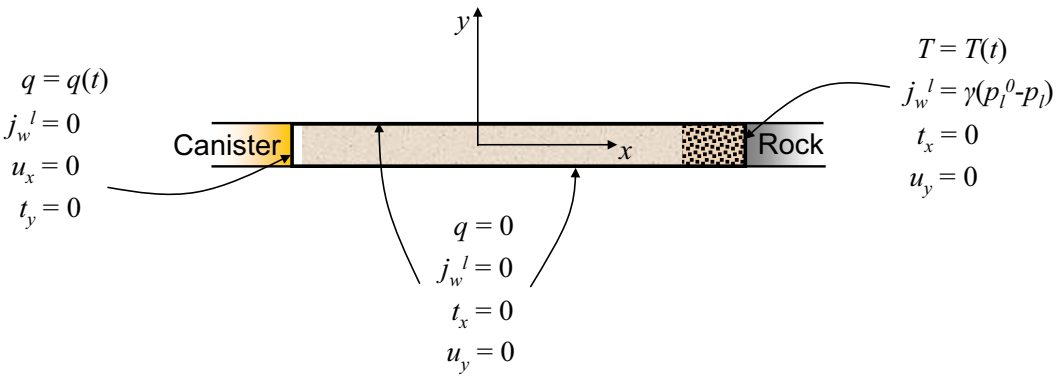

Figure 3-68. *Schematic geometry with the prescribed boundary conditions.*

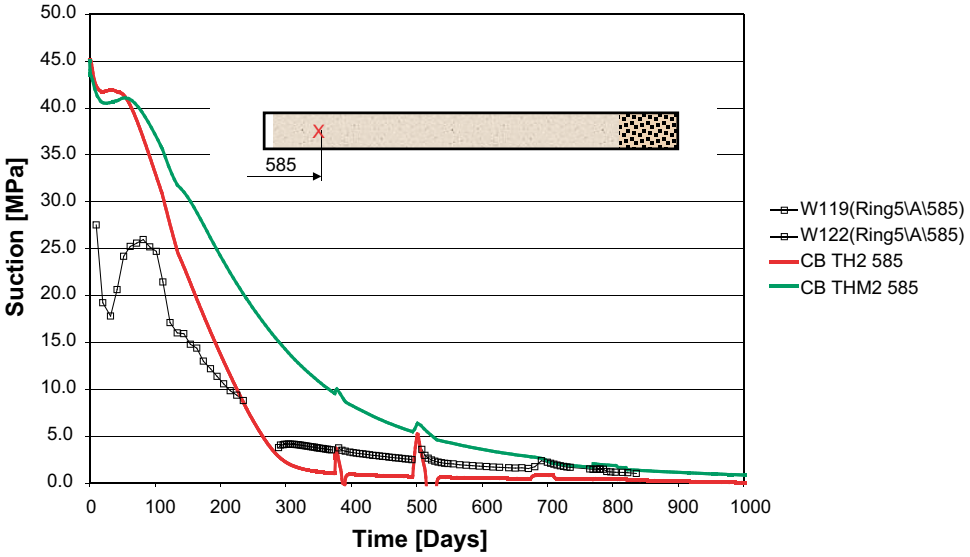

Figure 3-69. *Suction evolutions for TH and THM at r = 585 mm.*

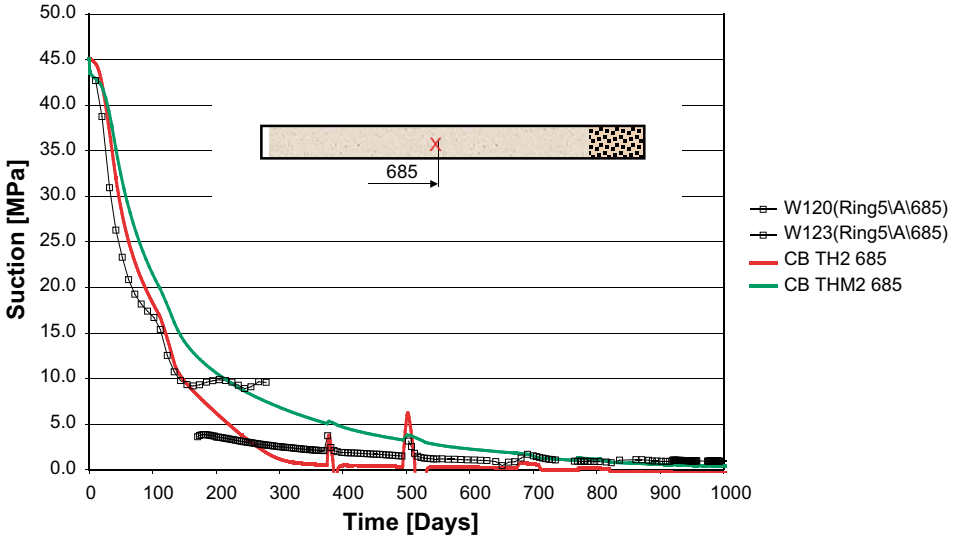

Figure 3-70. *Suction evolutions for TH and THM at r = 685 mm.*

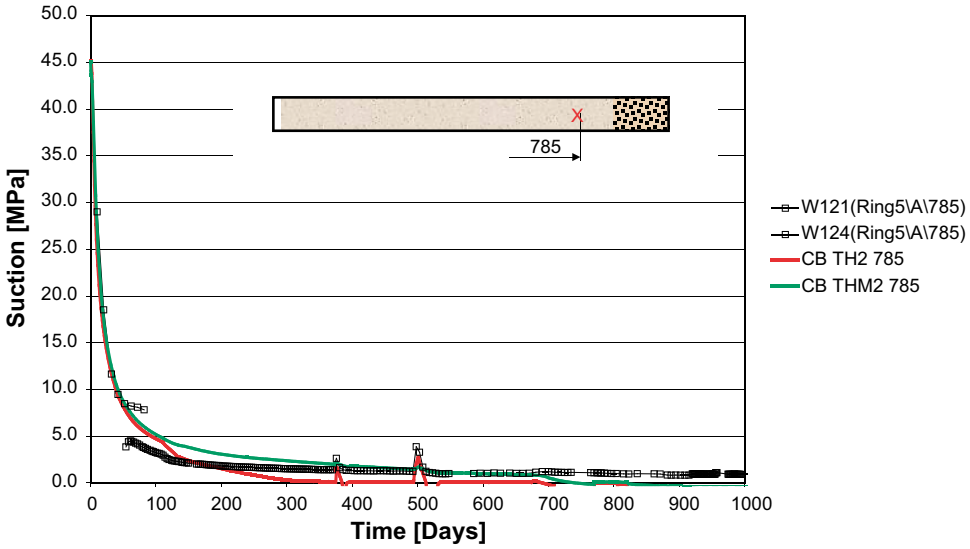

Figure 3-71. *Suction evolutions for TH and THM at r = 785 mm.*

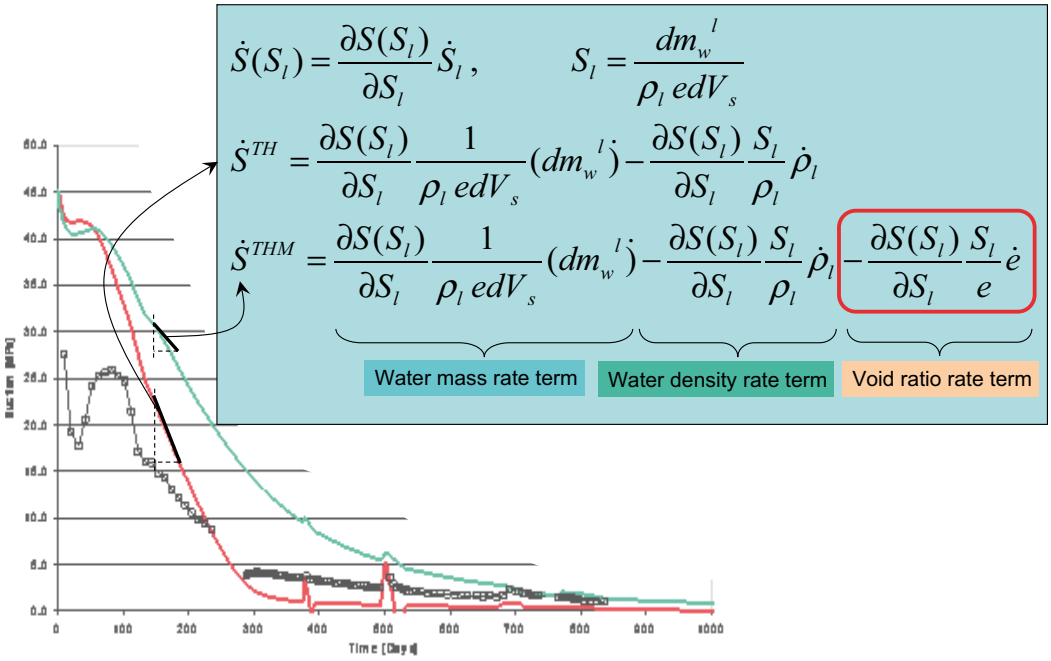

Figure 3-72. Origin of the difference in suction evolutions for the TH-model and THM-model is studied by evaluating the contributions to the suction rates.

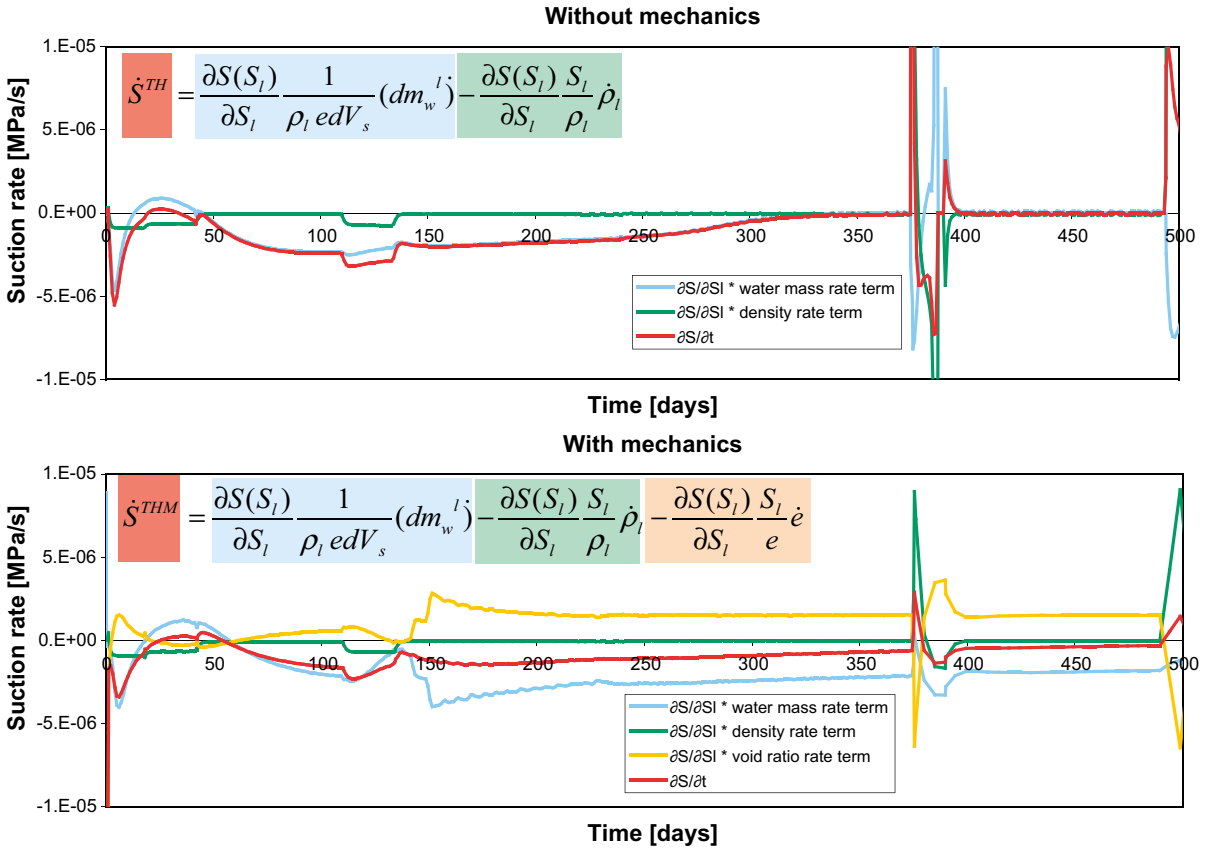

Figure 3-73. Evolution of the contributions to the suction rates for the TH-model and THM-model.

Effect from lowered retention curve (TH)

In Table 3-16 the retention law and the parameter sets adopted for the old and new retention representations shown in Figure 3-74 are presented. The new retention curve is obtained by fitting the relation to a retention model based on experimentally motivated expressions for the retention under unconfined (free) conditions and thermodynamically motivated retention relations for confined conditions.

To study what difference that is to be expected using this new retention curve the derivative of the old and new retention curves are plotted in Figure 3-75. If a pure wetting process is assumed from the initial state ($S_l = 0.85$) it can be seen that initially the new retention produces more decrease in suction for given S_l and dS_l. At $S_l = 0.944$ the derivatives become equal and for degrees of saturation larger than this value the new retention produces less decrease in suction for given S_l and dS_l.

When studying the suction evolutions at r = 585, 685 and 785 mm given in Figure 3-76, Figure 3-77 and Figure 3-78 the simplified analysis above seems to be correct. Initially the new retention produces faster decrease in suction but for lower suction values the decrease slows down as compared to the responses obtained using the old retention curve.

Table 3-16 Retention law and parameters.

Constitutive law	Parameter	Block	Pellets	Slot
Retention behavior, Van Genuchten $S_l = \left(1 + \left(\frac{S}{p_0}\right)^{1/(1-\lambda)}\right)^{-\lambda}$	p_0 [MPa]	69.398 38.161	0.266	0.5
	λ	0.4 0.2	0.235	0.6
$S = p_g - p_l$				

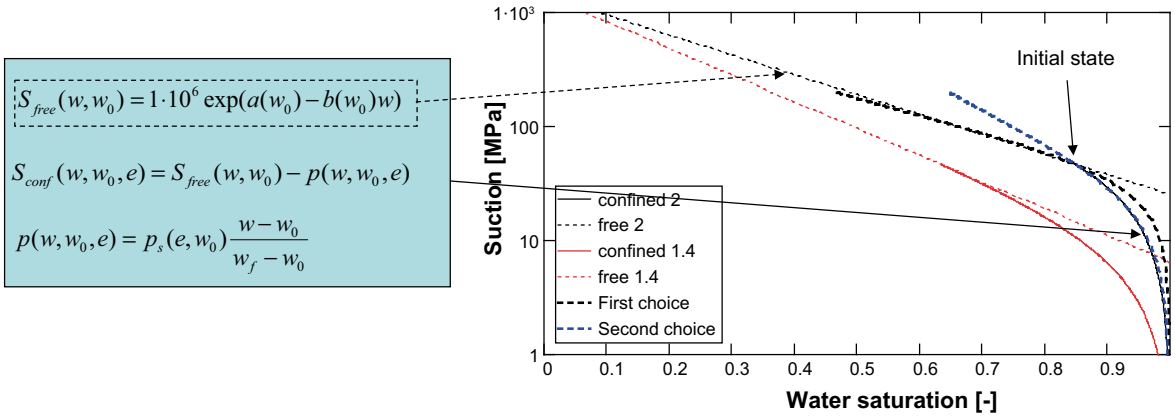

Figure 3-74. *The old and the new Van Genuchten retention curve together with experimentally motivated free retention relations which are used in thermodynamically motivated retention models for confined conditions.*

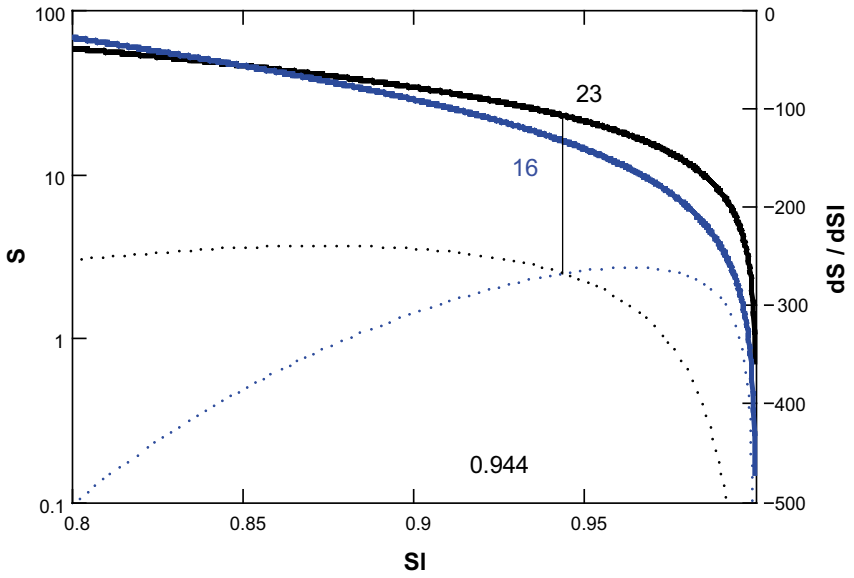

At S_l > 0.944 the inclination of the lower retention curve become less as compared with the higher curve.

With a somewhat simplified reasoning the suction decrease can therefore be expected to become slower above this saturation value.

Figure 3-75. *Old and new retention curve and their derivatives.*

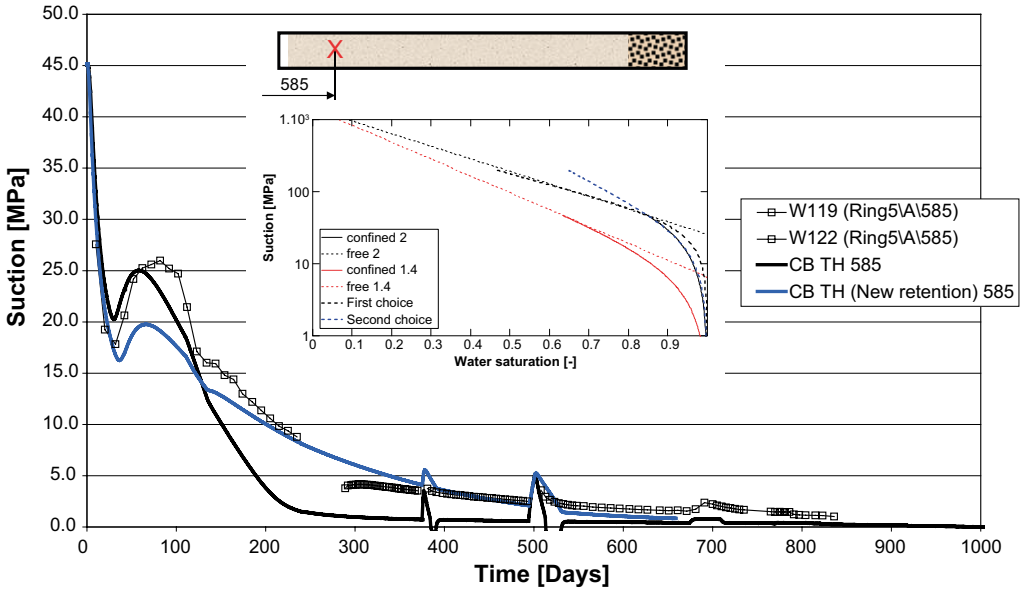

Figure 3-76. *Suction evolutions at r = 585 mm using the old and new retention curve.*

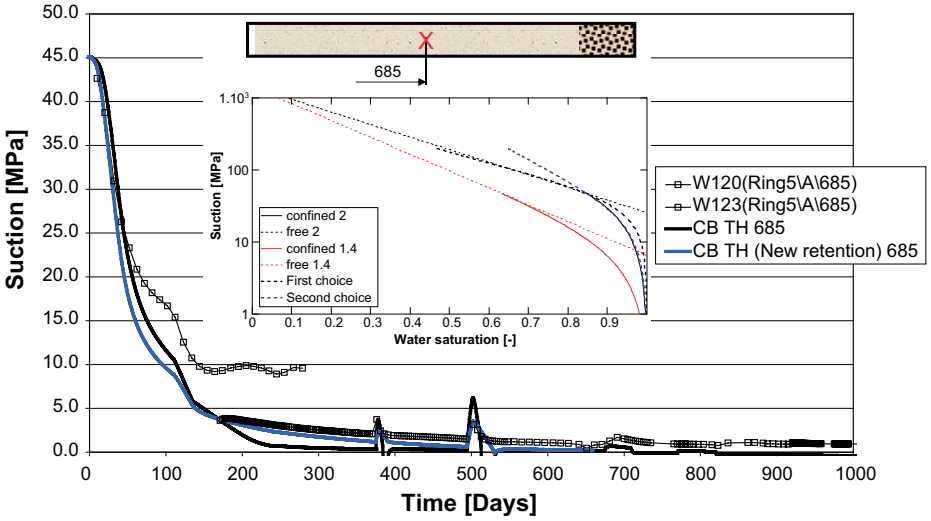

Figure 3-77. *Suction evolutions at r = 685 mm using the old and new retention curve.*

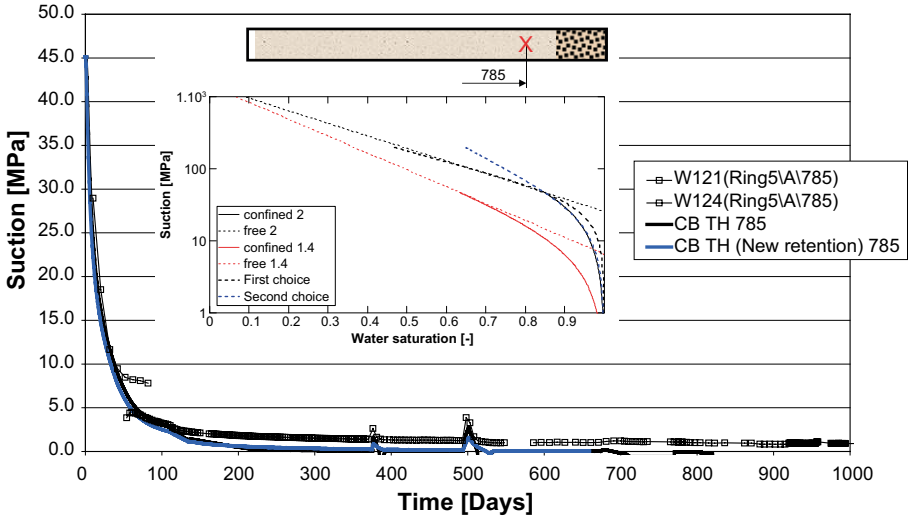

Figure 3-78. *Suction evolutions at r = 785 mm using the old and new retention curve.*

Effect from porosity dependent retention (THM)

In Table 3-17 the retention law and the parameter sets, $\{p_0, \lambda\}$ and $\{p_0, \lambda, A\}$, adopted for the retention representations independent and dependent on porosity, respectively, are presented. The graphs in Figure 3-79 show how the porosity dependence parameter A has been calibrated.

Figure 3-80, Figure 3-81 and Figure 3-82 show the suction evolutions obtained at r = 585, 685 and 785 mm, respectively, for both retention alternatives. The porosity dependence generates significantly lower suction rates compared to the independent relation. The "effective" retention curves the model attains at $r = r$ = 585, 685 and 785 mm during the simulation are plotted in Figure 3-83.

Table 3-17 Retention laws and parameters.

Constitutive law	Parameter	Block
Retention behavior, Van Genuchten $S_l = \left(1 + \left(\frac{S}{p_0}\right)^{1/(1-\lambda)}\right)^{-\lambda}$ $S = p_g - p_l$ $p_0(n) = p_0(n = n_0)\exp[A(n_0 - n)]$	$p_0(n = n_0)$ [MPa] A λ	38.161 20.33 0.2

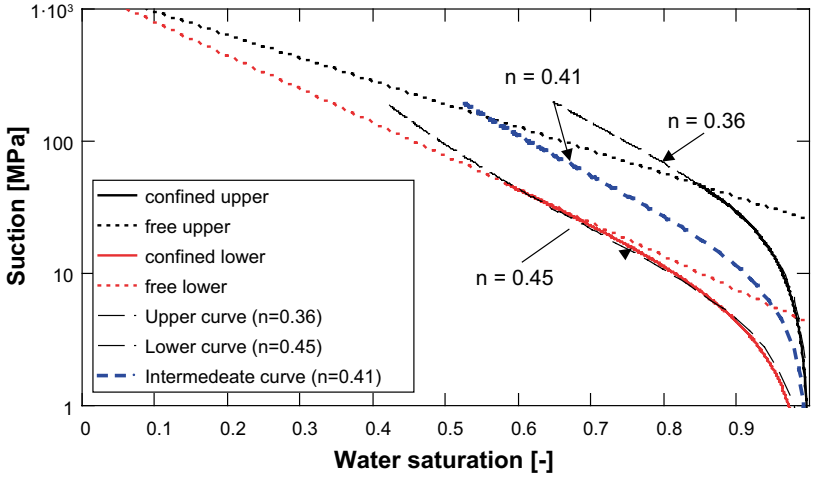

Figure 3-79. *Porosity dependent retention model for three different porosities.*

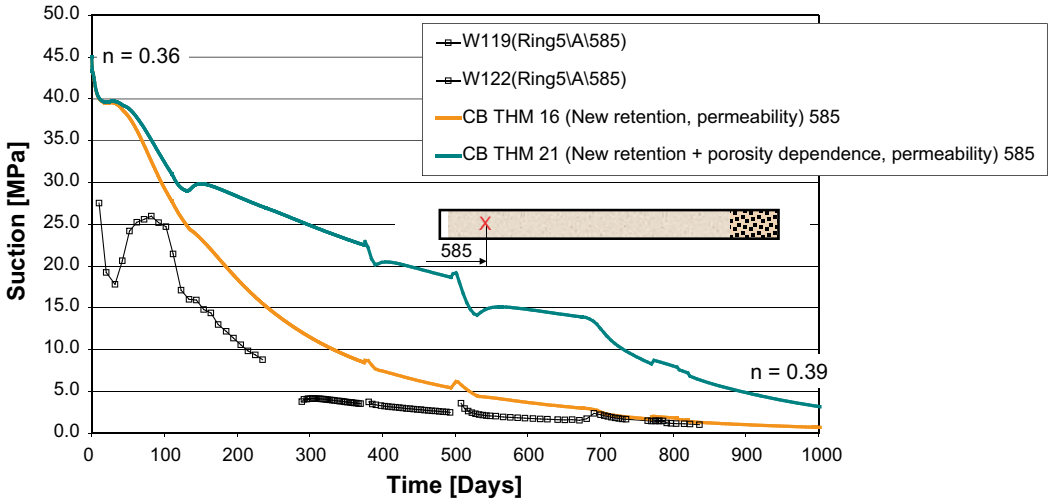

Figure 3-80. *Suction evolutions at r = 585 mm using the different retention curves.*

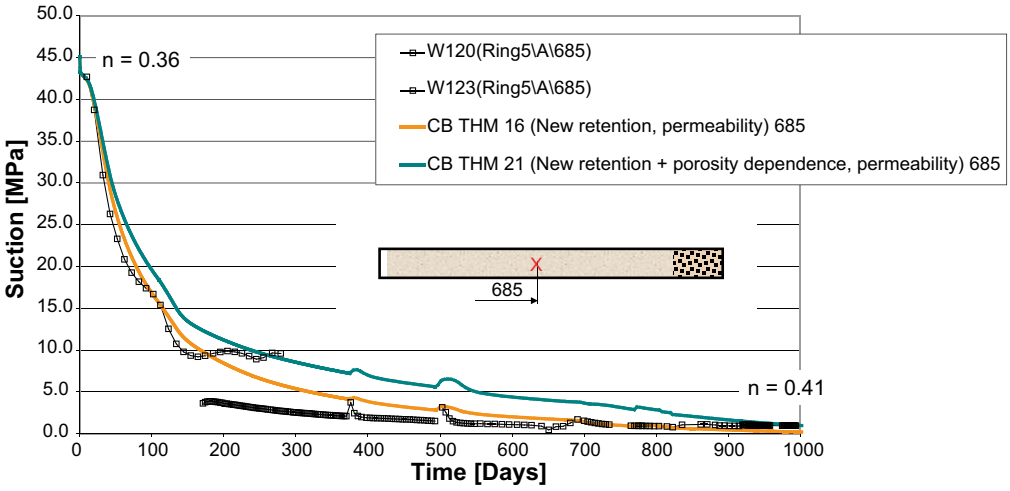

Figure 3-81. *Suction evolutions at r = 685 mm using the different retention curves.*

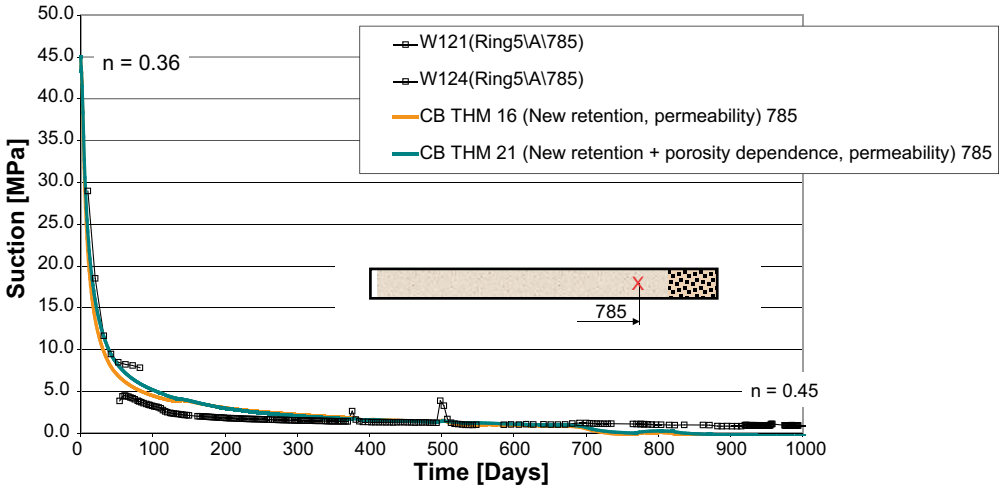

Figure 3-82. *Suction evolutions at r = 785 mm using the different retention curves.*

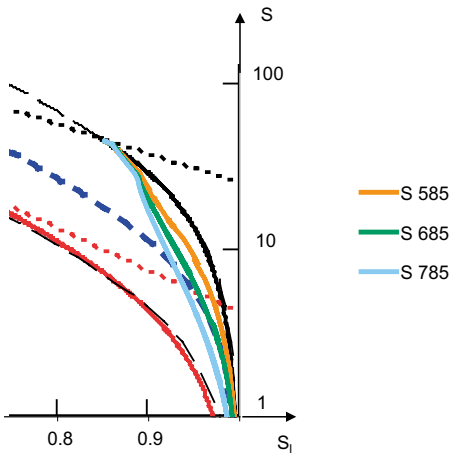

Figure 3-83. *"Effective" retention curves used in the porosity dependent retention model at r = 585, 685 and 785 mm.*

Effect from increased intrinsic permeability (TH)

Table 3-18 shows the relations and parameters used for modeling advective water flow. The permeability is increased to fit better to an expression (denoted TR-95-20 in the forthcoming) in good agreement with experimental data. This can be seen in Figure 3-84 where hydraulic conductivity are given as a function of void ratio and where the active void ratio range is indicated. The originally adopted permeability was fitted to TR-95-20 for the initial state of the buffer whereas the new permeability is more "correct" in an overall sense for the given void ratio range.

The results obtained at r = 585, 685 and 785 mm from using the two different permeability are shown in Figure 3-85, Figure 3-86 and Figure 3-87, respectively. Significant speedup of the decrease in suction is obtained for the higher permeability.

Table 3-18 Law for liquid flow and parameters.

Constitutive law	Parameter	Block
Flow through porous medium	k_0 [m^2]	(A) $2\cdot10^{-21}$ (B) $3\cdot10^{-21}$
$\boldsymbol{q}_l = -\frac{kk_{rl}}{\mu_l}\boldsymbol{I}\nabla p_l$	A	1
	λ	3
$k = k_0 \frac{n^3}{(1-n)^2}\frac{(1-n_0)^2}{n_0^3}$	a [MPa·s]	$2\cdot10^{-12}$
	b [K]	1 808.5
$k_{rl} = AS_l^{\lambda}$		
$\mu_l = a\exp\left(\frac{b}{273.15+T}\right)$		

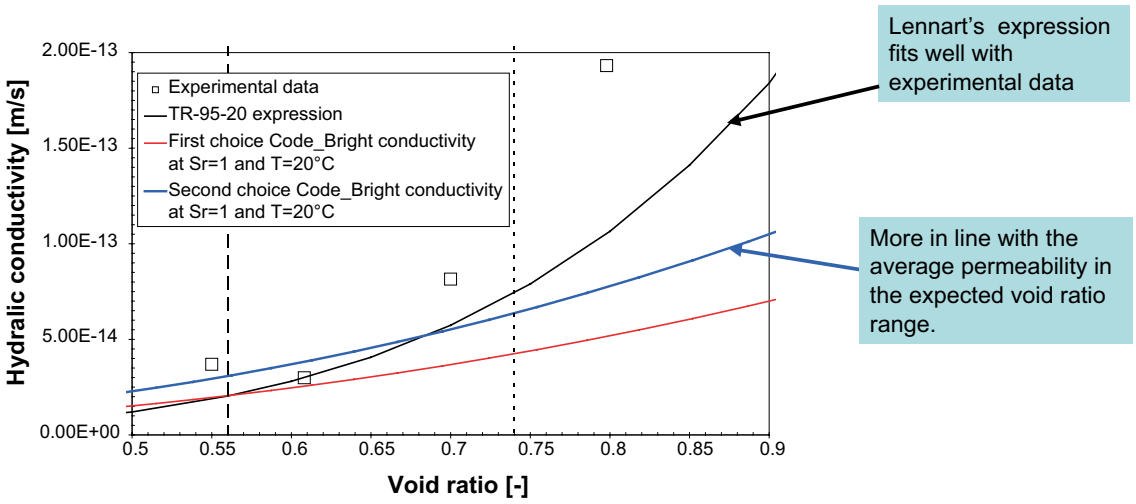

Figure 3-84. *Intrinsic permeability expressions.*

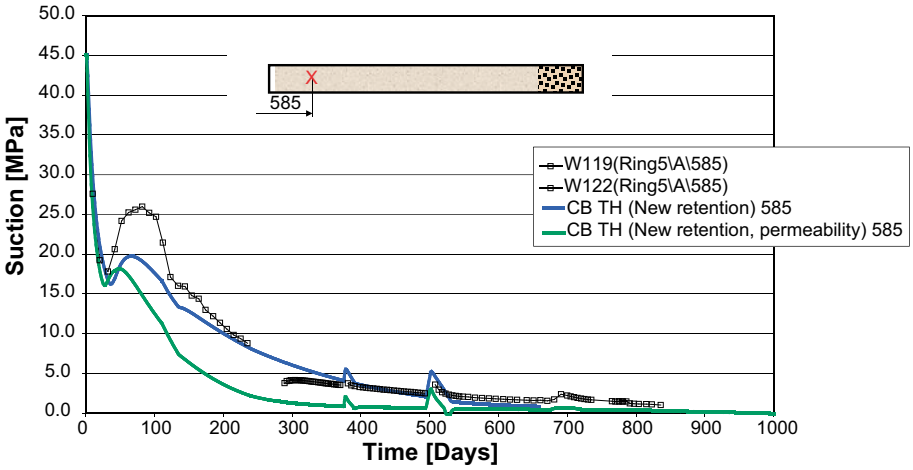

Figure 3-85. *Suction evolution at r = 585 mm when using the different intrinsic permeability.*

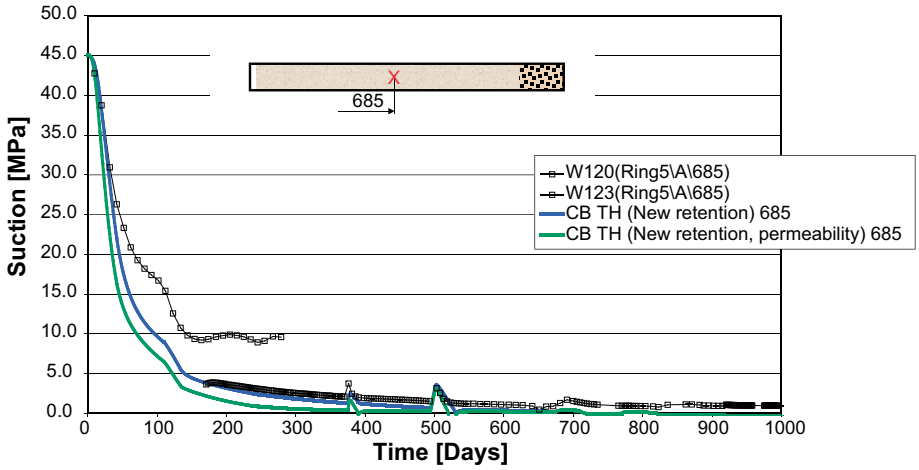

Figure 3-86. *Suction evolution at r = 685 mm when using the different intrinsic permeability.*

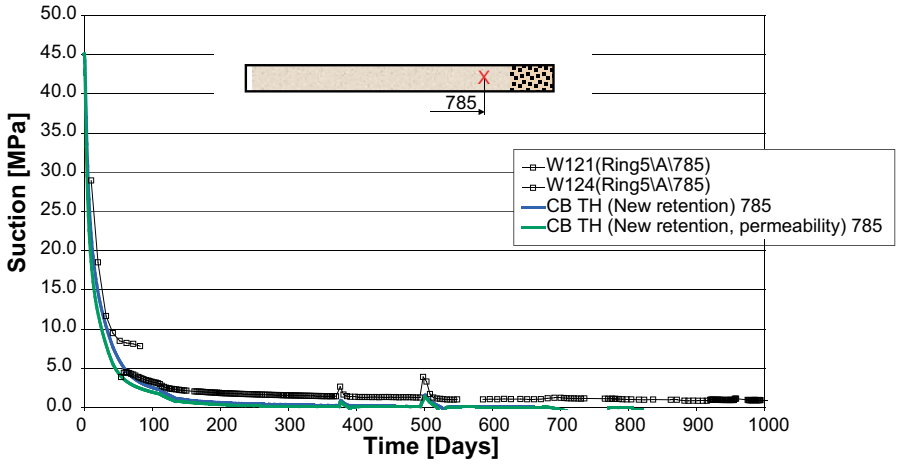

Figure 3-87. *Suction evolution at r = 785 mm when using the different intrinsic permeability.*

Effect from using different porosity dependency of the permeability (THM)

Table 3-19 contains the relations and parameters used for modeling advective water flow. Two different relations describing the porosity dependence (Kozeny and Exponential) are given in Table 3-19. Kozeny has been used in the previous investigations and now the Exponential model will be investigated. In Figure 3-88 the two CODE_BRIGHT models are plotted together with TR-95-20 and the active void ratio range is also indicated. The Exponential model has been fitted against TR-95-20 and as can be seen they match well. To have a comparison where the porosity dependence is singled out as much as possible, the Kozeny model is fitted to TR-95-20 in an average sense.

Figure 3-89, Figure 3-90 and Figure 3-91 show the results obtained at r = 585, 685 and 785 mm from using the two different porosity dependencies. A slight difference in suction evolution can be seen, where it generally takes longer time for the Kozeny-model to produce the same change in suction as compared to the Exponential model. This effect is however slight and the difference must be said to be insignificant for the process considered.

Table 3-19 Laws for liquid flow and parameters.

Constitutive law	Parameter	Block
Flow through porous medium $\boldsymbol{q}_l = -\frac{k k_{rl}}{\mu_l} \boldsymbol{I} \nabla p_l$ $k = k_0 \frac{n^3}{(1-n)^2} \frac{(1-n_0)^2}{n_0^3}$: Kozeny [(A)] $k = k_0 \exp(B(n-n_0))$: Exponential [(B)] $k_{rl} = A S_l^{\lambda}$ $\mu_l = a \exp\left(\frac{b}{273.15+T}\right)$	k_0 [m^2]	[(A)] $3 \cdot 10^{-21}$ [(B)] $2.04 \cdot 10^{-21}$
	A	1
	λ	3
	a [MPa·s]	$2 \cdot 10^{-12}$
	b [K]	1 808.5
	B	[(A)] – [(B)] 19

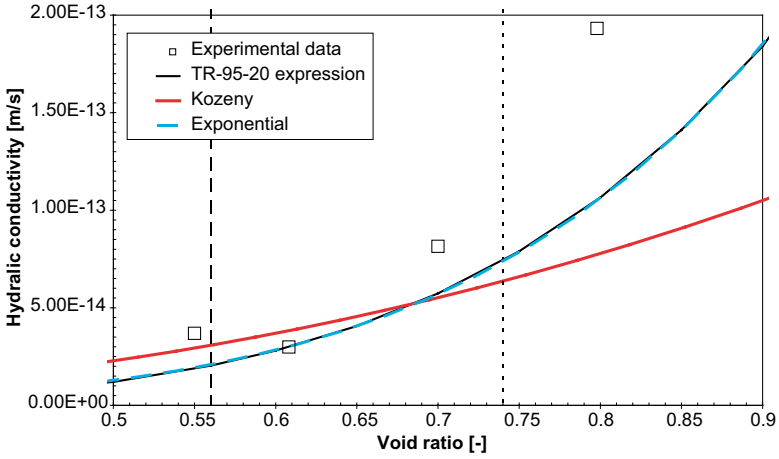

Figure 3-88. *Relations obtained for the different porosity dependency of intrinsic permeability.*

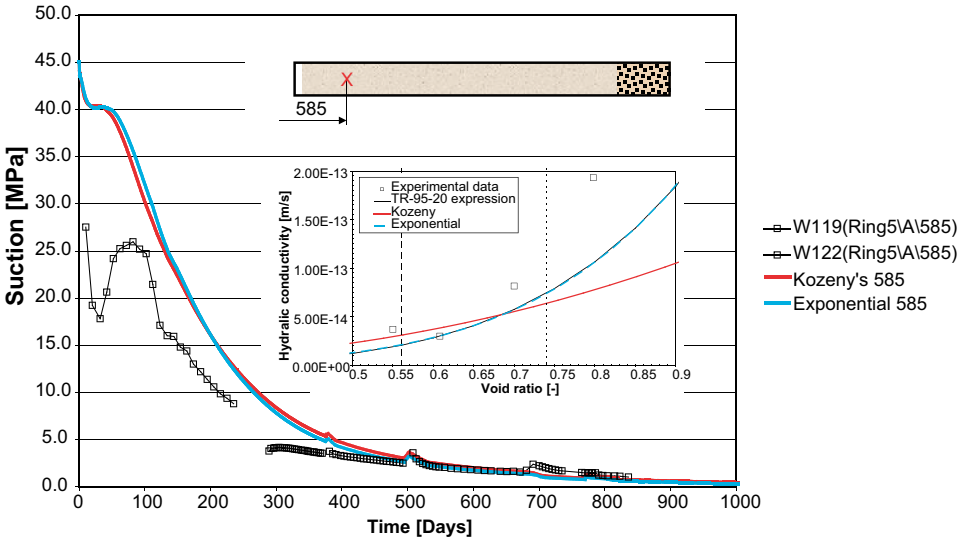

Figure 3-89. *Suction evolution at r = 585 mm when using the different porosity dependencies of intrinsic permeability.*

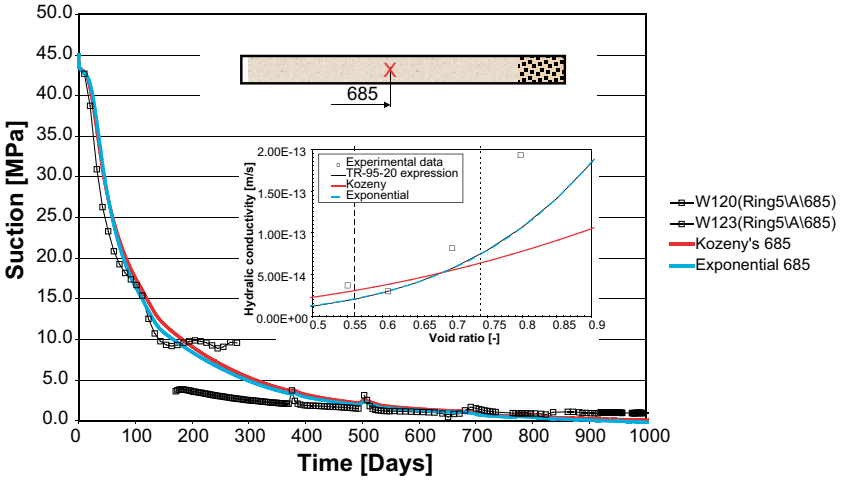

Figure 3-90. *Suction evolution at r = 685 mm when using the different porosity dependencies of intrinsic permeability.*

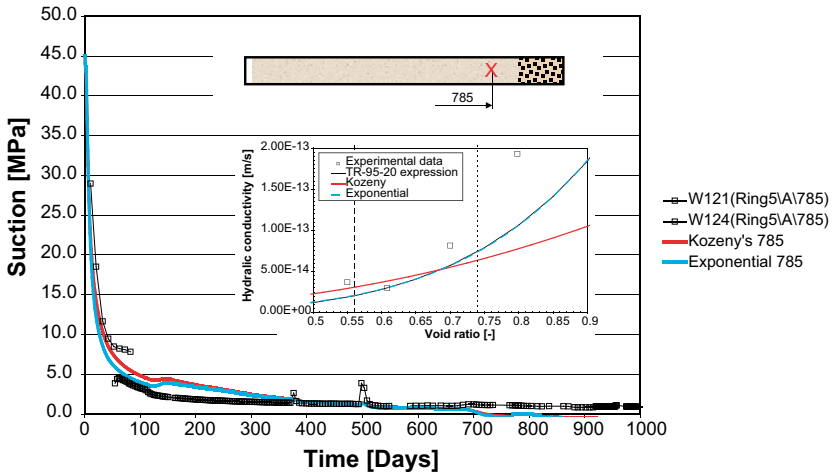

Figure 3-91. *Suction evolution at r = 785 mm when using the different porosity dependencies of intrinsic permeability.*

3.4 Modelling results with Abaqus

3.4.1 Introduction

SKB uses two codes for numerical simulation of the wetting and homogenisation processes in a KBS-3 repository. The modelling is made by two different modelling groups. The results presented in this section are derived by the group SKB 2, which consists of Lennart Börgesson, Clay Technology AB and Jan Hernelind 5T-Engineering AB. This group uses the code Abaqus for the modelling.

Section 3.4 includes two appendices: Appendix 6 Generation of retention curves for the three bentonite block types in CRT and Appendix 7 Results of the 2D-calculation.

3.4.2 Finite element code Abaqus

General

The finite element code ABAQUS was used for the calculations. ABAQUS contains a capability of modelling a large range of processes in many different materials as well as complicated three-dimensional geometry.

The code includes special material models for rock and soil and ability to model geological formations with infinite boundaries and in situ stresses by e.g. the own weight of the medium. It also includes capability to make substructures with completely different finite element meshes and mesh density without connecting all nodes. This technique has been used in the modelling of CRT. Detailed information of the available models, application of the code and the theoretical background is given in the ABAQUS Manuals (2008).

Hydro-mechanical analyses in ABAQUS

The hydro-mechanical model consists of porous medium and wetting fluid and is based on equilibrium, constitutive equations, energy balance and mass conservation using the effective stress theory.

Equilibrium

Equilibrium is expressed by writing the principle of virtual work for the volume under consideration in its current configuration at time *t*:

$$\int_V \boldsymbol{\sigma} : \delta\boldsymbol{\varepsilon}\, dV = \int_S \mathbf{t}\cdot\delta\mathbf{v}\, dS + \int_V \hat{\mathbf{f}}\cdot\delta\mathbf{v}\, dV \tag{3-15}$$

where $\delta\mathbf{v}$ is a virtual velocity field, $\delta\varepsilon^{def} = sym(\partial\delta v/\partial x)$ is the virtual rate of deformation, σ is the true (Cauchy) stress, **t** are the surface tractions per unit area, and **f** are body forces per unit volume. For our system, **f** will often include the weight of the wetting liquid,

$$\mathbf{f}_w = S_r n \rho_w \mathbf{g}, \tag{3-16}$$

where S_r is the degree of saturation, n the porosity, ρ_w the density of the wetting liquid and **g** is the gravitational acceleration, which we assume to be constant and in a constant direction (so that, for example, the formulation cannot be applied directly to a centrifuge experiment unless the model in the machine is small enough that g can be treated as constant). For simplicity we consider this loading explicitly so that any other gravitational term in **f** is only associated with the weight of the dry porous medium. Thus, we write the virtual work equation as

$$\int_V \boldsymbol{\sigma} : \delta\boldsymbol{\varepsilon}\, dV = \int_s \mathbf{t}\cdot\delta\mathbf{v} dS + \int_V \mathbf{f}\cdot\delta\mathbf{v} dV + \int_V S_r n \rho_w \mathbf{g}\cdot\delta\mathbf{v} dV, \tag{3-17}$$

where **f** are all body forces except the weight of the wetting liquid.

The simplified equation used in ABAQUS for the effective stress is:

$$\bar{\boldsymbol{\sigma}}^* = \boldsymbol{\sigma} + \chi\, u_w \mathbf{I}. \tag{3-18}$$

where σ is the total stress, u_w is the pore water pressure, χ is a function of the degree of saturation (usual assumption $\chi = S_r$), and **I** the unitary matrix.

Energy balance

The conservation of energy implied by the first law of thermodynamics states that the time rate of change of kinetic energy and internal energy for a fixed body of material is equal to the sum of the rate of work done by the surface and body forces. This can be expressed as (not considering the thermal part, which is solved as uncoupled heat transfer; cf Equation 3-29):

$$\frac{\mathrm{d}}{\mathrm{dt}}\int_{\mathrm{V}}\left(\tfrac{1}{2}\rho\mathbf{v}\cdot\mathbf{v}+\rho\mathrm{U}\right)\mathrm{dV}=\int_{\mathrm{s}}\mathbf{v}\cdot\mathbf{t}\mathrm{dS}+\int_{\mathrm{V}}\mathbf{f}\cdot\mathbf{v}\mathrm{dV} \tag{3-19}$$

where

ρ is the current density,

v is the velocity field vector,

U is the internal energy per unit mass,

t is the surface traction vector,

f is the body force vector

Constitutive equations

The constitutive equation for the solid is expressed as:

$$d\boldsymbol{\tau}^{\mathrm{c}}=\mathbf{H}:d\boldsymbol{\varepsilon}+\mathbf{g}, \tag{3-20}$$

where $d\tau^c$ is the stress increment, **H** the material stiffness, $d\varepsilon$ the strain increment and **g** is any strain independent contribution (e.g. thermal expansion). **H** and **g** are defined in terms of the current state, direction for straining, etc., and of the kinematic assumptions used to form the generalised strains.

The constitutive equation for the liquid (static) in the porous medium is expressed as:

$$\frac{\rho_{\mathrm{w}}}{\rho_{\mathrm{w}}^{0}}\approx 1+\frac{\mathrm{u}_{\mathrm{w}}}{\mathrm{K}_{\mathrm{w}}}-\varepsilon_{\mathrm{w}}^{\mathrm{th}}, \tag{3-21}$$

where ρ_w is the density of the liquid, ρ_w^0 is its density in the reference configuration, $K_w(T)$ is the liquid's bulk modulus, and

$$\varepsilon_w^{th}=3\alpha_w(T-T_w^0)-3\alpha_{w|T^I}(T^I-T_w^0) \tag{3-22}$$

is the volumetric expansion of the liquid caused by temperature change. Here $\alpha_w(T)$ is the liquid's thermal expansion coefficient, T is the current temperature, T^I is the initial temperature at this point in the medium, and T_w^0 is the reference temperature for the thermal expansion. Both u_w/K_w and ε_w are assumed to be small.

Mass conservation

The mass continuity equation for the fluid combined with the divergence theorem implies the pointwise equation:

$$\frac{1}{J}\frac{d}{dt}(J\rho_{\mathrm{w}}S_r n)+\frac{\partial}{\partial\mathbf{x}}\cdot(\rho_{\mathrm{w}}S_r n\mathbf{v}_{\mathrm{w}})=0. \tag{3-23}$$

where J is the determinant of the Jacobian matrix of the skeleton motion and **x** is position. The constitutive behaviour for pore fluid is governed by Darcy's law, which is generally applicable to low fluid velocities. Darcy's law states that, under uniform conditions, the volumetric flow rate of the wetting liquid through a unit area of the medium, $S_r n\mathbf{v}_w$, is proportional to the negative of the gradient of the piezometric head:

$$S_r n \mathbf{v}_w = -\hat{\mathbf{k}} \frac{\partial \phi}{\partial \mathbf{x},} \tag{3-24}$$

where $\hat{\mathbf{k}}$ is the permeability of the medium and ϕ is the piezometric head, defined as:

$$\phi \overset{def}{=} z + \frac{u_w}{g\rho_w} \tag{3-25}$$

where z is the elevation above some datum and g is the magnitude of the gravitational acceleration, which acts in the direction opposite to z. $\hat{\mathbf{k}}$ can be anisotropic and is a function of the saturation and void ratio of the material. **k** has units of velocity (length/time). [Some authors refer to **k** as the hydraulic conductivity and define the permeability as

$$\hat{\mathbf{K}} = \frac{\nu}{g}\hat{\mathbf{k}} \tag{3-26}$$

where ν is the kinematic viscosity of the fluid.]

We assume that g is constant in magnitude and direction, so

$$\frac{\partial \phi}{\partial \mathbf{x}} = \frac{1}{g\rho_w}\left(\frac{\partial u_w}{\partial \mathbf{x}} - \rho_w \mathbf{g}\right) \tag{3-27}$$

Vapour flow

Vapour flow is modelled as a diffusion process driven by a temperature gradient (coded as UEL user supplied routine with stiffness and flow).

$$\mathbf{q}_v = -D_{Tv}\frac{\partial T}{\partial \mathbf{x}} \tag{3-28}$$

where $\mathbf{q}_v$ is the vapour flux and D_{Tv} the thermal vapour diffusivity.

Uncoupled heat transfer analysis

Energy balance

The basic energy balance is (neglecting mechanical contribution; cf. Equation 3-19)

$$\int_V \rho \dot{U} dV = \int_S q dS + \int_V r dV \tag{3-29}$$

where V is a volume of solid material, with surface area S; ρ is the density of the material; $\dot{U}$ is the material time rate of the internal energy; q is the heat flux per unit area of the body, flowing into the body; and r is the heat supplied externally into the body per unit volume.

It is assumed that the thermal and mechanical problems are uncoupled in the sense that $U = U(T)$ only, where T is the temperature of the material, and q and r do not depend on the strains or displacements of the body. For simplicity a Lagrangian description is assumed, so "volume" and "surface" mean the volume and surface in the reference configuration.

Constitutive definition

The relationship is usually written in terms of a specific heat, neglecting coupling between mechanical and thermal problems:

$$c(T) = \frac{dU}{dT}, \tag{3-30}$$

Heat conduction is assumed to be governed by the Fourier law.

$$\mathbf{f}_q = -\mathbf{k}\frac{\partial T}{\partial \mathbf{x}} \tag{3-31}$$

where $\mathbf{f}_q$ is the heat flux and $\mathbf{k}$ is the heat conductivity matrix, $\mathbf{k} = \mathbf{k}(T)$. The conductivity can be fully anisotropic, orthotropic, or isotropic.

Coupling of thermal and hydro-mechanical solutions

In ABAQUS the coupled problem is solved through a "staggered solution technique" as sketched in Figure 3-92 below.

1. First a thermal analysis is performed where heat conductivity and specific heat are defined as functions of saturation and water content. In the first analysis these parameters are assumed to be constant and in the subsequent analyses they are read from an external file.
2. The hydromechanical model calculates stresses, pore pressures, void ratios, degree of saturation etc. as function of time. Saturation and void ratio histories are written onto an external file.
3. The material parameters update module reads the file with saturation and void ratio data and creates a new file containing histories for saturation and water content.
4. The saturation and water content histories are used by the thermal model in the following analysis.
5. Steps 1–3 are repeated if parameter values are found to be different compared to those of the previous solution.

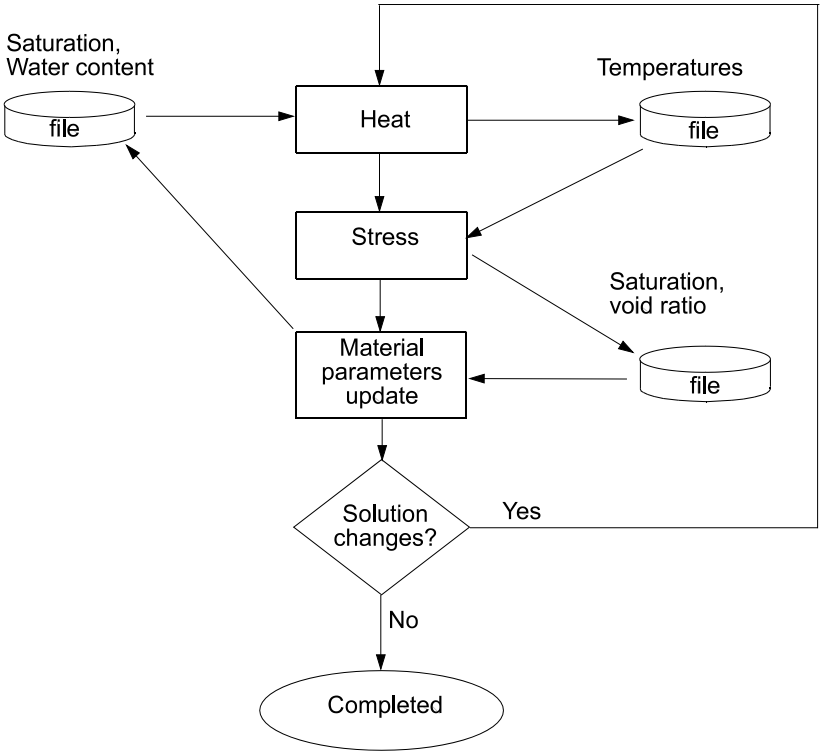

Figure 3-92. *In ABAQUS, heat transfer calculations and hydro-mechanical calculations are decoupled. By using the iteration procedure schematically shown above, the effects of a fully coupled THM model are achieved.*

3.4.3 Finite element models

Two element models, one that is a 1D axial symmetric model and one that is a 2D axial symmetric model have been used. These models refer to the two subtasks 2.2.2 and 2.2.3 described in Sections 3.2.6 and 3.2.7.

1D model

A 1D-model of the buffer section at canister mid-height is used for modelling Task 2.2.2: Thermo-hydro-mechanical simulation of the engineered buffer at canister mid-height.

Figure 3-93 shows the geometry of the 1D model. The mesh consists of 350 axis-symmetric elements with 1 mm thickness. The model represents a horizontal section located close to the centre of the canister. The canister and rock are not modelled but are represented by mechanical and hydraulic boundaries. There are two materials with different properties: the bentonite ring and the pellets filling. In addition there is a slot of 1 cm between the canister and the bentonite rings that has been assumed to be filled during the water filling of the pellets filling. This slot is modelled as water filled space between two contact surfaces. The model is axial symmetric around the centre axis of the canister.

The properties of the bentonite ring and the pellets filled slot are identical to the properties of those parts in the 2D model. These materials are described in Section 3.5.4.

2D model

A 2D-model of the entire test is used for modelling Task 2.2.3: Thermo-hydro-mechanical simulation of the entire CRT experiment.

Figure 3-94 shows the geometry and the element mesh of the 2D model. The model includes altogether five different bentonite materials (ring shaped blocks, solid blocks, bricks, pellets and the empty slot) and four other materials (canister, rock, concrete plug and steel lid).

The dimensions and material names of the different parts in the model are shown in Table 3-20.

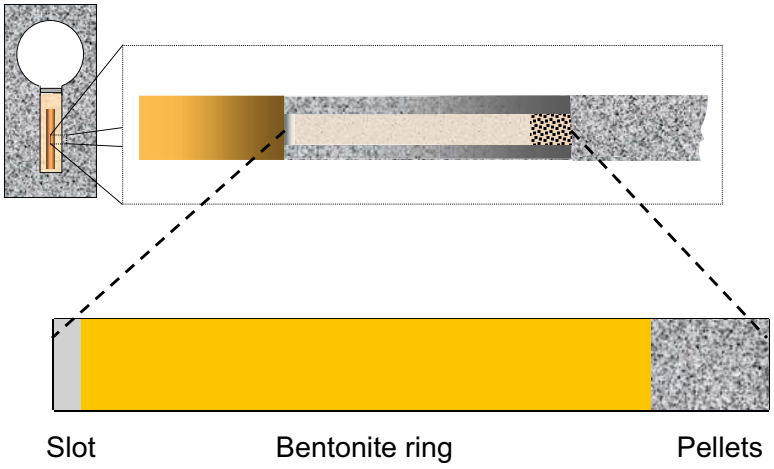

Figure 3-93. *The 1D model represents an axi-symmetric cross section through the centre of the canister with the following dimensions*

- *Canister $r < 0.525$ m*
- *Slot $\Delta r = 0.01$ m*
- *Buffer ring $\Delta r = 0.285$ m*
- *Pellets $\Delta r = 0.055$*
- *Rock $r > 0.875$ m*

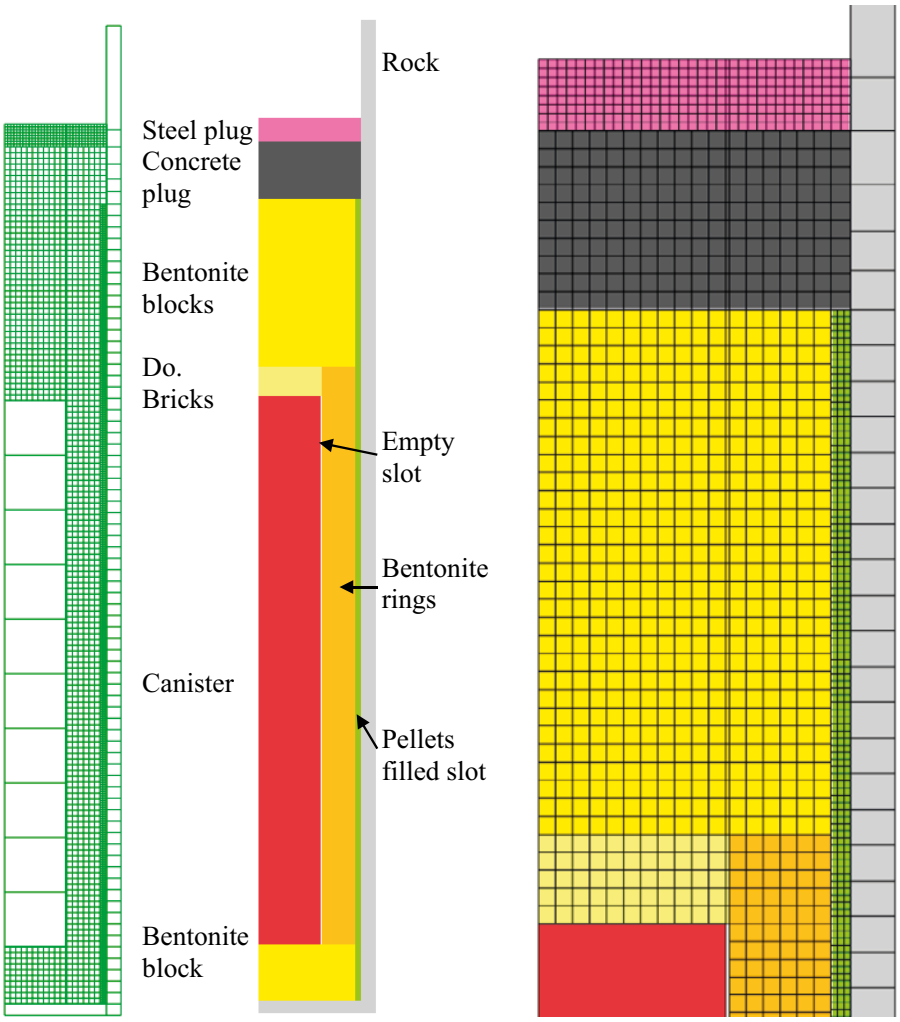

Figure 3-94. *Element mesh and property areas of the 2D model. The model is axial symmetric around the left boundary.*

Table 3-20. Dimensions and material name of the different parts of the model.

Model part	Radial thickness (m)	Axial thickness (m)	Material name
Steel plug	r = 0.875	0.2	Steel
Concrete plug	r = 0.875	0.5	Concrete
Bentonite top blocks	r = 0.82	1.5	Blocks
Bentonite bricks	r = 0.535	0.25	Bricks
Canister	r = 0.525	4.75	Canister
Bentonite bottom block	r = 0.82	0.5	Blocks
Empty slot	Δr = 0.01	4.75	Slot
Bentonite rings	Δr = 0.285	5.0	Rings
Pellets filled slot	Δr = 0.055	7.0	Pellets
Bottom rock	r = 0.875	0.1	Rock
Radial rock	Δr = 0.12	8.55	Rock

3.4.4 Material properties

General

The model is composed of eight different materials, of which four are different bentonite models. The bentonite material MX-80 is used for all bentonite parts but with different densities and water contents, resulting in the same material model but different initial conditions. Table 3-21 shows the basic properties for the four bentonite parts. Pellets I refer to the pellets filled slot before water filling and Pellets II after water filling.

Table 3-21. Basic properties of four of the five bentonite parts.

Section	Density (kg/m^3)	Water ratio	Dry density (kg/m^3)	Void ratio	Degr. of saturation
Solid block	1 991	0.172	1 699	0.636	0.751
Ring shaped block	2 087	0.171	1 782	0.560	0.849
Bricks	1 883	0.165	1 616	0.720	0.637
Pellets I (dry)	1 101	0.100	1 001	1.778	0.156
Pellets II (water filled)	1 574	0.572	1 001	1.778	0.895

The three types of blocks are modelled as water unsaturated bentonite with the models developed for Abaqus. The pellets filling will change its density significantly during the wetting due to the swelling of the blocks. Since the model of unsaturated bentonite is not well suited for large volume changes and since the degree of saturation after the water filling is very high the pellets filling has been modelled as completely water saturated.

In addition there is a slot of 1 cm between the canister and the bentonite rings that has been assumed to be filled during the water filling of the pellets filling. This slot is modelled as water filled space between two contact surfaces.

Bentonite blocks, rings and bricks

General

This section contains a description of the material models for the three types of bentonite blocks and the parameters included in the models.

The following processes are modelled:

Thermal:

- Thermal flux from conduction

Hydraulic:

- Water liquid flux
- Water vapour flux
- Hydraulic coupling between the pore water and the pore gas

Mechanical:

- Mechanical behaviour of the structure
- Thermal expansion
- Mechanical behaviour of the separate phases
- Mechanical coupling between the structure and the pore water

The model includes complete coupling between all processes. The processes may be a function of the following variables:

- Temperature
- Degree of water saturation
- Void ratio

Required parameters

The required input parameters for the described THM model in Abaqus are the following:

Thermal:

- Tables of thermal conductivity $\boldsymbol{\lambda}$ and specific heat $\boldsymbol{c}$ as function of void ratio $\boldsymbol{e}$, degree of saturation $\boldsymbol{S_r}$.

Hydraulic:

- Table of the hydraulic conductivity of water saturated material $\boldsymbol{K}$ as function of void ratio $\boldsymbol{e}$ and temperature $\boldsymbol{T}$.
- Influence of degree of saturation $\boldsymbol{S_r}$ on the hydraulic conductivity $\boldsymbol{K_p}$ expressed as the factor $\boldsymbol{\delta}$ in Equation 3-33.
- The basic water vapour flow diffusivity $\boldsymbol{D_{vTb}}$ and the parameters $\boldsymbol{a}$ and $\boldsymbol{b}$ in Equations 3-36 to 3-37
- The retention curve (table of the matric suction $\boldsymbol{u_w}$ as a function of the degree of saturation $\boldsymbol{S_r}$.)

Mechanical:

- Porous bulk modulus κ according to Equation 3-40 and Poisson's ratio ν.
- Drucker Prager plasticity parameters β, d, ψ, and the yield function.
- Bulk modulus and coefficient of thermal expansion of water (B_w, α_w) and bulk modulus solids (B_s).
- Bishops parameter χ in Equation 3-18 (usual assumption $\chi = S_r$).
- The volume change correction ε_v as a function of the degree of saturation S_r (the "moisture swelling" procedure).

Initial conditions

The following initial conditions of the elements in the structure need to be specified:

- void ratio $\boldsymbol{e}$
- degree of saturation $\boldsymbol{S_r}$
- pore pressure $\boldsymbol{u}$ (kPa)
- average effective stress $\boldsymbol{p}$ (kPa)
- temperature $\boldsymbol{T}$ (°C)

Material models of the ring-shaped blocks, solid blocks and the bricks

The models and data used for the buffer are essentially the same as used for modelling the wetting of KBS-3V for SR-Can (Börgesson et al. 2006), but the parameters used are mainly valid for the void ratios 0.7–0.9. In the CRT the initial void ratio is 0.56–0.72 (except for the pellets filling), which requires recalibration of some of the data.

Thermal flux from conduction

The only thermal flux that is included in the model is thermal conduction with the following parameters:

λ = thermal conductivity

c = specific heat

The *thermal conductivity* has been measured as a function of the degree of saturation and density (Börgesson et al. 1994). The parameter values for the ABAQUS model are shown in Table 3-22 (linear interpolation between the values).

Table 3-22. Thermal conductivity λ of the buffer material as a function of the degree of saturation S_r and the void ratio *e*.

S_r	λ W/m,K		
	e = 0.5	e = 0.78	e = 1.0
0	0.4	0.3	0.2
0.2	0.4	0.3	0.2
0.3	0.5	0.4	0.3
0.4	0.65	0.55	0.45
0.5	0.85	0.75	0.65
0.6	1.05	0.95	0.85
0.7	1.2	1.1	1.0
0.8	1.3	1.2	1.1
0.9	1.35	1.25	1.15
1.0	1.4	1.3	1.2

The *specific heat* has been calculated as the weight average of the specific heat of water and particles according to Equation 3-32.

$$c = 800/(1+w) + 4\,200w/(1+w) \tag{3-32}$$

Equation 3-32 yields the input parameters shown in Table 3-23 (linear interpolation).

Table 3-23. Heat capacity *c* of the buffer material as a function of the water ratio *w*.

w	c Ws/m,kg
0	800
0.1	1 109
0.2	1 367
0.3	1 585
1.0	2 500

Water liquid flux

The water flux in the liquid phase is modelled to be governed by Darcy's law with the water pressure difference as driving force in the same way as for water saturated clay.

The magnitude of the hydraulic conductivity K_p of partly saturated clay is a function of the void ratio, the degree of saturation and the temperature. K_p is assumed to be a function of the hydraulic conductivity K of saturated clay and the degree of saturation S_r according to Equation 3-33.

$$K_p = (S_r)^{\delta} K \tag{3-33}$$

where

K_p = hydraulic conductivity of partly saturated soil (m/s)

K = hydraulic conductivity of completely saturated soil (m/s)

δ = parameter (usually between 3 and 10)

For the MX-80 the standard value

$\delta = 3$

has been found to be satisfactory according to the calibration calculations.

Water transport driven by gravity and density gradients is included in the model as well.

The *hydraulic conductivity* of water saturated bentonite has been measured at different temperatures and void ratios (Börgesson et al. 2006). Table 3-24 shows the values for the model.

Table 3-24. Hydraulic conductivity *K* as a function of void ratio *e* and temperature *T*.

T °C	*e*	*K* m/s
20	0.4	0.035×10^{-13}
20	0.6	0.2×10^{-13}
20	0.8	0.65×10^{-13}
20	1.0	1.75×10^{-13}
40	0.4	0.05×10^{-13}
40	0.6	0.31×10^{-13}
40	0.8	1.0×10^{-13}
40	1.0	2.75×10^{-13}
60	0.4	0.07×10^{-13}
60	0.6	0.44×10^{-13}
60	0.8	1.45×10^{-13}
60	1.0	3.85×10^{-13}
80	0.4	0.1×10^{-13}
80	0.6	0.55×10^{-13}
80	0.8	1.8×10^{-13}
80	1.0	4.9×10^{-13}

Water vapour flux

The water vapour flux is modelled as a diffusion processes driven by the temperature gradient and the water vapour pressure gradient (at isothermal conditions) according to Equation 3-34.

$$q_v = -D_{Tv}\nabla T - D_{pv}\nabla p_v \qquad (3\text{-}34)$$

where α

q_v = vapour flow

D_{Tv} = thermal vapour flow diffusivity

T = temperature

D_{pv} = isothermal vapour flow diffusivity

p_v = vapour pressure

The isothermal vapour flow is neglected and thus $D_{pv} = 0$.

The thermal water vapour diffusivity D_{Tv} can be evaluated from moisture redistribution tests by calibration calculations. The following relations were found to yield acceptable results:

$$D_{Tv} = D_{Tvb} \qquad 0.3 \le S_r \le 0.7 \qquad (3\text{-}35)$$

$$D_{Tv} = D_{Tvb} \cdot \cos^{a}\left(\frac{S_r - 0.7}{0.3} \cdot \frac{\pi}{2}\right) \qquad S_r \geq 0.7 \qquad (3\text{-}36)$$

$$D_{Tv} = D_{Tvb} \cdot \sin^{b}\left(\frac{S_r}{0.3} \cdot \frac{\pi}{2}\right) \qquad S_r \leq 0.3 \qquad (3\text{-}37)$$

a and b are factors that regulates the decreased vapour flux at high and low degree of saturation.

The diffusivity is thus constant with a basic value D_{Tvb} between 30 % and 70 % degree of saturation. It decreases strongly to $D_{Tv} = 0$ at 0 % and 100 % saturation. The influence of temperature and void ratio on the diffusivity is not known and not considered in the model.

The *thermal vapour flow diffusivity* D_{Tvb} and the parameters a and b according to Equations 3-35 to 3-37 have originally been evaluated for the void ratio 0.8 with calibration calculations of moisture redistribution tests. New tests performed at lower void ratios and confirm those values:

$\boldsymbol{D}_{Tvb} = 0.7 \times 10^{-11}$ m^2/s,K

$a = 6$

$b = 6$

Hydraulic coupling between the pore water and the pore gas

The pore pressure u_w of the unsaturated buffer material, which is always negative, is modelled as being a function of the degree of saturation S_r independent of the void ratio (*water retention curve*).

$$u_w = f(S_r) \qquad (3\text{-}38)$$

The pore air pressure is not modelled.

The water retention curves have been evaluated according to a method developed by Dueck et al. (see Dueck and Börgesson 2007). The evaluation is described in Appendix 6. Since the void ratio differs in the different buffer blocks different curves are required. Figure 3-95 shows the evaluated retention curves.

Since the water transport in ABAQUS is governed by the pore water pressure (u_w) but the measurements are in relative humidity (R_h) a conversion from calculated negative pore water pressure to relative humidity has also been done. The conversion according to Equation 3-39, which is derived from thermodynamic considerations (see e.g. Dueck 2004), has been used.

$$R_h = exp(u_w/462T) \qquad (3\text{-}39)$$

where T = absolute temperature (t+273)

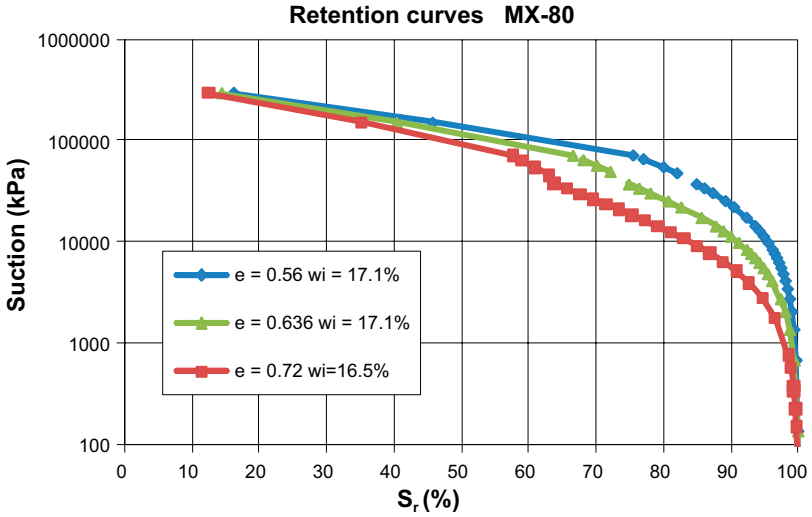

Figure 3-95. *Retention curve of MX-80 at the void ratio 0.56 (rings), 0.636 (blocks) and 0.72 (bricks).*

Mechanical behaviour of the structure

The mechanical behaviour has been modelled with a non-linear Porous Elastic Model and Drucker-Prager Plasticity model. The effective stress theory is applied and adapted to unsaturated conditions and the shortcomings of this theory are compensated for by a correction called moisture swelling (see below).

The *Porous Elastic Model* implies a logarithmic relation between the void ratio e and the average effective stress p according to Equation 3-40.

$$\Delta e = \kappa \Delta \ln p \qquad (3\text{-}40)$$

where κ = porous bulk modulus

Poisson's ratio ν is also required.

Drucker Prager Plasticity model contains the following parameters:

β = friction angle in the p-q plane

d = cohesion in the p-q plane

ψ = dilation angle

$q = f(\varepsilon^d_{pl})$ = yield function

The yield function is the relation between Mises' stress q and the plastic deviatoric strain ε^d_p at a specified stress path. The dilation angle determines the volume change during shear.

The following data has been used for the *Porous Elastic* model:

$\kappa = 0.20$

$\nu = 0.4$

The value of κ has been derived from oedometer and swelling pressure tests (Börgesson et al. 1995).

The following data was used for the *Drucker Prager Plasticity* model

$\beta = 0.001°$

d = 3 000 kPa

$\psi = 2°$

Table 3-25. Yield function.

q (kPa)	ε_{pl}
1	0
50	0.005
100	0.02
150	0.04
200	0.1

The low friction angle and high cohesion are motivated by evidence that the strength is mainly a function of the void ratio, independently of the degree of saturation, and not the effective stress.

Thermal expansion

The volume change caused by the thermal expansion of water and particles can be modelled with the parameters

α_s = coefficient of thermal expansion of solids

α_w = coefficient of thermal expansion of water

Only the expansion of the separate phases is taken into account. The possible change in volume of the structure by thermal expansion (not caused by expansion of the separate phases) is not modelled. However, a thermal expansion in water volume will change the degree of saturation which in turn will change the volume of the structure. The following values have been used:

$\alpha_w = 3.0 \times 10^{-4}$

$\alpha_s = 0$

Mechanical behaviour of the separate phases

The water and the particles are mechanically modelled as separate phases with linear elastic behaviour. The pore air is not mechanically modelled. The following standard values have been used for the *properties of the water and solid phases*:

$B_w = 2.1 \times 10^6$ kPa (bulk modulus of water)

$B_s = 2.1 \times 10^8$ kPa (bulk modulus of solids)

$\rho_w = 1\ 000$ kg/m^3 (density of water)

$\rho_s = 2\ 780$ kg/m^3 (density of solids)

Mechanical coupling between the structure and the pore water

The mechanical behaviour is modelled to be governed by the effective stress theory and a procedure called moisture swelling.

Effective stress theory

The effective stress concept according to Bishop is used for modelling the mechanical behaviour of the water-unsaturated buffer material:

$$s_e = (s - u_a) + \chi(u_a - u_w) \quad (3\text{-}41)$$

Equation 4-10 is simplified in the following way:

$u_a = 0$ (no account is taken to the pressure of enclosed air)

$\chi = S_r$

Moisture swelling

The shortcomings of the effective stress theory can be compensated in ABAQUS by a correction called "*moisture swelling*". This procedure changes the volumetric strain ε_v by adding a strain that can be made a function of the degree of saturation S_r.

The effective stress theory decomposes the total stress into pore pressure and effective stress (which only depends on deviatoric strains). However, the effective strain can be made dependent on saturation by using the concept of *moisture swelling* which modify the effective strain by this user defined saturation dependent volumetric strain (*moisture swelling*). In this application the moisture swelling contribution is calibrated by using the measured swelling pressure and assuming that the effective strain (after adding the moisture swelling) should be zero. Neglecting moisture swelling will imply an effective strain defined by the elastic material (porous elastic) and thus the moisture swelling strain can be calculated from Equations 3-42 and 3-43.

$$\Delta\varepsilon_v = f(S_r) = \ln(p_0/p)\cdot\kappa/(1+e_0) \quad (3\text{-}42)$$

$$p = p_{tot} - u_w \cdot S_r \quad (3\text{-}43)$$

where

ε_v = volumetric strain

p_0 = initial effective stress taken from the initial conditions

p = actual effective stress
κ = porous bulk modulus (from Equation 3-40)
e_0 = initial void ratio
p_{tot} = actual total stress
u_w = pore water pressure
S_r = degree of water saturation

The moisture swelling relation (*M.S.*) that is needed as input is the logarithmic volumetric strain according to Equation 3-44 where $\Delta\varepsilon_v$ is taken from Equation 3-42.

$$M.S. = \ln(1 + \Delta\varepsilon_v) \tag{3-44}$$

The data for the *moisture swelling procedure* is derived from the assumption that the relation between total stress and degree of saturation of a confined sample (constant volume) is linear when the degree of saturation is increased from its initial value to 100 % (Dueck and Börgesson 2007). This relation is linked to the retention curve. The derivation of the retention curve and the moisture swelling relation is described in Appendix 6.

The derived moisture swelling relations are shown in Figure 3-96 for all three bentonite block types.

In order to check that the different bentonite block types behave as expected a one element tests of drying and wetting have been simulated. The volume was kept constant and the degree of saturation stepwise changed from the initial conditions to 100 % and to 0 %. Figure 3-97 shows the calculated average stress in the element as a function of the degree of saturation.

Figure 3-97 shows that the bentonite block types behave according to the model. From the stress-less initial state the total average stress increases linearly with increasing degree of saturation until the swelling pressure at full saturation is reached at the degree of saturation 100 %. The behaviour at decreasing degree of saturation is identical but merely theoretical since real samples cannot keep their original volumes but will shrink instead of having negative stress. In the real model high tensile average stresses will be kept but if they are transferred to the boundary the contact elements will open up, which leads to shrinkage of the buffer, since the contacts have no cohesion.

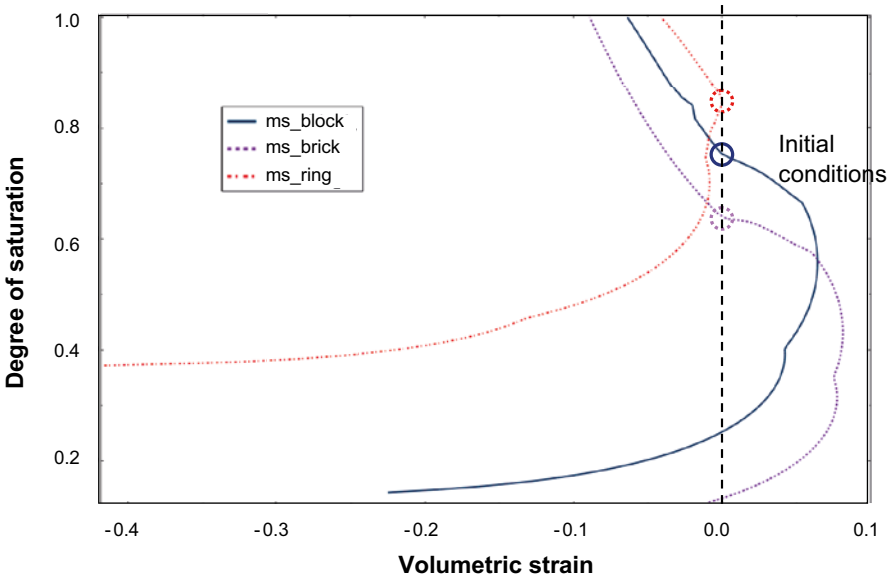

Figure 3-96. *Volume change correction $\Delta\varepsilon_v$ used in the moisture swelling procedure for the three different bentonite block types. The initial conditions are also noted in the figure.*

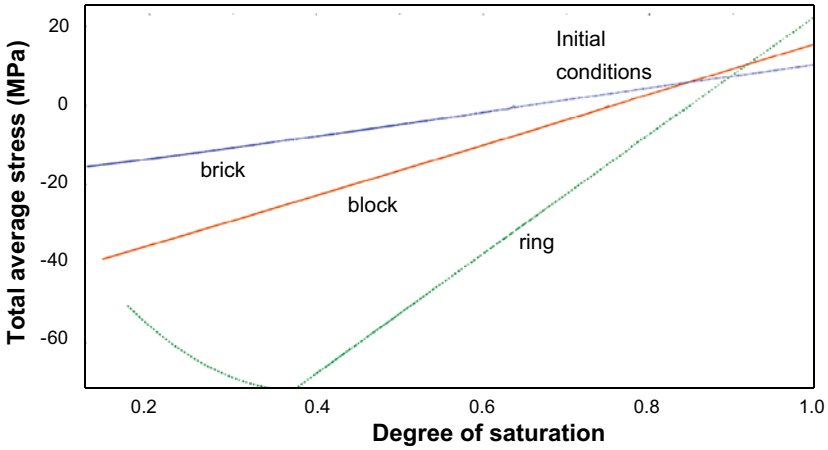

Figure 3-97. *One element tests of confined samples of the three different block types.*

Other buffer parts

The bentonite pellet filling is modelled as water saturated bentonite since the slot with pellets was artificially filled with water at the start of the experiment. This is an approximation since the individual pellets are not water saturated. The actual degree of saturation is 0.895 as shown in Table 3-21, but the difference is not considered significant for the results.

Bentonite pellets

Thermal: Thermal conductivity λ according to Table 3-26 and specific heat *c* according to Table 3-23 (above).

Table 3-26. Relation between thermal conductivity λ and void ratio *e* for the pellets filling.

e	λ **W/m,K**
0.78	1.3
1.0	1.2
1.4	1.1
1.78	1.0

Hydraulic: See Table 3-24.

Mechanical: Porous elastic and Drucker Prager plasticity with the same properties as the bentonite blocks

Gap between rings and the canister

Thermal:

λ = 0.5 W/m,K

c = 4 200 Ws/m,kg

Hydro-mechanical:

The gap has been modelled by using contact definitions between the buffer and the canister where the initial gap volume is assumed to be filled with water.

Other materials

The other parts of the CRT than the bentonite parts have been modelled in a very simplified way, mostly as boundary conditions. Since the thermal calculations have been simplified and use the calculation described in Section 3.2.5 as boundary conditions for the bentonite parts no description of the thermal properties will be made.

Canister

The canister has been modelled as a rigid impermeable body

Rock

The rock has been modelled as a rigid impermeable body

Concrete plug

The concrete plug has been modelled as an impermeable elastic material with the following properties:

$E = 3 \cdot 10^7$ kPa

$v = 0.15$

$a = 1.0\ 10^{-5}$ °C^{-1} (coefficient of thermal expansion)

Steel lid

The steel plug is made of a 20 cm thick steel plate. It is anchored by 9 anchor rods fixed to the top of the steel plate. In order for the plug to simulate a deformable backfill the anchor rods were fixed about 5 m deep into the anchor holes leaving about 5 m rods that elastically can be lengthened. Measurements of the force in the anchors and the displacement of the plug have showed that the plug was displaced 17 mm at the total force of 8 000 kN.

In order to simulate the elasticity in the rods the steel plate was made with an E-modulus that gives the same deformation as the lengthening of the rods. Back-calculation of 17 mm displacement from the force 8 000 kN along a 20 cm thick plate with the diameter 1.75 m gives the following E-modulus that was applied for the plate:

$E = 3.9 \cdot 10^4$ kPa

$v = 0.3$ (standard value for steel)

3.4.5 Initial conditions

The following initial conditions have been applied for the bentonite parts:

Buffer rings

$e = 0.56$

$u = -37\ 000$ kPa

$S_r = 0.849$

$p = 31\ 413$ kPa

$T = 17$ °C

Buffer blocks

$e = 0.636$

$u = -37\ 000$ kPa

$S_r = 0.751$

$p = 27\ 787$ kPa

$T = 17$ °C

Buffer bricks

e = 0.72

u = –37 500 kPa

S_r = 0.637

p = 23 888 kPa

T = 17 °C

Pellets

e = 1.78

u = –50 kPa

S_r = 1.0

p = 50 kPa

T = 17 °C

3.4.6 Boundary conditions and couplings

The structure is axi-symmetric around the centre line of the deposition hole. The following boundary conditions were applied:

Mechanical

- Fixed outer boundaries of the rock.
- Common nodes between buffer blocks, rings and bricks.
- Tied contacts between buffer blocks and pellets and buffer rings and pellets.
- Contact surfaces with friction at the vertical boundaries between the buffer and the canister (ϕ_c = 11.3°).
- Contact surfaces without friction at the other boundaries.
- The steel lid top surface locked (the lid simulates the anchor stiffness).
- Canister free to move.

The rock/buffer and rock/pellets interfaces had to be modelled without friction in order to reach convergence in the calculation. The reason is not clear and the actual friction angle is not zero. However, as shown by the results there is no or very small displacements in these contact surfaces, which shows that the results would have been the same if friction had been applied.

Thermal

- Temperature history on canister and rock surfaces according to the results from the modelling shown in Section 3.3.2.

Hydraulic boundaries of the buffer

- Inner: No flow
- Outer: In filters according to water pressure protocol
- No flow in buffer block/rock contact

The filters reached from the bottom of the hole up to 0.75 m from the top of the buffer i.e. the uppermost 75 cm were not artificially wetted. The filters were simulated with prescribed water pressure according to the water pressure protocol.

The water pressure protocol for the filters is shown in Table 3-27 (see also Figure 3-8).

Table 3-27. Water pressure protocol for the filters in CRT.

Date	Day	Water pressure (MPa)	Comments
00-10-26	0	0	
02-09-05	679	0	Gradual increased water pressure
02-10-10	714	0.8	
02-12-05	770	0.1	
03-01-09	805	0.4	
03-01-23	819	0.8	
05-03-12	1 598	0	Probably dry after this date
05-12-16	1 877	0	Air flushed

3.4.7 Calculation cases and sequences

Two models have been made:

- 1D axial symmetric model of a horizontal section through the centre of the canister.
  - Until start excavation (1 919 days).
- 2D axial symmetric model of the entire test geometry.
  - Until start excavation (1 919 days).

All calculations have been done in the following steps:

1. Thermal calculation with the initial conditions of the materials.
   - Boundary conditions: Evolution of canister and rock temperature according to the temperature model in Section 3.3.2.
2. Hydro-Mechanical calculation.
   - Establishment of equilibrium at initial conditions.
   - HM-calculation with temperature results according to step 1 and hydraulic boundary conditions according to the water pressure protocol.
3. Repetition of 1 and 2 until the results are identical.

3.4.8 Results from the 1D calculation and comparisons with measurements

Complete water saturation does not mean that the homogenisation process is completed but the pore water pressure has also to be equalised in the entire section. Both measurements and calculations show that the buffer between the canister and the rock was completely water saturated and had finished its homogenisation process at the end of the test.

The modelled evolution of temperature and degree of saturation in some points in the cross section between the canister and the rock is shown in Figure 3-98. Figure 3-99 shows corresponding diagrams of the pore water pressure and dry density.

The figures clearly show that the homogenisation is completed at the end of the test since the pore pressure has equilibrated. The saturation and the pore pressure equalisation as well as the swelling/compression seem to be finished after about 1 000 days or slightly less than 3 years although there are some small effects caused by the change in water pressure and temperature also later.

Figure 3-100 shows the evolution of radial and axial total stress while Figure 3-101 shows the evolution of the radial displacements.

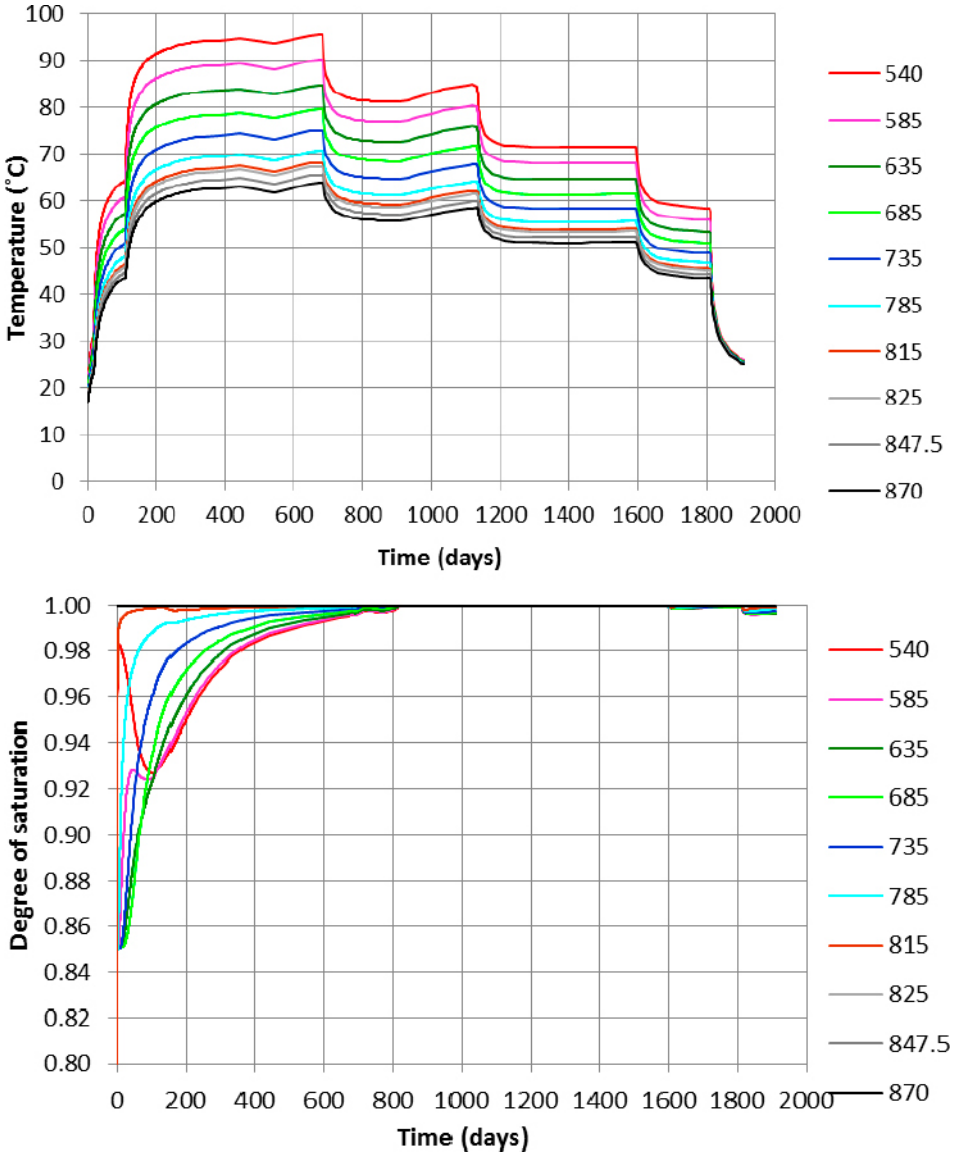

Figure 3-98. *Calculated evolution of temperature and degree of saturation in the central section of the buffer in the CRT. The legend shows the radial distance from the centre line (mm). The canister/buffer interface is located at r = 525 mm and the buffer/rock interface is located at r = 875 mm.*

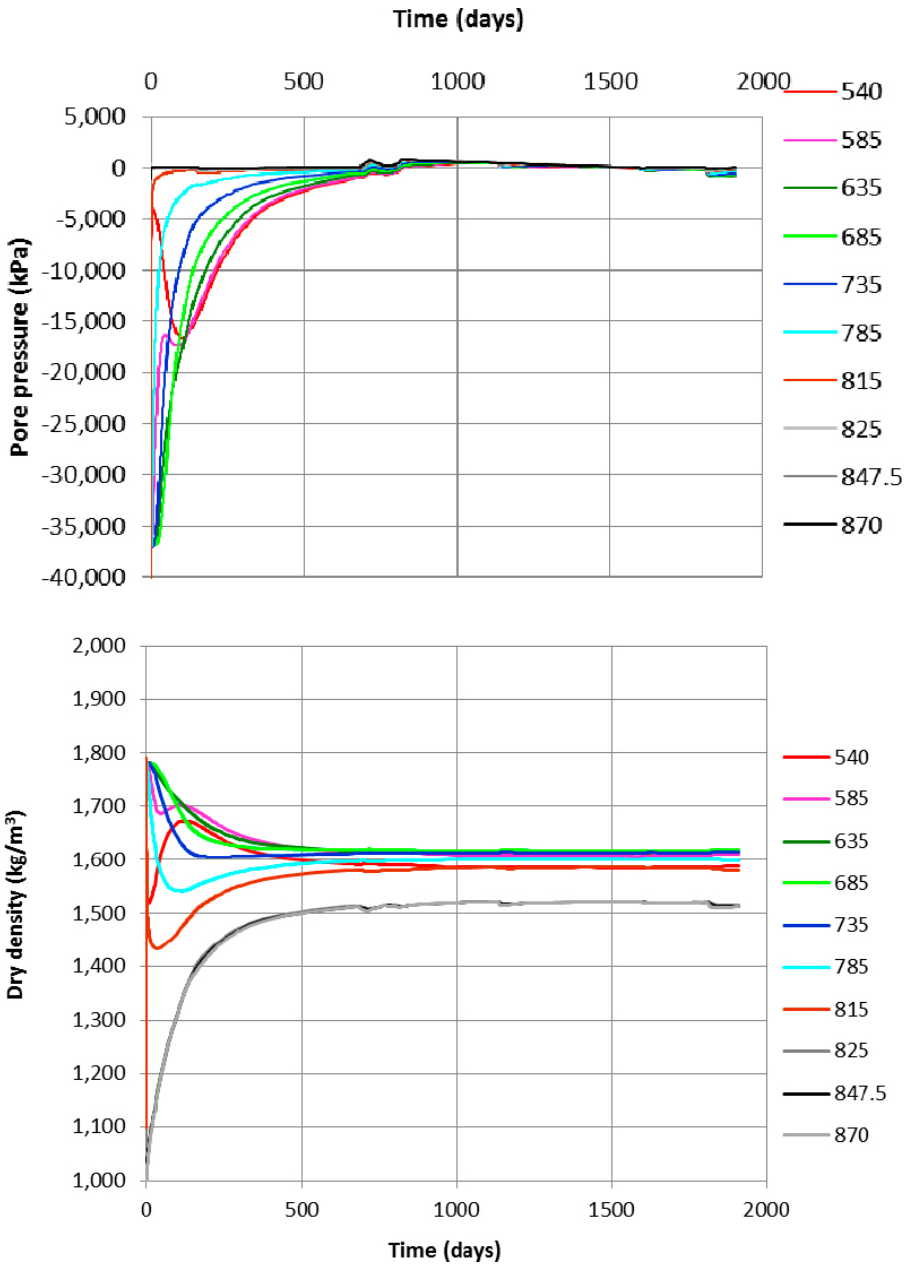

Figure 3-99. *Calculated evolution of pore water pressure and dry density in the central section of the buffer in the CRT. The legend shows the radial distance from the centre line (mm). The canister/buffer interface is located at r = 525 mm and the buffer/rock interface is located at r = 875 mm.*

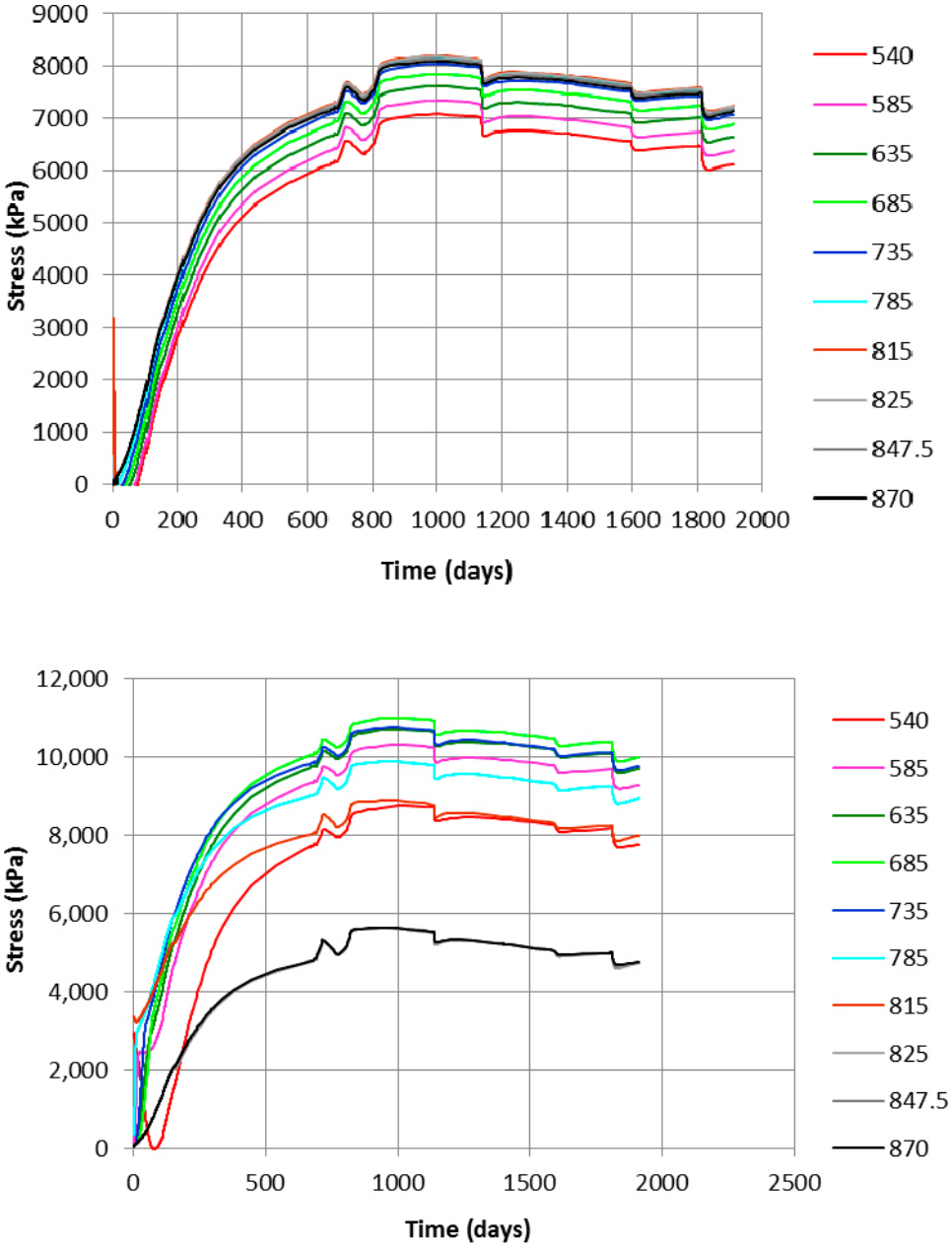

Figure 3-100. *Calculated evolution of radial (upper) and axial stresses in the central section of the buffer in the CRT. The legend shows the radial distance from the centre line (mm). The canister/buffer interface is located at r = 525 mm and the buffer/rock interface is located at r = 875 mm.*

Figure 3-100 shows that

- The axial stresses are always higher than the radial (20–25 %) except for locally at the vertical rock boundary and just above and below the canister.
- Small difference between the stresses at different radiuses except for in the pellet filling.
- The radial stresses are higher close to the rock than close to the canister while axial stresses have no clear trend.

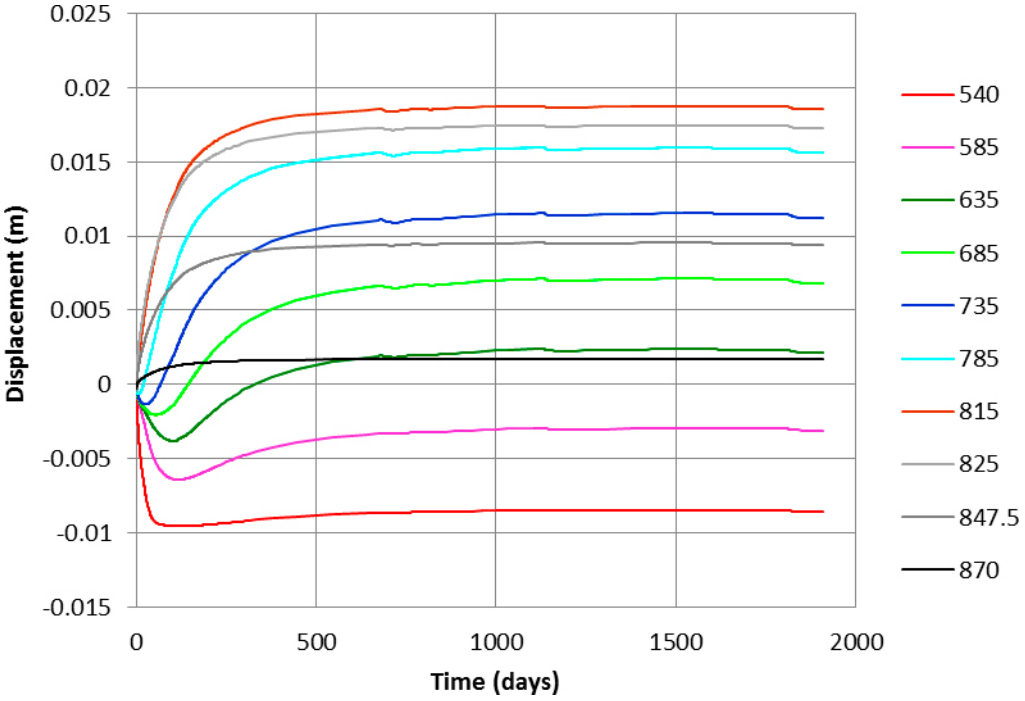

Figure 3-101. *Calculated evolution of radial displacement in the central section of the buffer in the CRT. The legend shows the radial distance from the centre line (mm). The canister/buffer interface is located at r = 525 mm and the buffer/rock interface is located at r = 875 mm.*

Figure 3-101 shows that

- The largest outwards swelling takes logically place at the block/pellets interface.
- The largest inwards swelling takes logically place close the inner slot at the canister.

The evolution of suction, pore water pressure, total pressure and temperature in the buffer was continuously measured with a large number of instruments. Figure 3-102 shows results from suction measurements in three different positions between the rock and the canister and comparisons with modelling results. Two different types of transducers were used; Wescor psychrometers for suction values below 5 MPa and Vaisala RH sensors of capacity type for higher suction. The comparison shows that the modelling results and the measurements agree very well with exception of the final remaining measured suction of about 1.5 MPa that is not modelled (part of which is caused by the salt concentration in the ground water).

The measurements thus confirm that the buffer in this region is water saturated a long time before the end of the test and thus also has had time to complete the homogenisation process.

It is thus relevant to compare the modelled and measured density distribution at the end of the test in order to evaluate if the homogenisation of the buffer is well modelled. Figure 3-103 shows a comparison between modelled and measured density distribution at the end of the test. The density distribution was measured after careful sampling (Johannesson 2007).

Figure 3-103 shows that there is a very good agreement between measured and modelled dry density distribution. The swelling of the bentonite ring from the dry density of almost 1 800 kg/m^3 to slightly higher than 1 600 kg/m^3 is well modelled as well as the compression of the pellets filling from the dry density 1 000 kg/m^3 to about 1 500 kg/m^3. The 1 cm gap has been closed but there is still a slightly lower density at the canister contact both according to the model and the measurements. The measured density of the pellets filled slot varies somewhat between the different directions, which probably is caused be a difference in initial slot width due to that the ring is placed somewhat off centre. The average value though seems to fit the modelled value well.

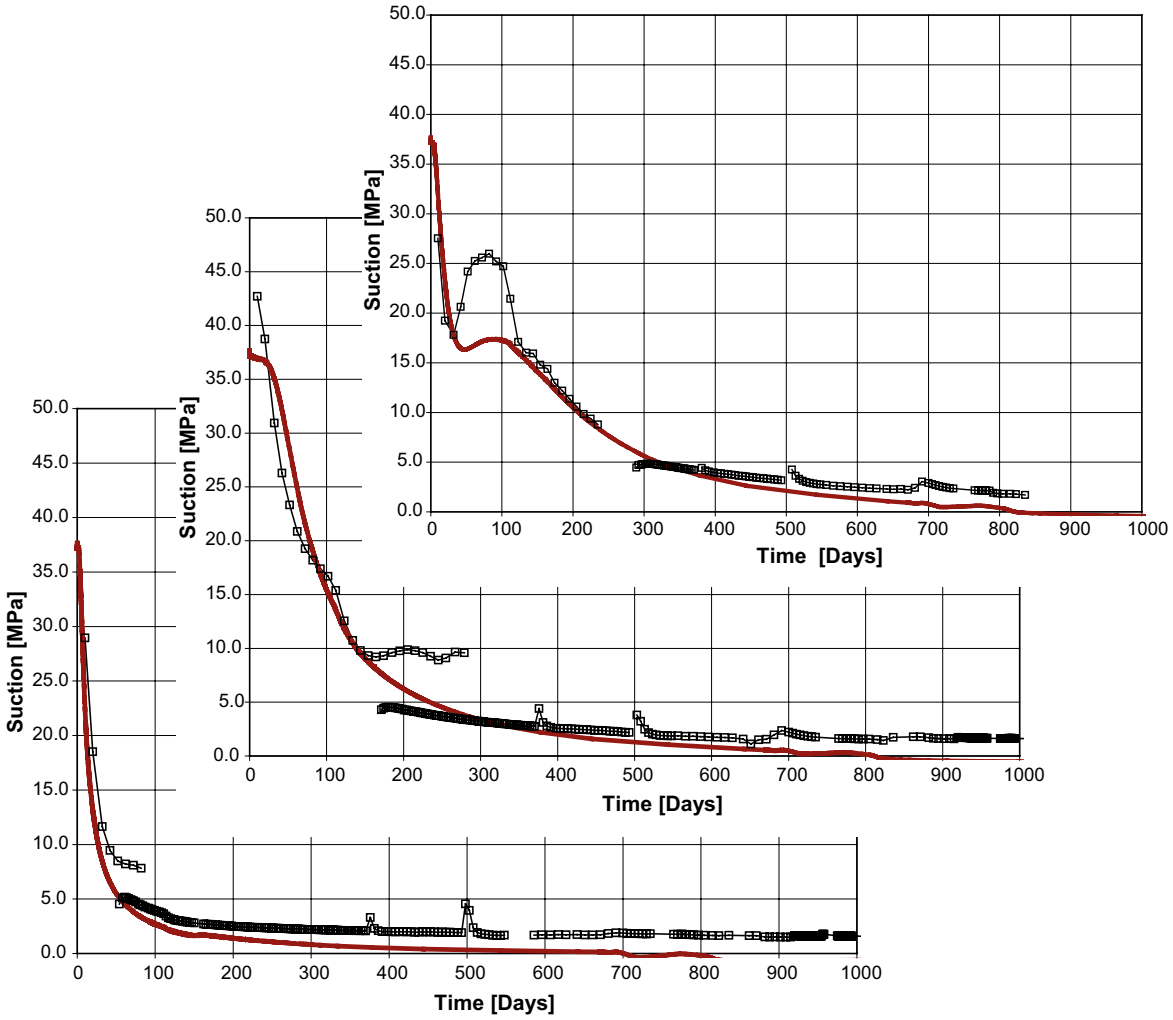

Figure 3-102. *Measured and modelled (brown line) suction at the radius 785 mm (left), 685 mm (middle) and 585 mm (right) in a central section of the buffer.*

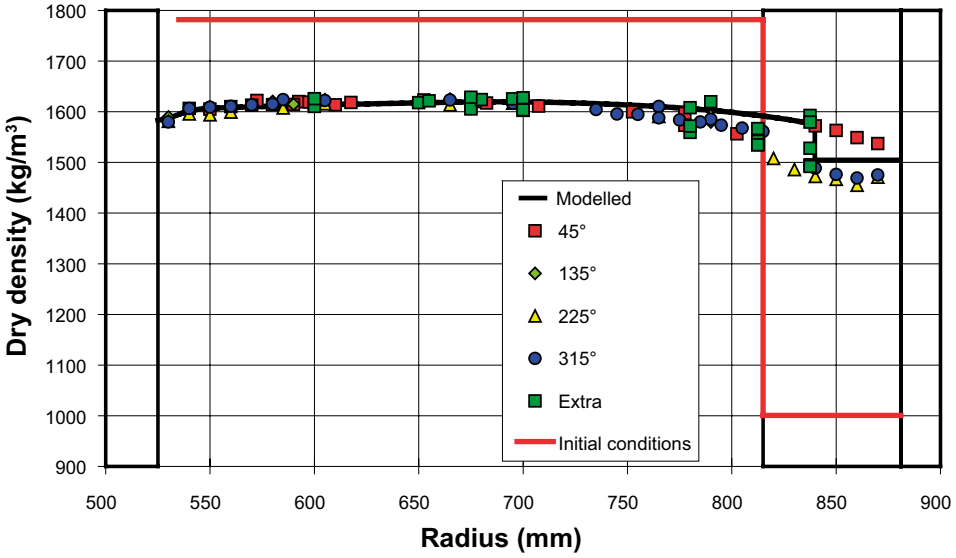

Figure 3-103. *Measured and modelled (black line) density distribution at the end of the test. The initial conditions are shown as a red line. The measurements have been done along radiuses with four different directions marked as different angles.*

The measured axial total stresses in a central part of the buffer are shown in Figure 3-104. A comparison with Figure 3-100 shows that:

- The measured maximum axial stresses are 3-7 MPa while the calculated ones are 9-11 MPa or about twice as high.
- The effect of the heater break-down and the subsequent temperature decrease is seen in both the measured and the calculated results but the effect is much stronger in the measurements. This effect is especially pronounced at the end of the test when the heater was shut down.
- There is some delay in measured total stress compared to modelled.

The results from the 1D calculation thus seem to verify the material model of the unsaturated buffer. However, the modelled stresses in the bentonite were generally about 2 times larger than the measured ones, but those measurements can be questioned since the gauges turned out to be not well suited for these types of measurements. Calibration of the sensors afterwards indicated that the sensors measured too low stresses (see Section 3.3.4). In addition the expected swelling pressure at the measured dry density 1 620 kg/m^3 (corresponding to e = 0.72) is 9–10 MPa.

It is worth mentioning that the modelled results are not derived after parameter adaptation in order to reach the best agreement. On the contrary, the parameter values have been derived directly from laboratory tests and used in the calculation without any changes.

3.4.9 Results from the 2D calculation of the entire CRT

Introduction

The element mesh and the material models used in the 2D calculation of the entire CRT were described in Section 3.5.3. The material models of the bentonite rings and the pellet filled slot are identical to the material models used for the 1D calculation, while the cylinders and the bricks have slightly different initial conditions but otherwise identical properties as the rings. The results will mainly be shown as history plots, as paths of calculated values vs the radius and as contour plots, the latter two at selected times.

A large amount of results are generated and examples will be shown in this chapter. More detailed results are shown in Appendix 7. Comparisons with measured results are shown in Section 3.4.10.

The results are presented in three different figure types namely contour plots at different times, paths at different times and history plots for various points.

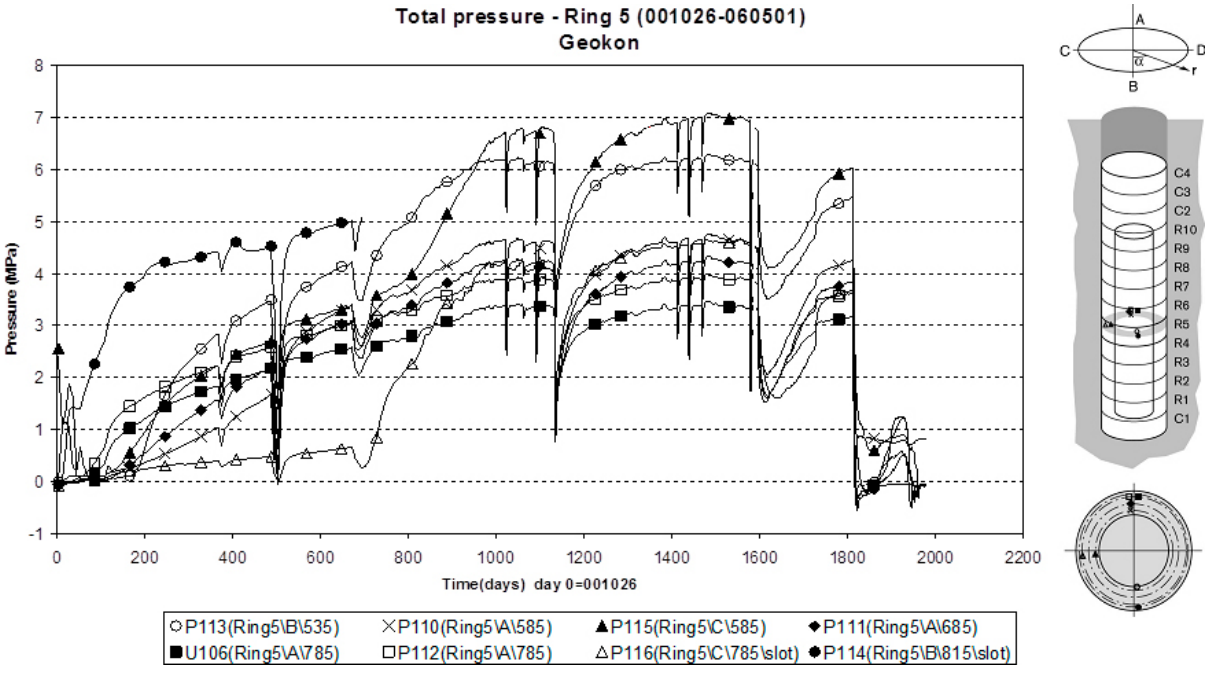

Figure 3-104. *Measured total axial stress in a central part of the buffer.*

Contour plots

The temperature distribution at two times is shown in Figure 3-105.

Figure 3-105 shows the temperature after 200 days when the temperature is close to its peak values and after the 90 days cooling period just before start excavation.

The degree of saturation at different times is shown in Figure 3-106. The figures show that there is drying of the buffer above and below the canister but not radially along the canister.

The dry density at different times is shown in Figure 3-107. The figures show that there is shrinkage resulting in increased density at the drying parts above and below the canister.

The relative humidity in the buffer at different times is shown in Figure 3-108. The same trend with drying of the buffer down to RH = 45 % at the end parts of the canister can be seen.

Other interesting results are the distribution of the axial and radial total stresses and the axial displacements at the end of the test. These results are shown in Figure 3-109. One can see that the axial stresses are always higher than the radial stresses in the buffer block parts, while the relation is the opposite in the pellet filled slot. The reason is of course that the blocks expand radially while the pellets slot is compressed radially.

The axial displacements take place in the buffer blocks parts and the canister follows the buffer and heaves about 4 mm, while the contact between the pellets filling and the rock hardly moves at all. Most of the shear deformation seems to take place in the pellets filling.

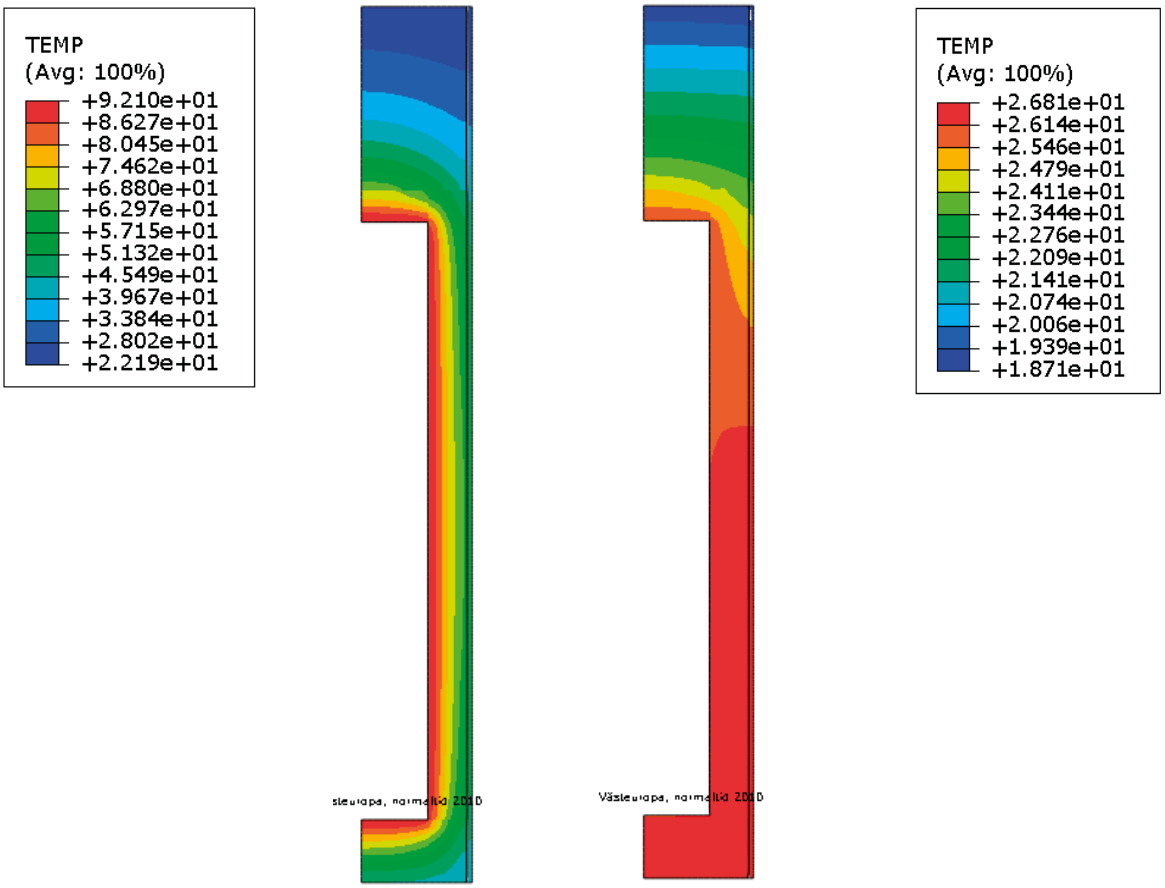

Temperature after 200 days Temperature after 1910 days

Figure 3-105. *Temperature (°C) distribution in the bentonite at two different times.*

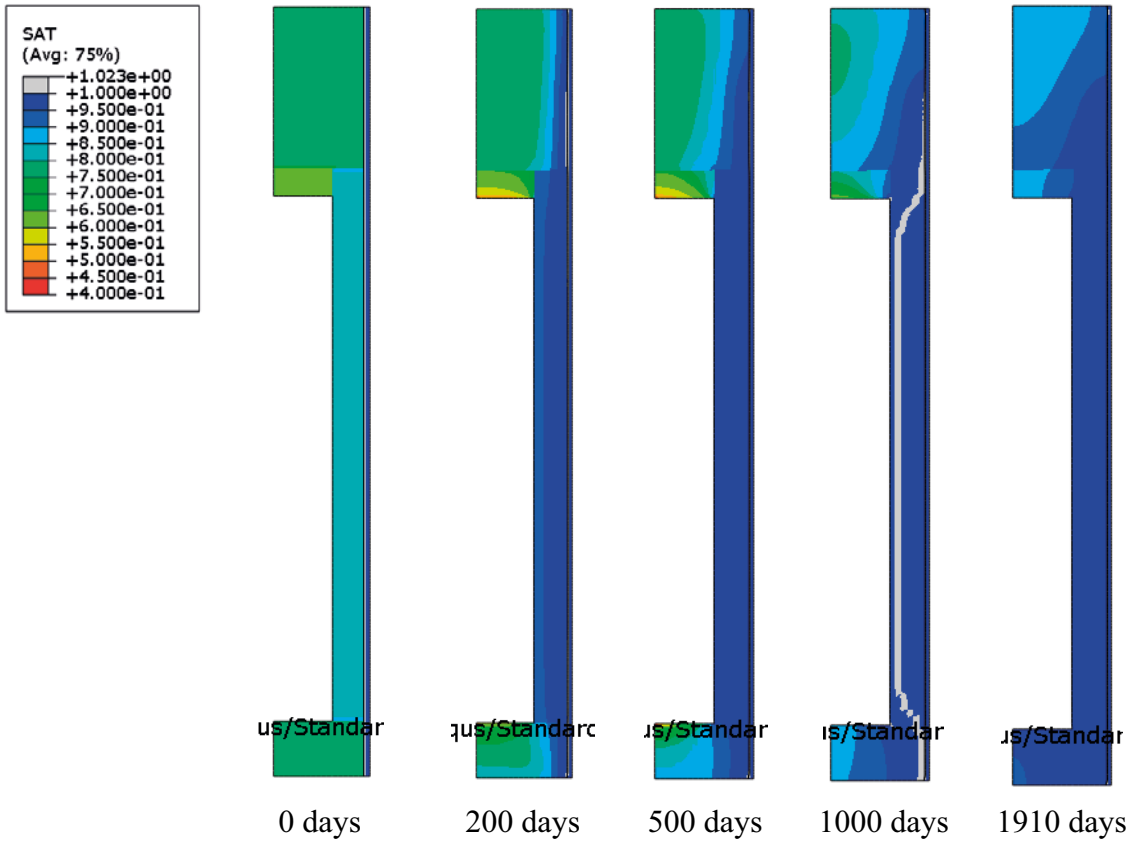

Figure 3-106. *Distribution of degree of saturation at different times.*

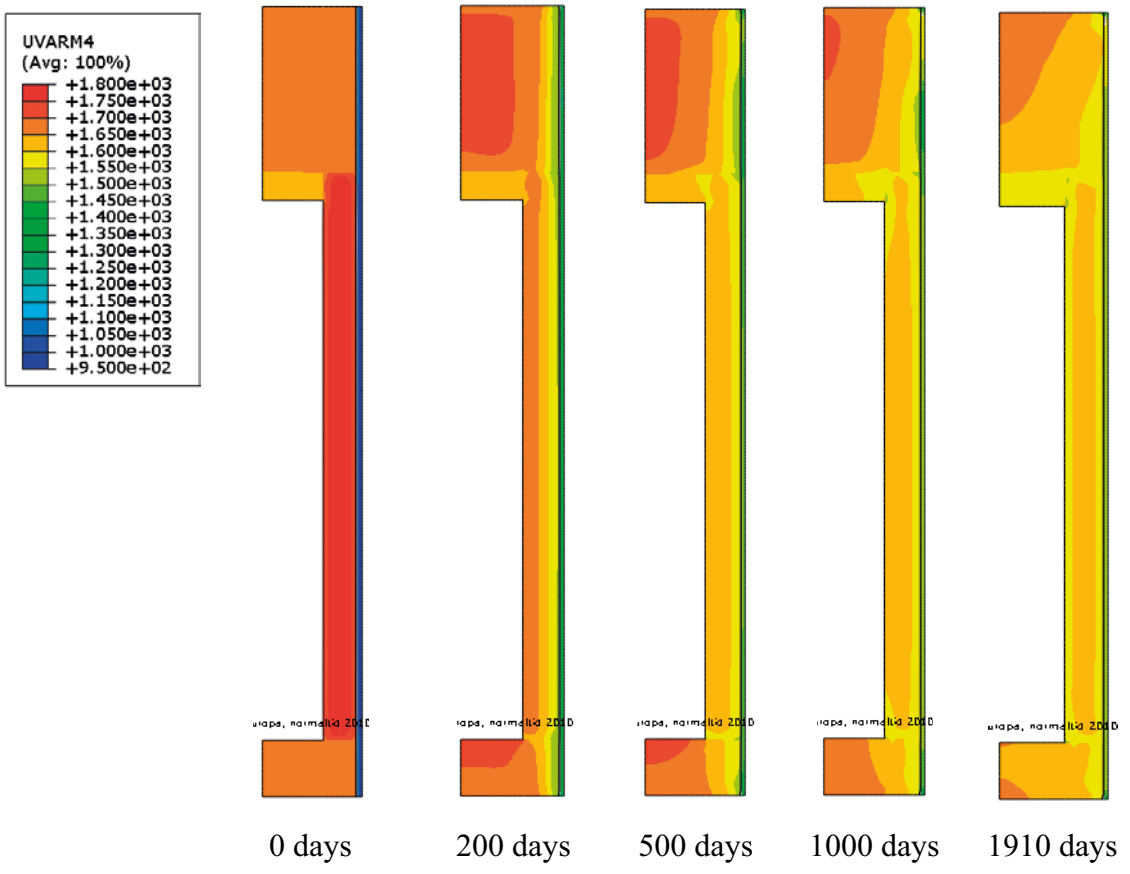

Figure 3-107. *Dry density (kg/m^3) distribution at different times (denoted uvarm4).*

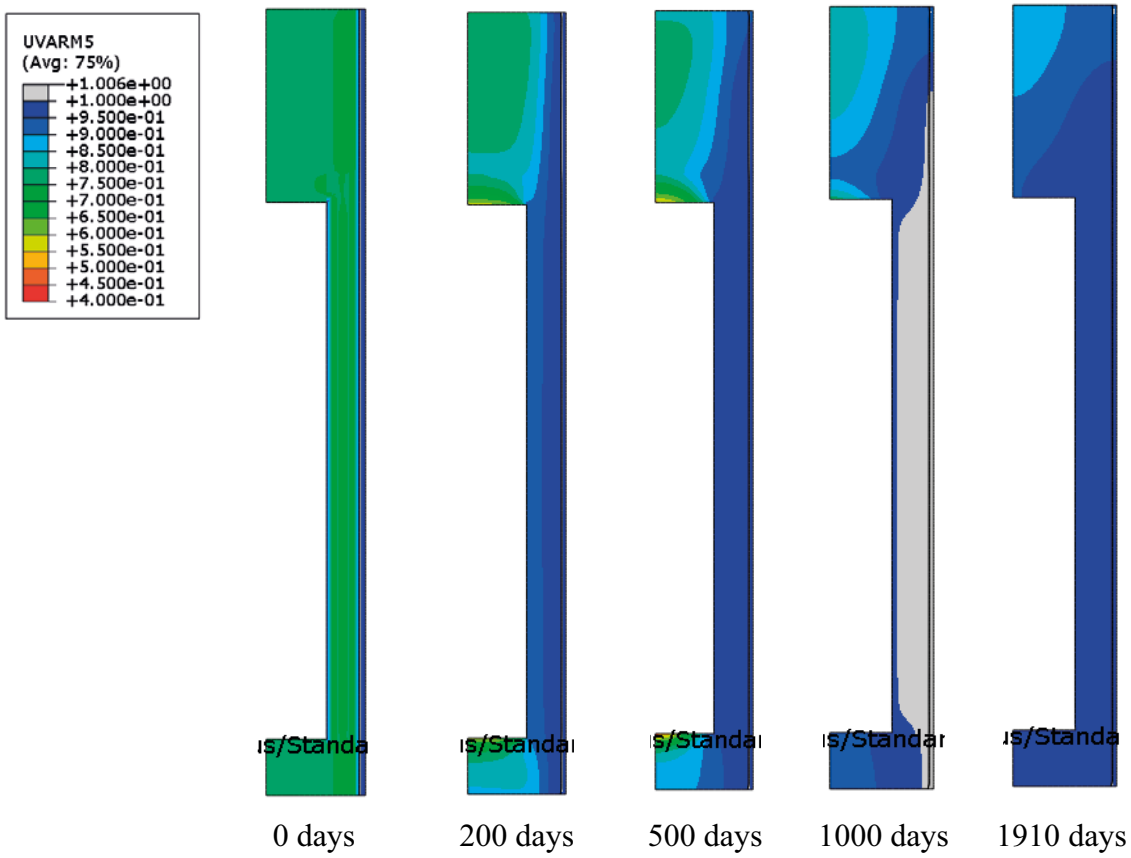

Figure 3-108. *Relative humidity distribution at different times (denoted uvarm5).*

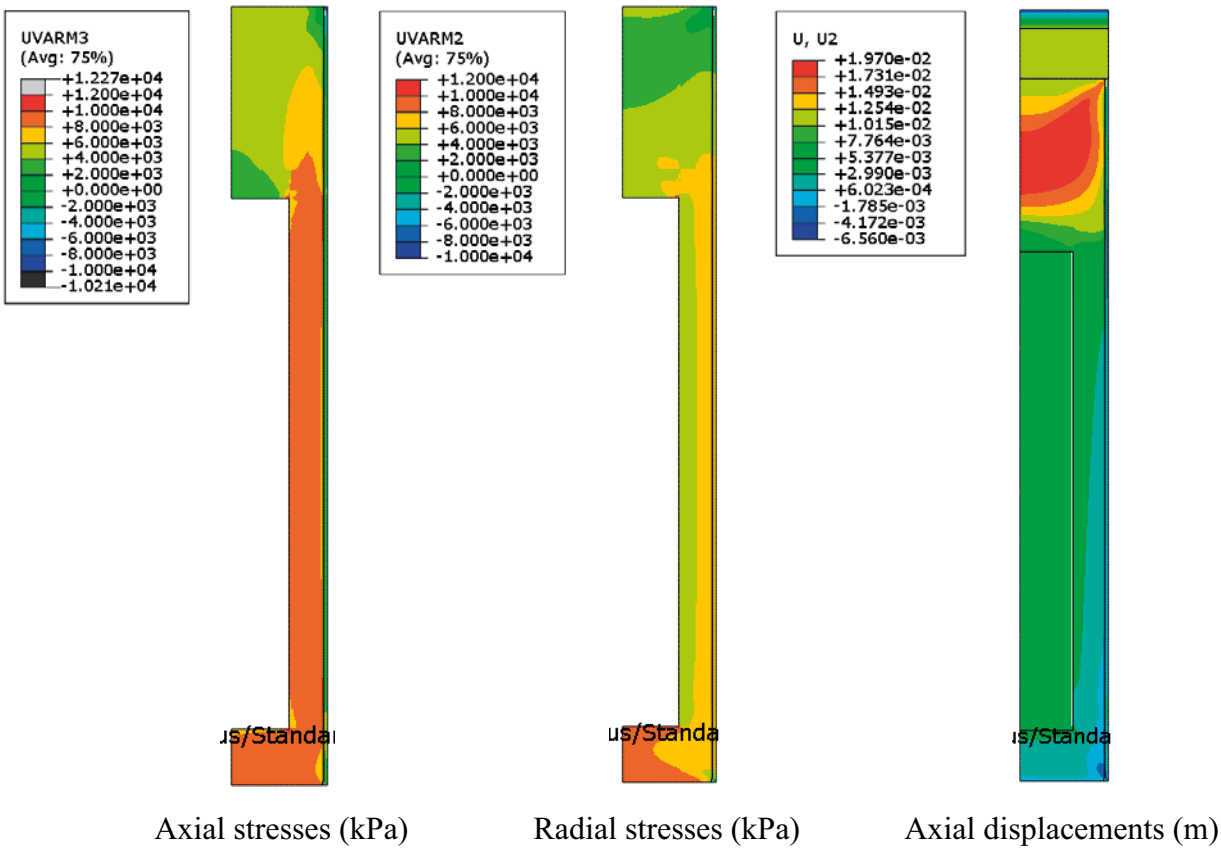

Figure 3-109. *Distribution of axial and radial stresses (kPa) and axial displacements (m) at the end of the test.*

Paths

Radial distributions of variables (called paths) are plotted for three different locations as shown in Figure 3-110: through block C3, 10 cm above the canister lid through ring R10 and the bentonite bricks, and in ring R5.

The degree of saturation and the dry density are shown for these paths in Figures 3-111 to 3-113.

It is interesting to compare the results in path R5, which would correspond to the position as modelled with the 1D calculation. The comparison shows that the density distribution at the end of the test is straighter in the 2D calculation at the location of the compacted ring, since the reduction in density close to the canister and close to the pellets slot is not captured in the 2D calculation. The reason for this difference is most likely the difference in mesh resolution. The 29 cm thick ring is modelled with 6 radial elements in the 2D calculation while there are 29 elements in the 1D calculation. Another difference is the average dry density in the "ring-part" which is slightly lower in the 2D calculation. The reason for this is most likely that there is some vertical expansion that is not modelled in the 1D calculation but also that the pellets slot is slightly more compressed in the 2D calculation. The reason for the larger compression of the pellets slot is not clear.

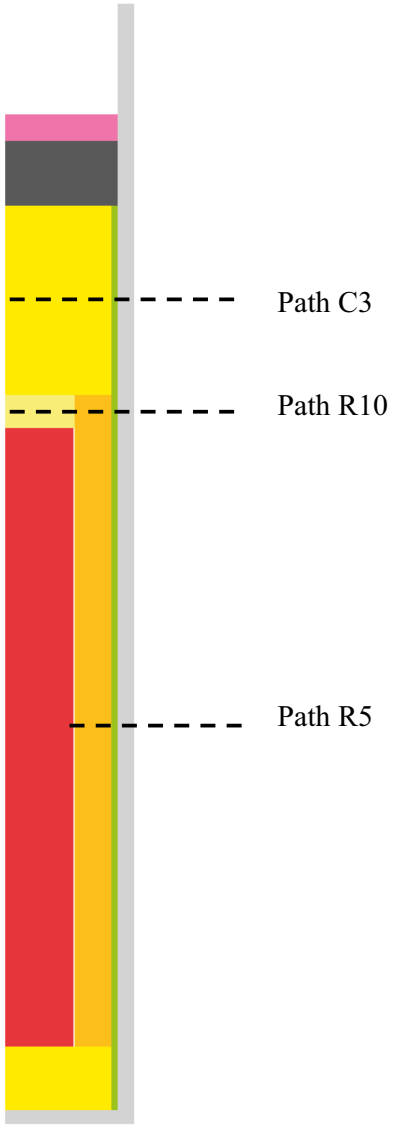

Figure 3-110. *Location of paths.*

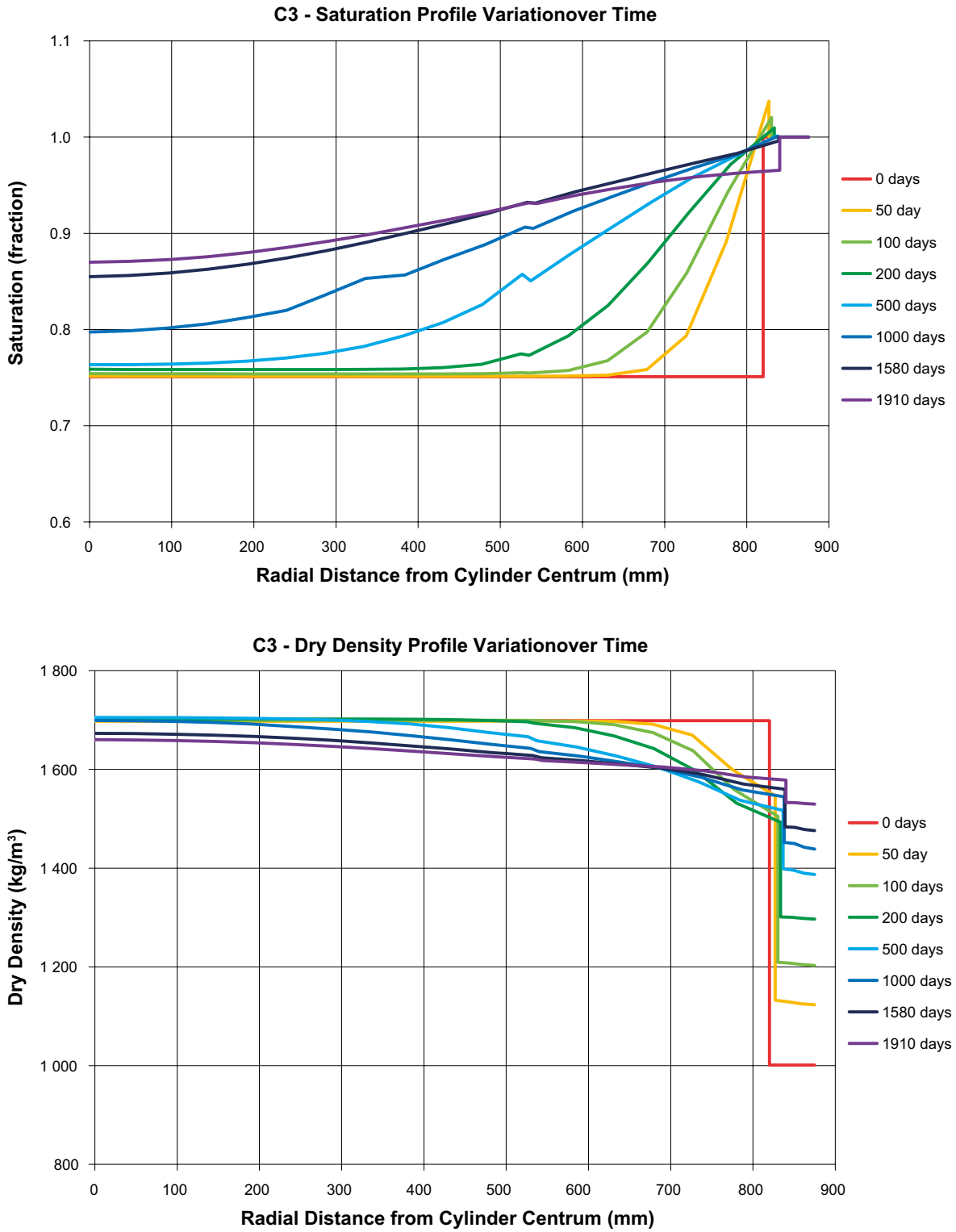

Figure 3-111. *Degree of saturation and dry density as function of the radial distance for path C3.*

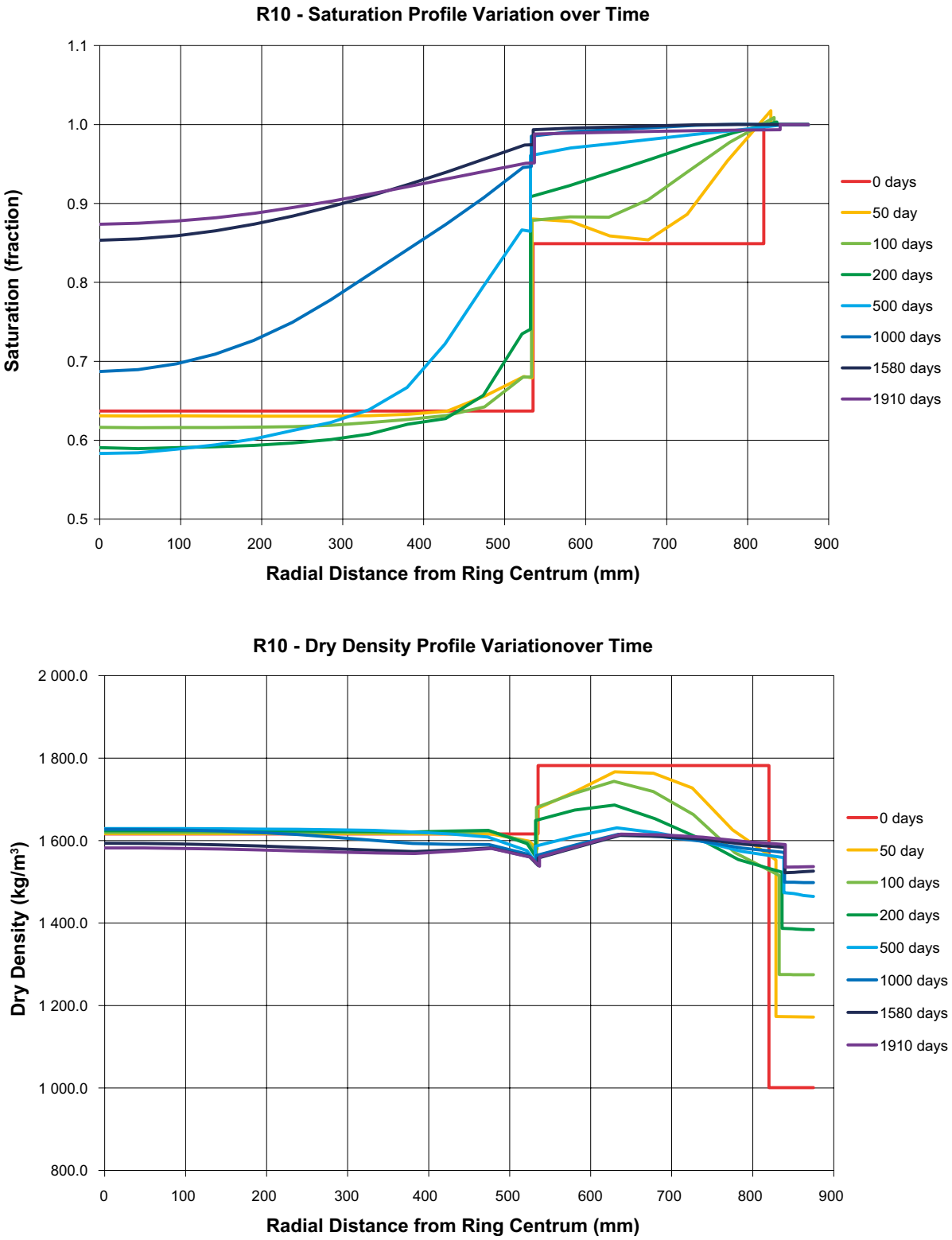

Figure 3-112. *Degree of saturation and dry density as function of the radial distance for path R10.*

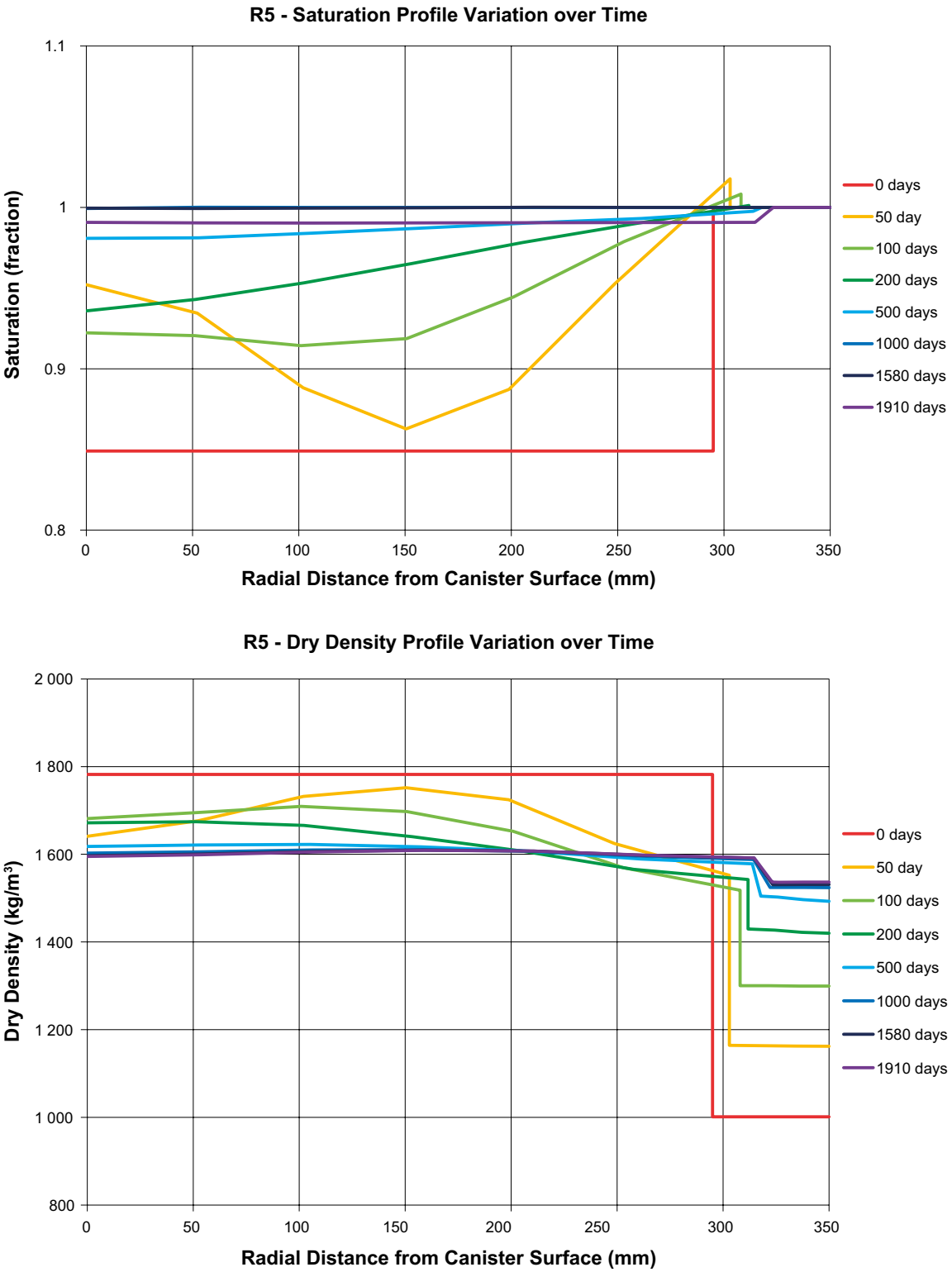

Figure 3-113. *Degree of saturation and dry density as function of the radial distance for path R5.*

History plots

A large amount of history plots are generated at the points of interest and required points according to the task description. All these plots are included in Section 3.5.13. They show history of dry density, degree of saturation, vertical total stress, horizontal total stress, vertical displacements, horizontal displacements, relative humidity and suction. Here only a few plots will be shown and only for sections R10 and C5 since the results in section R5 are very similar to the results of the 1D calculation shown in Section 3.5.8.

Figure 3-114 shows dry density and degree of saturation in section R10 and Figure 3-115 shows horizontal and vertical total stresses in this section.

Figures 3-116 and 3-117 show corresponding results in section C3.

The force on the plug and corresponding displacement of the plug are also included in the modelling. The history plots of these variables are shown in Section 3.5.10 together with measured results.

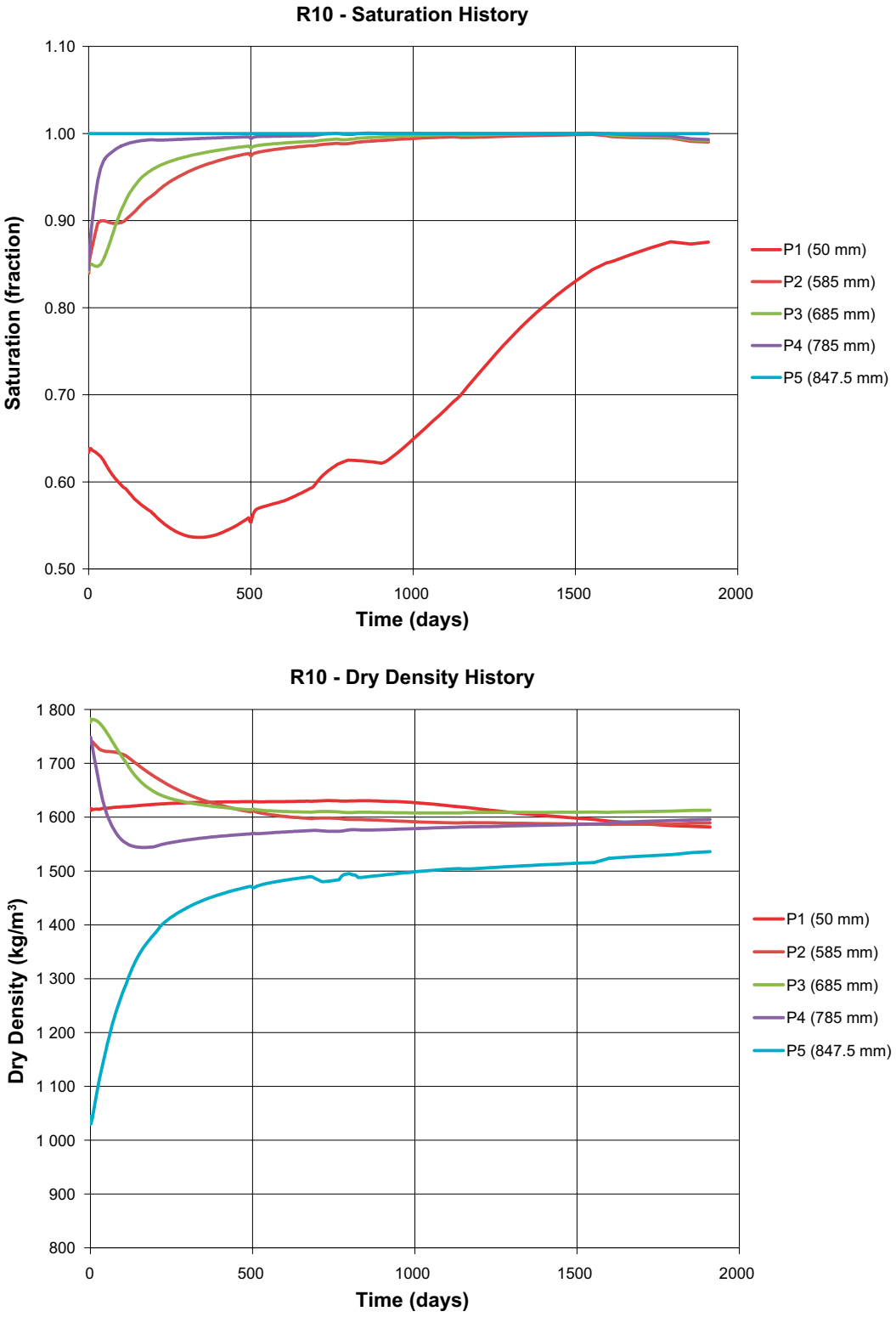

Figure 3-114. *Degree of saturation and dry density as function of time in section R10.*

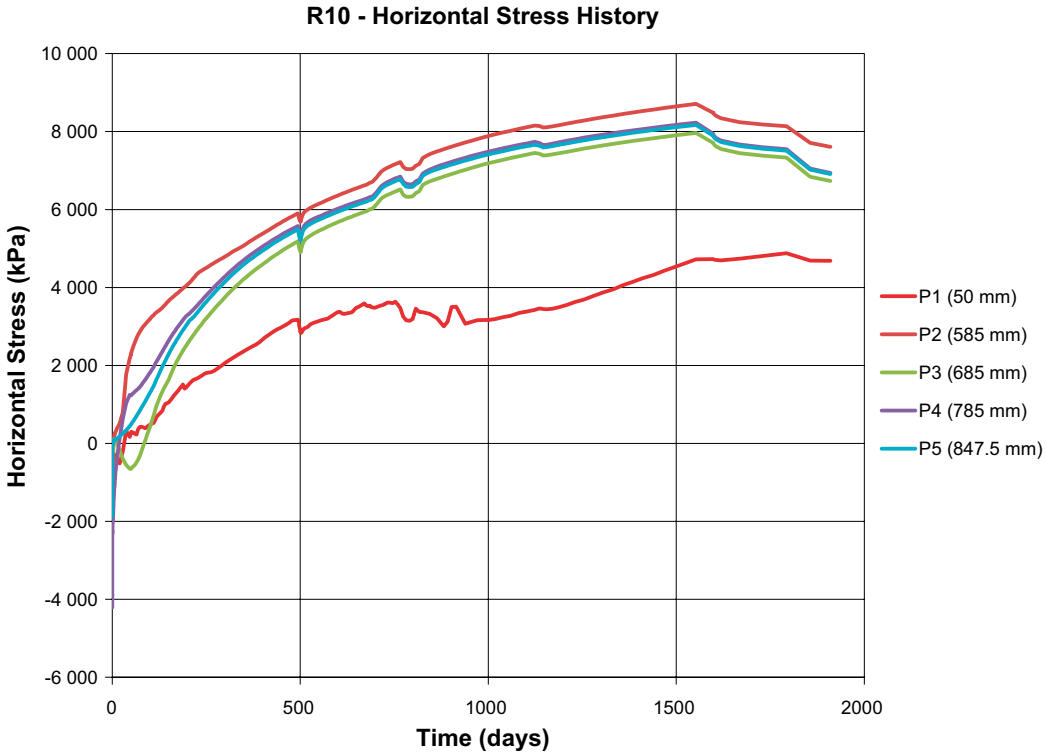

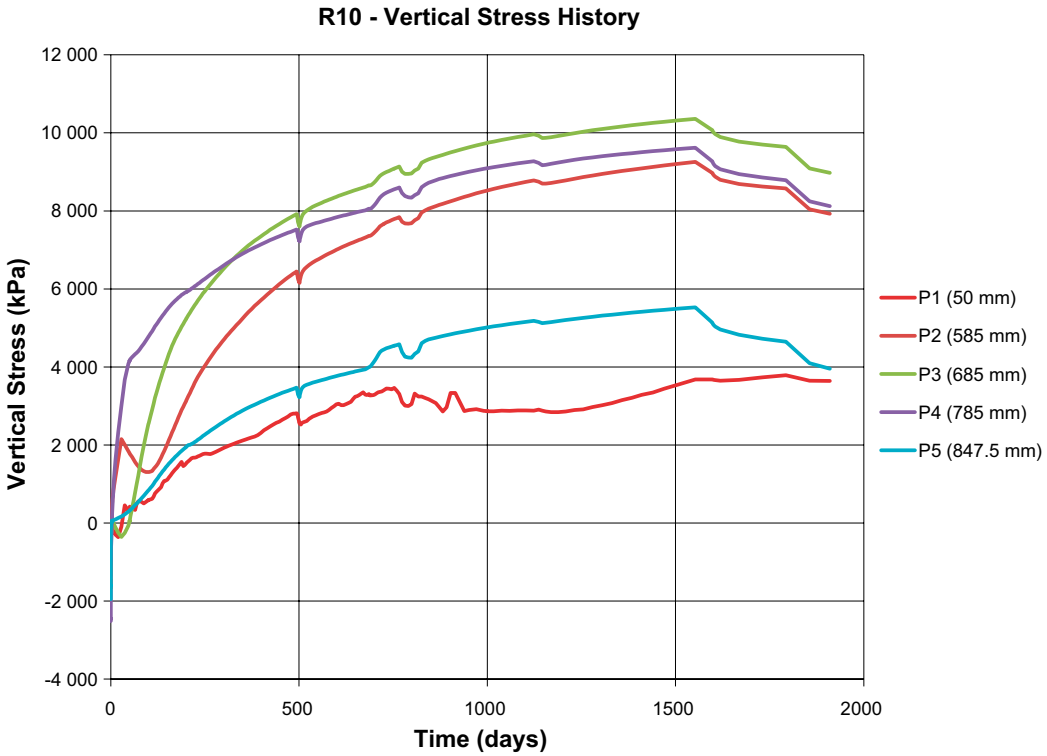

Figure 3-115. *Horizontal (radial) and vertical (axial) total stress as function of time in section R10.*

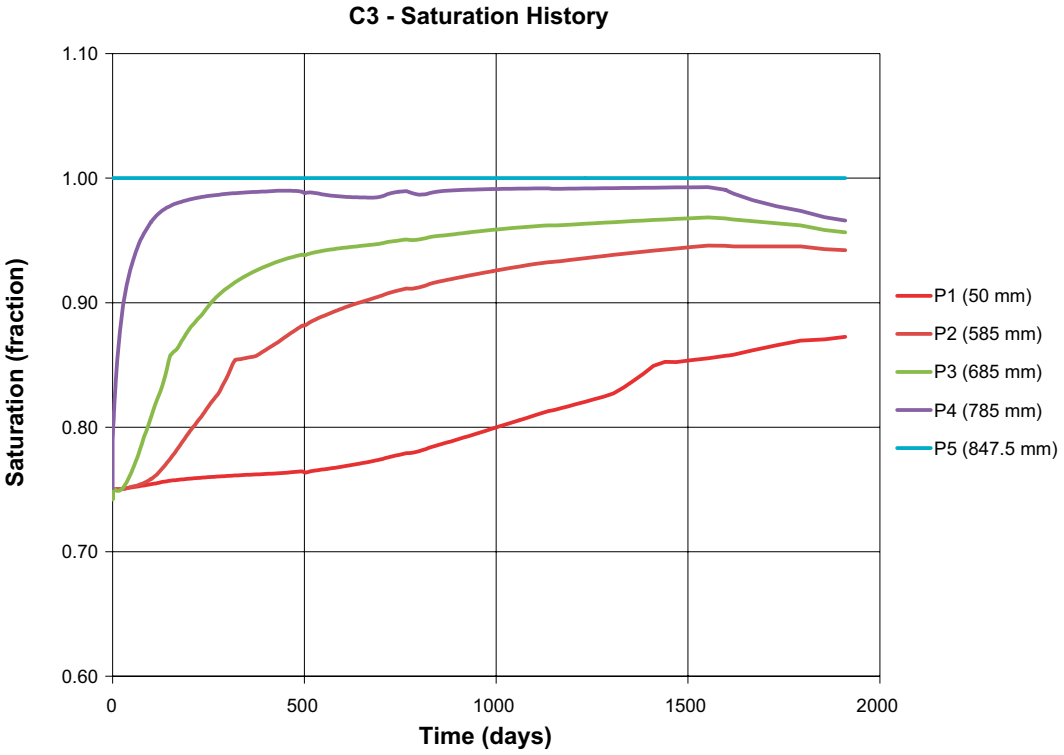

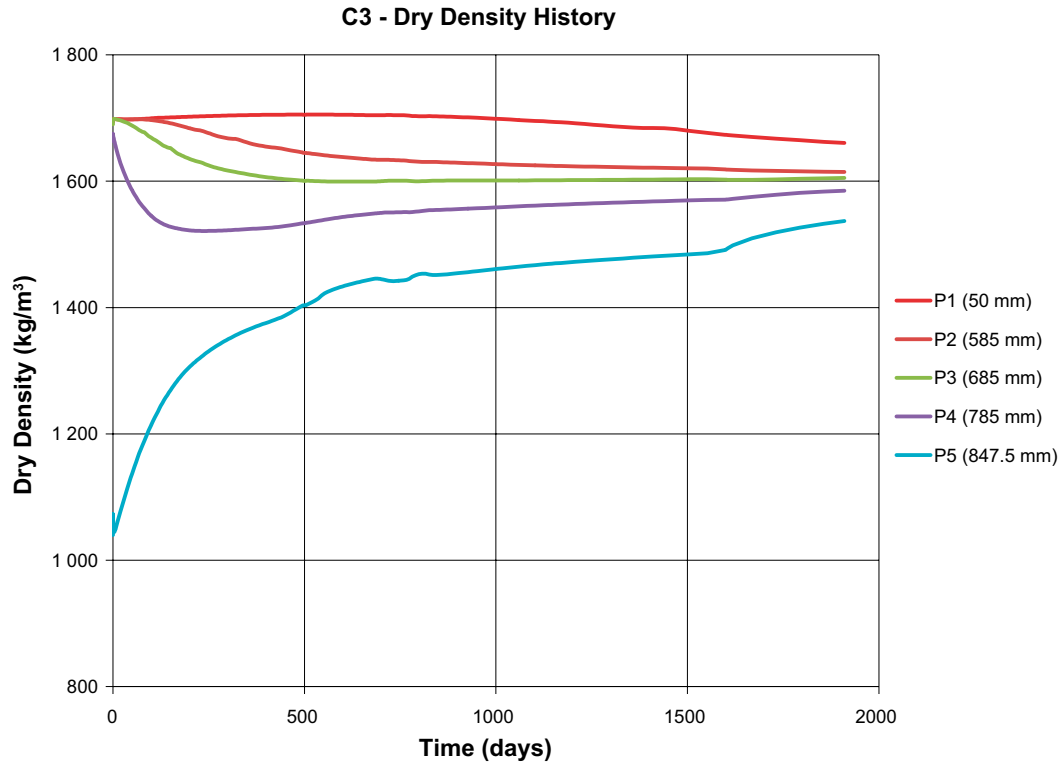

Figure 3-116. *Degree of saturation and dry density as function of time in section C3.*

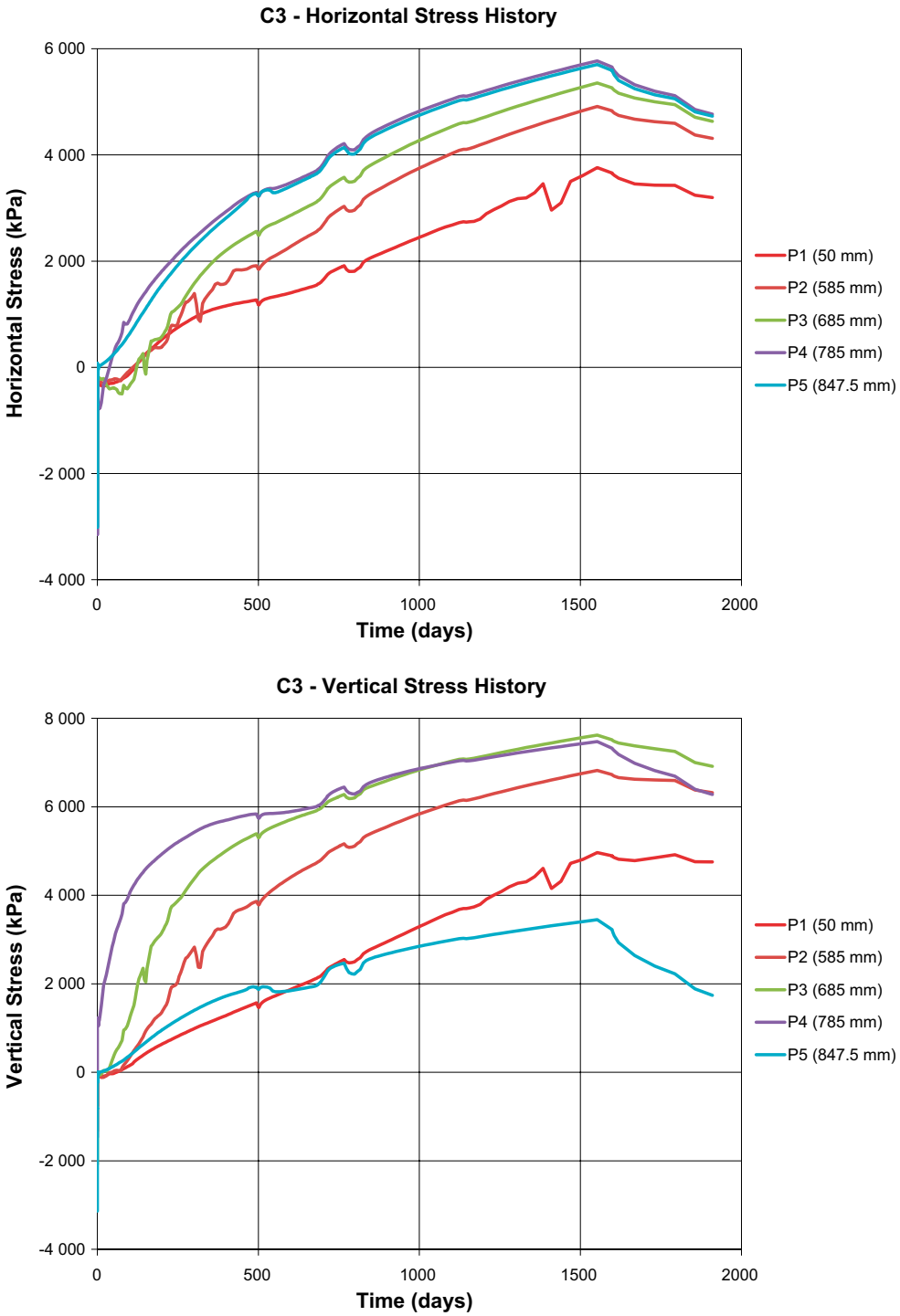

Figure 3-117. *Horizontal (radial) and vertical (axial) total stress as function of time in section C3.*

3.4.10 Comparison between results calculated with the 2D model and measured results

As mentioned in Section 3.2.4 there are several results from measurements that can be used to compare with the modelling results. These comparisons can be made both as variables plotted as function of time and as end of test results plotted as paths.

Temperature

Figure 3-118 to 3-120 show measured and modelled temperature as function of time for points located on the paths in sections R5, R10 and C3.

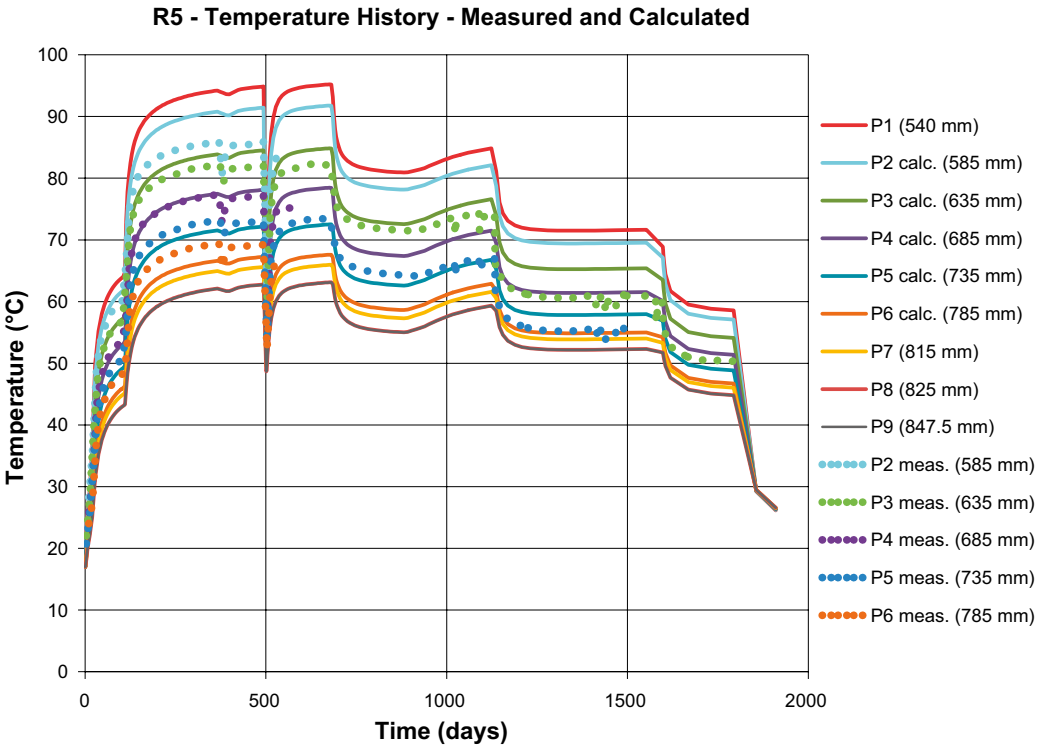

Figure 3-118. *Modelled and meausred temperature in section R5.*

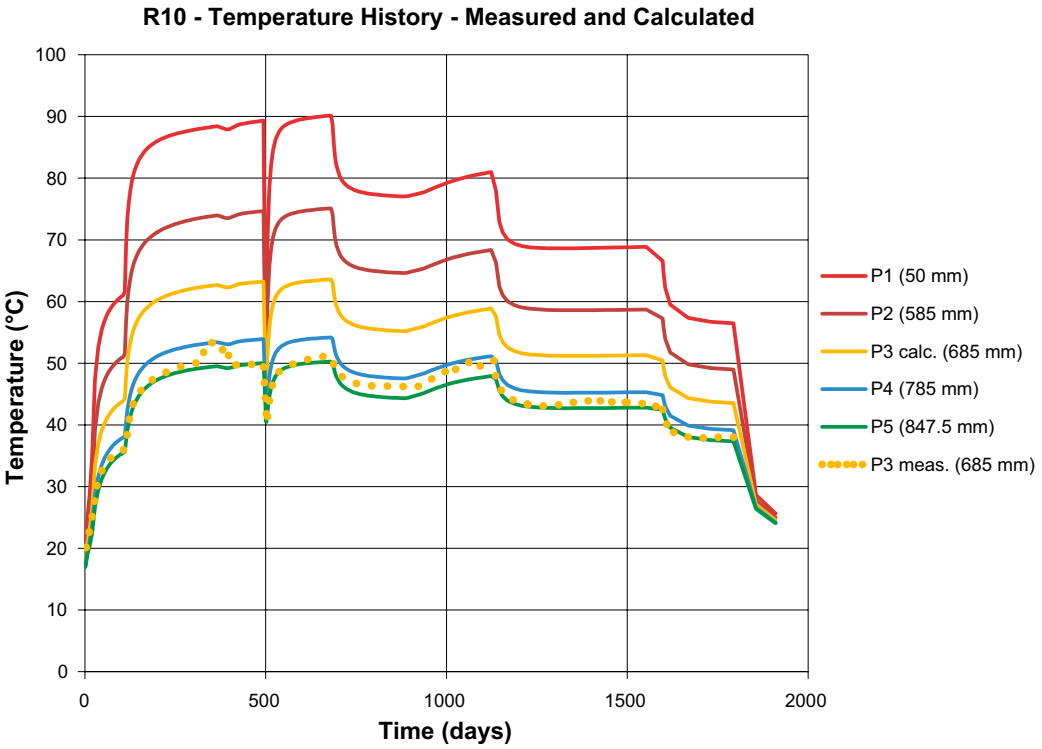

Figure 3-119. *Modelled and meausred temperature in section R10.*

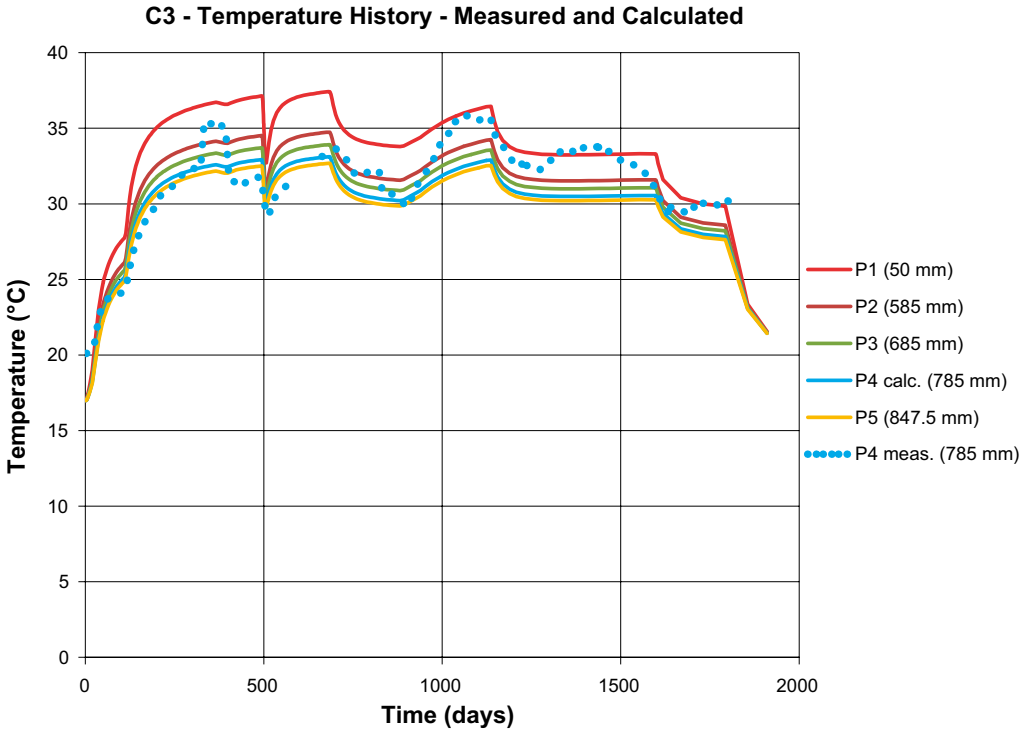

Figure 3-120. *Modelled and measured temperature in section C3.*

The comparisons show that the general agreement is good but also that there are some differences that are larger than might be expected considering the bases of the temperature calculations. However, the unsymmetrical heat from the neighbouring TBT experiment is not taken into account since the model is axial symmetric so the temperatures may differ depending on what side of the canister they are measured.

Relative humidity and pore pressure

The moisture increase and redistribution is measured with two instruments that yield relative humidity (up to RH = 95 %) and suction (lower than 5 000 kPa). The instruments thus complement each other. Figure 3-121 to 3-123 show measured and modelled results.

The results for section R5 are almost identical to the results of the 1D-model. The comparison shown in Figure 3-102 has a way of comparison with RH recalculated to suction with both types of transducers plotted in the same diagram yielding better resolution. Both figures show though that the agreement is rather good with exception of the parts close to the limitations of the transducer validity and close to full saturation. The latter is dealt with in Section 3.5.8.

Also for section R10 the modelled and measured results agree well with the same remarks as for section R5. Unfortunately the RH-transducers stopped working rather early but as can be seen the drying and subsequent wetting of the central part was very well modelled.

Section C3 shows similar results with very good agreement in the centre of the section. The wetting/drying process seems to be well captured since the absence of drying at this section is well modelled. The wetting rate closer to the periphery at the radius is overestimated according to the RH-transducer but not according to the late results of the suction transducer.

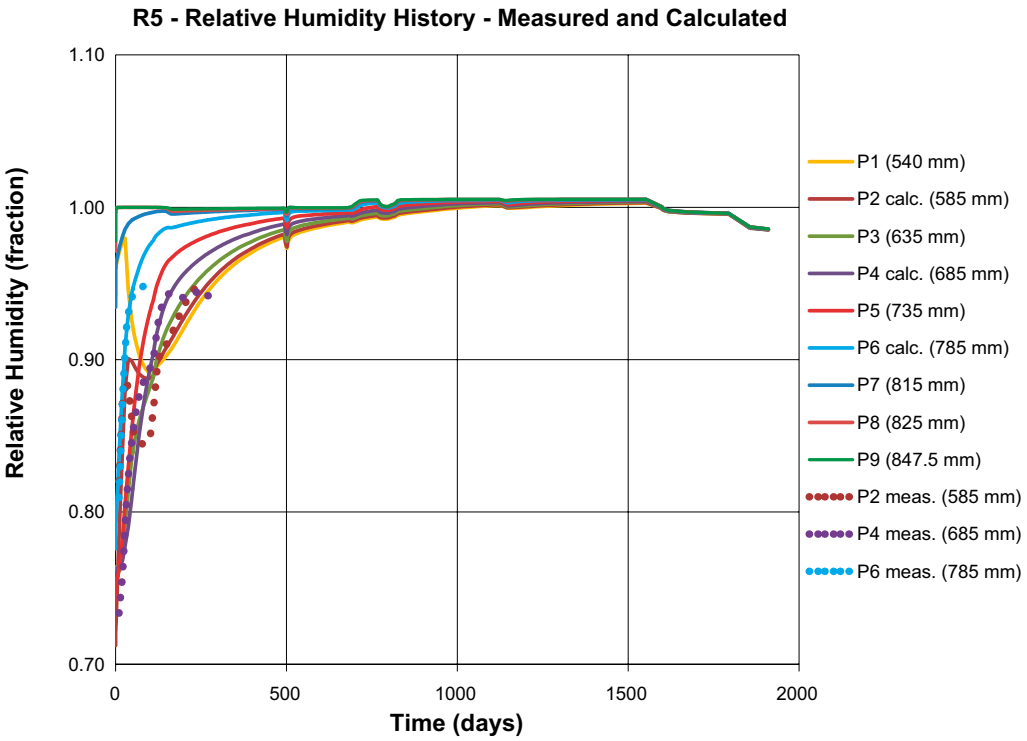

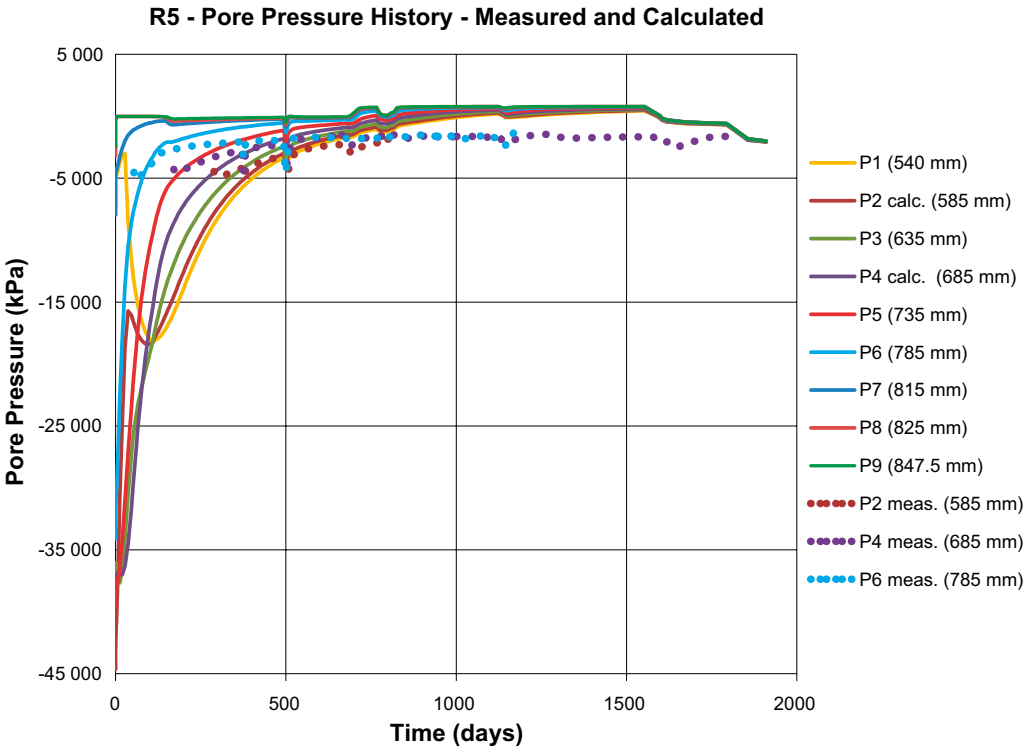

Figure 3-121. *Modelled and measured moisture history in section R5.*

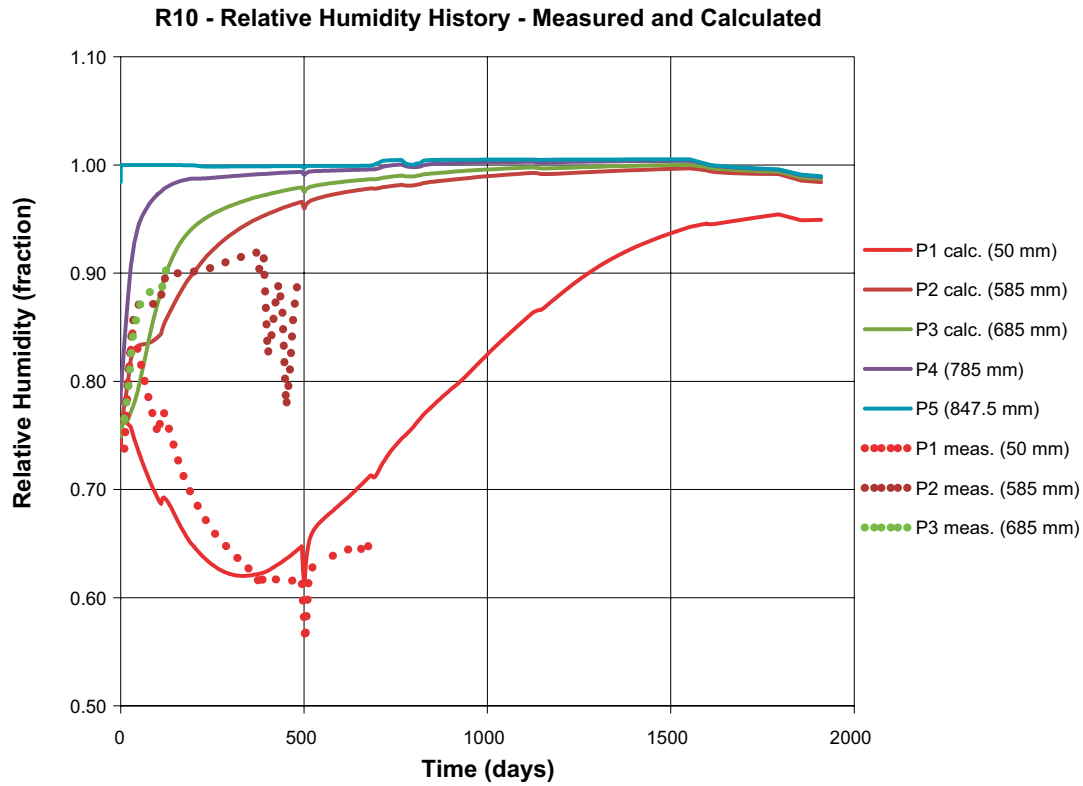

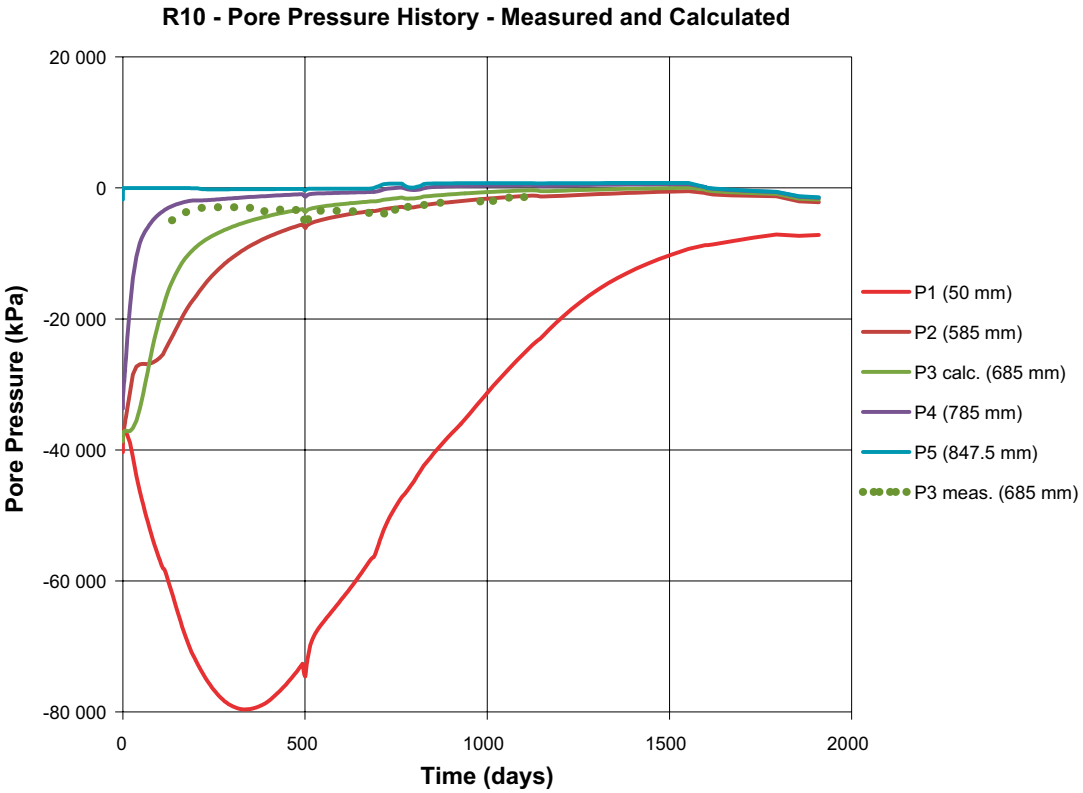

Figure 3-122. *Modelled and measured moisture history in section R10.*

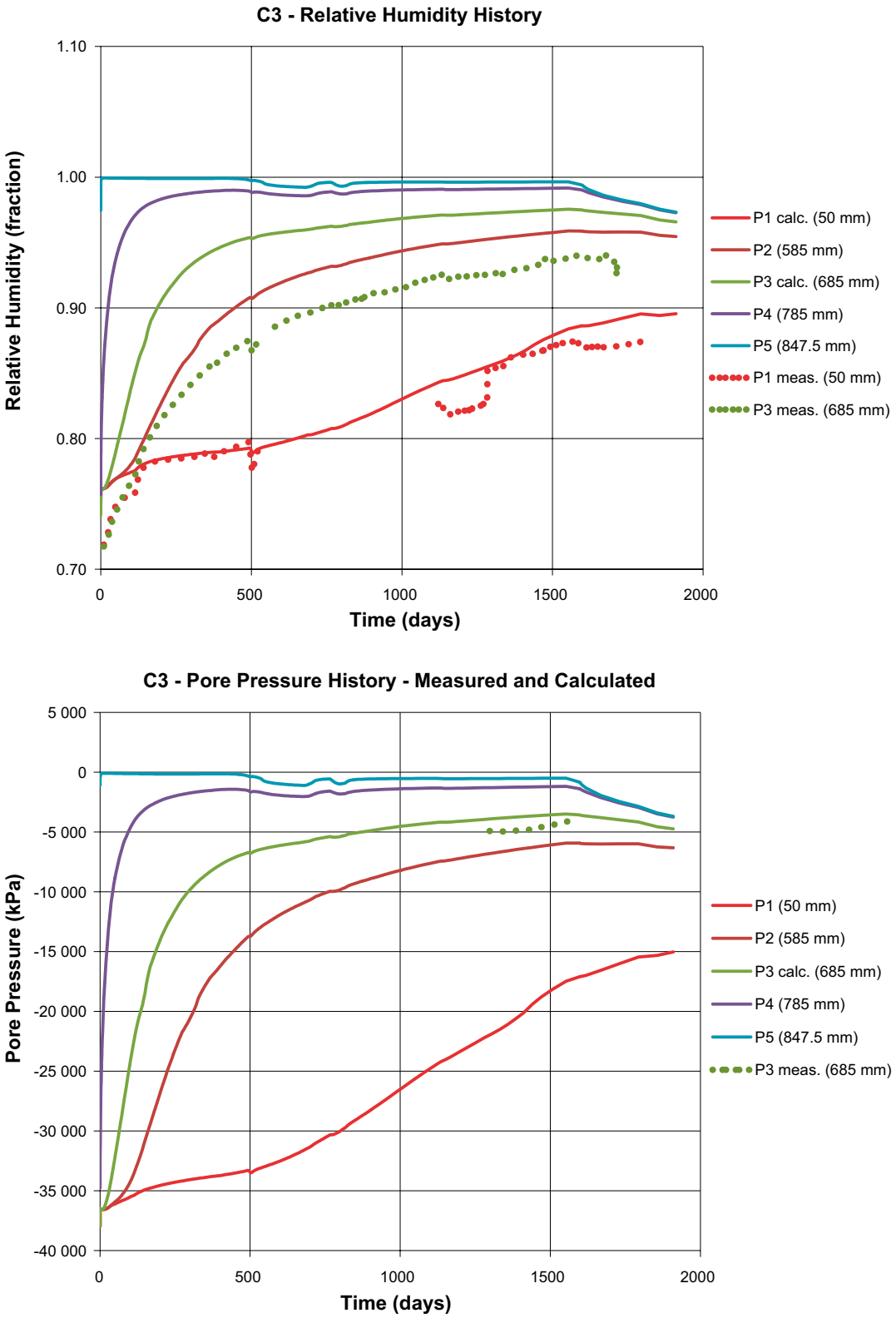

Figure 3-123. *Modelled and measured moisture history in section C3.*

Total axial stress

The total stress was measured with long tube-shaped instruments that turned out to be not very good. They seem to strongly underestimate the total pressure as analysed earlier. The modelled and measured results are shown in Figures 3-124 to 3-126

Section R5 is completely water saturated so there should be a chance to measure correct total stress with proper transducers. However as shown in Figure 3-124 the measured values are less than half the modelled values.

Sections R10 and C3 are not water saturated so measurements are even less reliable. In section R10 the measured value is only a third of the calculated value and in section C3 there were no measured stress at all but this is a consequence of the low degree of water saturation.

That these discrepancies are largely caused by the transducer design is supported by the measurements in the Prototype Repository with identical hole and bentonite block geometries, where the measured swelling pressures are higher and more in agreement with the modelled.

It is also interesting to study the effect of the sudden temperature drops that occurred due to heater failures. Clear drops in total stress as consequence of the temperature drops are modelled but the magnitude of the pressure drops are much smaller than measured. The reason for this discrepancy is not clear and should be further studied.

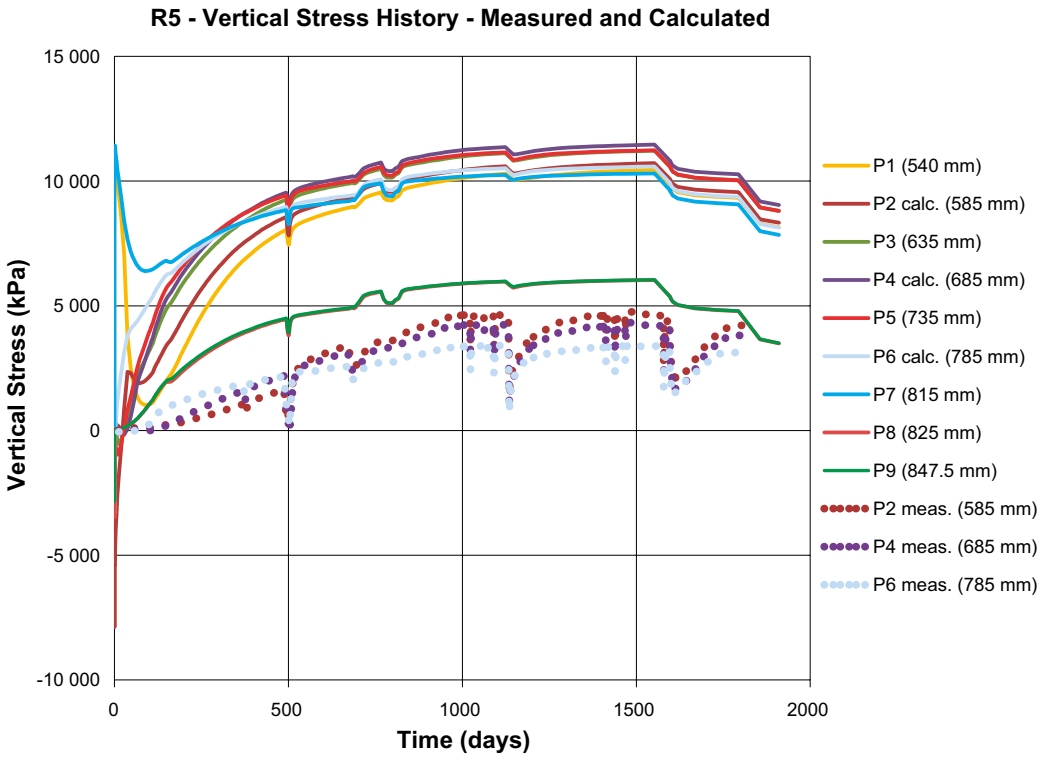

Figure 3-124. *Modelled and measured total axial stress in section R5.*

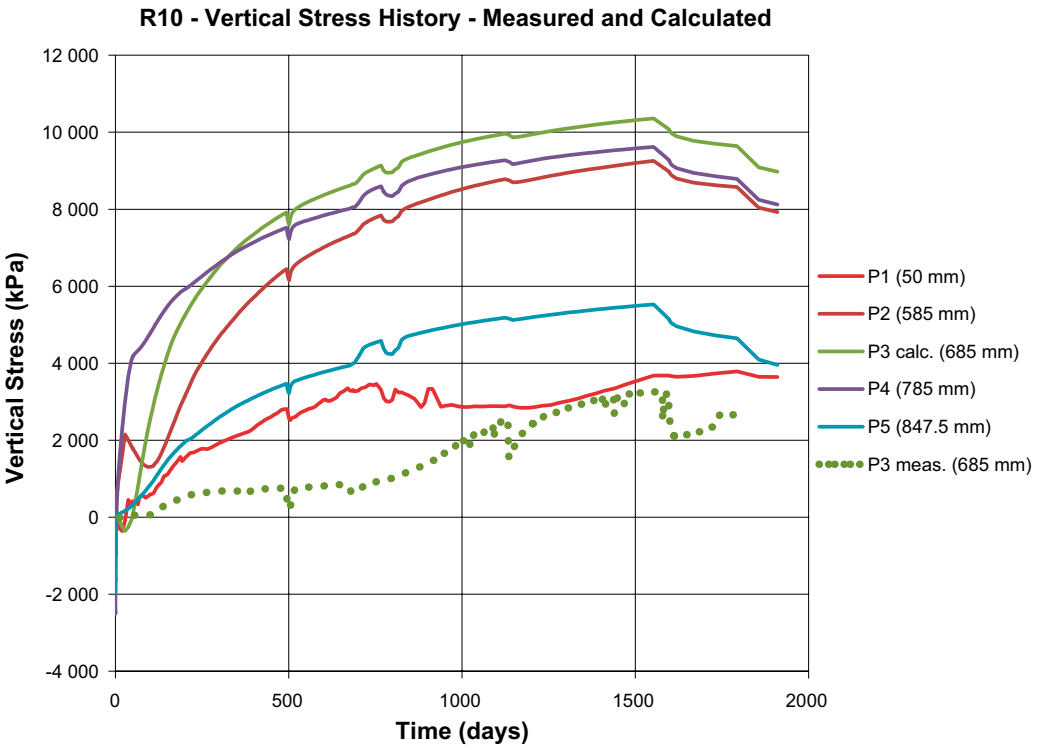

Figure 3-125. *Modelled and measured axial total stress in section R10.*

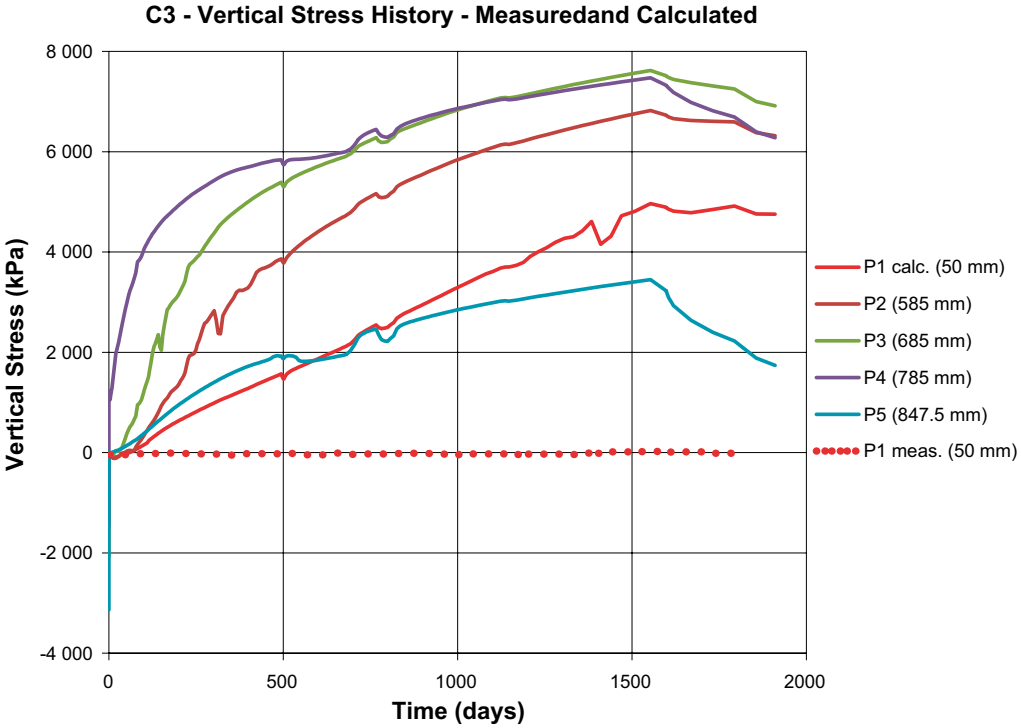

Figure 3-126. *Modelled and measured total axial stres in section C3.*

Density and saturation at the end of test

The bulk density ρ and the water ratio *w* were measured after sampling at the end of the test. Using the density of solids $\rho_m = 2\ 780$ kg/m^3 and the density of water $\rho_w = 1\ 000$ kg/m^3 the measured values can be transformed to dry density and degree of water saturation.

Figures 3-127 to 3-129 show comparison between measured and modelled values plotted as paths in sections R6, R10 and C3. The results are in fair agreement although there are some differences.

For ring 6, which was used since no sampling was undertaken in ring R5, the agreement is good in both degree of saturation and dry density, although the modelled density distribution is not as fine-tuned as in the 1D calculation due to the coarse element mesh.

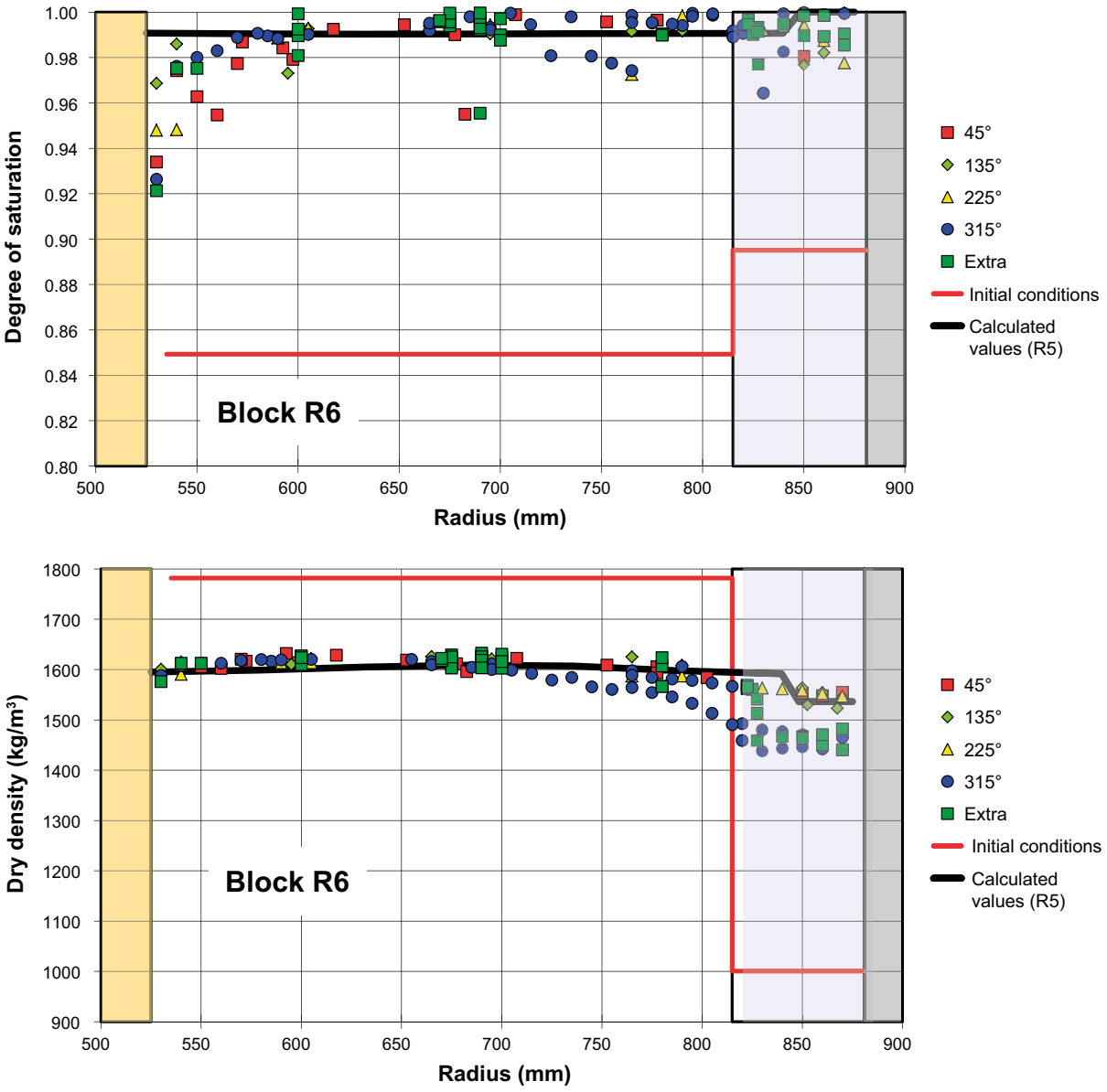

Figure 3-127. *Degree of saturation and dry density at the end of test plotted as function of the radius in section R6. Sampling was made in four directions noted as 45° etc.*

For ring R10 there is a slight difference in both variables. The degree of saturation is somewhat overestimated and the density distribution a little different. It seems as the water saturation is slower than modelled although that is not seen by the results of the RH-measurements in the beginning of the test (they stopped functioning after 600 days), but may be the case at the later stage of the test. The dry density is overestimated in the central part (brick section) and underestimated at the outer part (ring section). The measurements show that the density of the brick part, which was lower than the density of the ring part, has increased its density and ends with a higher density than the ring part. This is difficult to understand and not modelled. The most probable explanation is that the initial dry density of the brick section used in the modelling and showed in the figure $\rho_d = 1\ 616$ kg/m^3 is the average dry density that includes a thin layer of bentonite powder, while the dry density of the brick "stones" was 1 690 kg/m^3. Since the sampling actually was made in the bricks, the real process was a swelling of both the bricks and the ring yielding a decreased density as modelled and not the increased density of the bricks that is shown in the figure.

For block C3 the degree of saturation is overestimated in the central part, which is not in agreement with the measurement of RH. The dry density distribution seems to be well modelled.

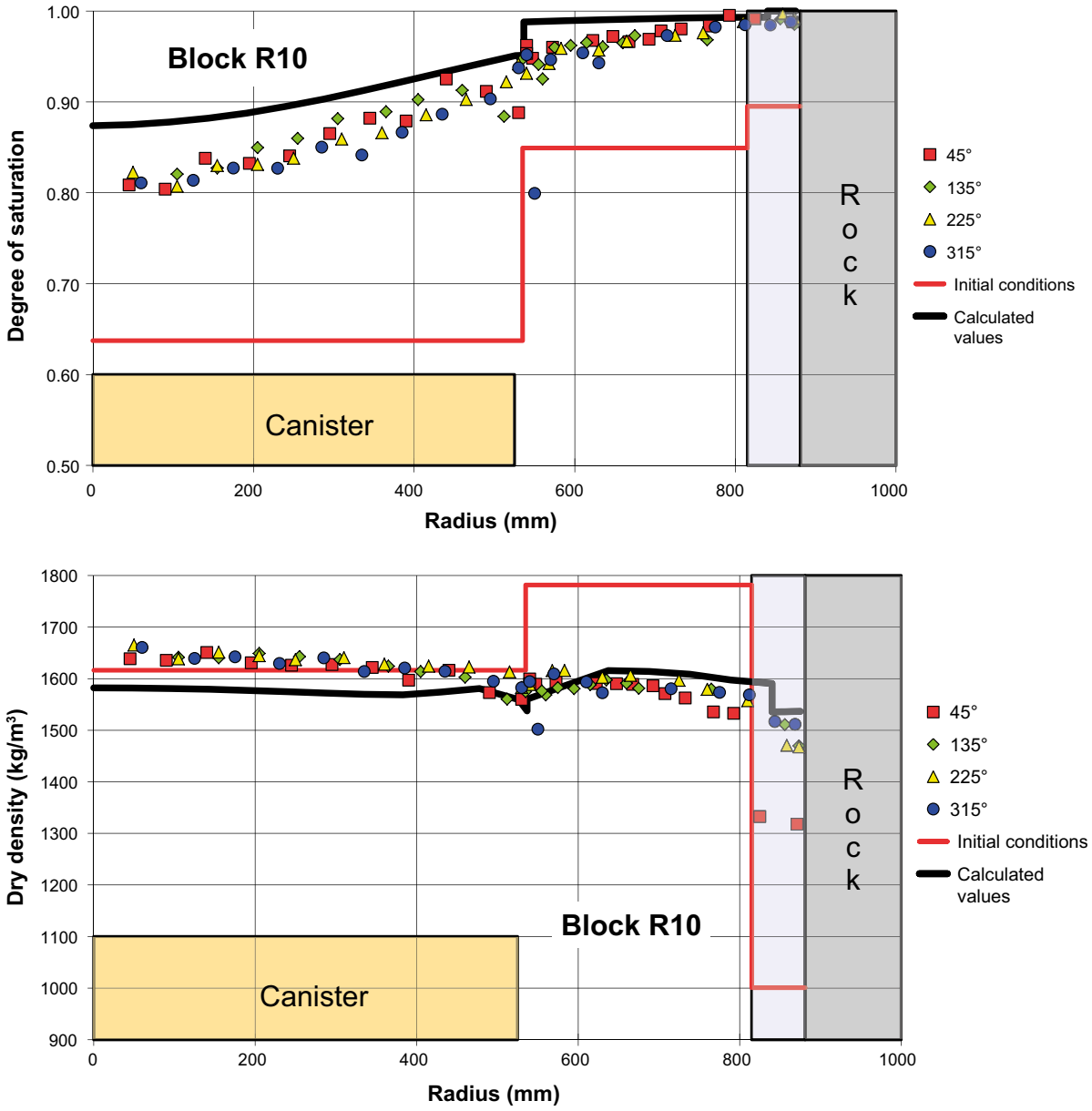

Figure 3-128. *Degree of saturation and dry density at the end of test plotted as function of the radius in section R10. Sampling was made in four directions noted as 45° etc.*

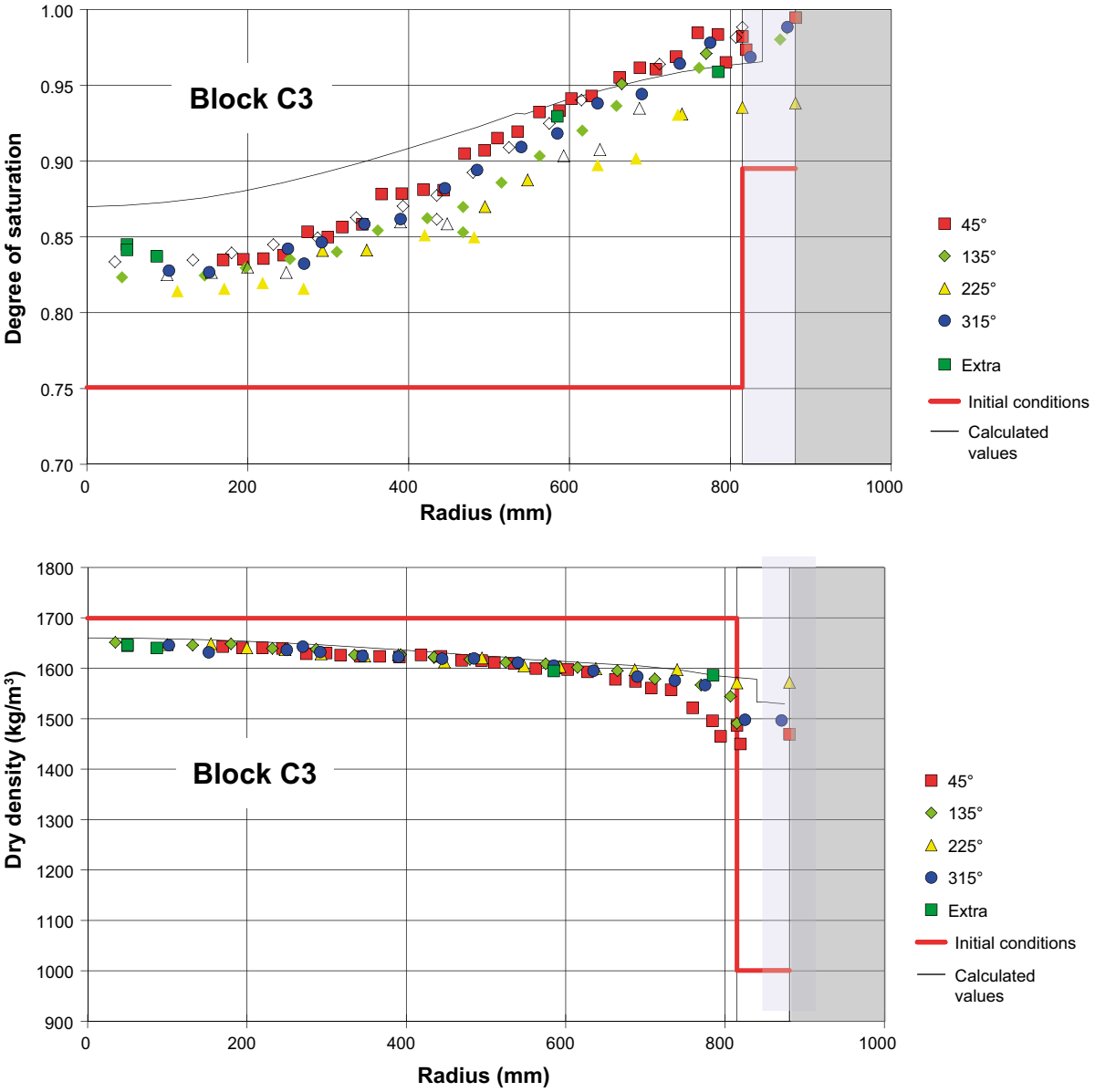

Figure 3-129. *Degree of saturation and dry density at the end of test plotted as function of the radius in section C3. Sampling was made in four directions noted as 45° etc.*

Plug response

The force on the plug and the displacement of the plug were measured. Figures 3-130 and 3-131 show the modelled and measured results as a function of time.

The modelled total force agree very well with the measured force, although it is a little higher in the first part of the test and ends a little lower than measured.

The modelled plug displacement seems to be underestimated but the difference stem from the start-up of the test, where the measurements during the first days show a heave of the plug while the modelling shows a slight sinking of the plug. The measured heave of the plug is caused by the initial lack of confinement before the rock anchors were fixed. The modelled sinking of the plug stems from an initial lack of force equilibrium that resulted in some displacements. The reason for this is not yet analysed. If these two anomalies are removed the agreement is as good as for the force, which is logical since the anchors are elastic and their elasticity well known.

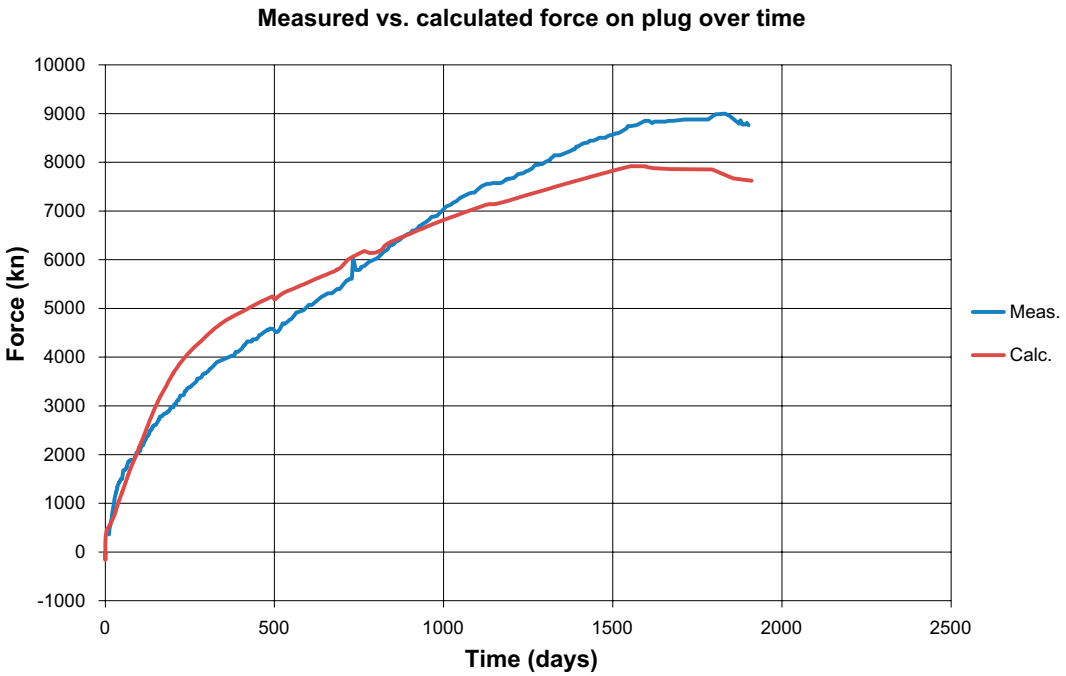

Figure 3-130. Modeled and measured history of the total force on the plug.

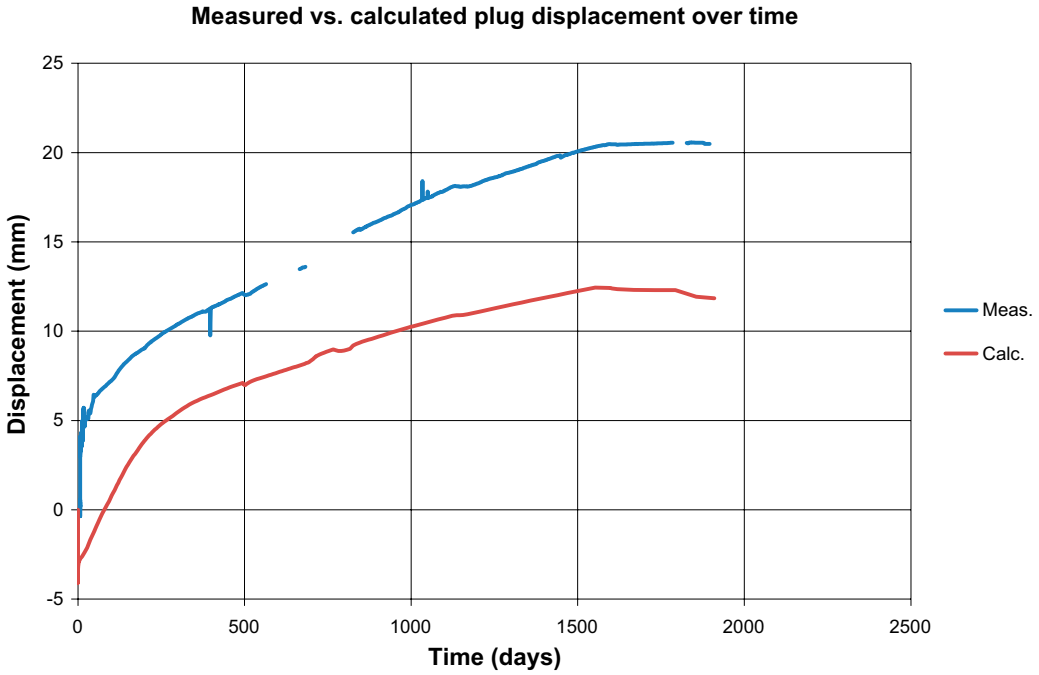

Figure 3-131. Modeled and measured history of the displacement of the plug.

3.4.11 Conclusions

The THM-processes in the full scale Canister Retrieval Test (CRT) has been modeled with the code Abaqus with two different axisymmetric models and compared with measured data, both during the test time and at the end of the test after excavation, sampling and measurement of water ratio and bulk density. A central section through ring 5 was modeled with a 1D axisymmetric model and the entire test including the plug and the canister were modeled with a 2D axisymmetric model.

It is worth mentioning that the modelled results are not derived after parameter adaptation in order to reach the best agreement. On the contrary, the parameter values have been derived directly from laboratory tests and used in the calculation without any changes.

Ring 5:

The 1D model of the central ring 5 yielded good results, both mechanically and hydraulically. The measured moisture evolution agrees very well with the modeled and the end of test results of degree of saturation and dry density also agree very well. However, the measured swelling pressure was less than half of the modelled, a discrepancy that was shown to mainly depend on the improper measuring devices.

The entire CRT:

The 2D model of the entire test also yielded good agreement between modeled and calculated results.

For ring 5 the results were equal to the 1D calculation with exception of the density distribution that differed slightly due to the vertical displacements that could not take place in the 1D model and also due to the difference in element mesh. The element mesh was much finer in the 1D calculation which yielded a better density distribution that captured the influence of the inner gap and the outer pellets filled slot better.

The modeled moisture history just above the canister in section R5 and further up in section C3 agreed well with measurements but the degree of saturation at the end of the test was a little lower than measured in both sections.

The modeled density distribution in sections R10 and C3 agreed well with measured. The small discrepancy at the brick filled part of section R10 above the canister was concluded to depend on that the sampling was done in the bricks while the average initial density used in the model was lower and also included a layer filled with bentonite powder. The modeled total axial stress was higher than measured, which can be explained by the transducer design and is especially critical when the bentonite is not water saturated.

The modeled history of the force on the plug agreed very well with measured, which additionally support that the modeled stresses are more correct than the measured ones. The disagreement between the measured and modeled displacement of the plug could be explained by early effects before start of the actual test.

The overall conclusion is that the test was well modeled and that the material models and calculation technique have been validated.

References

SKB's (Svensk Kärnbränslehantering AB) publications can be found at www.skb.com/publications.

ABAQUS Manuals, 2008. Dassault Systemes Simulia Corp.

Birgersson M, Karnland O, Nilsson U, 2010. Freezing of bentonite. Experimental studies and theoretical considerations. SKB TR-10-40, Svensk Kärnbränslehantering AB.

Börgesson L, 1985. Water flow and swelling pressure in non-saturated bentonite-based clay barriers. Engineering Geology 21, 229–237.

Börgesson L, Hernelind J, 1999. Coupled thermo-hydro-mechanical calculations of the water saturation phase of a KBS-3 deposition hole. Influence of hydraulic rock properties on the water saturation phase. SKB TR-99-41, Svensk Kärnbränslehantering AB.

Börgesson L, Fredriksson A, Johannesson L-E, 1994. Heat conductivity of buffer materials. SKB TR 94-29, Svensk Kärnbränslehantering AB.

Börgesson L, Johannesson L-E, Sandén T, Hernelind J, 1995. Modelling of the physical behaviour of water saturated clay barriers. Laboratory tests, material models and finite element application. SKB TR 95-20, Svensk Kärnbränslehantering AB.

Börgesson L, Fälth B, Hernelind J, 2006. Water saturation phase of the buffer and backfill in the KBS-3V concept. Special emphasis given to the influence of the backfill on the wetting of the buffer. SKB TR-06-14, Svensk Kärnbränslehantering AB.

Börgesson L, Åkesson M, Birgersson M, Hökmark H, Hernelind J, 2016. EBS TF – THM modelling. BM 1 – small scale laboratory tests. SKB TR-13-06, Svensk Kärnbränslehantering AB.

CIMNE, 2002. CODE_BRIGHT. A 3-D program for thermo-hydro-mechanical analysis in geological media. Departamento de Ingeneria del Terreno; Cartgrafica y Geofisica, UPC, Barcelona, Spain.

Croney D, Coleman J D, Black W P M, 1958. Movement and distribution of water in soil in relation to highway design and performance. In Water and its conduction in soils. Highway Research Board, 226–252. (Highway Research Board Special Report 40)

Dixon D, Chandler N, Stroes-Gascoyne S, Kozak E, 2001. The isothermal buffer–rock–concrete plug interaction test: Final report. Report 06819-REP-01200-10056-R00, Ontario Power Generation, Nuclear Waste Management Division, Canada.

Dixon D, Chandler N, Graham J, Gray M N, 2002. Two large-scale sealing tests conducted at Atomic Energy of Canada's underground research laboratory: the buffer–container experiment and the isothermal test. Canadian Geotechnical Journal 39, 503–518.

Dueck A, 2004. Hydro-mechanical properties of a water unsaturated sodium bentonite: laboratory study and theoretical interpretation. PhD thesis. Department of Building and Environmental Technology, Division of Soil Mechanics and Foundation Engineering, Lund University.

Dueck A, 2007. Results from suction controlled laboratory tests on unsaturated bentonite – Verification of a model. In Schanz T (ed). Experimental unsaturated soil mechanics. Berlin Springer-Verlag, 329–335.

Dueck A, Börgesson L, 2007. Model suggested for an important part of the hydro-mechanical behaviour of a water unsaturated bentonite. Engineering Geology 92, 160–169.

Dueck A, Nilsson U, 2010. Thermo-hydro-mechanical properties of MX-80. Results from advanced laboratory tests. SKB TR-10-55, Svensk Kärnbränslehantering AB.

EBS, 2005. Specification of Benchmark THM 1.1, Bentonite THM Mock-up Experiments Performed by CEA. Notes for Task force on Engineered Barrier System.

Fredlund D G, Rahardjo H, 1993. Soil mechanics for unsaturated soils. New York: Wiley.

Fälth B, Hökmark H, 2006. TBT – Evaluation Modeling Program. In Åkesson M (ed). Äspö Hard Rock Laboratory. Temperature Buffer Test. Evaluation modeling – Field test. SKB IPR-06-10, Svensk Kärnbränslehantering AB.

Gens A, 2016. Äspö Hard Rock Laboratory. SKB Task Force on Engineered Barrier System (EBS) Task 1: Laboratory tests. SKB TR-14-24, Svensk Kärnbränslehantering AB.

Goudarzi R, Börgesson L, Röshoff K, Edelman M, 2006. Äspö Hard Rock Laboratory. Canister Retrieval Test. Sensors data report (Period: 001026–060501), Report no. 12. SKB IPR-06-35, Svensk Kärnbränslehantering AB.

Graham J (ed), 1997. The buffer/container experiment: results, synthesis, issues. AECL-11746, COG-97-46-I, Whiteshell Laboratories, Manitoba, Canada.

Guo R, Dixon D, Priyanto D, 2006. The buffer/container experiment: description and materials parameters for use by the engineering barriers systems modeling taskforce. Technical Memorandum. Ontario Power Generation.

Houlsby G T, Puzrin A M, 2000. A thermomechanical framework for constitutive models for rate-independent dissipative materials. International Journal of Plasticity 16, 1017–1047.

Ingelstam E, Rönngren R, Sjöberg S, 1982. TEFYMA: handbok för teknisk fysik, fysik och matematik. Bromma: Sjöberg. (In Swedish.)

Johannesson L-E, 2007. Äspö Hard Rock Laboratory. Canister Retrieval Test. Dismantling and sampling of the buffer and determination of density and water ratio. SKB IPR-07-16, Svensk Kärnbränslehantering AB.

Kahr G, Kränbühl F, Stoeckli H F, Müller-Vonmoos M, 1990. Study of the water–bentonite system by vapour adsorption, immersion calorimetry and x-ray techniques. 2. Heats of immersion, swelling pressures and thermodynamic properties. Clay Minerals 25, 499–506.

Karnland O, Olsson S, Nilsson U, 2006. Mineralogy and sealing properties of various bentonites and smectite-rich clay materials. SKB TR-06-30, Svensk Kärnbränslehantering AB.

Kristensson O, Åkesson M, 2011. Homogenization of engineered barriers, simulations verified against Canister Retrieval Test data. Physics and Chemistry of the Earth 36, 1848–1856.

Low P F, Anderson D M, 1958. Osmotic pressure equations for determining themodynamic properties of soil water. Soil Science 86, 251–253.

Philip J R, de Vries D A, 1957. Moisture movement in porous materials under temperature gradients. Eos, Transactions American Geophysical Union 38, 222–232.

Sugita Y, Chijimatsu M, Suzuki H, 2005. Fundamental properties of bentonite pellet for Prototype Repository Project. In Alonso E E, Ledesma A (eds). Advances in understanding engineered clay barriers. London: Taylor & Francis. Material behavior and laboratory testing, 293–301.

Thorsager P, Börgesson L, Johannesson L-E, Sandén T, 2002. Äspö Hard Rock Laboratory. Canister Retrieval Test. Report on installation. Äspö Hard Rock Laboratory. SKB IPR-02-30, Svensk Kärnbränslehantering AB.

Wadsö L, Svennberg K, Dueck A, 2004. An experimentally simple method for measuring sorption isotherms. Drying Technology 22, 2427–2440.

Åkesson M (ed), 2008. Äspö Hard Rock Laboratory. Temperature Buffer Test. Evaluation modelling – TBT_3 Mock-up test. SKB IPR-08-09, Svensk Kärnbränslehantering AB.

Åkesson M, Kristensson O, Börgesson L, Dueck A, Hernelind J, 2010a. THM modelling of buffer, backfill and other system components. Critical processes and scenarios. SKB TR-10-11, Svensk Kärnbränslehantering AB.

Åkesson M, Börgesson L, Kristensson O, 2010b. SR-Site Data report. THM modelling of buffer, backfill and other system components. SKB TR-10-44, Svensk Kärnbränslehantering AB.

Appendix 1

Progressing saturation front for 1D axis-symmetric geometry

The hydration of the ITT buffer is simplified as a purely radial problem (Figure A1-1). The pressure at some distant radius (r_o) is held constant (P). The pressure at the interface between the buffer and the rock (at radius r_i) is denoted p_i. The pressure at the saturation front (at radius r_f) is zero.

The volumetric flow is the same at all radii, and a relation between the p_i and r_f can thus be derived as:

$$q = \frac{2 \cdot \pi \cdot K_{rock} \cdot (P - p_i)}{\ln(r_o) - \ln(r_i)} = \frac{2 \cdot \pi \cdot K_{buffer} \cdot (p_i - 0)}{\ln(r_i) - \ln(r_f)} \qquad (m^3 / m, s) \qquad \text{A1-1}$$

Which yields:

$$p_i(r_f) = \frac{P}{1 + \frac{(\ln(r_o) - \ln(r_i)) \cdot K_{buffer}}{(\ln(r_i) - \ln(r_f)) \cdot K_{rock}}} \qquad \text{A1-2}$$

The progressing saturation front can be quantified by the pore volume in-between to successive radii. This volume is equal to the product of the current flow (q) and the time increment (Δt):

$$q \cdot \Delta t = n \cdot (1 - S_l) \cdot \pi \cdot \left(\left(r_f^i\right)^2 - \left(r_f^{i+1}\right)^2 \right) \qquad \text{A1-3}$$

where indices i and i+1 represent two successive points in time. The updated radius can thus be derived as:

$$r_f^{i+1} = \sqrt{\left(r_f^i\right)^2 - \frac{q \cdot \Delta t}{n \cdot (1 - S_l) \cdot \pi}} \qquad \text{A1-4}$$

An algorithm has been elaborated for tracking a progressing front. The calculation is performed iteratively in such a way the flow rate for each step is derived from the current pressure at the rock wall (Equation A1-1). This flow and the specified time step are in turn used to calculate the subsequent radius of the front (Equation A1-4). Finally the pressure at the interface between the buffer and the rock is updated (Equation A1-2).

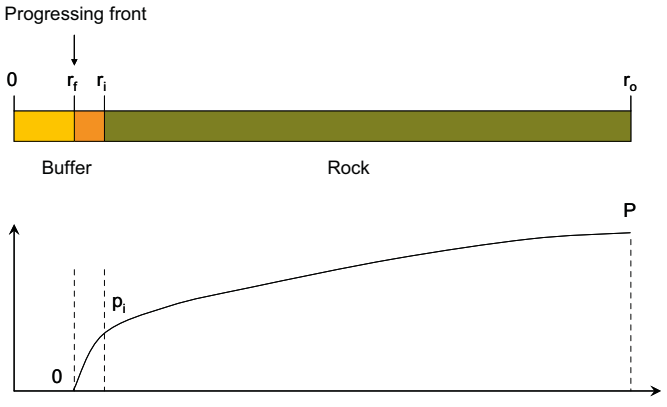

Figure A1-1. *Cylindrical flow geometry and boundary conditions.*

The parameter setting shown in Table A1-1 may be regarded as representative for ITT. Calculated evolutions of the radius of the front and the pore-pressure at the rock wall are shown in Figure A1-2 (left). From this it can be seen that total saturation was reached after approx. 11 years. The build-up of the pore-pressure is highlighted in the right graph. This includes the pressure at a radius of 1.42 m, which corresponds to the position of the IRP4 piezometer. The level and the slope of this graph are fairly close to the experimental data for this sensor. Pore pressure profiles are shown in Figure A1-3. The long range results are shown in the left graph together with experimental data. The right graph shows the details in the vicinity of the borehole.

Table A1-1. Used parameter values.

n (–)	S_l (–)	P (kPa)	r_o (m)	r_i (m)	K_{rock} (m/s)	K_{buffer} (m/s)	Δt (d)
0.359	0.843	1 500	30	0.62	10^{-12}	$5 \cdot 10^{-13}$	1

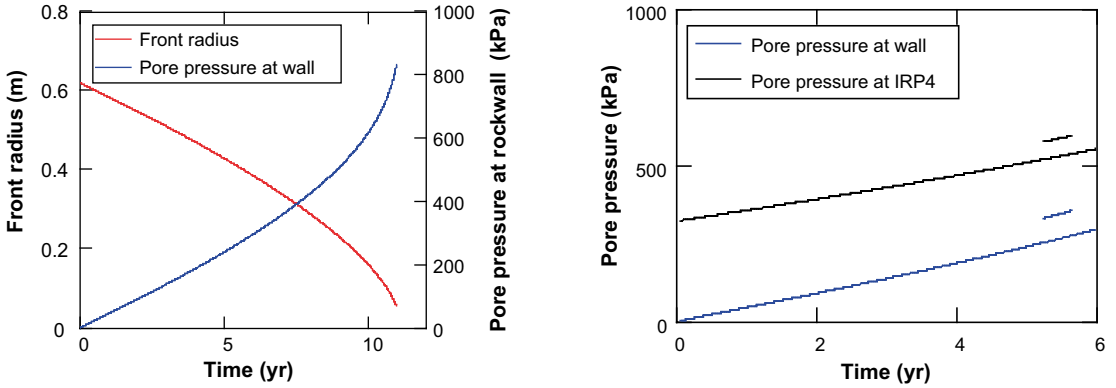

Figure A1-2. Evolution of front radius and pore pressure as rock wall (left). Pore pressure at rock wall and at radius corresponding to piezometer IRP4 (right).

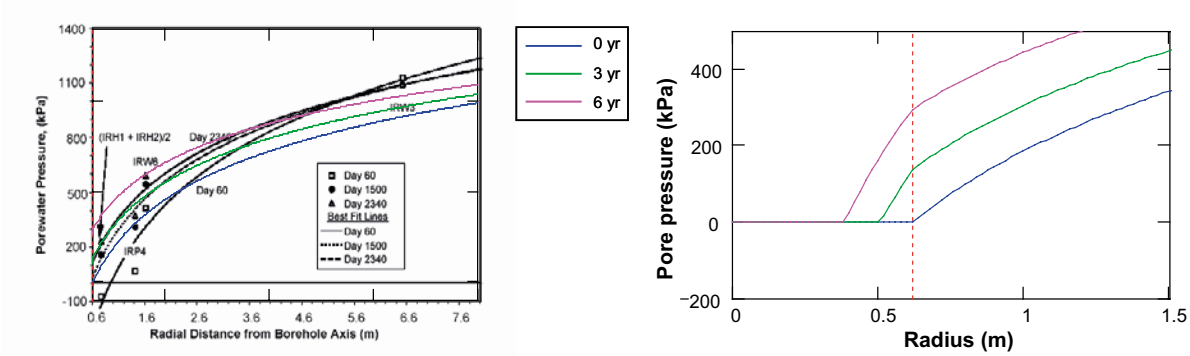

Figure A1-3. Pore pressure profiles at different times. Overlain experimental data (left) and detail (right). Measured data from Dixon et al. (2002).

Appendix 2

Material properties

The text in this section was included as an Appendix in the notes describing the experiment and assignment. That is why the numbers of tables and figures are not consistent with the rest of the document.

Bentonite buffer

Below in Table A2-1 estimated averaged values for the different bentonite parts before the saturation phase are shown, a solid density of 2 780 kg/m^3 has been used.

Table A2-1. Initial conditions of the CRT experiment.

Section	Density (kg/m^3)	Water ratio	Dry density (kg/m^3)	Void ratio	Degr. of saturation
Solid block	1 991	0.172	1 699	0.636	0.751
Ring shaped block	2 087	0.171	1 782	0.560	0.849
Bricks	1 883	0.165	1 616	0.720	0.637
Pellets I	1 101	0.100	1 001	1.778	0.156
Pellets II	1 574	0.572	1 001	1.778	0.895

Bentonite blocks

- MX-80.
- Ring-shaped (Rx) or cylindrical (Cx).

Block name	Date of compaction (yy-mm-dd)	Water ratio	Density (kg/m^3)	Weight (kg)	Average height (mm)	Degree of sat.	Void ratio
CRT NR R1	99-11-04	0.173	2 091.9	1 280.0	506.5	0.859	0.558
CRT NR R6	99-11-04	0.171	2 102.7	1 282.0	505.0	0.867	0.548
CRT NR R8	99-11-08	0.171	2 099.8	1 286.0	507.1	0.865	0.551
CRT NR R9	99-11-08	0.171	2 098.3	1 288.0	508.0	0.861	0.551
CRT NR R7	99-11-09	0.172	2 099.5	1 290.0	508.7	0.866	0.552
CRT NR R3	99-11-09	0.167	2 102.7	1 280.0	503.9	0.855	0.543
CRT NR R2	99-11-10	0.172	2 095.4	1 288.0	508.5	0.861	0.555
CRT NR R4	99-11-10	0.170	2 116.3	1 290.0	504.6	0.879	0.537
CRT NR R5	99-11-11	0.175	2 086.5	1 278.0	506.9	0.859	0.565
CRT NR R10	00-01-10	0.171	2 069.1	1 272.0	509.2	0.830	0.574
CRT NR C4	00-01-12	0.173	2 016.4	2 156.0	505.4	0.780	0.617
CRT NR C3	00-01-12	0.171	2 004.8	2 094.0	493.7	0.761	0.623
CRT NR C2	00-01-13	0.170	2 003.1	2 104.0	496.7	0.759	0.624
CRT NR C1	00-01-14	0.173	1 987.7	2 128.0	506.3	0.751	0.641

Bentonite pellets

- MX-80.
- “Pillow-shaped”.
- Width and length of 16.3 mm, thickness 8.3 mm.
- Bulk density of individual pellet 1 970–2 110 kg/m^3.
- Water ratio ≈ 10 %.

Figure A2-1. *Pellet geometry.*

Bentonite bricks

- MX-80.
- Dimensions: 115 × 234 × 64 mm.
- Average dry density: 1 800 kg/m^3.
- Water ratio: ≈ 10 %.

MX-80 properties

The used compact density of the bentonite is 2 780 kg/m^3 (Börgesson et al. 1995).

Thermal properties

The heat capacity c of the bentonite block and pellet-filled slot is c = 800 J/(m·K).

In Börgesson et al. (1994) the thermal conductivity of buffer materials was carefully characterized, and different models were compared. In Figure A2-2, taken from Börgesson et al. (1995), experimentally data of the thermal conductivity for MX-80 is given as a function of water saturation.

The work in Börgesson et al. (1994) concluded with a relation used in Börgesson et al. (1995) which is summarized in graphical form in Figure A2-3.

In accordance with Figure A2-3 (Sugita et al. 2005) found that the thermal conductivity for swollen pellets was slightly lower as compared to the thermal conductivity of blocks at comparable densities with the pellet cell. A2-4 shows the results given in Sugita et al. (2005)

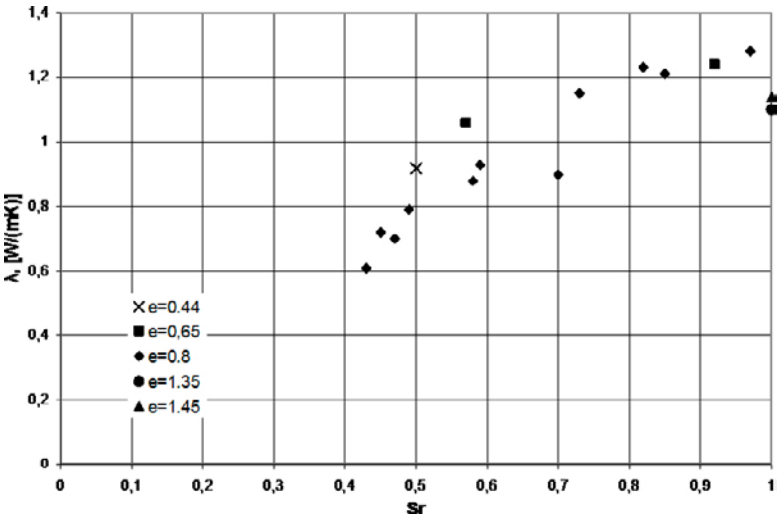

Figure A2-2. *MX-80 thermal conductivity as a function of the degree of saturation for different void ratios. From Börgesson et al. (1995).*

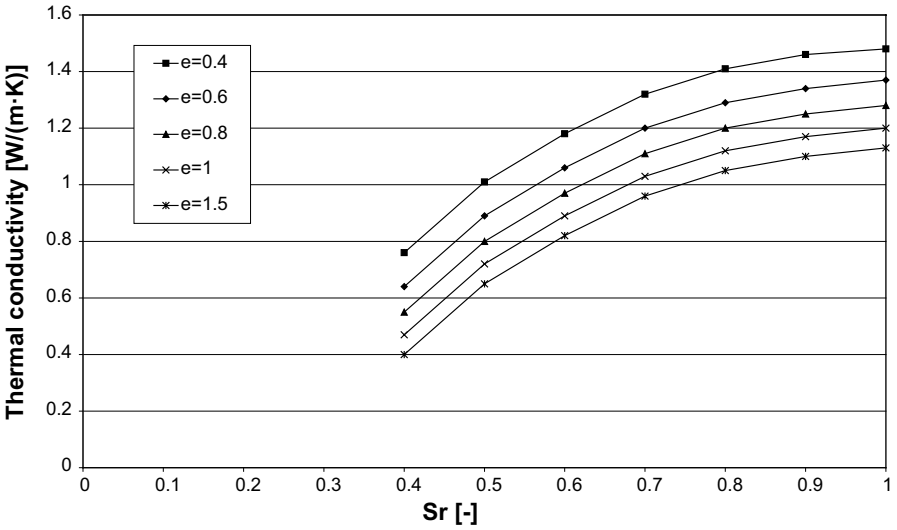

Figure A2-3. *Relation between void ratio, water saturation and thermal conductivity used in Börgesson et al. (1995).*

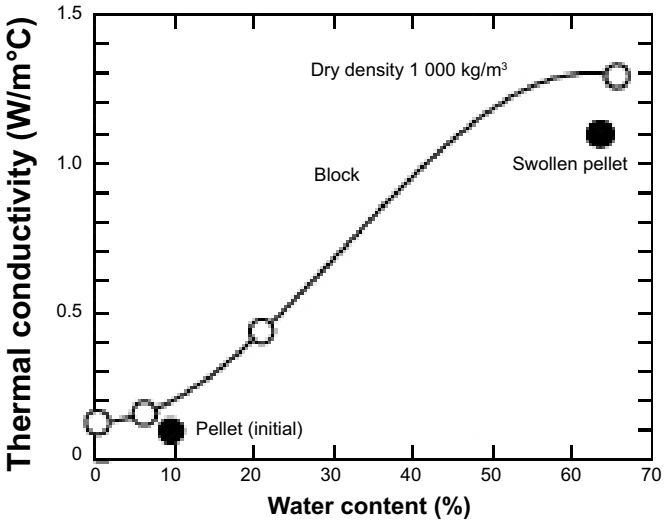

Figure A2-4. *The thermal conductivity variation with water content for block and pellet. From Sugita et al. (2005).*

Hydraulic properties

Figure A2-5 shows a compilation of experimental findings for the confined retention properties of MX-80 for a number of dry densities. The figure is taken from an earlier EBS task (Börgesson et al. 2016) and is taken from an earlier EBS task. Below follows a short investigation of the retention.

The retention of a free swelling sample can be estimated using the expression given below (Kahr et al. 1990)

$$S_{free}(w, w_0) = 1 \cdot 10^6 \exp(a(w_0) - b(w_0)w) \qquad \text{(A2-1)}$$

where the constants a and b is dependent on the initial water ratio, w_0. Table (A2-2) shows the constants (a,b), taken from Dueck (2007), obtained for different initial water ratios w_0.

Table A2-2 (a,b) parameter values in the retention expression for different initial water ratios.

w_0	0.100	0.175	0.270
(*a*, *b*)	(6.3, 16)	(7.25, 20)	(7.5, 20)

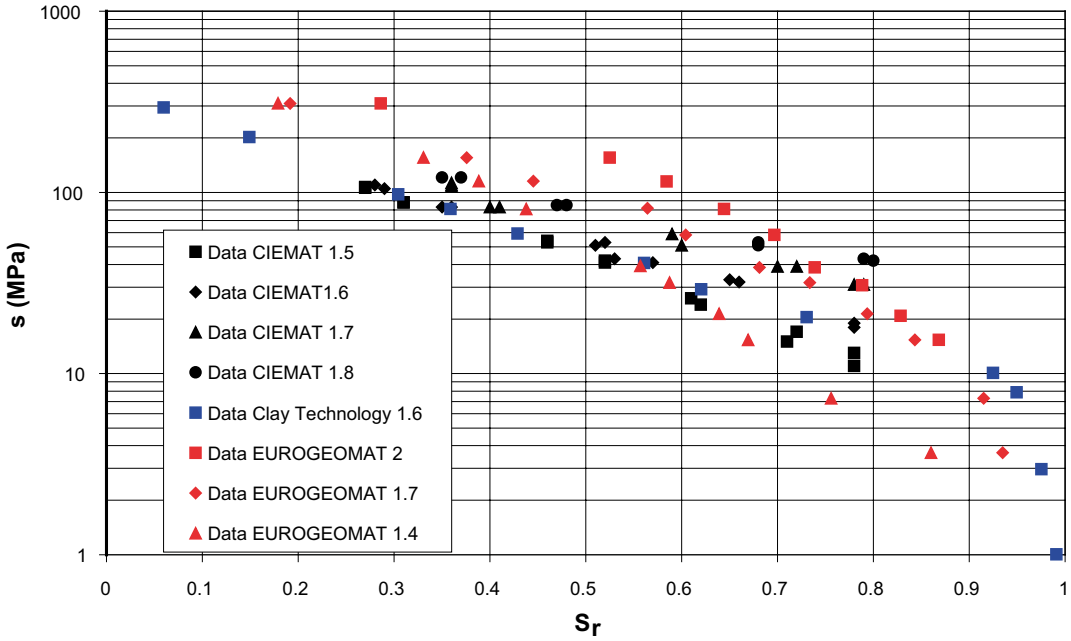

Figure A2-5. *Retention of MX-80 at constant volume and several dry densities.*

Figure A2-6 shows that the expression (A2-1) captures the retention behavior well in the range where the corresponding curve is shown. The parameters in Table A2-2 are fitted so that the response is close to the experimental data at high RH.

It can be shown thermodynamically, see Low and Andersson (1958), that the swelling pressure, p_s, is related to the suction at full water saturation under free swelling conditions, S_{free}, according to

$$p_s(e, w_0) = S_{free}\,(w_f(e), w_0) \qquad \text{(A2-2)}$$

where $w_f(e) = \rho_w/\rho_s e$. As Figure A2-7 shows, the experimental graph taken from Börgesson et al. (2016), that the obtained swelling pressure – dry density relation resembles the experimental findings.

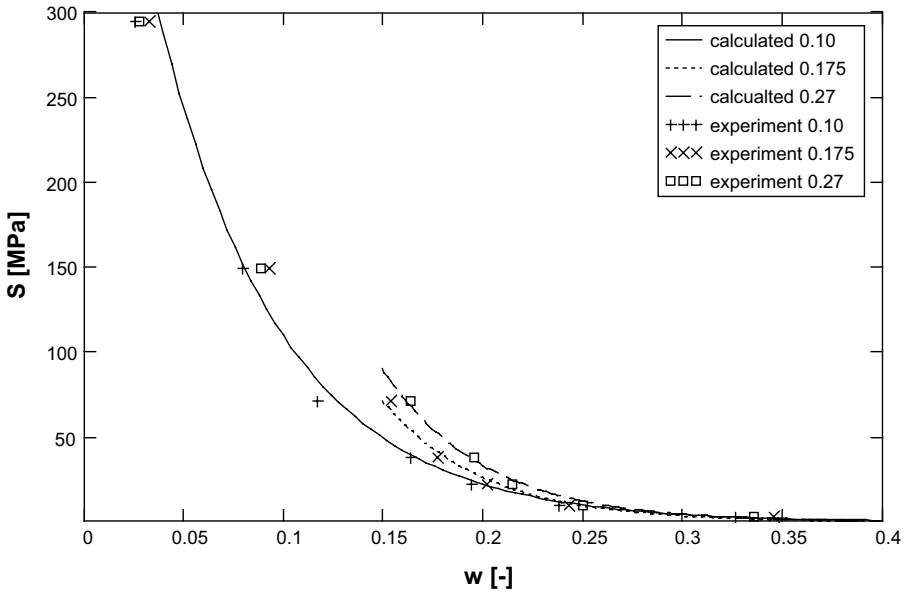

Figure A2-6. *Experimental and model retention.*

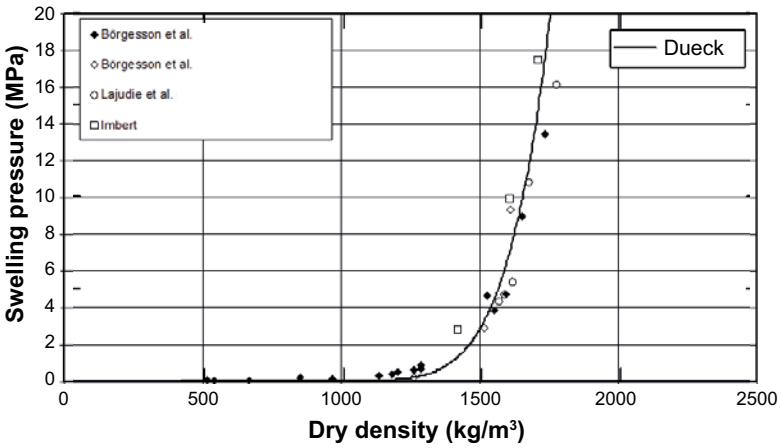

Figure A2-7. *Experimental and model swelling pressure.*

To account for the effect of an external pressure, p, on the water retention (A2-3) have been suggested, see Croney et al. (1958).

$$S_{conf}(w, w_0, e) = S_{free}(w, w_0) - \alpha p(w, w_0, e) \quad \text{(A2-3)}$$

A simple assumption is that $\alpha = 1$ and that the pressure depends linearly on the water ratio up to the swelling pressure, see Börgesson (1985) and Dueck (2004),

$$p(w, w_0, e) = p_s(e, w_0)\frac{w - w_0}{w_f - w_0} \quad \text{(A2-4)}$$

(A2-1)–(A2-4) can be used to obtain an estimate of retention curves of bentonite under confined conditions with an initial water ratio w_0 and void ratio e_0. In Figure A2-8 results obtained by using the equation above, with the dry densities 2 000 kg/m^3 (black curves) and 1 400 kg/m^3 (red curves) and the initial water ratio $w_0 = 0$, are shown together with the experimental data in Figure A2-5.

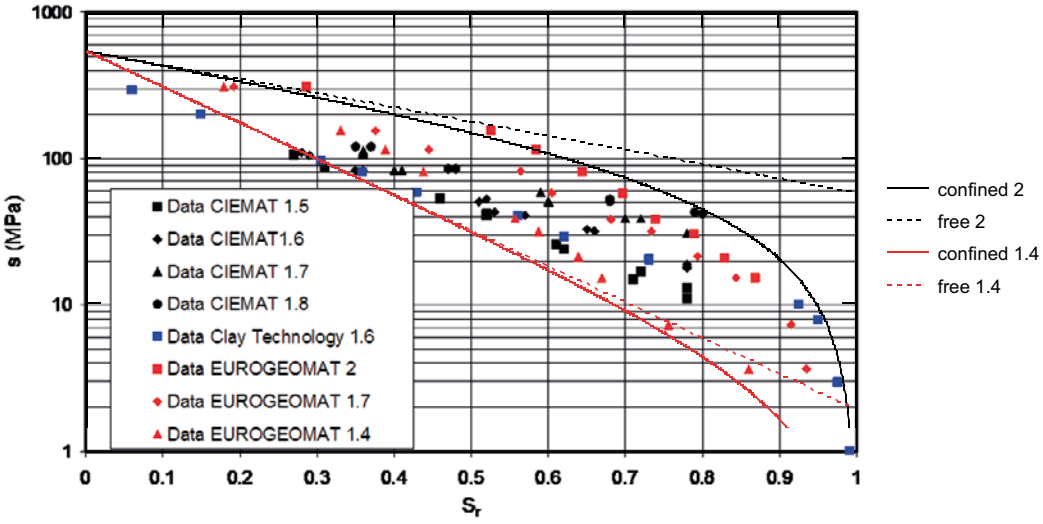

Figure A2-8. *Experimental and model data for confined retention. The model corresponds to a dry density of 2 000 kg/m^3 and 1 400 kg/m^3 respectively.*

The model produces a process window containing most experimental points and the boundaries of the process window are not very far from the corresponding experimental points considering that the initial water ratio of the experiments is not known. The accuracy of the model is probably improved if the parameter set (a,b) corresponding to the correct initial water ratio is used.

However, the analytical expressions (A2-1)–(A2-4) are considered to be accurate enough to give a possibility to calculate a process window inside which the bentonite block retention is likely to exist under the HM process. Below in Figure A2-9 such curves produced by (A2-1) and (A2-1)–(A2-4) are shown together with the experimental retention data given earlier in Figure A2-5. The black curves show the initial state retention curve for $e = e_0 = 0.564$, $w_0 = 0.174$ and the red curves show the retention of an estimated final state where some swelling has occurred and therefore $e = e_f = 0.75$. The final void ratio e_f is estimated as the volume average of the initial void ratio, taking the inner slot, the bentonite and the pellet-filled slot into account. The dotted curves indicate free swelling retention and the solid lines indicate retention curves obtained under confined conditions. The arrow indicates the initial state.

A process window is also indicated with the shaded area. The three numbered boundaries are defined by:

1. A free swelling block from the initial condition.
2. An assumption of constant water ratio during expansion.
3. Confined swelling of the expanded block.

Note that the three steps above is not an actual process, it is just a way to obtain the boundaries of a possible process window.

The same procedure is done for the pellet filled slot, but now with the initial state given by $e = 1.78$, $w_0 = 0.57$ and the final void ratio is assumed to be $e_f = 0.75$ i.e. equal to the volume average initial pore volumes. Figure A2-10 shows the obtained retention curves, but the initial state is not contained in the graph and for a more complete view Figure A2-11 is also showing lower values of suction. When producing these results a parameter set (a,b) = (6.3, 14) ,calibrated against an unpublished retention curve for $w_0 = 0.63$, has been used.

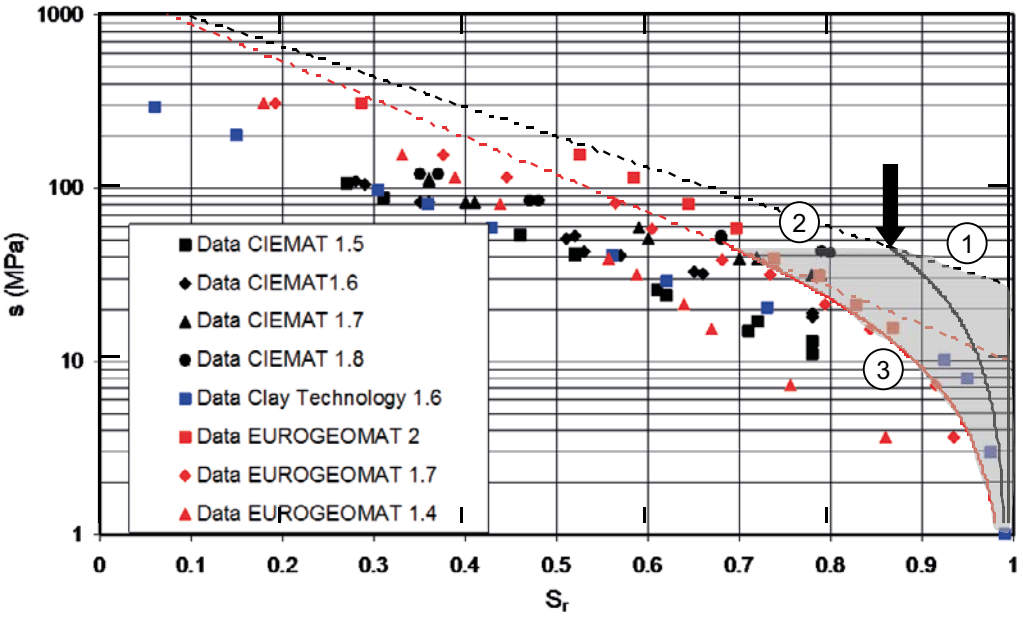

Figure A2-9. *Retention process window for bentonite block properties.*

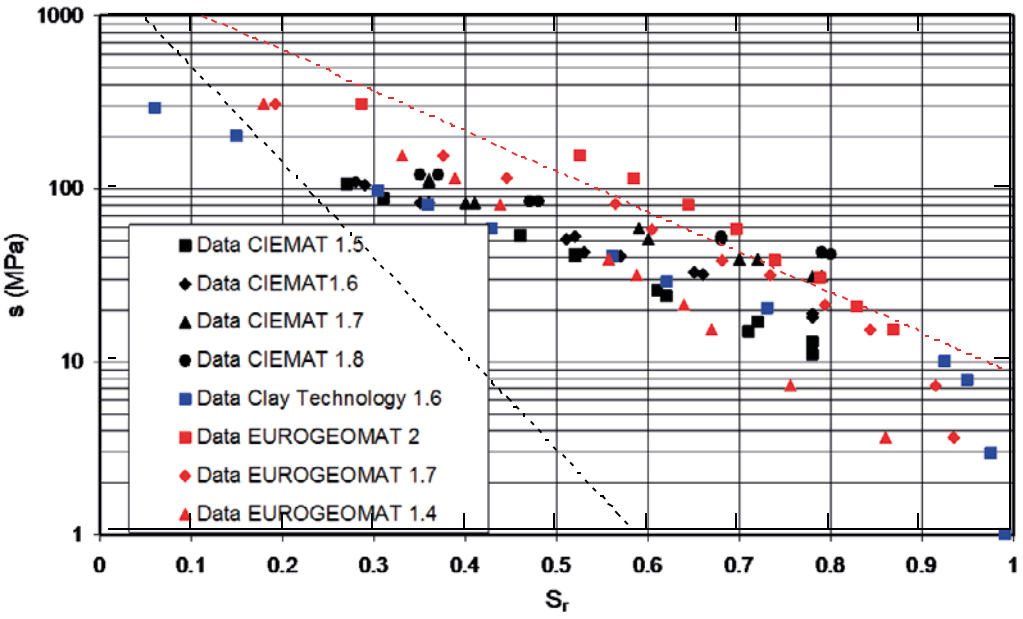

Figure A2-10. *Retention for homogenized pellet-filled slot. Experimental and model data.*

Also here a process window is indicated. Here only one of the boundaries has a clear definition.

1. Confined swelling from the initial state.

For the pellet-filled slot the estimated process window in retention is probably rather rough. The validity of the assumption of a homogenized media has not been confirmed. But as a point of departure the produced process window is considered to be of some relevance.

In Figure A2-12, taken from EBS (2005), a compilation of experimental results of the variation of the intrinsic permeability with porosity of MX-80 is shown.

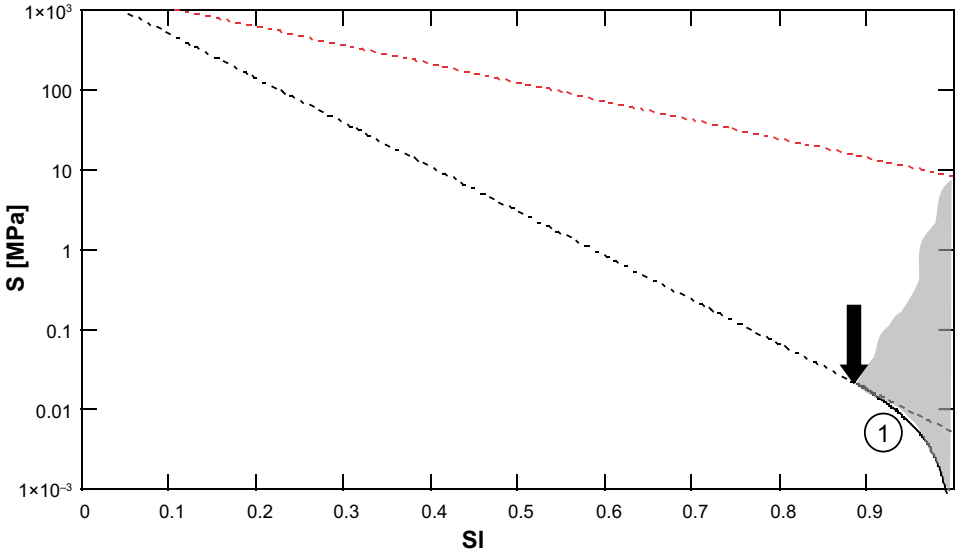

Figure A2-11. *Retention process window for homogenized pellet-filled slot.*

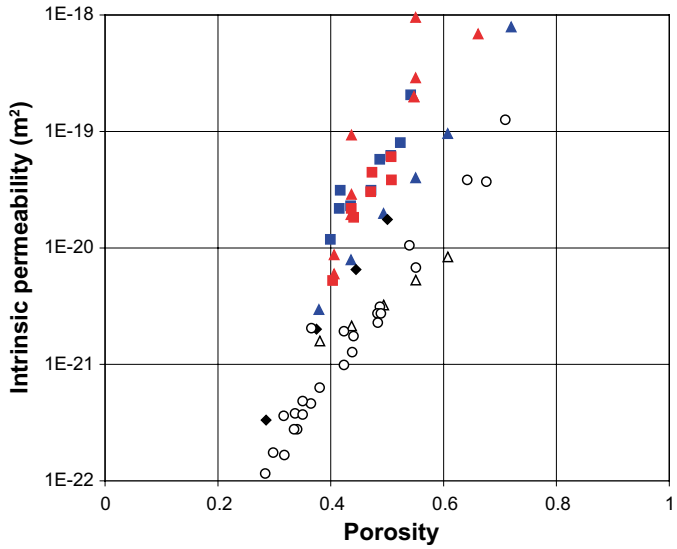

Figure A2-12. *Variation of intrinsic permeability with porosity as obtained by several laboratories in water-saturated samples.*

Mechanical properties

In Figure A2-13, taken from EBS (2005), the swelling pressure is given as a function of the dry density.

In Figure A2-14 the relation between pressure and void ratio is shown at different values of suction, *S*. The data is taken from Dueck and Nilsson (2010).

The experimental setup from which the results were obtained consisted of a steel cylinder where a pre-compressed bentonite sample was inserted. The sample was then allowed to attain equilibrium with the suction *S*, given by the RH obtained from a salt solute, at a small prescribed token axial stress. The sample was then subjected to different magnitudes of axial stress σ_a. From the recorded displacement of the loaded surface the void ratio *e* was obtained. The steel cylinder was also equipped with a force transducer in the radial direction from which the radial stress σ_r can be obtained. From the principal stresses, (σ_a, σ_r), the pressure $p = (\sigma_a + 2\,\sigma_r)/3$ and deviatoric stress $q = \sigma_a - \sigma_r$ can be calculated.

For each experiment, performed at a different level of suction, three graphs are showed in Figure A2-14.

1. The left graph shows (σ_a, σ_r), and is defining the prescribed load situation.
2. The center graph shows (p,q), which gives an overview of the load situation in the p–q space.
3. The right graph shows (p,e), where the p–e relation can be studied.

The load path is indicated with arrows in the graphs.

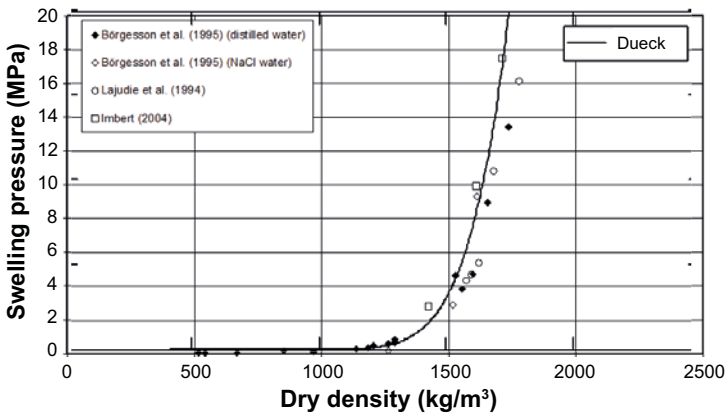

Figure A2-13. *Swelling pressure vs dry density as obtained by different laboratories.*

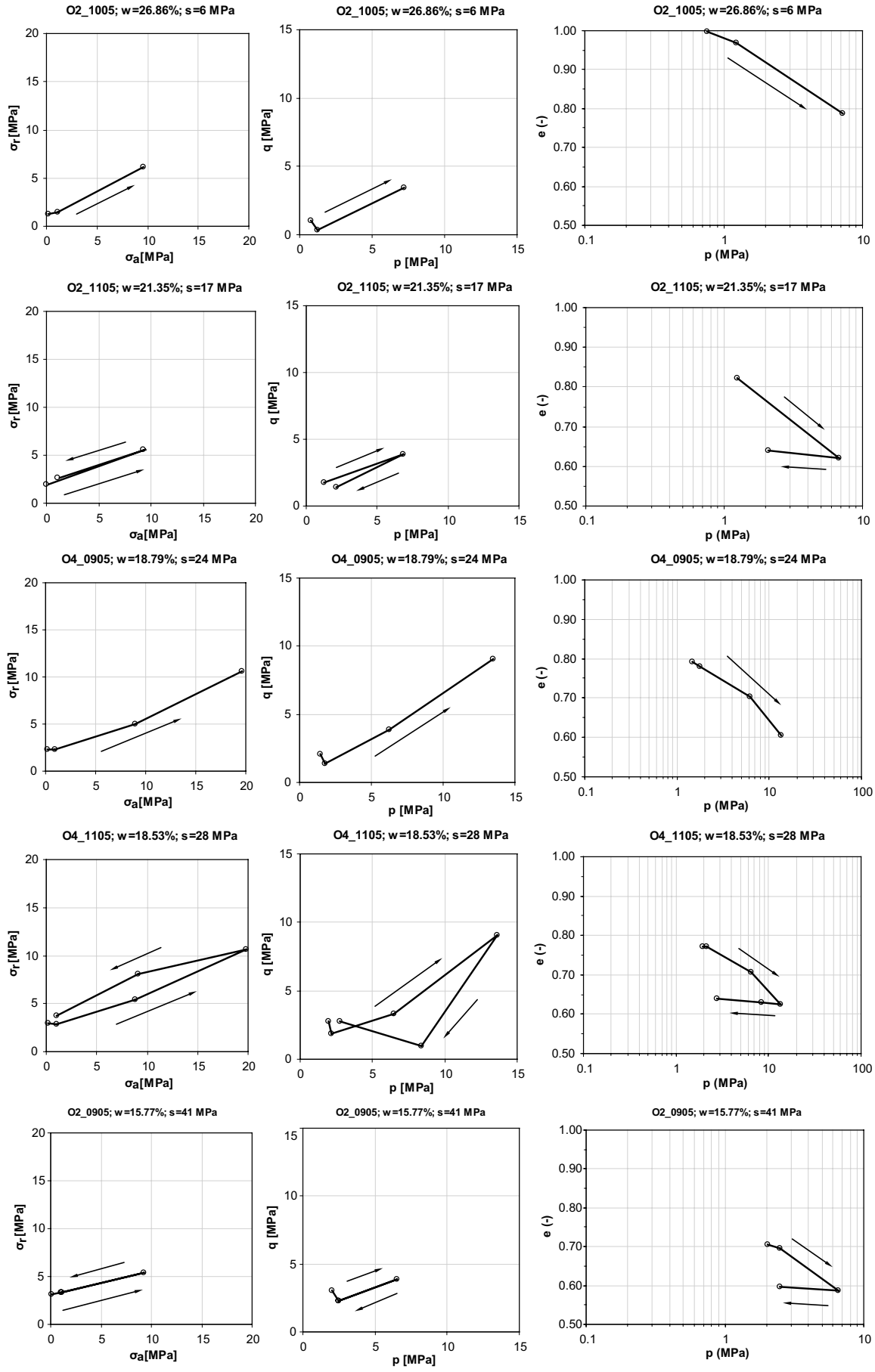

Figure A2-14. *Pressure – void ratio relation at different levels of suction.*

Below in Figure A2-15 the experimental results from EBS (2005) are recapitulated.

Below in Figure A2-16 the relation between void ratio, *e*, and suction, *S*, are shown at different levels of pressure *p*. The experimental data is taken from Dueck and Nilsson (2010). The experimental setup is identical to the one described above used when the relation between void ratio and pressure at constant suction were investigated. The sample was subjected to a constant axial stress during changes in suction. The radial stress was recorded during the suction change and the corresponding level of pressure could then be calculated.

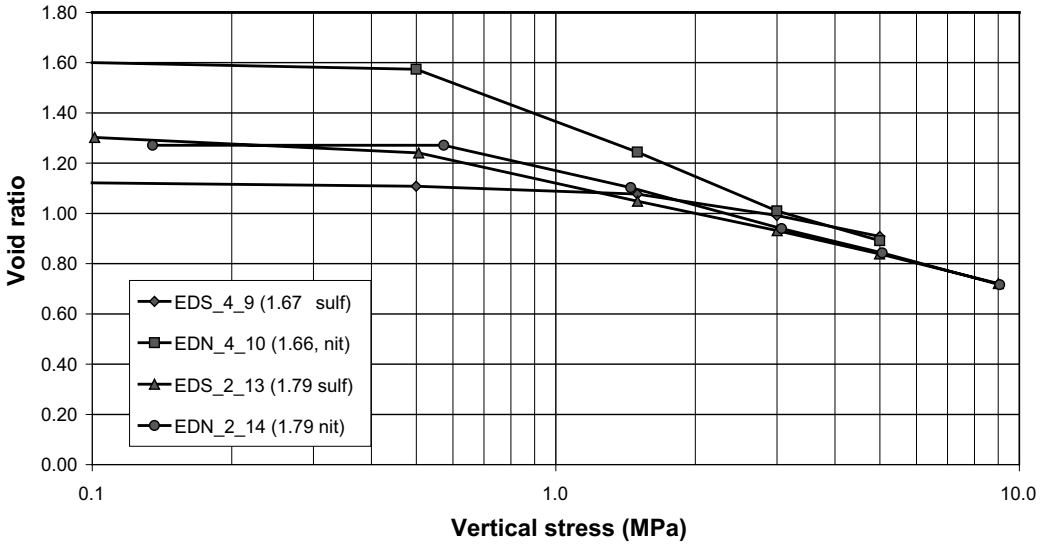

Figure A2-15. *Compression lines obtained during the drained loading following the saturation stage for samples EDN_4_9, EDN_4_10, EDN_2_13 and EDN_2_14 (Börgesson et al. 2016).*

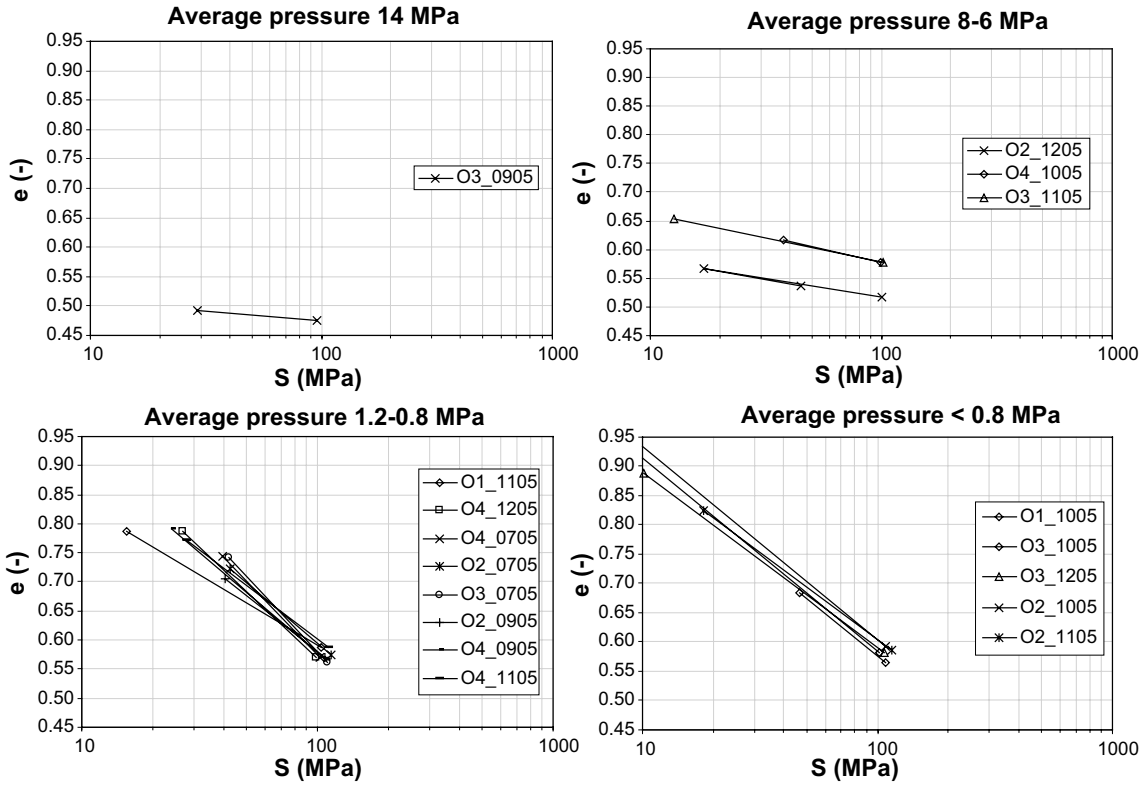

Figure A2-16. *The relation between void ratio and suction given at different pressure levels.*

In Figure A2-17 below the relation between void ratio and suction is given at an axial load of 0.1 MPa (Börgesson et al. 2016).

A thermal expansion coefficient of $3 \cdot 10^{-6}$ °C^{-1} at $T = 20$ °C models the relation between temperature and void ratio well for a bentonite particle (Börgesson et al. 1985).

Rock properties

The parameter values below are site data. No mechanical or hydraulic properties are presented since these processes are not considered necessary to model in the rock material for the experimental setup.

$\rho = 2\ 770$ kg/m^3

$c = 770$ J/(kg·°C)

$\lambda = 2.6$ W/(m·°C)

Concrete plug properties

Handbook values of concrete are presented, the reinforcement is not considered. No hydraulic properties are presented, since the concrete plug is protected from wetting by the impermeable rubber shield.

$\rho = 2\ 400$ kg/m^3

$c = 770$ J/(kg·°C)

$\lambda = 2.7$ W/(m·°C)

$E = 30$ GPa

$v = 0.15$

$\alpha = 10 \cdot 10^{-6}$ °C^{-1}

Steel lid properties

Handbook values for S355JR are presented below. Hydraulic properties are not considered to be necessary.

$\rho = 7\ 840$ kg/m^3

$c = 460$ J/(kg·°C)

$\lambda = 47$ W/(m·°C)

$E = 206$ GPa

$v = 0.3$

$\alpha = 12 \cdot 10^{-6}$ °C^{-1}

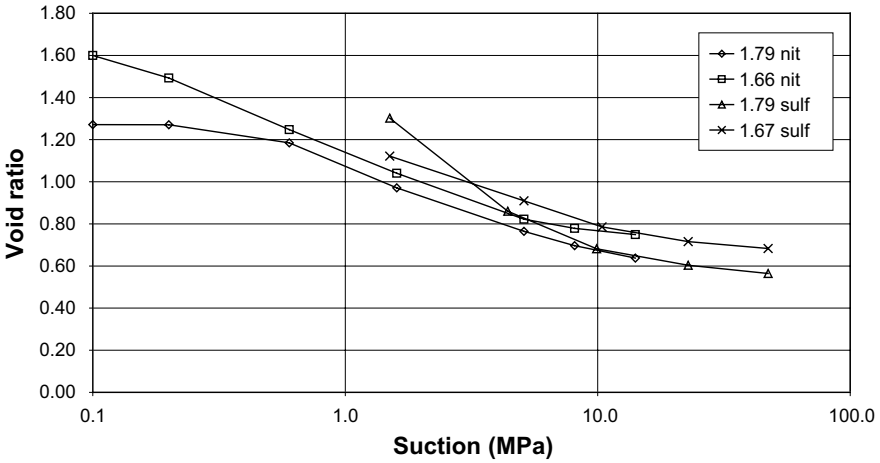

Figure A2-17. *Evolution of void ratio with applied suction during a wetting path performed in an oedometer cell under a constant load of 0.1 MPa (Börgesson et al. 2016).*

Rock anchors properties

In Figure A2-18 below the total force acting on the plug is plotted against the plug displacement at the corresponding time. An assumption of a linear relation, $\Delta F = k\Delta u$, between the force and displacement seems appropriate. A stiffness $k \approx 2.08$ GN/m is obtained for the red curve. Figure A2-18 was obtained using the average value of all three measured anchor forces and the "displacement2" measurement.

To check the measurements somewhat, Young's modulus for the wires was calculated from knowing the force – displacement data in Figure A2-18 together with the known geometry (wire inclination = 22°, free wire length = 5 m and nominal anchor area = 19 × 98.7 mm^2). From the calculation the value E = 163 GPa was obtained. In manufacturer data sheets for the wire the Young's modulus is specified as approximately 197 GPa.

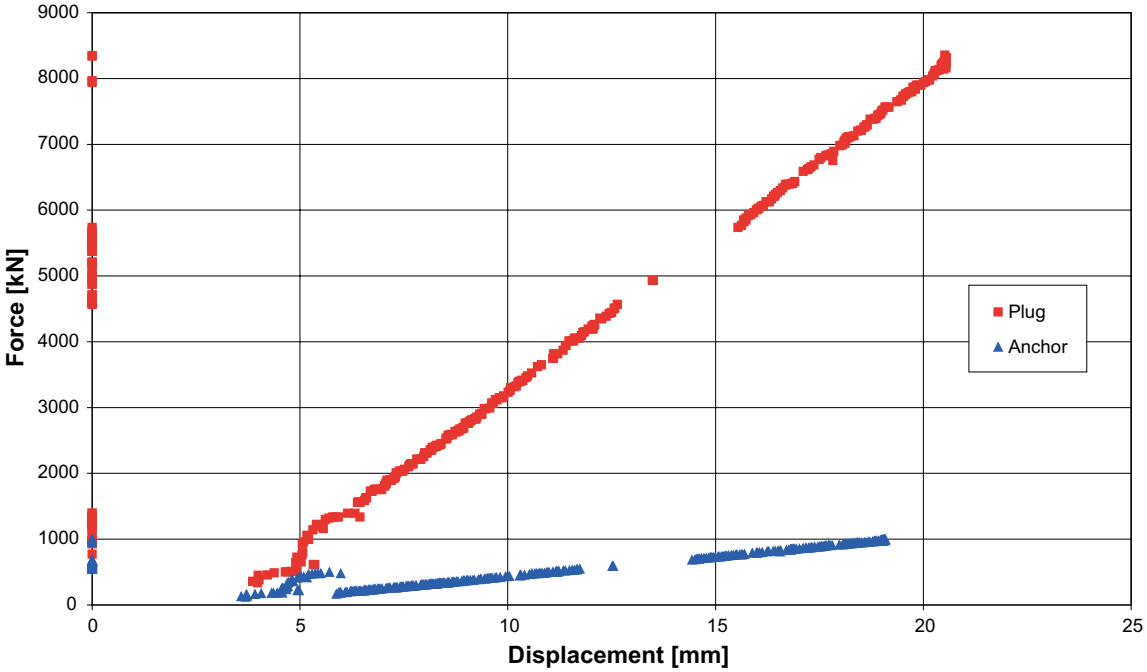

Figure A2-18. *The total force acting on the plug and the average force in all anchors plotted against total vertical displacement of the plug and the anchor elongation respectively.*

Appendix 3

Description of BBM

Short review of BBM

The traditional mechanical constitutive model bridges the gap between the displacements $\boldsymbol{u} = \boldsymbol{x} - \boldsymbol{X}$, where $\boldsymbol{x}$ and $\boldsymbol{X}$ denotes the position vectors to a point in the deformed configuration and reference configuration respectively, and the forces $d\boldsymbol{P}$ acting on a oriented surface element $d\boldsymbol{a}$ at position $\boldsymbol{x}$. Rather than formulating the constitutive laws directly in displacements and forces, the strains $\boldsymbol{\varepsilon} = 1/2(\partial\boldsymbol{u}/\partial\boldsymbol{x} + (\partial\boldsymbol{u}/\partial\boldsymbol{x})^{\mathrm{T}})$ and stresses $\boldsymbol{\sigma}$, defined by the relation $d\boldsymbol{P} = \boldsymbol{\sigma} d\boldsymbol{a}$, are used. The used strain measure is the infinitesimal Eulerian strain, i.e. it is assumed that $\partial\boldsymbol{u}/\partial\boldsymbol{x} >> (\partial\boldsymbol{u}/\partial\boldsymbol{x})^{\mathrm{T}}\partial\boldsymbol{u}/\partial\boldsymbol{x}$. The Eulerian strain is here approximated using the updated Lagrangean strain.

The material is deformed not only due to purely mechanical processes but also by hydraulic and thermal processes. The total strain $\boldsymbol{\varepsilon}$ is additatively decomposed in mechanical $\boldsymbol{\varepsilon}^m$, hydraulic $\boldsymbol{\varepsilon}^h$ and thermal $\boldsymbol{\varepsilon}^t$ strains

$$\boldsymbol{\varepsilon} = \boldsymbol{\varepsilon}^m + \boldsymbol{\varepsilon}^h + \boldsymbol{\varepsilon}^t.$$

The strain can be decomposed in a hydrostatic part $1/3\mathrm{tr}(\boldsymbol{\varepsilon})\boldsymbol{1} = -1/3\varepsilon_v\boldsymbol{1}$, where the volumetric strain $\varepsilon_v \approx -(dv - dv_0)/dv$ (dv and dv_0 denotes a material volume in the current and reference configuration respectively and the approx. sign is present due to that higher order terms are neglected) is introduced, and a deviatoric part, $\boldsymbol{e} = \boldsymbol{\varepsilon} + 1/3\varepsilon_v\boldsymbol{1}$. Note that the definition of the volumetric strain gives that $\varepsilon_v > 0$ in compression. Thus, we obtain

$$\varepsilon = -\frac{1}{3}\varepsilon_v^{\,m}\boldsymbol{1} + \boldsymbol{e}^m - \frac{1}{3}\varepsilon_v^{\,h}\boldsymbol{1} + \boldsymbol{e}^h - \frac{1}{3}\varepsilon_v^{\,t}\boldsymbol{1} + \boldsymbol{e}^t .$$

A material volume dv is thought of as constituted of a solid volume dv_s and a pore volume dv_p. In the formulation the specific volume field $v' = dv/dv_s = 1 + dv_p/dv_s = 1 + e$ is used, where e denotes the void ratio. We also obtain that $-\varepsilon_v \approx (v' - v_0')/v' = (e - e_0)/(1 + e)$ if we use the constraint that the solid part of the material is incompressible, i.e. $ds = ds_0$. Thus, a volumetric strain increment is related to increments in specific volume and void ratio according to, $-d\varepsilon_v \approx dv'/v' = de/(1 + e)$.

The effective stress tensor $\boldsymbol{\sigma}'$ is defined by $\boldsymbol{\sigma}' = \boldsymbol{\sigma} + \max(p_l, p_g)\boldsymbol{1}$, where p_l denotes the liquid pressure and p_g denotes the gas pressure. The effective stress tensor are decomposed in a hydrostatic part $1/3\mathrm{tr}(\boldsymbol{\sigma}')\boldsymbol{1} = -p'\boldsymbol{1}$, where the effective pressure p' is introduced, and a deviatoric part $\boldsymbol{s} = \boldsymbol{\sigma}' + p'\boldsymbol{1}$. Invariants of the stress useful in the following are:

$$J_2 = \frac{1}{2}\mathbf{s}\cdot\mathbf{s}$$

$$J_3 = \det(\mathbf{s})$$

$$\cos 3\theta = \frac{3\sqrt{3}}{2}\frac{J_3}{J_2^{\,3/2}} .$$

where, $\cdot$ denotes the scalar product and det( ) the determinant. CODE_BRIGHT uses the invariant θ', defined by

$$\sin(-3\theta') = \frac{3\sqrt{3}}{2}\frac{J_3}{J_2^{\,3/2}},$$

i.e., $\theta' = -\theta - \pi/6$.

The suction s, defined by $s = p_g - p_l$, is used in the formulation to describe the materials driving force to absorb the liquid. This variable is present in the mechanical material model to incorporate a hydraulic dependence on the deformation, when the material absorbs liquid is swells and when the material dries it shrinks. Finally a dependence on the temperature T is introduced in order to describe the thermally induced strains.

Mechanical strains

The total mechanical strain $\boldsymbol{\varepsilon}^m$ is decomposed in elastic $\boldsymbol{\varepsilon}^e$ and plastic $\boldsymbol{\varepsilon}^p$ strains

$$\boldsymbol{\varepsilon}^m = \boldsymbol{\varepsilon}^e + \boldsymbol{\varepsilon}^p.$$

The elastic strain is reversible, i.e. when deformed the original shape of the body can be recovered without energy is lost. The plastic strain is irreversible. When undergoing plastic deformation, the original shape of the body cannot be recovered without energy input.

Elastic strains

The volumetric elastic strain increments are defined as

$$d\varepsilon_v^{\,e} = \frac{1}{K^m} dp',$$

where the "mechanical bulk modulus"

$$K^m = \frac{(1+e)p'}{\kappa_i(s)}.$$

The function $\kappa_i(s)$ is defined

$$\kappa_i(s) = \kappa_{i0}\left[1 + \alpha_i s + \alpha_{ils} \ln\left(\frac{s+0.1}{0.1}\right)\right].$$

The deviatoric elastic strain increments are defined as

$$d\boldsymbol{e}^e = \frac{1}{2G} d\boldsymbol{s},$$

where G is calculated using a constant Poisson's ratio ν, according to

$$G = \frac{3(1-2\nu)}{2(1+\nu)} K^m.$$

Plastic strains

The elastic region is bounded by the flow surface

$$f = \frac{q^2}{g_y(\theta)^2} - \frac{M^2}{g_y(\theta=0)^2}\left(p' + p_s(s,T)\right)\left(p_0\left(s,\varepsilon_v^{\,p},T\right) - p'\right) = 0,$$

geometrically represented in Figure A3-1. The flow surface is a function of stress, suction, temperature and plastic volumetric strain, $f = f(\boldsymbol{\sigma}, s, T, \varepsilon_v^{\,p})$.

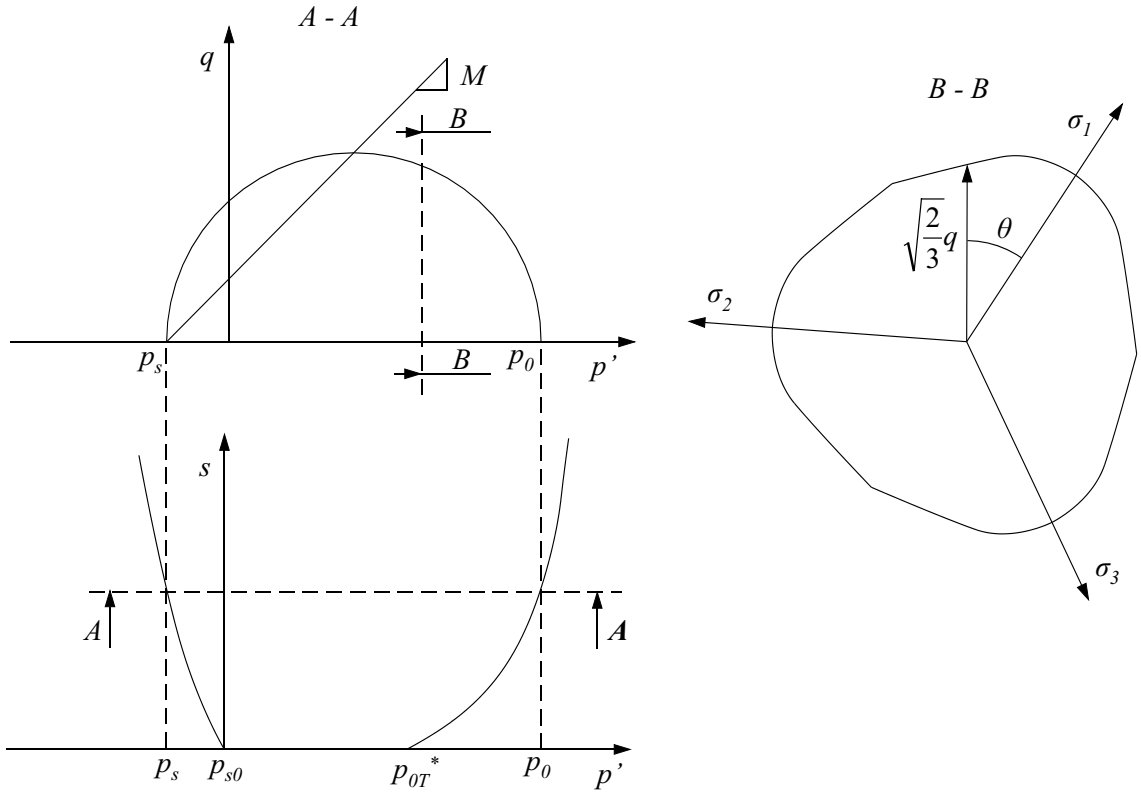

Figure A3-1. *Geometrical representation of the flow surface.*

θ is the stress invariant called Lode's angle, and the function $g_y(\theta)$ describes the shape of the flow surface in the deviatoric plane shown in the left picture in Figure A3-1. Note that the parameter $q = (3J_2)^{1/2}$, is not equal to the length of the deviatoric principal stress vector $(s_1^2+s_2^2+s_3^2)^{1/2} = (2J_2)^{1/2}$. The chosen definition of q gives that for uniaxial tension $q = \sigma$.

M is the slope of the critical state line defining the current maximal deviatoric, or shear, strength. The parameter M can be expressed in the variable angle of shearing φ, present in the Mohr-Coulomb failure criterion $\tau_f = c + \sigma'_f \tan\varphi$, $M = 3(2\sin^{-1}\varphi - 1)^{-1}$. The function

$$p_s(s,T) = p_{s0} + ks e^{-\rho\Delta T}$$

is describing the current pure tensile strength as a function of suction and temperature difference, $\Delta T = T - T_0$, by increasing the cohesion.

$p_0(s, \varepsilon_v^p, T)$ is the current pure pressure strength which is expressed

$$p_0(s,\varepsilon_v{}^p,T) = p^c\left(\frac{p_{0T}{}^*(\varepsilon_v{}^p,T)}{p^c}\right)^{\frac{\lambda_0-\kappa_{i0}}{\lambda(s)-\kappa_{i0}}},$$

where $p_{0T}{}^*(T) = p_0{}^* + 2(\alpha_1\Delta T + \alpha_3\Delta T|\Delta T|)$ is the pure pressure strength at full saturation, containing $p_0{}^*(\varepsilon_v^p) = p_{0T}{}^*(T_0)$ which is a hardening parameter having the evolutional law

$$dp_0{}^* = \frac{1+e}{\lambda_0-\kappa_{i0}} p_0{}^* d\varepsilon_v^p.$$

$\lambda(s)$ is a function describing the increase in soil stiffness with suction. $\lambda(s)$ appears in the expression adopted for describing the specific volume $v' = N(s) - \lambda(s)\ln(p'/p^c)$, where p^c is a reference pressure. $\lambda(s)$ is here taken as

$$\lambda(s) = \lambda_0\left((1-r)e^{-\beta s} + r\right).$$

When the stress state is on the flow surface the plastic strains are obtained from the flow rule

$$d\varepsilon^p = d\Lambda \frac{\partial g}{\partial \boldsymbol{\sigma}},$$

where $d\Lambda$ is the plastic multiplier obtained from the consistency condition $df = 0$ and g is the plastic potential defined by

$$g = \frac{\alpha q^2}{g_y(\theta)^2} - \frac{M^2}{g_y(\theta=0)^2}\left(p' + p_s(s,T)\right)\left(p_0\left(s,\varepsilon_v^{\,p},T\right) - p'\right),$$

where α is the parameter that gives rise to the non-associative model, i.e. $g \neq f$.

Hydraulic strains

The hydraulically induced strains are purely volumetric (i.e. $\boldsymbol{e}^h = \mathbf{0}$)

$$d\varepsilon_v^{\,h} = \frac{1}{K^h} ds$$

where the "hydraulic bulk modulus" is defined

$$K^h = \frac{(1+e)(s + p_{atm})}{\kappa_s(p', s)}$$

where

$$\kappa_s(p', s) = \kappa_{s0}\left(1 + \alpha_{sp} \ln\frac{p'}{p_{ref}}\right) e^{\alpha_{ss} s}$$

Thermal strains

The thermal model is purely volumetric (i.e. $\boldsymbol{e}^t = \mathbf{0}$) and reads

$$d\varepsilon_v^{\,t} = (\alpha_0 + 2\alpha_2 \Delta T) dT = \alpha^t dT.$$

Note that in order to obtain a thermal expansion for $dT > 0$, $\alpha^t < 0$.

Derivation of a strain/suction/temperature driven format for BBM

An explicit strain/suction/temperature driven format of the constitutive relations is used in CODE_BRIGHT, where elastoplastic stiffness tensors replace the elastic stiffness tensors in the constitutive formulation when the material yields. The consistency condition $f = 0$ is used when deriving the elastoplastic stiffness tensors and in this way indirect considered. The integration from 1 (the known state at the start of the current increment) to 2 (the new state at the end of the current increment) can formally be described as

$$\boldsymbol{\sigma}^2 = \boldsymbol{\sigma}^1 + \int_1^c (\mathbf{C}^e d\varepsilon + \mathbf{c}^{eh} ds + \mathbf{c}^{et} dT) + \int_c^2 (\mathbf{C}^{ep} d\varepsilon + \mathbf{c}^{eph} ds + \mathbf{c}^{ept} dT),$$

$$p_0^{*2} = p_0^{*1} + \int_c^2 dp_0^{\,*}$$

where some numerical method is utilized to perform the integration. It should also be noted that the contact state, here denoted with c, which is the state when yield starts within the increment, have to be identified using this method.

A strain/suction driven format of the constitutive law is derived in this section. This type of format is useful when solving problems numerically. Note that a flow surface independent on Lode's angle has been assumed in the derivations below, i.e. $g_y(\theta) = 1$, which is not as general as the formulation described above permits.

First we address the elastic part of the material model. The stress increment $d\boldsymbol{\sigma}$ can be related to the elastic strain increment $d\boldsymbol{\varepsilon}^e$ according to

$$d\boldsymbol{\sigma} = \boldsymbol{C}^e\, d\boldsymbol{\varepsilon}^e,$$

where $\boldsymbol{C}^e$ is the (fourth order) elastic stiffness tensor defined by

$$\boldsymbol{C}^e = \left(K^m - \frac{2G}{3} \right) \boldsymbol{1} \otimes \boldsymbol{1} + 2G\mathrm{I},$$

where $\boldsymbol{1}$ and $\mathbf{I}$ denotes the second and forth order unit tensors respectively. Thus, expressing the elastic strain increment in terms of total, hydraulic and thermal strain increments, the elastic constitutive law can be expressed as

$$d\boldsymbol{\sigma} = \boldsymbol{C}^e\, d\boldsymbol{\varepsilon} + \boldsymbol{c}^{eh}\, ds + \boldsymbol{c}^{et}\, dT,$$

where

$$\boldsymbol{c}^e = \frac{1}{3K^h} \boldsymbol{C}^e \boldsymbol{1} \quad \text{and} \quad \boldsymbol{c}^{et} = \frac{\alpha^t}{3} \boldsymbol{C}^e \boldsymbol{1}.$$

Now the plastic part of the material model is considered. To obtain a strain/suction driven format for the elasto-plastic constitutive law, where the stress increment is given by the strain increment and the suction increment, we start with the elastic constitutive law

$$d\boldsymbol{\sigma} = \boldsymbol{C}^e\, d\boldsymbol{\varepsilon}^e.$$

Expressing the elastic strain increment in total, plastic and hydraulic strain increments, using the flow rule and the expression for the hydraulic strain increment gives

$$d\boldsymbol{\sigma} = \boldsymbol{C}^e \left(d\boldsymbol{\varepsilon} - d\Lambda \frac{\partial g}{\partial \boldsymbol{\sigma}} + \frac{1}{3K^h} \boldsymbol{1} ds + \frac{\alpha^t}{3} \boldsymbol{1} dT \right). \tag{A3-1}$$

The next step is to derive an expression for the plastic multiplier, $d\Lambda$. For this task the consistency condition, $df = 0$, is used. The flow surface is a function of the stress, suction and volumetric plastic strain, i.e. $f = f(\boldsymbol{\sigma}, s, \varepsilon_v^{\,p})$. Differentiating the flow surface to obtain an expression for the consistency condition in these variables gives

$$df = \frac{\partial f}{\partial \boldsymbol{\sigma}} \cdot d\boldsymbol{\sigma} + \frac{\partial f}{\partial s} ds + \frac{\partial f}{\partial \varepsilon_v^{\,p}} d\varepsilon_v^{\,p} = 0. \tag{A3-2}$$

To obtain the expression of the plastic multiplier, we first operate with the scalar product on (A3-1) and $\frac{\partial f}{\partial \boldsymbol{\sigma}}$. Then (A3-2) together with the flow rule are used in the obtained expression. $d\Lambda$ is now given by

$$d\Lambda = \frac{1}{A} \frac{\partial f}{\partial \boldsymbol{\sigma}} \cdot \boldsymbol{C}^e d\boldsymbol{\varepsilon} + \frac{1}{A} \left(\frac{\partial f}{\partial s} + \frac{1}{3K^h} \frac{\partial f}{\partial \boldsymbol{\sigma}} \cdot \boldsymbol{C}^e \boldsymbol{1} \right) ds + \frac{1}{A} \left(\frac{\partial f}{\partial T} + \frac{\alpha^t}{3} \frac{\partial f}{\partial \boldsymbol{\sigma}} \cdot \boldsymbol{C}^e \boldsymbol{1} \right) dT,$$

where

$$A = -\frac{\partial f}{\partial \varepsilon_v^{\,p}} \frac{\partial g}{\partial p'} + \frac{\partial f}{\partial \boldsymbol{\sigma}} \cdot \boldsymbol{C}^e \frac{\partial g}{\partial \boldsymbol{\sigma}}.$$

If the expression for the plastic multiplier is inserted in (3-13) and the terms are collected the following strain/suction driven format of the constitutive law is obtained when the material behaves plastic

$$d\boldsymbol{\sigma} = \boldsymbol{C}^{ep}\, d\boldsymbol{\varepsilon} + \boldsymbol{c}^{eph}\, ds + \boldsymbol{c}^{ept}\, dT,$$

where

$$\boldsymbol{C}^{ep} = \boldsymbol{C}^{e} - \frac{1}{A}\boldsymbol{C}^{e}\frac{\partial g}{\partial \boldsymbol{\sigma}} \otimes \boldsymbol{C}^{e}\frac{\partial f}{\partial \boldsymbol{\sigma}},$$

$$\boldsymbol{c}^{eph} = \boldsymbol{c}^{eh} - \frac{1}{A}\left(\frac{\partial f}{\partial s}\boldsymbol{C}^{e}\frac{\partial g}{\partial \boldsymbol{\sigma}} + \frac{1}{3K^{h}}\left(\boldsymbol{C}^{e}\frac{\partial g}{\partial \boldsymbol{\sigma}} \otimes \boldsymbol{C}^{e}\frac{\partial f}{\partial \boldsymbol{\sigma}}\right)\boldsymbol{1}\right),$$

and

$$\boldsymbol{c}^{ept} = \boldsymbol{c}^{et} - \frac{1}{A}\left(\frac{\partial f}{\partial T}\boldsymbol{C}^{e}\frac{\partial g}{\partial \boldsymbol{\sigma}} + \frac{\alpha^{t}}{3}\left(\boldsymbol{C}^{e}\frac{\partial g}{\partial \boldsymbol{\sigma}} \otimes \boldsymbol{C}^{e}\frac{\partial f}{\partial \boldsymbol{\sigma}}\right)\boldsymbol{1}\right).$$

Appendix 4

Modifications of BBM

Both modifications described below were used in the main analysis.

A swelling modulus κs dependent on a swelling pressure curve

A new function governing the swelling modulus κ_s in the hydraulic strain increment of BBM, (A4-1), has been implemented in Code Bright in order to mimic the behaviour of bentonite clay.

$$d\varepsilon_v^{\ h} = \frac{\kappa_s(p',e)}{(1+e)(s+p_{atm})}ds \qquad \text{(A4-1)}$$

The idea behind the new expression is to utilize a swelling pressure curve (the pressure obtained at full water saturation under confined conditions) obtained from analyzing experimental data. The adopted function has following form,

$$\kappa_s(p',e) = \kappa_{s0} f(p',e)$$

$$f(p',e) = \begin{cases} 1 & \text{if } p' < p_{ref} \\ 10^{-20} & \text{if } p' > p_{swell}(e) \\ 1 - \dfrac{\ln p' - \ln p_{ref}}{\ln(p_{swell}(e)) - \ln p_{ref}} & \text{otherwise} \end{cases}$$

$$p_{swell}(e) = 10^{\left[-4.741+4.117\cdot10^{-3}\frac{\rho_s}{1+e}-3.94\cdot10^{-7}\left(\frac{\rho_s}{1+e}\right)^2\right]}$$

In Figure A4-1 the pressure dependence of the normalized function (κ_i / κ_{i0}) is shown for two constant void ratios. When the pressure, p', is less than the referential pressure, p_{ref}, the function equals the referential value κ_{i0}. Thus, the upper "knee" occurs when $p' = p_{ref}$. When $p' = p_{swell}(e)$ the function equals zero (or rather 10^{-20} to avoid division by zero). I.e., swelling may occur until the pressure equals the swelling pressure at the current void ratio.

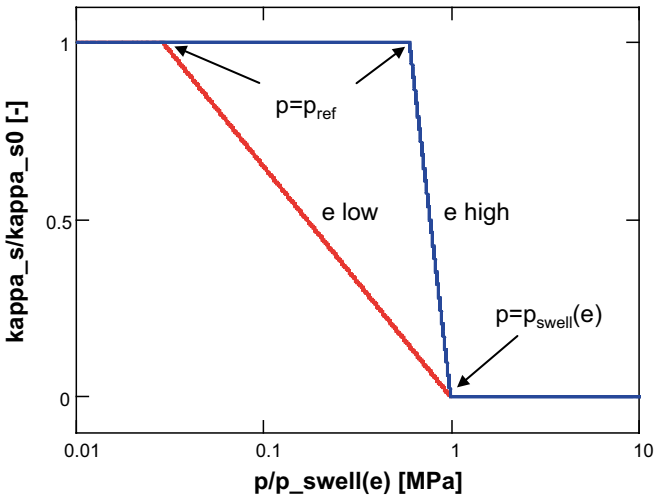

Figure A4-1. *Pressure dependence of the normalized swelling modulus.*

The void ratio dependence is shown in Figure A4-2 where the normalized modulus is given for three constant pressures. The void ratio is normalized against the void ratio, e_s, that give the specified pressure when inserted in the swelling pressure function. As can be seen, the modulus decreases with increasing void ratio.

Test and validation

In the following some simple elastic and isotropic examples are studied using MathCad and the CodeBright implementation. Thus, only states inside the yield surface during wetting are considered. At the higher void ratios used this is probably not a very suitable representation, but this exercise is only performed to study the performance of the modulus-function and the implementation in CodeBright.

Wetting under constant pressure

First, wetting under constant pressure is investigated when using the modulus function. The unsaturated clay sample can be thought of being contained within a soft membrane that is subjected to an outer constant pressure p'. When water is added to the clay, the specimen should swell until the swelling pressure equals the outer prescribed pressure.

The parameters used are:

- $\kappa_{s0} = 0.3$
- $p_{ref} = 1$ MPa
- $\rho_s = 2\ 780$ kg/m^3
- $p_{atm} = 0.1$ MPa

The initial states are given by $e = 0.57$ and $p' = \{2,5,10,15\}$ MPa.

In the normalized responses, shown in Figure A4-3, obtained from using MathCad, it can be seen that the void ratio obtained at full water saturation, e_s, is given by $p_{swell}(e_s) = p'$, exactly as expected for a correct implementation.

To check the CodeBright implementation the results obtained from using MathCad and CodeBright are compared in Figure A4-4. The agreement between the solutions is very good.

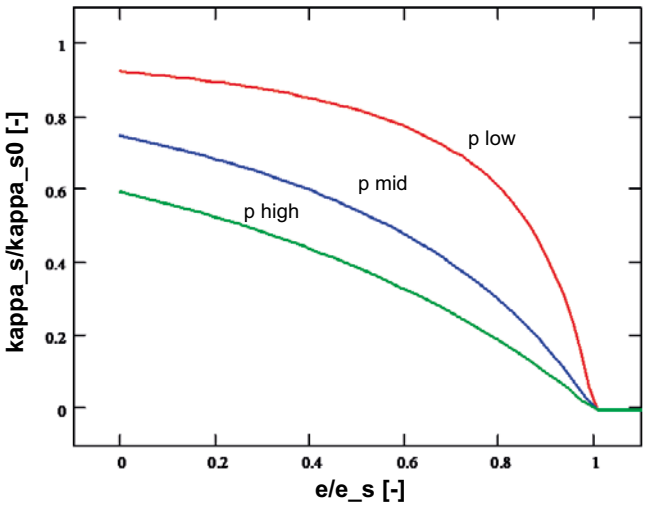

Figure A4-2. *Void ratio dependence of the normalized swelling modulus.*

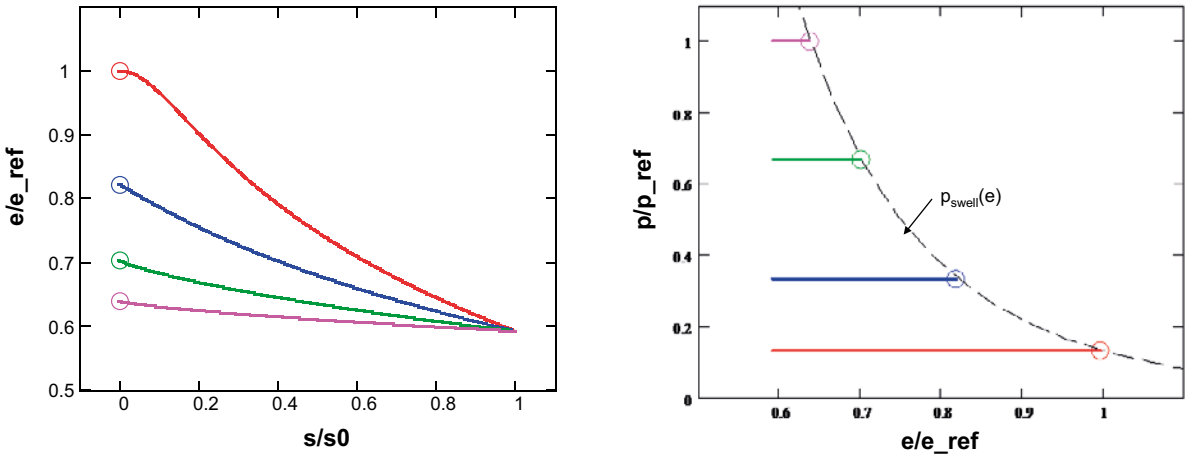

Figure A4-3. *MathCad responses for wetting under constant pressure.*

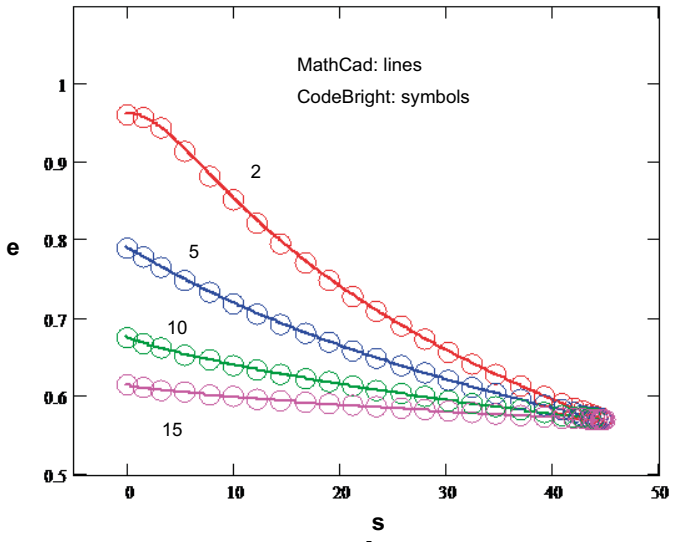

Figure A4-4. *MathCad and CodeBright responses for wetting under constant pressure. The net mean stress used is indicated close to the corresponding response curve.*

Wetting under constant void ratio (confined swelling)

The next simple case that is studied is wetting under constant void ratio e (confined swelling). Two different void ratios are used. Here, the final pressure p', at full water saturation, should match the swelling pressure curve so that $p' = p_{swell}(e)$.

In this example, also the elastic part of BBM comes into play, where the elastic modulus K is present, see (A4-2). For the two different void ratios the parameters in K have been kept the same.

$$d\varepsilon_v^{\,e} = \frac{dp'}{K}$$

$$K = \max\left\{\frac{(1+e)p'}{\kappa_i(s)}, K_{\min}\right\} \qquad \text{(A4-2)}$$

$$\kappa_i(s) = \kappa_{i0}\left[1+\alpha_i s\right]$$

The parameters used are:

- $\kappa_{s0} = 0.3$
- $p_{ref} = 1$ MPa
- $\rho_s = 2\,780$ kg/m^3
- $p_{atm} = 0.1$ MPa
- $\kappa_{i0} = 0.13$
- $\alpha_i = -0.02$
- $K_{min} = 13$ MPa

The initial states are given by $e = \{0.57, 0.8\}$ and $p' = 0$ MPa.

As can be seen in Figure A4-5, the MathCad results from using the modulus function follow the adopted swelling pressure curve.

To check the CodeBright implementation the results obtained from using MathCad and CodeBright are compared in Figure A4-6. The agreement between the solutions is very good.

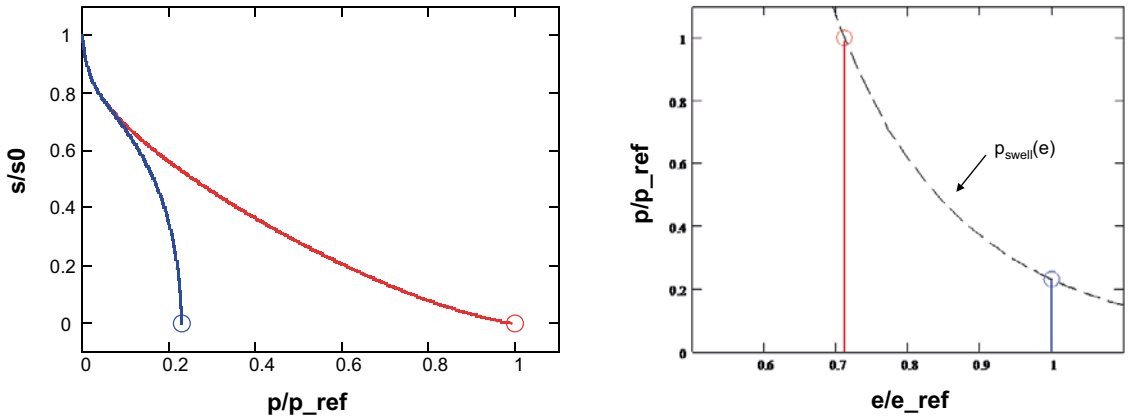

Figure A4-5. *MathCad Responses for confined wetting.*

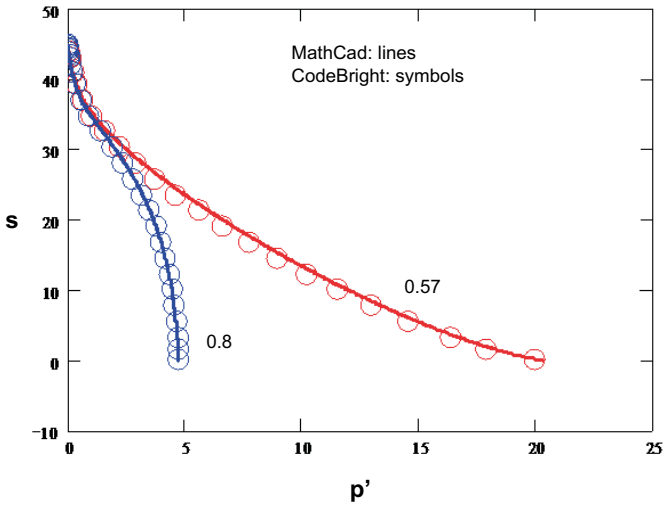

Figure A4-6. *MathCad and CodeBright responses for confined wetting. The void ratio used is indicated close to the corresponding response curve.*

Incorporation of a varying critical state line slope parameter M in BBM

The underlying idea with this modification is to incorporate a dependence of M (representing the slope of the critical state line) in the plastic part of BBM (A4-3) so that an experimentally validated expression of the type $q_f = q_f(p')$ that are found for bentonite clay are fulfilled.

$$
\begin{aligned}
&d\boldsymbol{\varepsilon}^{p} = d\Lambda \frac{\partial g}{\partial \boldsymbol{\sigma}} \\
&f = q^2 - M^2 (p' + p_s)(p_0 - p') \\
&g = \alpha q^2 - M^2 (p' + p_s)(p_0 - p') \\
&M = M(p_0, p_s) \\
&p_0(s, p_0^{\,*}) = p^c \left(\frac{p_0^{\,*}}{p^c} \right)^{\frac{\lambda_0 - \kappa_{i0}}{\lambda(s) - \kappa_{i0}}} \\
&\lambda(s) = \lambda_0 \\
&dp_0^{\,*} = \frac{1+e}{\lambda_0 - \kappa_{i0}} p_0^{\,*} d\varepsilon_v^p
\end{aligned}
\qquad \text{(A4-3)}
$$

In BBM the deviatoric failure stress q_f occurs at the mid-point pressure $p'_{\text{mid}} = (p_0 - p_s)/2$ of the yield surface f. When failure occurs the material model behaves plastic, i.e. $f = 0$. The obtained expression reads,

$$f = q_f^2 - M^2(p'_{mid} + p_s)(p_0 - p'_{mid}) = 0.$$

The parameter M may accordingly be expressed as,

$$M = \frac{q_f(p'_{mid})}{\frac{p_0 + p_s}{2}}.$$

The experimentally validated $q_f = q_f(p')$ expression reads

$$q_f(p') = ap'^b,$$

where no cohesion is present. Since the presence of p_s means that the BBM model includes cohesion, the original expression of q_f has been altered to

$$q_f(p') = a(p' + p_s)^b.$$

If this altered expression is used in the expression of the variable M we obtain,

$$M(p_0, p_s) = \frac{q_f\left(\frac{p_0 - p_s}{2}\right)}{\frac{p_0 + p_s}{2}} = a\left(\frac{p_0 + p_s}{2}\right)^{b-1}.$$

Contributions to the stiffness tensors

Below the new relation $M = M(p_0, p_s)$ is introduced into the BBM framework and the new contributions are shown. A von Mises type yield surface is considered (meaning that it is independent of Lode's angle) and the temperature dependence is omitted.

The differential of the yield surface becomes,

$$df = \frac{\partial f}{\partial \boldsymbol{\sigma}} \cdot d\boldsymbol{\sigma} + \frac{\partial f}{\partial s} ds + \frac{\partial f}{\partial \varepsilon_v^{\,p}} d\varepsilon_v^{\,p},$$

where the new dependency of M will have an effect on the last two partial derivatives since $p_0 = p_0(s, \varepsilon_v^p)$ and $p_s = p_s(s)$. The additional contributions can be seen when evaluating the partial derivatives below.

$$\frac{\partial f}{\partial s}=\frac{\partial f}{\partial p_0}\frac{\partial p_0}{\partial s}+\frac{\partial f}{\partial p_s}\frac{\partial p_s}{\partial s}=\left(\left.\frac{\partial f}{\partial p_0}\right|_{dM=0}+\frac{\partial f}{\partial M}\frac{\partial M}{\partial p_0}\right)\frac{\partial p_0}{\partial s}+\left(\left.\frac{\partial f}{\partial p_s}\right|_{dM=0}+\frac{\partial f}{\partial M}\frac{\partial M}{\partial p_s}\right)\frac{\partial p_s}{\partial s}$$

$$\frac{\partial f}{\partial \varepsilon_v^{\,p}}=\frac{\partial f}{\partial p_0}\frac{\partial p_0}{\partial \varepsilon_v^{\,p}}=\left(\left.\frac{\partial f}{\partial p_0}\right|_{dM=0}+\frac{\partial f}{\partial M}\frac{\partial M}{\partial p_0}\right)\frac{\partial p_0}{\partial \varepsilon_v^{\,p}} \qquad \text{(A4-4)}$$

Since the partial derivatives above now have additional terms, there will be contributions to the elastoplastic stiffness tensors $\boldsymbol{C}^{ep}$ and $\boldsymbol{c}^{ep}$.

$$d\boldsymbol{\sigma}=\boldsymbol{C}^{ep}\,d\boldsymbol{\varepsilon}+\boldsymbol{c}^{ep}\,ds$$

$$\boldsymbol{C}^{ep}=\boldsymbol{C}^{e}-\frac{1}{A}\left(\boldsymbol{C}^{e}\frac{\partial g}{\partial \boldsymbol{\sigma}}\right)\otimes\left(\boldsymbol{C}^{e}\frac{\partial f}{\partial \boldsymbol{\sigma}}\right)$$

$$\boldsymbol{c}^{ep}=\boldsymbol{c}^{e}-\frac{1}{A}\frac{\partial f}{\partial s}\boldsymbol{C}^{e}\frac{\partial g}{\partial \boldsymbol{\sigma}}-\frac{1}{A}\frac{1}{3K^{h}}\left(\left(\boldsymbol{C}^{e}\frac{\partial g}{\partial \boldsymbol{\sigma}}\right)\otimes\left(\boldsymbol{C}^{e}\frac{\partial f}{\partial \boldsymbol{\sigma}}\right)\right)\boldsymbol{I}$$

$$A=-\frac{\partial f}{\partial \varepsilon_v^{\,p}}\frac{\partial g}{\partial p'}+\frac{\partial f}{\partial \boldsymbol{\sigma}}\cdot\left(\boldsymbol{C}^{e}\frac{\partial g}{\partial \boldsymbol{\sigma}}\right)$$

The additional terms in (A1.1) are here specified in the variables and parameters used

$$\frac{\partial f}{\partial M}=-2M(p'+p_s)(p_0-p')$$

$$\frac{\partial M}{\partial p_0}=\frac{a(b-1)}{2}\left(\frac{p_0+p_s}{2}\right)^{b-2}$$

$$\frac{\partial M}{\partial p_s}=\frac{a(b-1)}{2}\left(\frac{p_0+p_s}{2}\right)^{b-2}$$

Test and validation

The implementation in CodeBright is tested below for a case where a loose clay specimen is first subjected to an increasing hydrostatic stress state which is followed by a “triaxial test” stress state (shearing), where two of the principal stresses are held constant and the third is increased (compressively). Drained hydraulic conditions prevail during the process. A case with a constant M and the new varying M are used to investigate the differences of the two formulations. The shearing begin at two different levels of hydrostatic pressure in order to investigate the behaviour of the models for different stress evolutions and validate that the final stress state coincides with $q_f = q_f(p')$ for the variable M implementation.

The parameters used in the mechanical model are:

Elastic strain increment

- $\kappa_{i0} = 0.15$
- $\alpha_i = -0.02$
- $K_{min} = 2$ MPa

Plastic strain increment

- $\lambda_0 = 0.18$
- $p_{s0} = 0.05$ MPa
- $p^c = 1$ MPa
- $M = 5$) (with a = 0.5 and b = 0.77) or $M = 0.589$
- $\alpha = 0.5$
- $p_0^{\,*} = 0.242$ MPa

Hydraulic strain increment

- $\kappa_{s0} = 0.2$
- $p_{ref} = 0.1$ MPa
- $\rho_s = 2\,780$ kg/m^3
- $p_{atm} = 0.1$ MPa

The initial states are given by $e = 1.78$, $p = 0.2$ MPa and $p_l = 0.1$ MPa.

λ_0 is set to correspond to the void ratio e at the start of shearing at the higher level of hydrostatic stress. This has been done in order to enable evaluation against the closely related experimental conditions of experiment T17 in Börgesson et al. (1995). The used swelling pressure curve is utilized for obtaining a value of λ_0.

$$\lambda(e) = \left[\frac{\mathrm{d}\ln\left(p_{swell}(e)\right)}{\mathrm{d}e}\right]^{-1}$$

$$p_{swell}(e) = 10^{\left[-4.741+4.117\cdot10^{-3}\frac{\rho_s}{1+e}-3.94\cdot10^{-7}\left(\frac{\rho_s}{1+e}\right)^2\right]}.$$

As can be seen in Figure A4-7 the responses obtained using the variable M implementation are much more in agreement with the T17 data as compared to the constant M implementation. It can also be seen that both stress states for the variable M simulation coincide with the $q_f(p')$ expression. This indicates that the CodeBright implementation is correct.

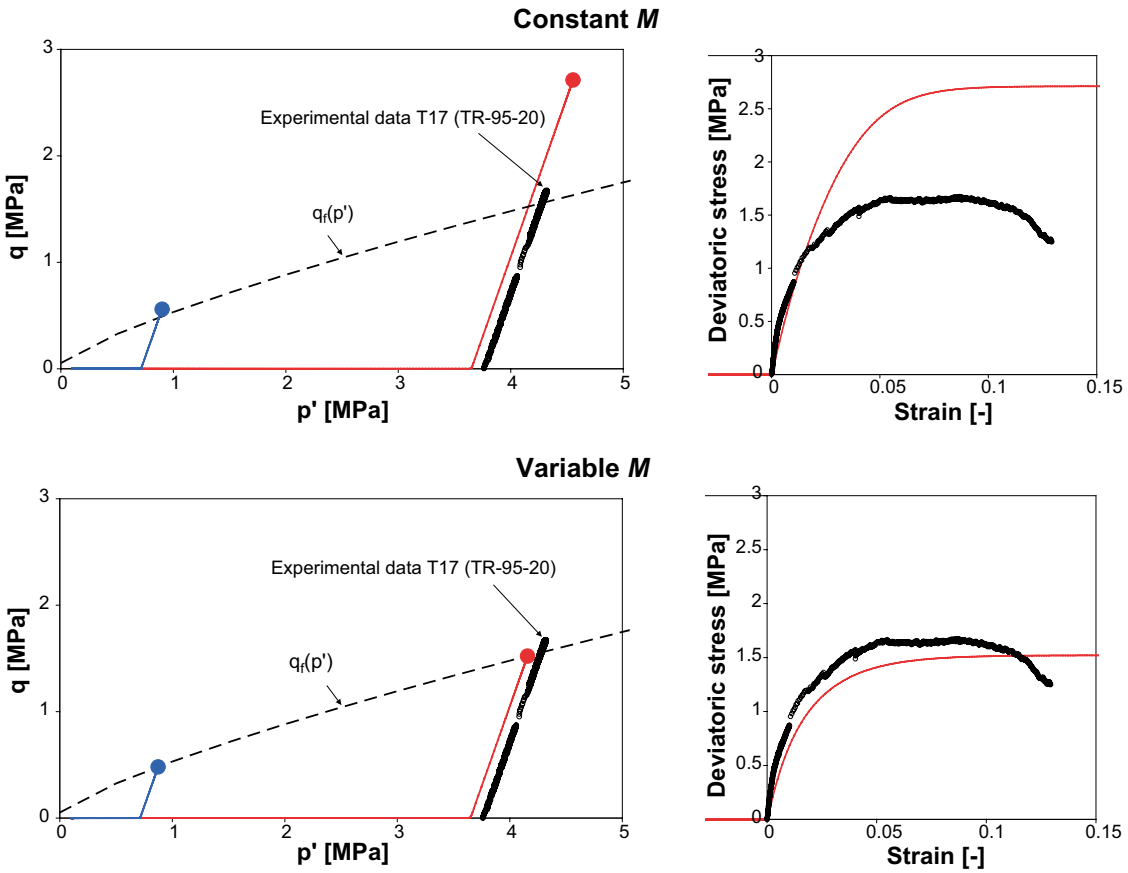

Figure A4-7. *Stress state (left) and q – strain relation (right) for the constant M (top) and variable M (bottom) models.*

Appendix 5

Notes on porosity update schemes using initial or updated coordinates

Initially the updated coordinate formulation was not used (the availability of this alternative was not known of) and due to this the obtained porosity field did not match the displacement field very well. In order to understand the mismatch, the underlying theory in kinematics was therefore studied and compared with the CODE_BRIGHT implementation. During the study, insight of the available formulation using updated coordinates was obtained and a comparison/investigation of the different updating schemes was performed.

In order to describe the two updating schemes the theory of kinematics is briefly reviewed below. First, the used definitions are given. These are followed by formulating the conservation of solid mass which give an expression used when updating the porosity. Then, relations from using the two alternatives are derived and finally a discussion of the differences is given.

Definitions

Two configurations, here denoted by the reference and current, will be used in the following. Entities belonging to the reference will be given names in upper case and entities belonging to the current will be given names in lower case.

Thus, $\boldsymbol{X}$ and $\boldsymbol{x}$ denote the position vectors to a point in the body in the reference and current configuration, respectively. The displacement of the point is defined $\boldsymbol{u} = \boldsymbol{x} - \boldsymbol{X}$. The line elements $d\boldsymbol{X}$ and $d\boldsymbol{x}$ and the volume elements dV and dv are present at the point. In the poromechanical theory the volume elements are divided in solid volume elements and porous volume elements, indicated by subscripts s and p, respectively. The porosities are defined $N = dV_p/dV$ and $n = dv_p/dv$. The volume elements have mass dm_s which can be expressed $dm_s = \rho_s^0 dV_s = \rho_s dv_s$ when introducing the density fields ρ_s^0 and ρ_s, belonging to the reference and current configuration, respectively.

The deformation gradient $\boldsymbol{F}=\partial\boldsymbol{x}/\partial\boldsymbol{X}$ links $d\boldsymbol{X}$ to the line increment current configuration, i.e. $d\boldsymbol{x} = \boldsymbol{F}\, d\boldsymbol{X}$. The deformation gradient also links the volume elements by $dv = \det(\boldsymbol{F})dV$, where the determinant $\det(\boldsymbol{F})$ is called the Jacobian which is denoted by $J = \det(\boldsymbol{F})$.

As a consequence of using initial or updated coordinates, two different strain measures are obtained: the Lagrangean strain $\boldsymbol{\varepsilon}_L = 0.5[\partial\boldsymbol{u}/\partial\boldsymbol{X} + (\partial\boldsymbol{u}/\partial\boldsymbol{X})^T]$ and the "updated Lagrangean" strain $\boldsymbol{\varepsilon}_{UL} = 0.5[\partial\boldsymbol{u}/\partial(\boldsymbol{x} - \mathrm{d}\boldsymbol{u}) + (\partial\boldsymbol{u}/\partial(\boldsymbol{x} - \mathrm{d}\boldsymbol{u}))^T]$. As can be seen it's the infinitesimal strain measures that are used, only the linear terms are present in the strain definitions.

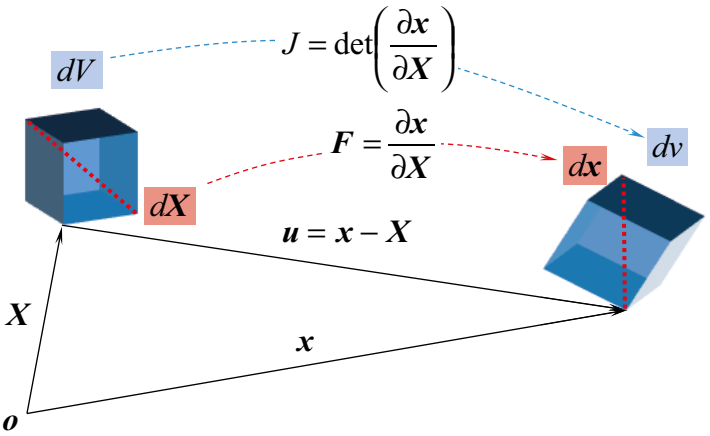

Figure A5-1. *Geometrical definitions.*

Solid mass conservation

The solid mass balance gives that the solid mass of any point should be conserved. Since the solid mass element at a point can be expressed as,

$dm_s = \rho_s dv_s = \rho_s(1-n)dv = \rho_s(1-n)JdV,$

it follows that,

$$\frac{(dm_s)^{\cdot}}{dV} = \dot{\rho}_s(1-n)J - \rho_s\dot{n}J + \rho_s(1-n)\dot{J} = 0$$

The solid mass is here prescribed as constant and an update scheme for the porosity is obtained by setting the rate of the solid mass in the equation above to zero. The relation,

$$\dot{J} = J\ \mathrm{tr}\left(\frac{\partial \dot{\boldsymbol{x}}}{\partial \boldsymbol{x}}\right) \tag{A5-1}$$

(not derived here) is used in the following. In the next section the right hand side of this relation is expressed in terms of Lagrangean strain and updated Lagrangean strain.

Using Lagrangian strain (initial coordinates)

The Lagrangean strain is defined as

$$\boldsymbol{\varepsilon}_L = \frac{1}{2}\left(\frac{\partial \boldsymbol{u}}{\partial \boldsymbol{X}} + \left(\frac{\partial \boldsymbol{u}}{\partial \boldsymbol{X}}\right)^{\mathrm{T}}\right),$$

which gives

$$\mathrm{tr}\dot{\boldsymbol{\varepsilon}}_L = \mathrm{tr}\left(\frac{\partial \dot{\boldsymbol{u}}}{\partial \boldsymbol{X}}\right)$$

The trace of the gradient of the velocity in (A5-1) can be expressed as

$$\mathrm{tr}\left(\frac{\partial \dot{\boldsymbol{x}}}{\partial \boldsymbol{x}}\right) = \mathrm{tr}\left(\frac{\partial \dot{\boldsymbol{u}}}{\partial \boldsymbol{X}}\frac{\partial \boldsymbol{X}}{\partial \boldsymbol{x}}\right) = \mathrm{tr}\left(\frac{\partial \dot{\boldsymbol{u}}}{\partial \boldsymbol{X}}\left(\frac{\partial \boldsymbol{X}}{\partial (\boldsymbol{X}+\boldsymbol{u})}\right)\right) \approx \mathrm{tr}\left(\frac{\partial \dot{\boldsymbol{u}}}{\partial \boldsymbol{X}}\right) = \mathrm{tr}\dot{\boldsymbol{\varepsilon}}_L \quad \text{if} \quad \boldsymbol{u} \approx \boldsymbol{0}$$

Thus,

$$\dot{J} \approx J\ \mathrm{tr}\dot{\boldsymbol{\varepsilon}}_L \quad \text{if} \quad \boldsymbol{u} \approx \boldsymbol{0}$$

Inserting this into the expression for the time derivative of the solid mass element divided by the reference volume element gives,

$$\frac{(dm_s)^{\cdot}}{dV} \approx \dot{\rho}_s(1-n) - \rho_s\dot{n} + \rho_s(1-n)\mathrm{tr}\dot{\boldsymbol{\varepsilon}}_L \quad \text{if} \quad \boldsymbol{u} \approx \boldsymbol{0} \tag{A5-2}$$

Using updated Lagrangian strain (updated coordinates)

The updated Lagrangean strain is defined as,

$$\boldsymbol{\varepsilon}_{UL} = \frac{1}{2}\left(\frac{\partial \boldsymbol{u}}{\partial (\boldsymbol{x}-d\boldsymbol{u})} + \left(\frac{\partial \boldsymbol{u}}{\partial (\boldsymbol{x}-d\boldsymbol{u})}\right)^{\mathrm{T}}\right)$$

, which gives,

$$\mathrm{tr}\dot{\boldsymbol{\varepsilon}}_{UL} = \mathrm{tr}\left(\frac{\partial \dot{\boldsymbol{u}}}{\partial (\boldsymbol{x}-d\boldsymbol{u})}\right)$$

The trace of the gradient of the velocity in Equation (A5-2) can be expressed as

$$\mathrm{tr}\left(\frac{\partial \dot{\boldsymbol{x}}}{\partial \boldsymbol{x}}\right) = \mathrm{tr}\left(\frac{\partial \dot{\boldsymbol{u}}}{\partial \boldsymbol{x}}\right) \approx \mathrm{tr}\left(\frac{\partial \dot{\boldsymbol{u}}}{\partial (\boldsymbol{x} - d\boldsymbol{u})}\right) = \mathrm{tr}\dot{\boldsymbol{\varepsilon}}_{UL} \quad \text{if} \quad d\boldsymbol{u} << \boldsymbol{u}$$

Thus,

$$\dot{J} \approx J\ \mathrm{tr}\dot{\boldsymbol{\varepsilon}}_{UL} \quad \text{if} \quad d\boldsymbol{u} << \boldsymbol{u}$$

Inserting this into the expression for the time derivative of the solid mass element divided by the reference volume element gives,

$$\frac{(dm_s^{\cdot})}{dV} \approx \dot{\rho}_s(1-n) - \rho_s \dot{n} + \rho_s(1-n)\mathrm{tr}\dot{\boldsymbol{\varepsilon}}_{UL} \quad \text{if} \quad d\boldsymbol{u} << \boldsymbol{u} \qquad \text{(A5-3)}$$

Discussion

When comparing the alternatives (A5-2) and (A5-3), the first is valid only if the displacements are close to zero and the second is valid if the displacement increments are much smaller as compared to the displacements. Thus, if a problem gives rise to strain (deformation), the updated coordinate alternative should be used to avoid erroneous solutions. It can also be noted that even when the updated coordinate scheme is used, small time increments are necessary.

Below in Figure A5-2, an example of uniaxial compression of a bar is given where the initial and updated coordinate alternatives have been used when updating the porosity (here the void ratio is shown instead). The volumetric strain is going from 0 to 0.35 and the void ratio (initially $e_0 = 1.78$) is updated using updated, or not updated, coordinates. This could represent the pellet slot. As can be seen, the results differ significantly.

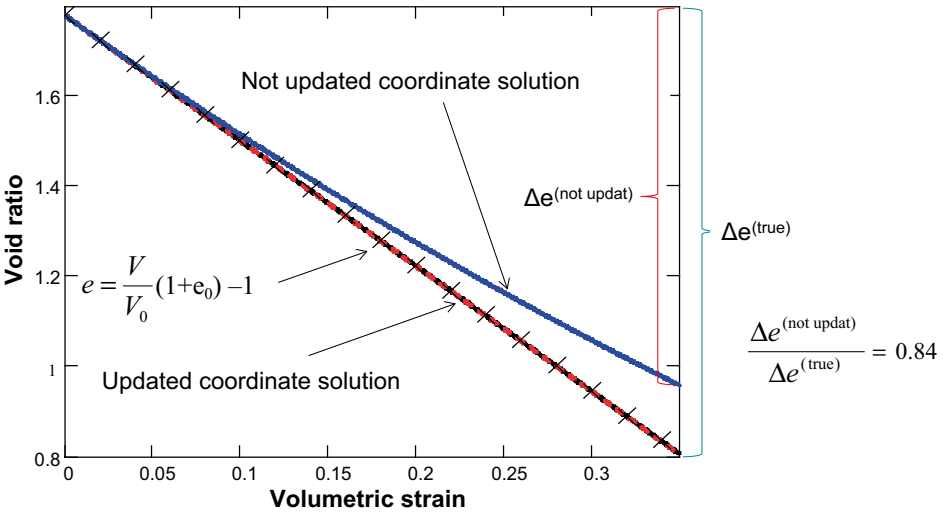

Figure A5-2. *The difference using Lagrangean or updated Lagrangean strain considering uniaxial compression of a bar.*

Appendix 6

Generation of retention curves for the three bentonite block types in CRT

General

The relation between water content and suction describes the main driving force for the saturation process. The relation is often called the retention curve. One application of the retention curve is as input data to material models used for prediction and evaluation of large field tests.

The retention curve can be determined as water contents w (the mass of water divided by the mass of solids) in equilibrium with a series of relative humidity at free swelling conditions. The appearance of this retention curve depends to some extent on the initial water content (e.g. Dueck 2004). The retention curve determined under free swelling condition and starting with an initial water content deviating from 0 % is called the specific retention curve.

When the retention curve is used as input data to material models the so called confined retention curve is also needed. This curve can be based on the specific retention curve but is valid for a confined volume. The retention curve used for modeling purpose is often expressed as suction versus degree of saturation. Equation (A6-1) is the definition of suction ψ according to Fredlund and Rahardjo (1993, Chapter 4). The degree of saturation S_r is calculated according to Equation (A6-2).

$$\psi = -\frac{R \cdot T \cdot \rho_w}{\omega_v} \cdot \ln\left(\frac{p}{p_{sat}}\right) \tag{A6-1}$$

$$S_r = \frac{w \cdot \rho_s}{e \cdot \rho_w} \tag{A6-2}$$

In Equation (A6-1) T is the temperature (K), R the universal gas constant (8.31432 J/(mol K)) and ω_v the molecular mass of water vapor (0.018 kg/mol). The relative humidity is defined as $RH = 100 \cdot (p/p_s)$ where p is the partial pressure of pore-water vapor and p_s is the saturation pressure of water vapor over a flat surface of pure water at the temperature T. In Equation (A6-2) ρ_s is the particle density, ρ_w is the density of water and e is the void ratio.

Material

The material is a commercially available sodium bentonite with a quality symbol MX-80 from American Colloid Co. The bentonite has montmorillonite as the dominating smectite clay mineral. The particle density ρ_s = 2 780 kg/m^3 and water density ρ_w = 1 000 kg/m^3 were used for evaluation of void ratio and degree of saturation from measured variables (Börgesson et al. 1995).

Specific retention curves for MX-80

Specific retention curves with different initial water contents were determined with a method described by Wadsö et al. (2004) using 10g samples placed in pans hanging from lids in glass jars. The sample weight was monitored by below balance weighing. Measurements were carried out at seven different RH values (11 %, 33 %, 59 %, 75 %, 85 %, 93 %, and 98 %). The jars were placed at laboratory room climate with a temperature of 20 ± 0.5 °C. According to Dueck (2004) the final water contents for the initial water contents 7.5 % and 17.5 % were (2.7, 7.2, 10.5 15.5, 18.4, 23.1, and 33.5) and (3.3, 9.3, 15.4, 17.7, 20.2, 24.3, and 34.6), respectively.

A continuous formulation of the specific retention curve according to Equation (A6-3) was used with different constants (B, b) to coincide with the measured values representing the different initial water contents; 7.5 % (–0.0007, –0.319) and 17.5 % (–0.00013, 0.28). The relation and the constants valid for relative humidity from 75 % to 98 % were presented by Dueck (2004) and Dueck and Börgesson (2007).

$$w = \left[B \cdot \ln(\frac{RH_{ret}}{100}) \right]^b \quad \text{(A6-3)}$$

Model for the development of confined stress at constant volume conditions

The model includes mainly two equations, Equations (A6-4) and (A6-5), which relate the variables stress, relative humidity, water content and void ratio. It was proposed by Dueck (2004) and mainly based on tests with constant volume conditions. The included relationships are further described by Dueck and Börgesson (2007).

Equation (A6-4) describes the relation between the mean stress P, the actual relative humidity RH_{act} in the sample and the relative humidity according to the retention curve at actual water content RH_{ret}. The retention curve is derived from Equation (A6-3) with the constants B and b corresponding to the appropriate initial water content.

$$P(RH_{act}, w) = -\frac{R \cdot T \cdot \rho_w}{\omega_v} \cdot \ln(\frac{RH_{ret}(w)}{RH_{act}}) \quad \text{(A6-4)}$$

Equation (A6-5) describes the relation between the mean stress and the degree of saturation S_r at a specified void ratio e. The initial degree of saturation of the unloaded sample $S_{r,ini}$ is included. The swelling pressure at saturation P_{ret} can be calculated from the retention curve (A6-6) which includes the void ratio e and the water content at saturation w_s (A6-7).

$$P(S_r, e) = \frac{S_r - S_{r,ini}}{1 - S_{r,ini}} \cdot P_{ret}(e) \quad \text{(A6-5)}$$

$$P_{ret}(e) = -\frac{R \cdot T \cdot \rho_w}{\omega_v} \cdot \ln(\frac{RH_{ret}(w_s)}{100}) \quad \text{(A6-6)}$$

$$w_s = 100 \cdot \frac{e \cdot \rho_w}{\rho_s} \quad \text{(A6-7)}$$

Retention curves f(Sr) at specific conditions

Three specific conditions were considered. The void ratio and the initial water content (e, w_{ini}) for the three conditions were (0.56, 17.1 %), (0.636, 17.1 %) and (0.72, 16.5 %).

The retention curve consists in this description of two main parts and a transition in between. In the dry part of the curve no influence of confinement was considered and the specific retention curve was used. In the wet part, starting from the specified initial degree of saturation $S_{r,ini}$ the confined retention curve was used. Between the specific and the confined curves an intermediate curve was drawn.

Specific retention curve

In the dry part (70 MPa < ψ < 300 MPa) the specific retention curve was used and the measurements from the conditions RH = 11 %, 33 and 59 % were used. Since the appearance of the retention curve depends on the initial water content, the final water contents used were linearly interpolated between the measured values mentioned above. Suction was calculated from Equation (A6-1) and the degree of saturation was calculated from Equation (A6-2) with the specified void ratio.

Confined retention curve

In the wet part (0.1 MPa < ψ < 37 MPa) the confined retention curve $\psi_{confined}$ was used. From Equations (A6-4) to (A6-7) a relation between suction and degree of saturation was explicitly expressed according to Equation (A6-8). Since the retention curve depends on the initial water content the constants B and b from Equation (A6-3) were linearly interpolated between the given values above to correspond to the specified initial water content.

$$\psi_{confined} = -\frac{R \cdot T \cdot \rho_w}{\omega_v} \cdot \left[\left(S_r \cdot e \cdot \rho_w / \rho_s \right)^{1/b} \right) / B - \frac{S_r - S_{r,ini}}{100 - S_{r,ini}} \cdot \left(100 \cdot e \cdot \rho_w / \rho_s \right)^{1/b} \right) / B \right] \quad \text{(A6-8)}$$

Intermediate curve

The intermediate curve, between the specific and the confined retention curves, was made with a best fit line between the final point from the specific curve and the first points of the confined curve. The shape of Equation (A6-9) was found suitable for this intermediate curve and for each specified condition the constants (*K, L*) were determined.

$$\psi = K \cdot \ln(S_r) + L \quad \text{(A6-9)}$$

Input data to the modeling

The resulting retention curves for the three conditions considered for modeling purpose are plotted in Figure A6-1.

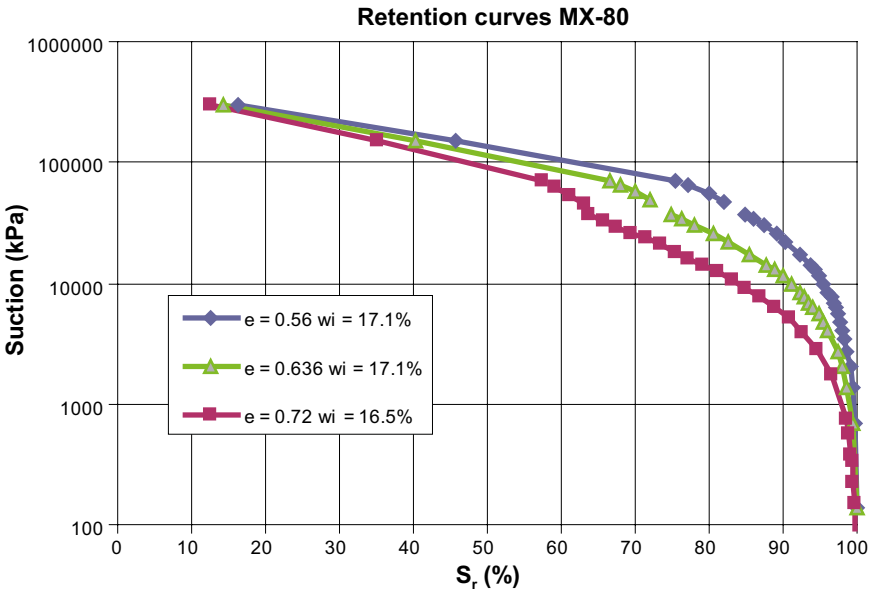

Figure A6-1. *Retention curves for three conditions considered for modeling purpose.*

Results of the 2D-calculation

Ring 5 (R5)

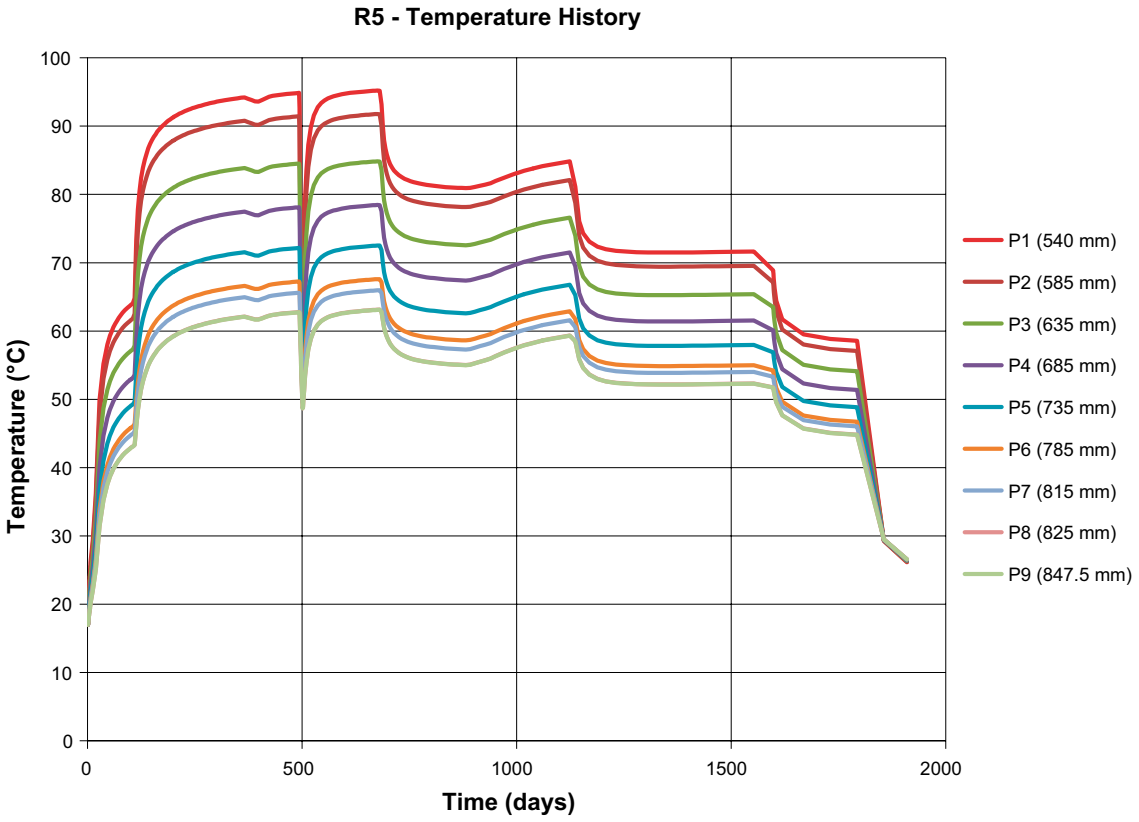

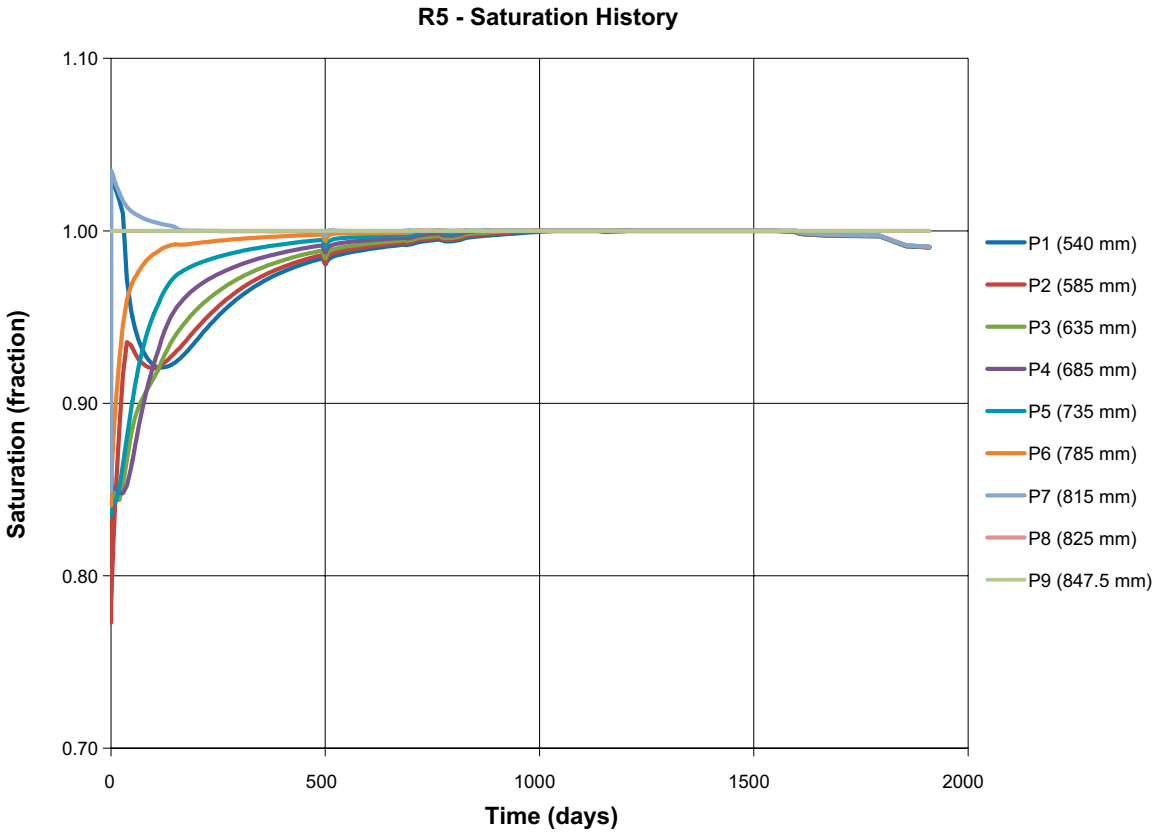

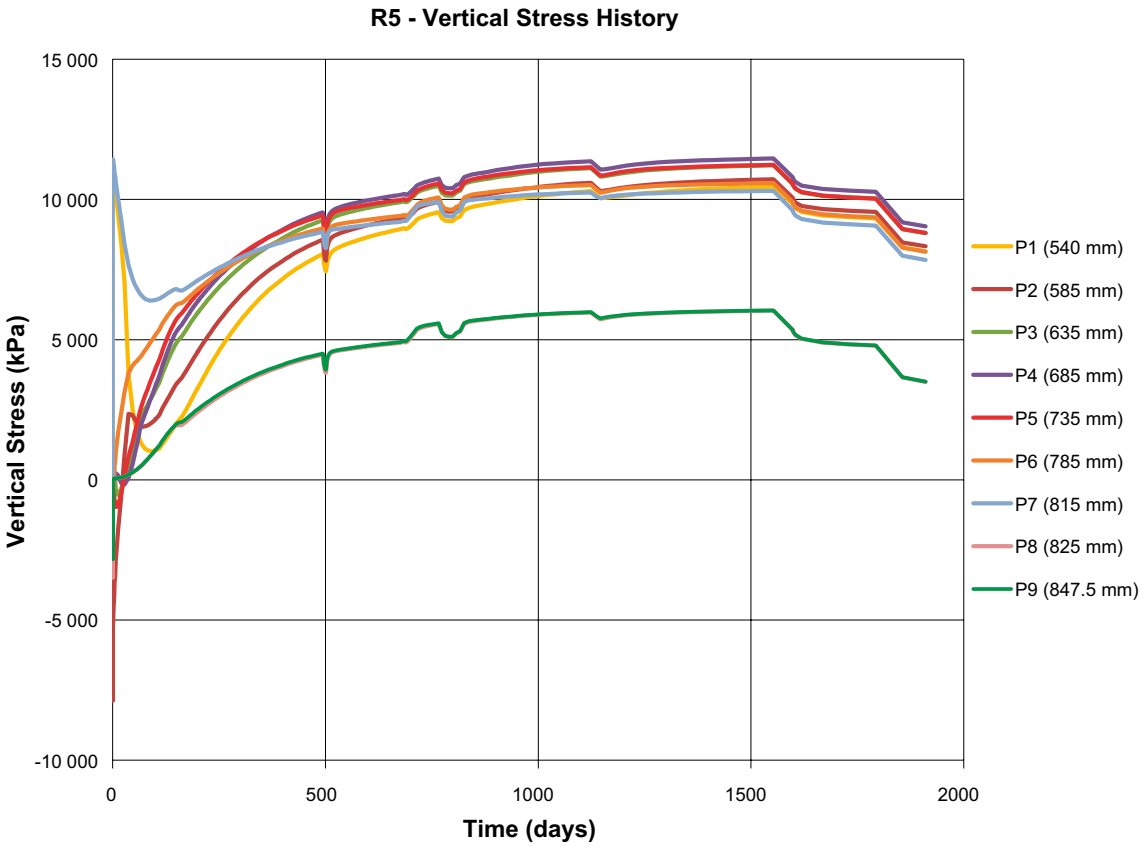
R5 - Vertical Stress History
15 000
10 000
5 000
0
-5 000
-10 000
Vertical Stress (kPa)
0
500
1000
1500
2000
Time (days)
P1 (540 mm)
P2 (585 mm)
P3 (635 mm)
P4 (685 mm)
P5 (735 mm)
P6 (785 mm)
P7 (815 mm)
P8 (825 mm)
P9 (847.5 mm)

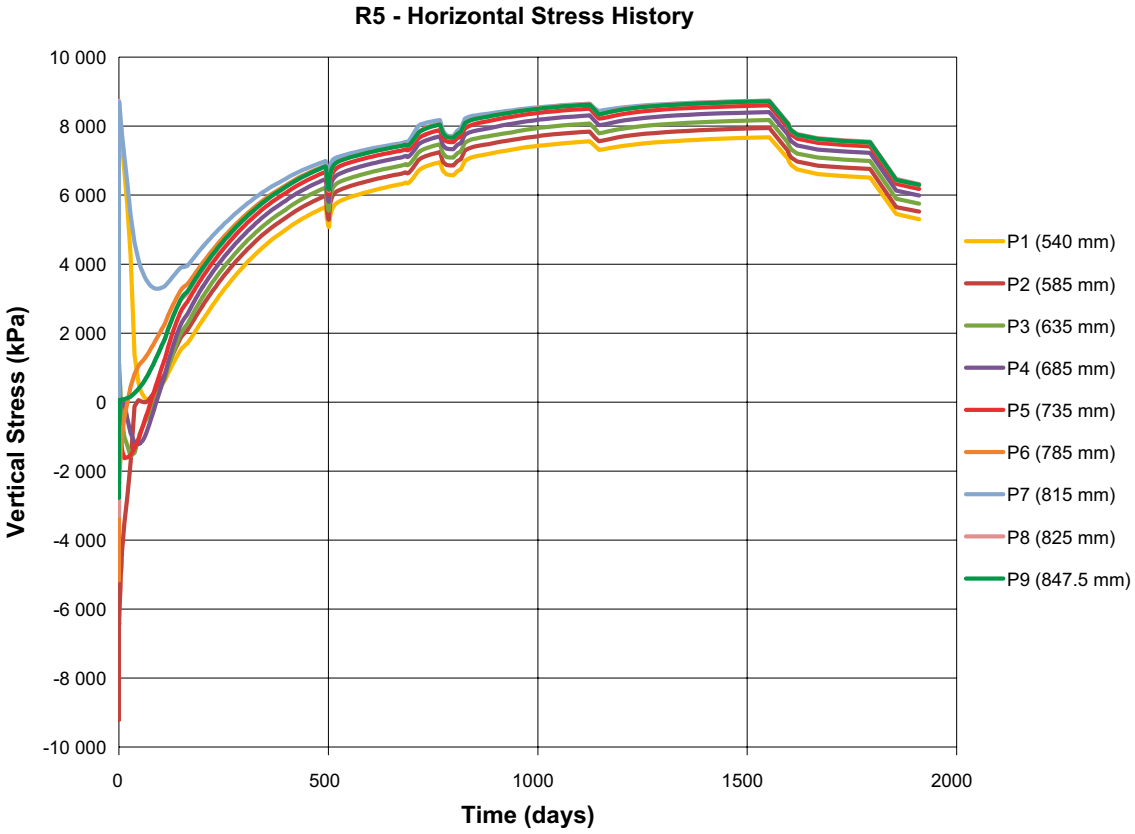
R5 - Horizontal Stress History
10 000
8 000
6 000
4 000
2 000
0
-2 000
-4 000
-6 000
-8 000
-10 000
Vertical Stress (kPa)
0
500
1000
1500
2000
Time (days)
P1 (540 mm)
P2 (585 mm)
P3 (635 mm)
P4 (685 mm)
P5 (735 mm)
P6 (785 mm)
P7 (815 mm)
P8 (825 mm)
P9 (847.5 mm)

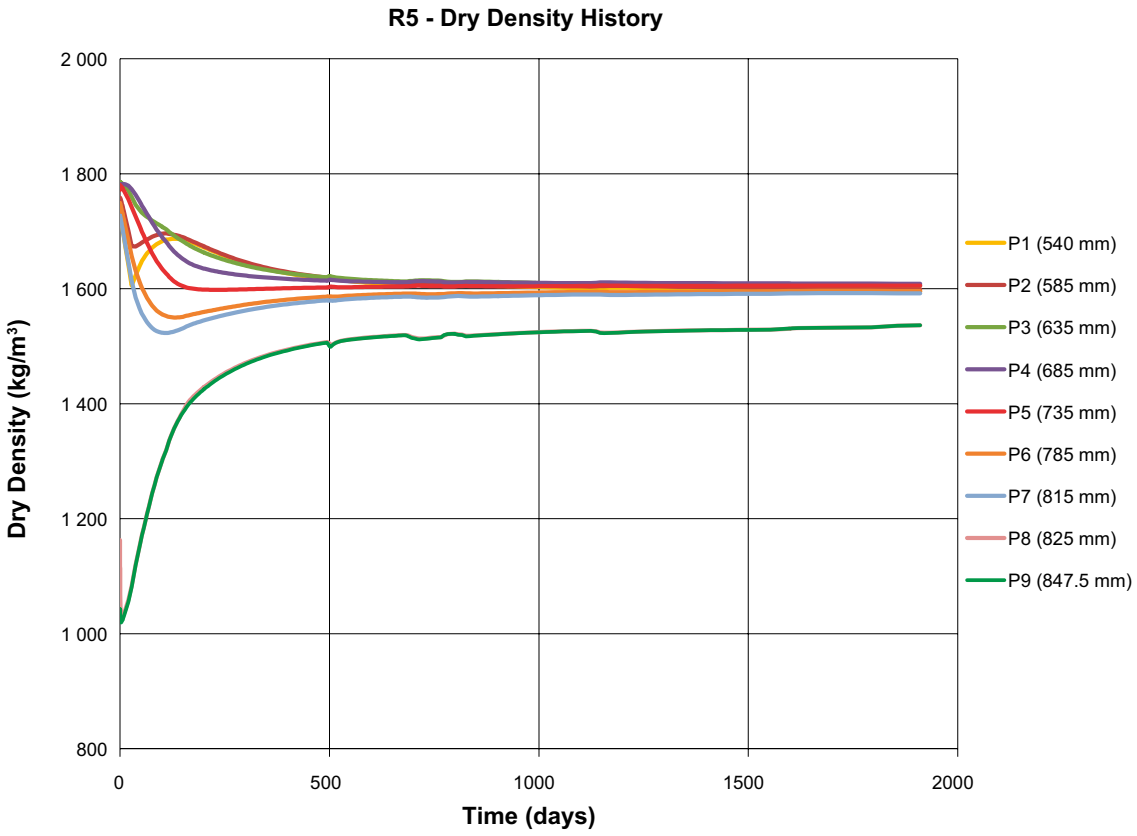
R5 - Dry Density History
Dry Density (kg/m³)
2 000
1 800
1 600
1 400
1 200
1 000
800
0
500
1000
1500
2000
Time (days)
P1 (540 mm)
P2 (585 mm)
P3 (635 mm)
P4 (685 mm)
P5 (735 mm)
P6 (785 mm)
P7 (815 mm)
P8 (825 mm)
P9 (847.5 mm)

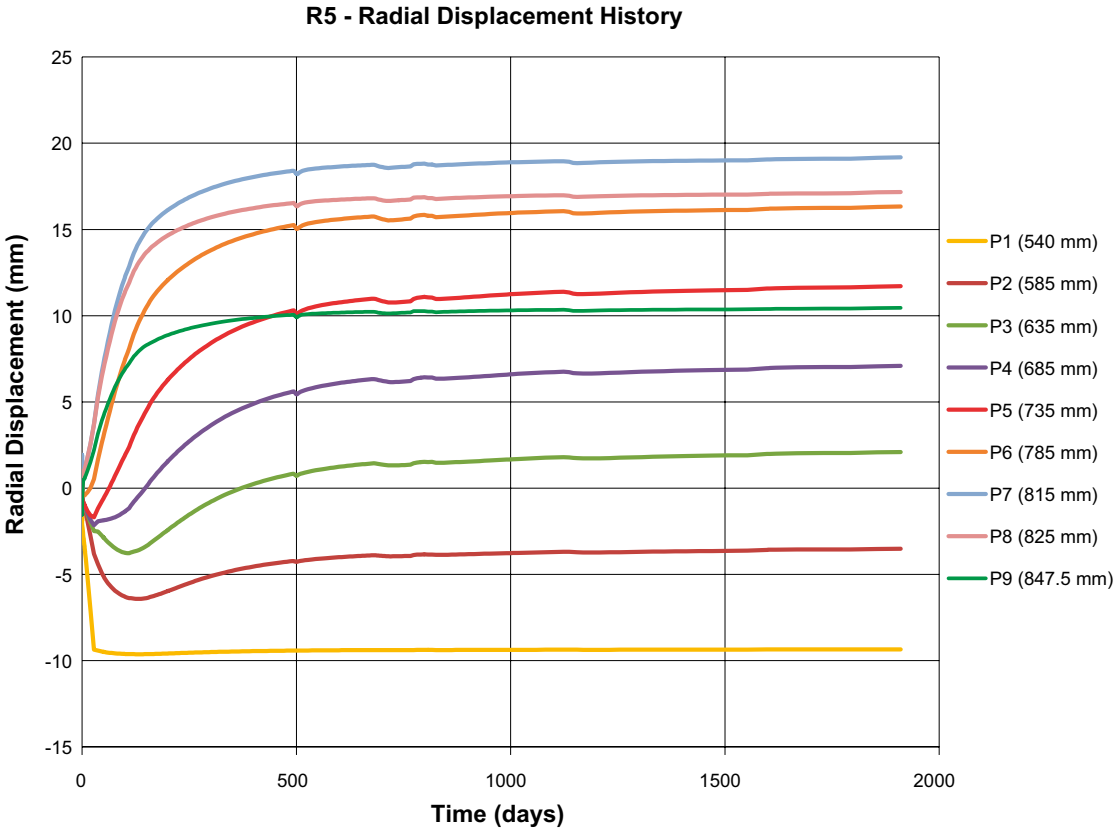
R5 - Radial Displacement History
Radial Displacement (mm)
25
20
15
10
5
0
-5
-10
-15
0
500
1000
1500
2000
Time (days)
P1 (540 mm)
P2 (585 mm)
P3 (635 mm)
P4 (685 mm)
P5 (735 mm)
P6 (785 mm)
P7 (815 mm)
P8 (825 mm)
P9 (847.5 mm)

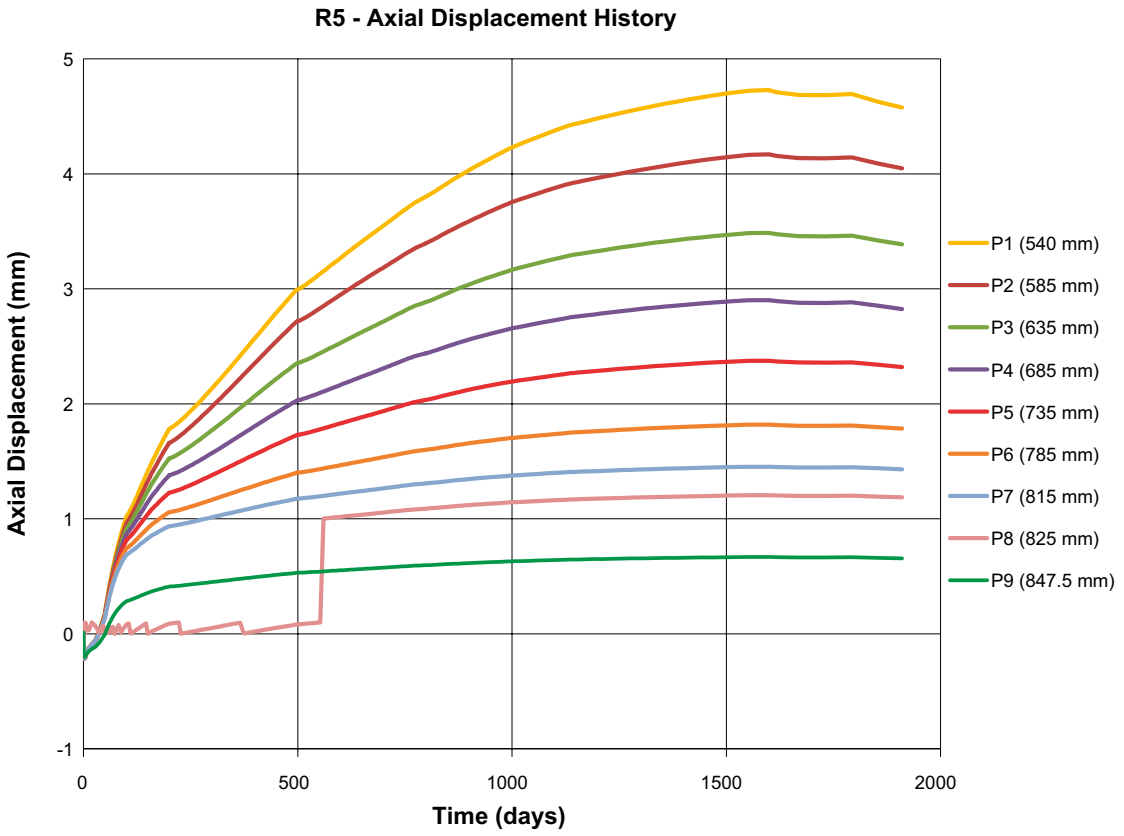
R5 - Axial Displacement History
Axial Displacement (mm)
5
4
3
2
1
0
-1
0
500
1000
1500
2000
Time (days)
P1 (540 mm)
P2 (585 mm)
P3 (635 mm)
P4 (685 mm)
P5 (735 mm)
P6 (785 mm)
P7 (815 mm)
P8 (825 mm)
P9 (847.5 mm)

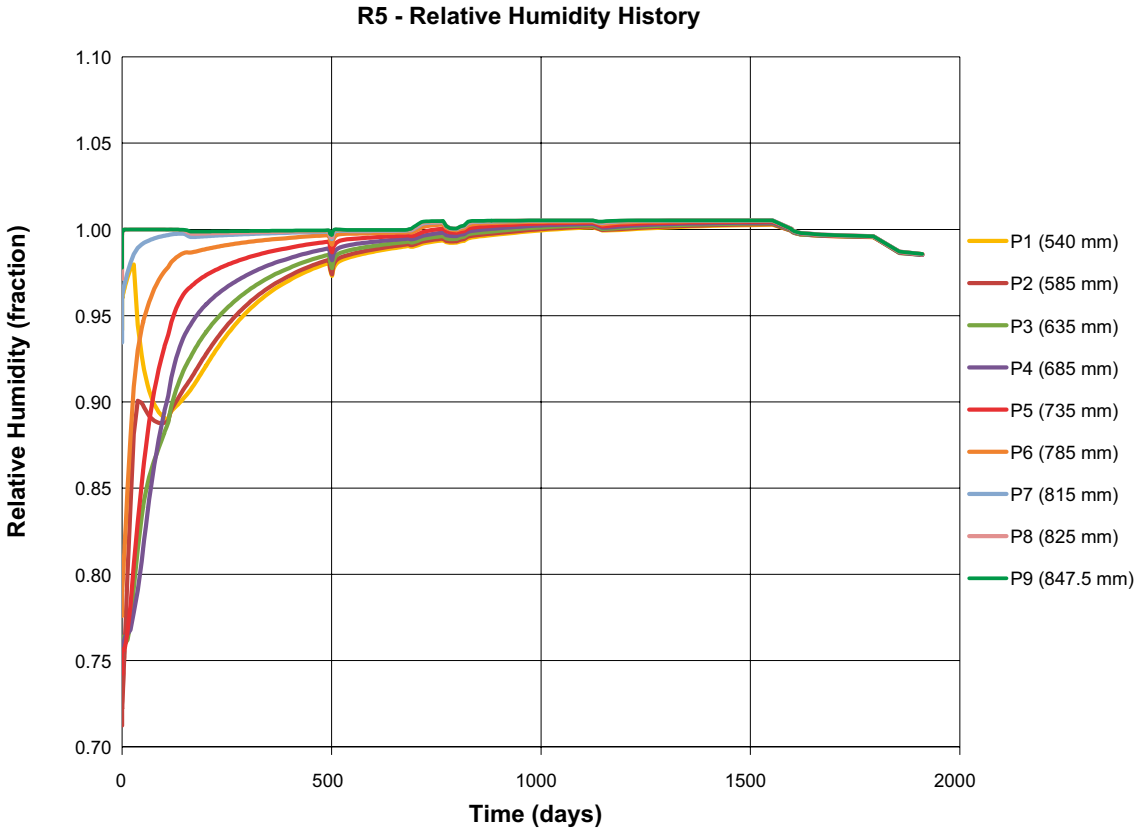
R5 - Relative Humidity History
Relative Humidity (fraction)
1.10
1.05
1.00
0.95
0.90
0.85
0.80
0.75
0.70
0
500
1000
1500
2000
Time (days)
P1 (540 mm)
P2 (585 mm)
P3 (635 mm)
P4 (685 mm)
P5 (735 mm)
P6 (785 mm)
P7 (815 mm)
P8 (825 mm)
P9 (847.5 mm)

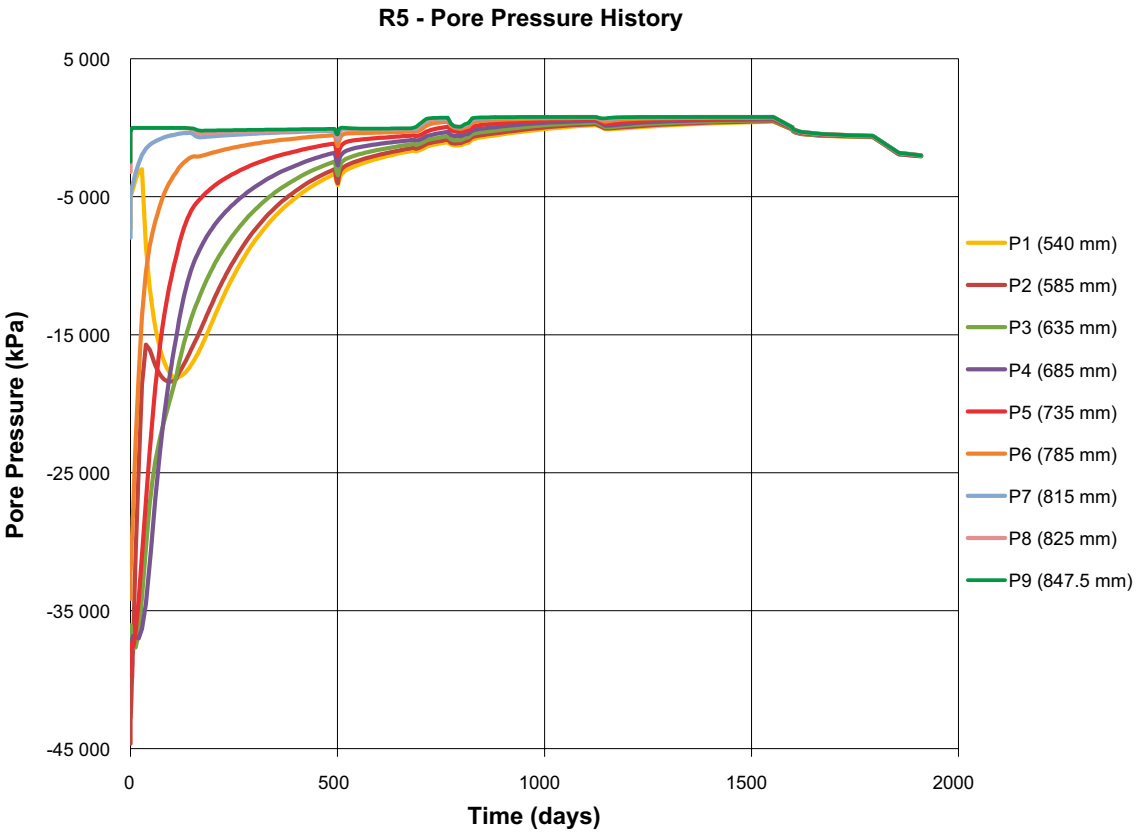
R5 - Pore Pressure History
Pore Pressure (kPa)
5 000
-5 000
-15 000
-25 000
-35 000
-45 000
0
500
1000
1500
2000
Time (days)
P1 (540 mm)
P2 (585 mm)
P3 (635 mm)
P4 (685 mm)
P5 (735 mm)
P6 (785 mm)
P7 (815 mm)
P8 (825 mm)
P9 (847.5 mm)

Ring 10 (R10)

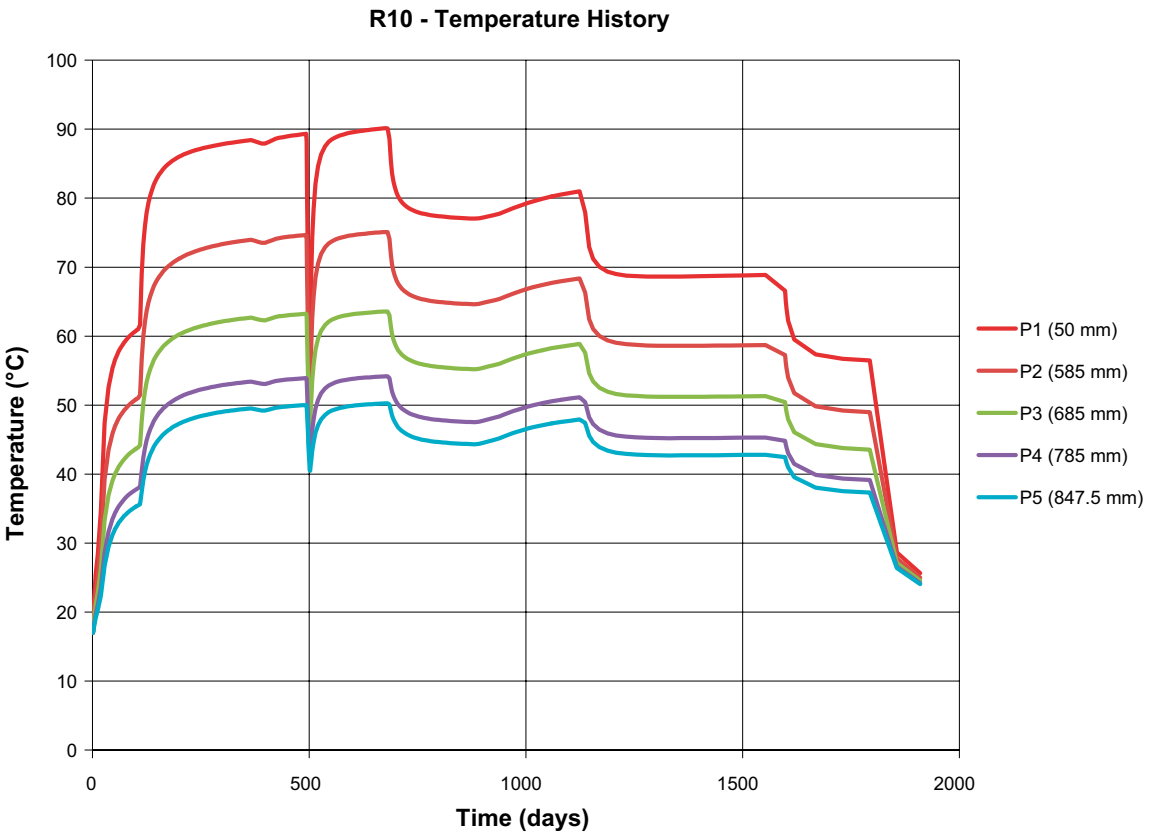
R10 - Temperature History
Temperature (°C)
Time (days)
0
10
20
30
40
50
60
70
80
90
100
0
500
1000
1500
2000
P1 (50 mm)
P2 (585 mm)
P3 (685 mm)
P4 (785 mm)
P5 (847.5 mm)

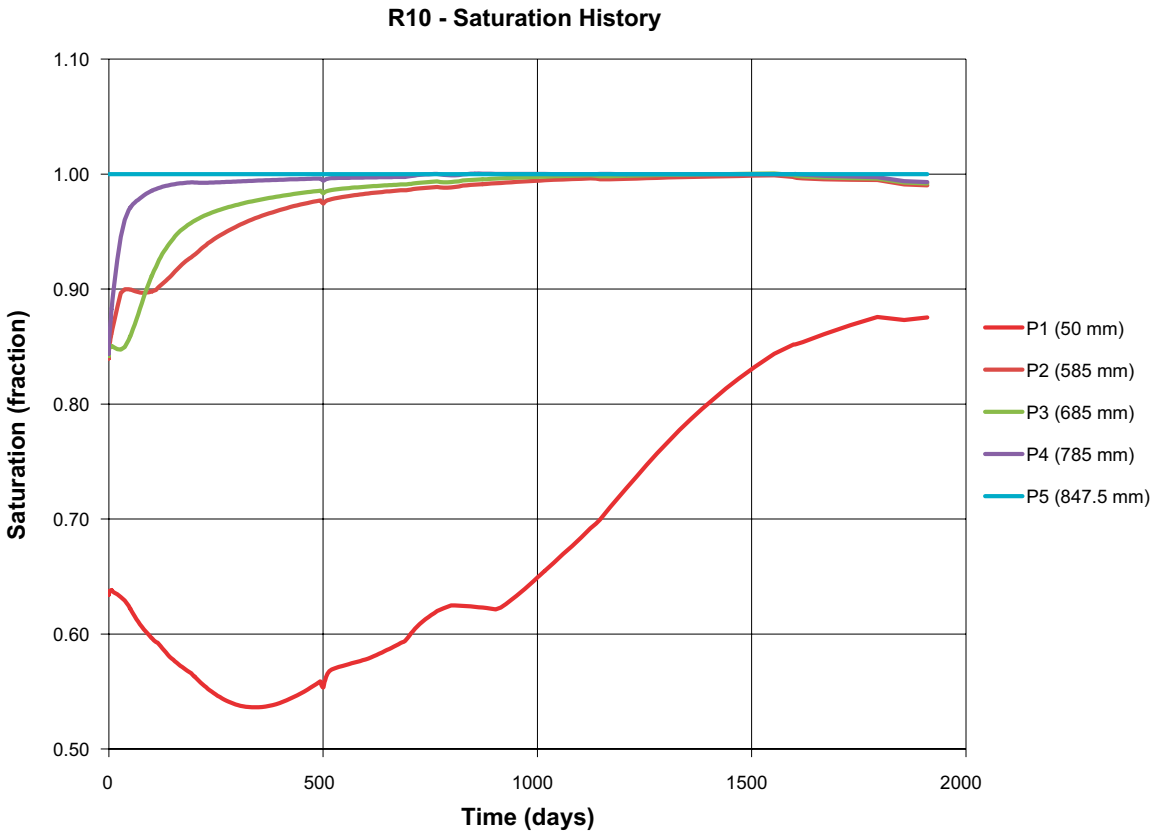
R10 - Saturation History
Saturation (fraction)
Time (days)
0.50
0.60
0.70
0.80
0.90
1.00
1.10
0
500
1000
1500
2000
P1 (50 mm)
P2 (585 mm)
P3 (685 mm)
P4 (785 mm)
P5 (847.5 mm)

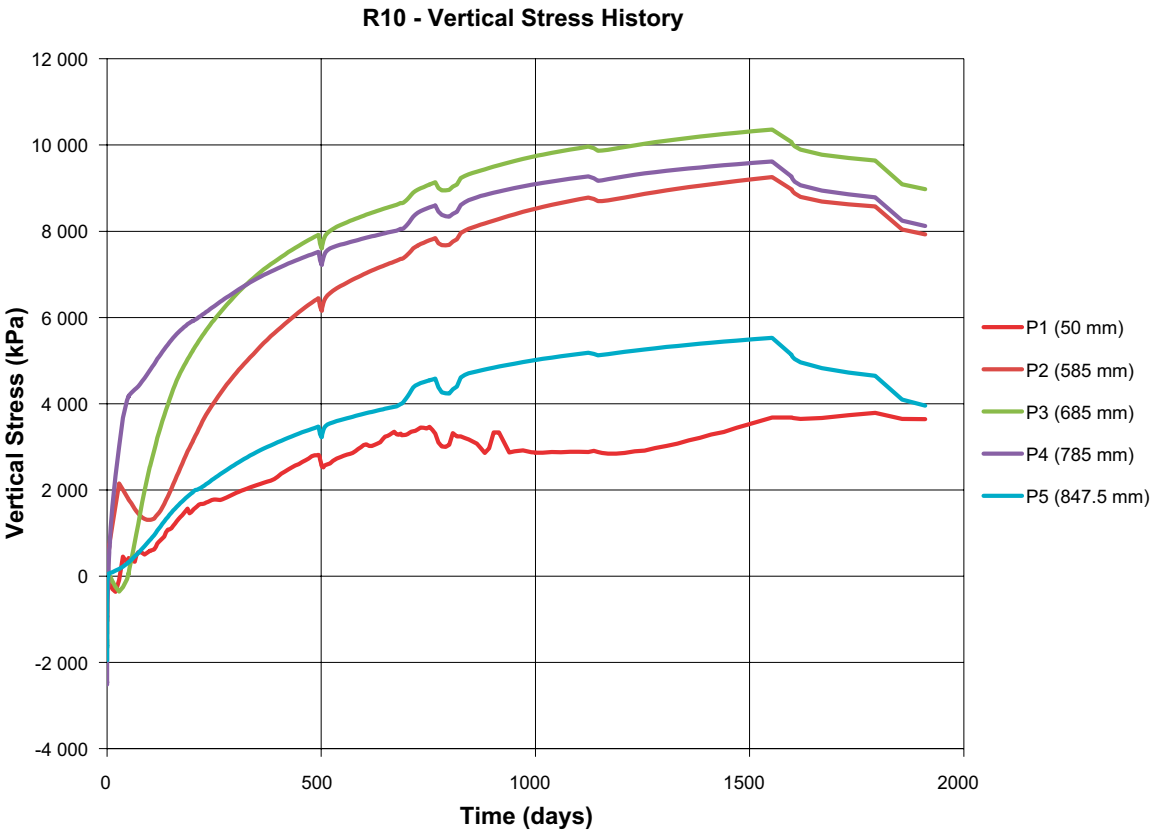
R10 - Vertical Stress History
12 000
10 000
8 000
6 000
4 000
2 000
0
-2 000
-4 000
Vertical Stress (kPa)
0
500
1000
1500
2000
Time (days)
P1 (50 mm)
P2 (585 mm)
P3 (685 mm)
P4 (785 mm)
P5 (847.5 mm)

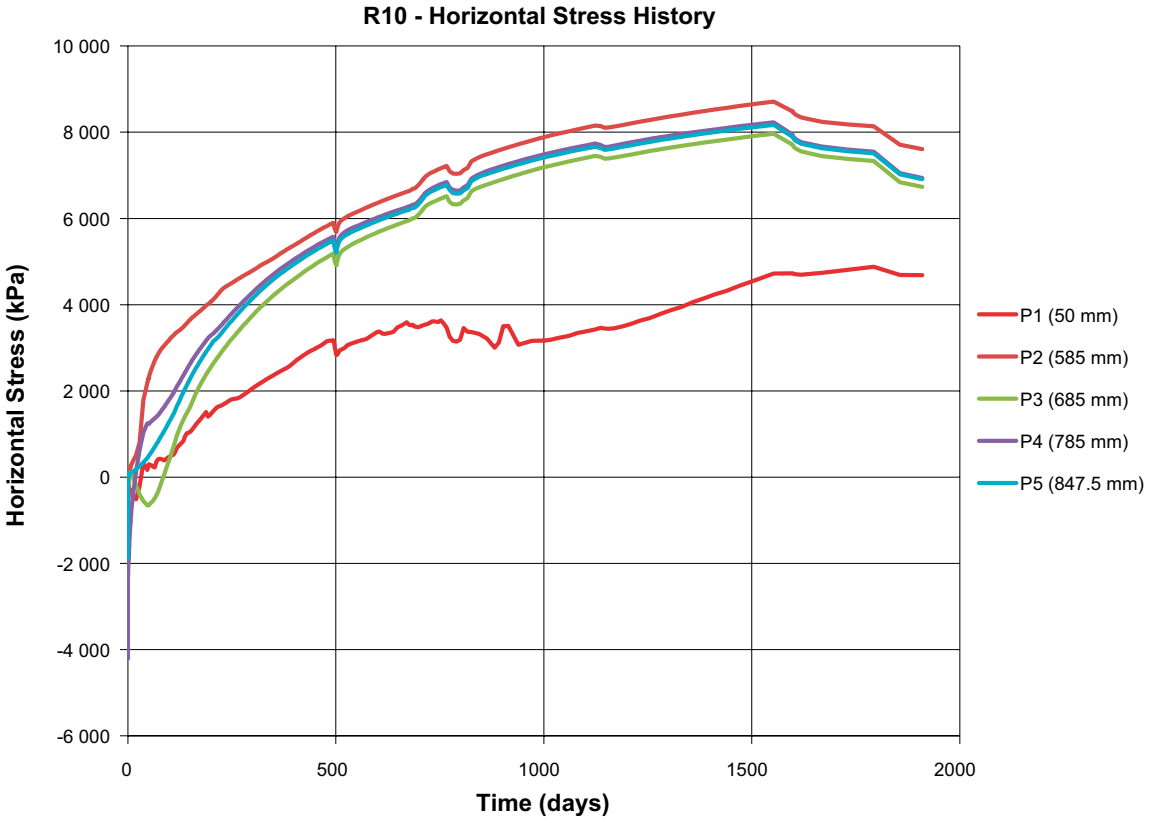
R10 - Horizontal Stress History
10 000
8 000
6 000
4 000
2 000
0
-2 000
-4 000
-6 000
Horizontal Stress (kPa)
0
500
1000
1500
2000
Time (days)
P1 (50 mm)
P2 (585 mm)
P3 (685 mm)
P4 (785 mm)
P5 (847.5 mm)

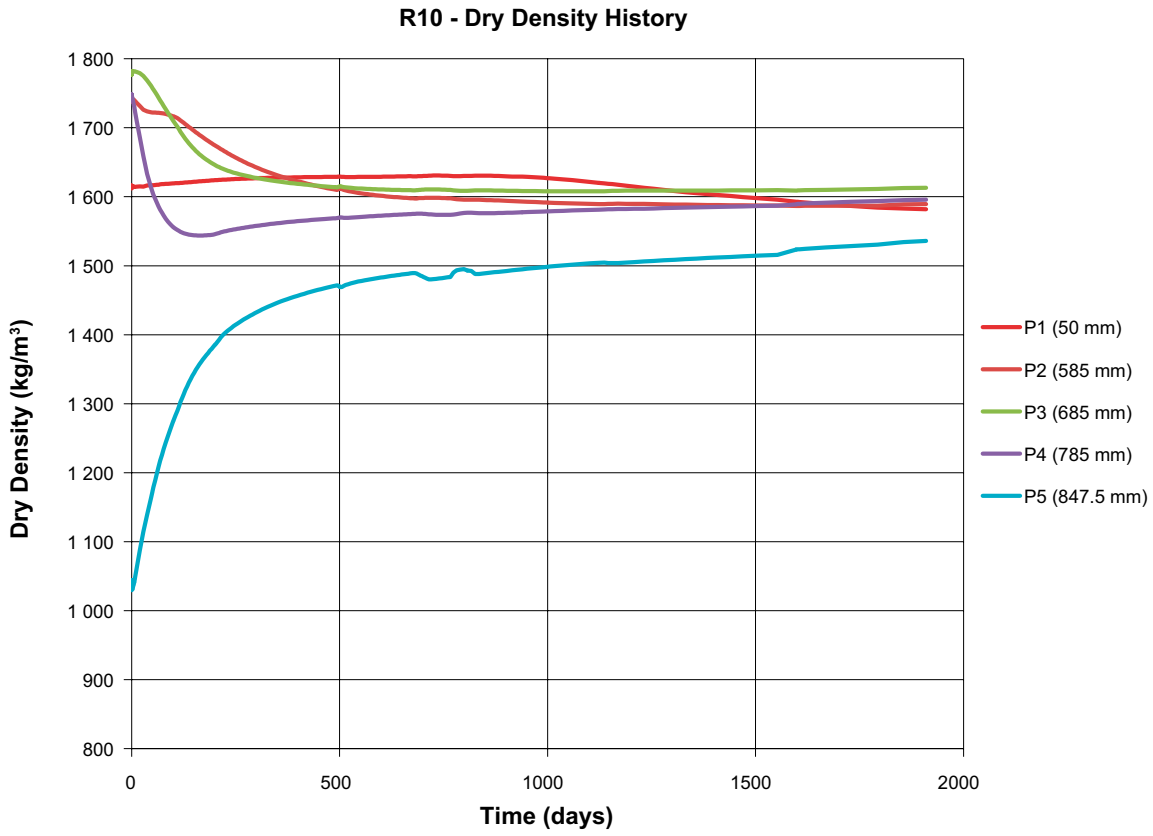
R10 - Dry Density History
Dry Density (kg/m³)
1 800
1 700
1 600
1 500
1 400
1 300
1 200
1 100
1 000
900
800
0
500
1000
1500
2000
Time (days)
P1 (50 mm)
P2 (585 mm)
P3 (685 mm)
P4 (785 mm)
P5 (847.5 mm)

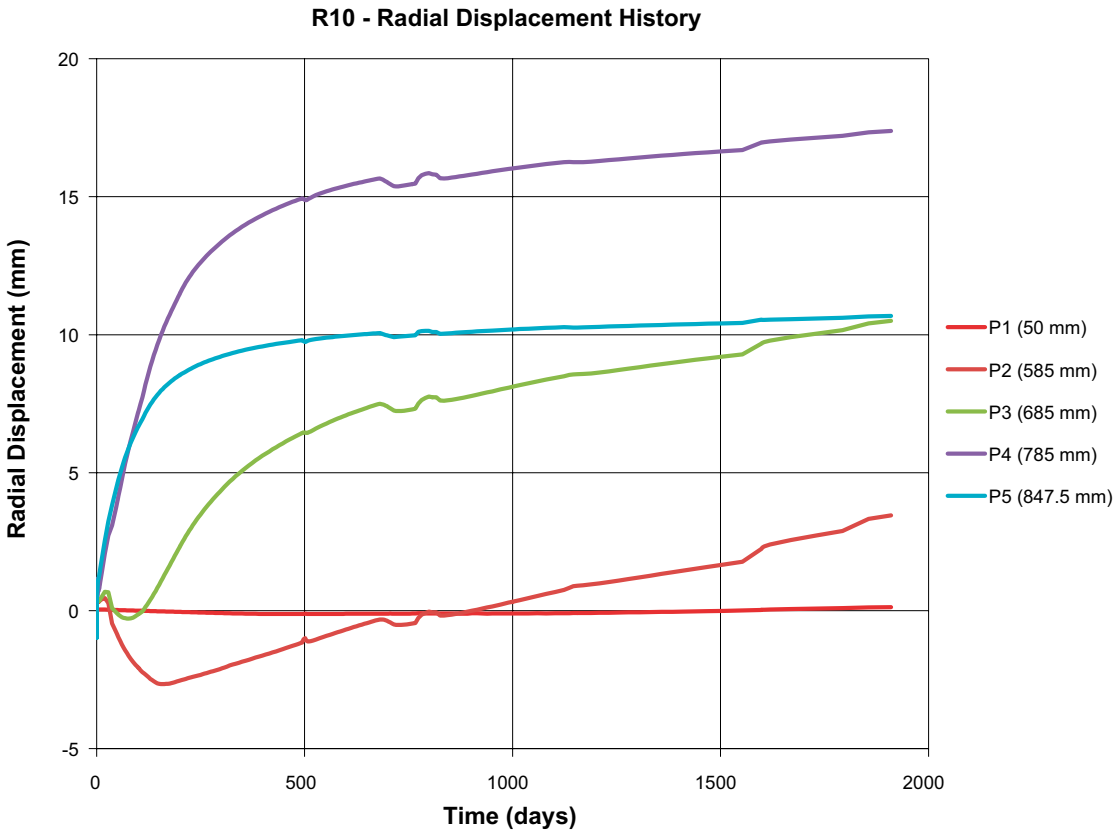
R10 - Radial Displacement History
Radial Displacement (mm)
20
15
10
5
0
-5
0
500
1000
1500
2000
Time (days)
P1 (50 mm)
P2 (585 mm)
P3 (685 mm)
P4 (785 mm)
P5 (847.5 mm)

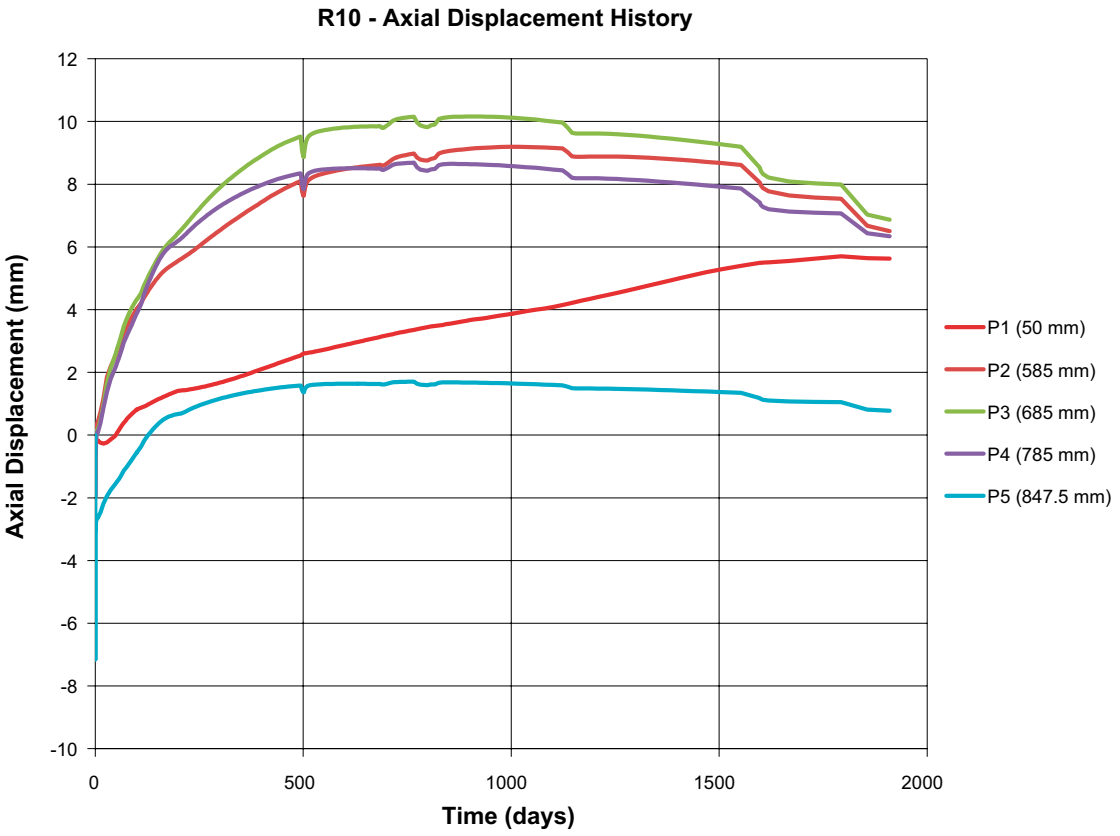
R10 - Axial Displacement History
Axial Displacement (mm)
12
10
8
6
4
2
0
-2
-4
-6
-8
-10
0
500
1000
1500
2000
Time (days)
P1 (50 mm)
P2 (585 mm)
P3 (685 mm)
P4 (785 mm)
P5 (847.5 mm)

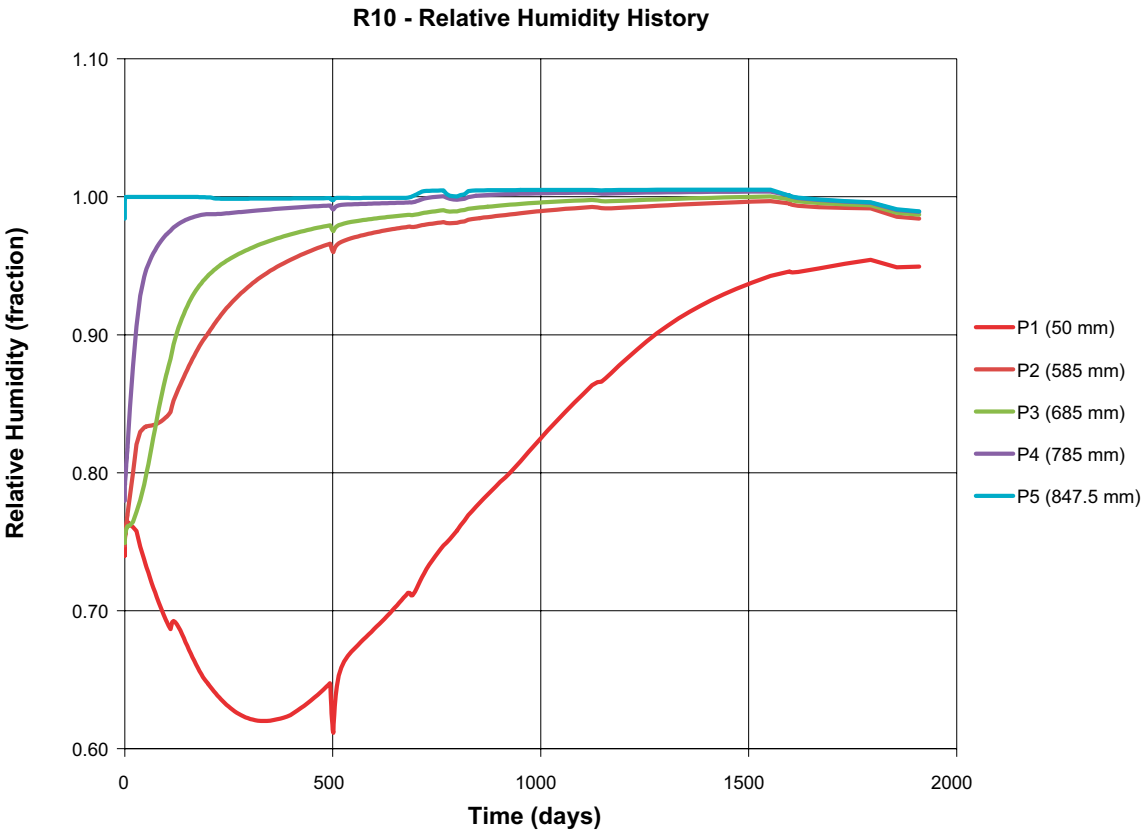
R10 - Relative Humidity History
Relative Humidity (fraction)
1.10
1.00
0.90
0.80
0.70
0.60
0
500
1000
1500
2000
Time (days)
P1 (50 mm)
P2 (585 mm)
P3 (685 mm)
P4 (785 mm)
P5 (847.5 mm)

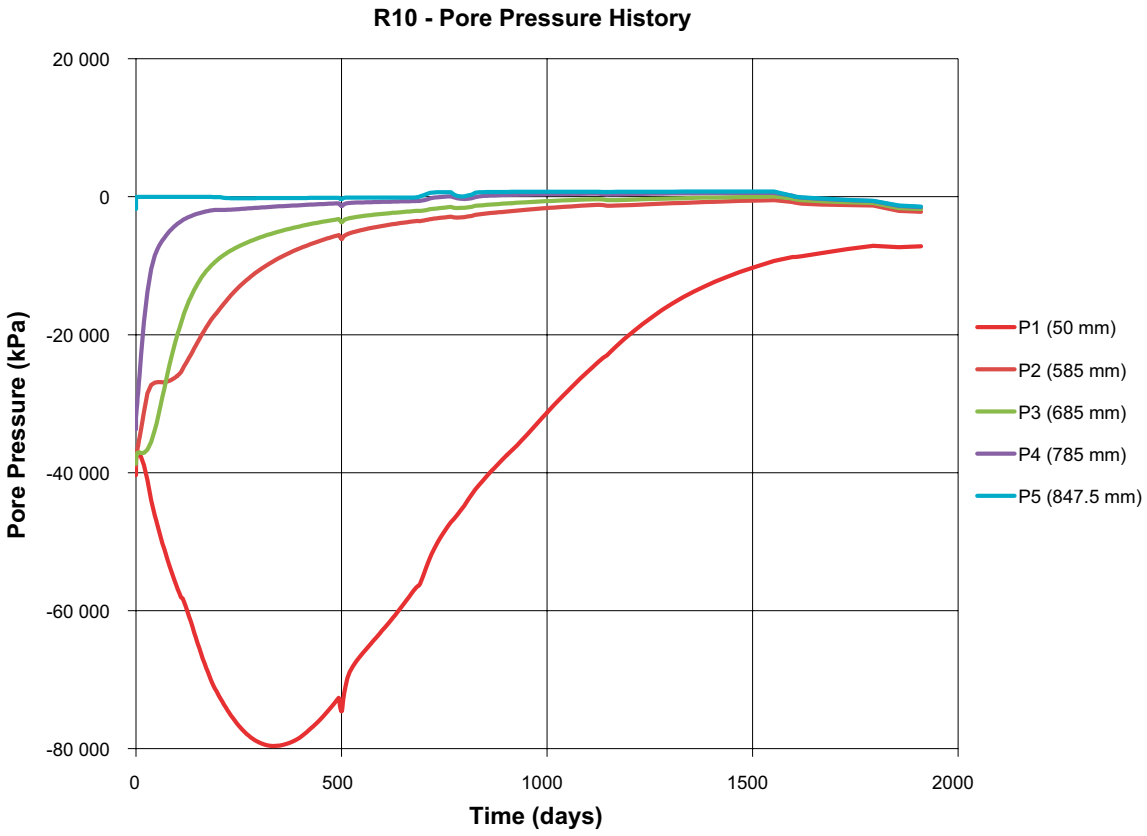
R10 - Pore Pressure History
20 000
0
-20 000
-40 000
-60 000
-80 000
Pore Pressure (kPa)
0
500
1000
1500
2000
Time (days)
P1 (50 mm)
P2 (585 mm)
P3 (685 mm)
P4 (785 mm)
P5 (847.5 mm)

Cylinder C3

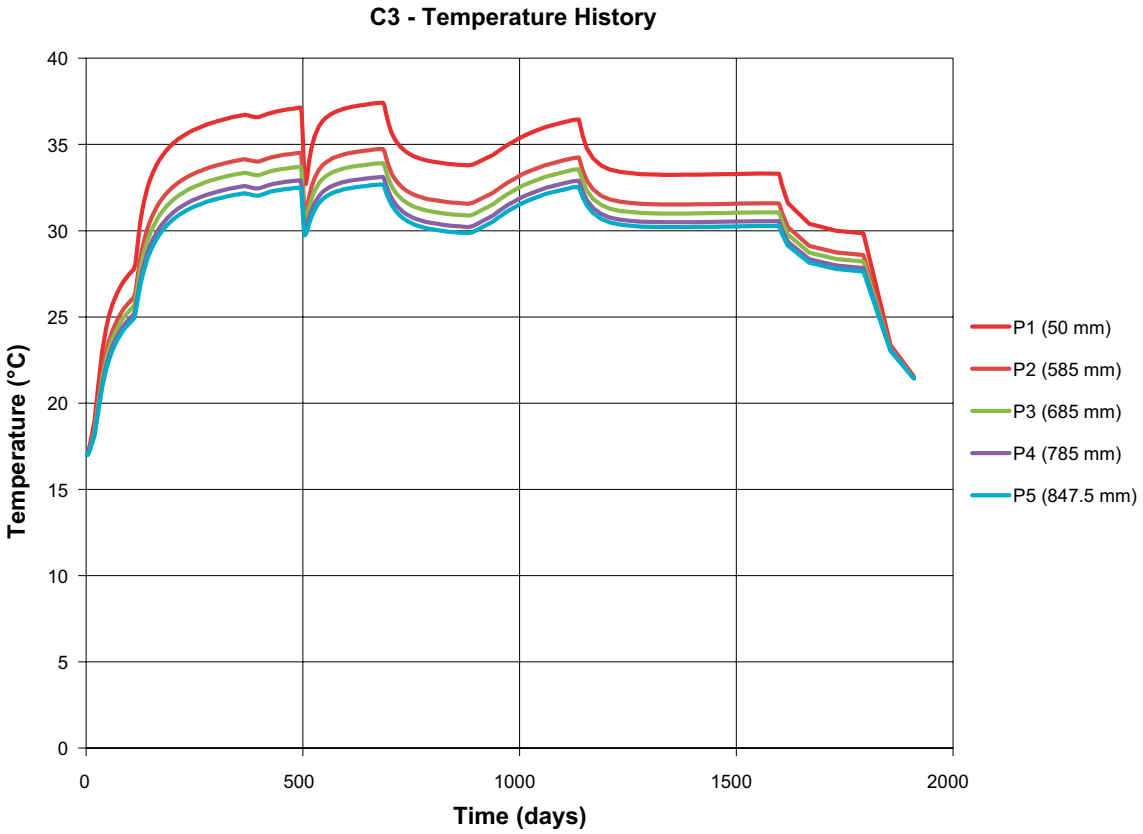
C3 - Temperature History
Temperature (°C)
Time (days)
0
5
10
15
20
25
30
35
40
0
500
1000
1500
2000
P1 (50 mm)
P2 (585 mm)
P3 (685 mm)
P4 (785 mm)
P5 (847.5 mm)

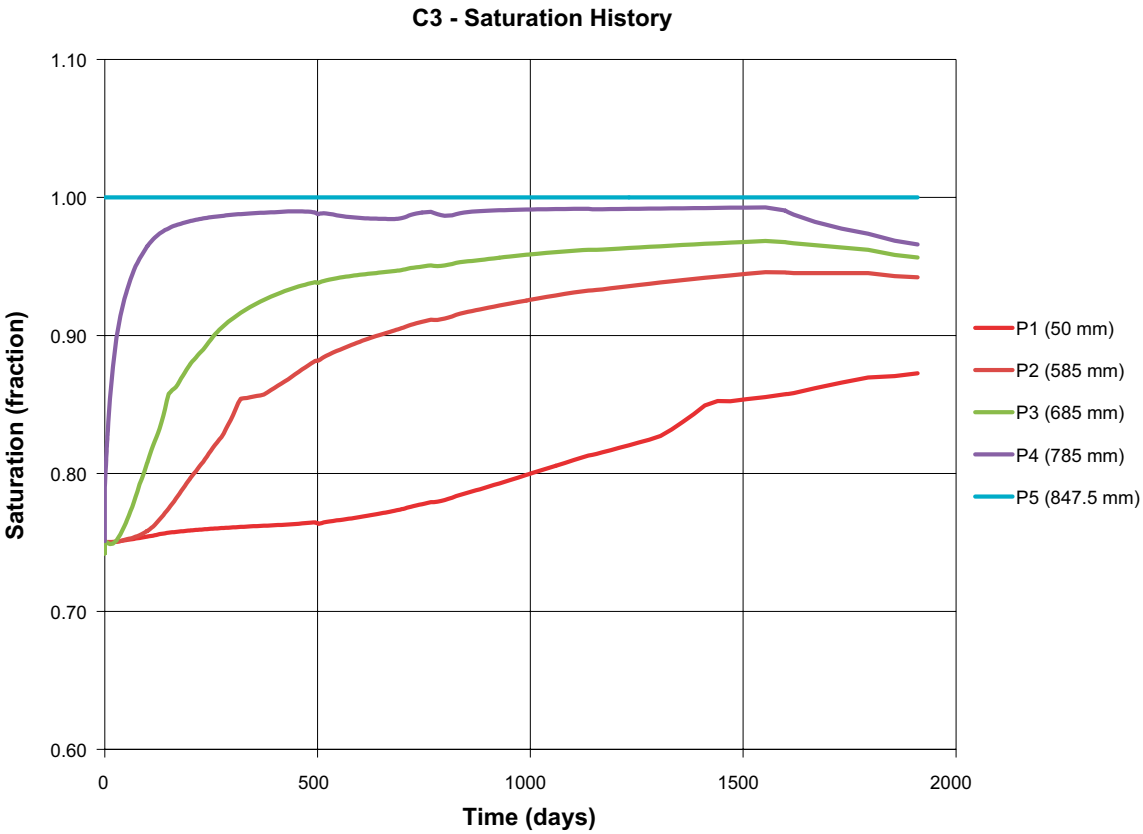
C3 - Saturation History
Saturation (fraction)
Time (days)
0.60
0.70
0.80
0.90
1.00
1.10
0
500
1000
1500
2000
P1 (50 mm)
P2 (585 mm)
P3 (685 mm)
P4 (785 mm)
P5 (847.5 mm)

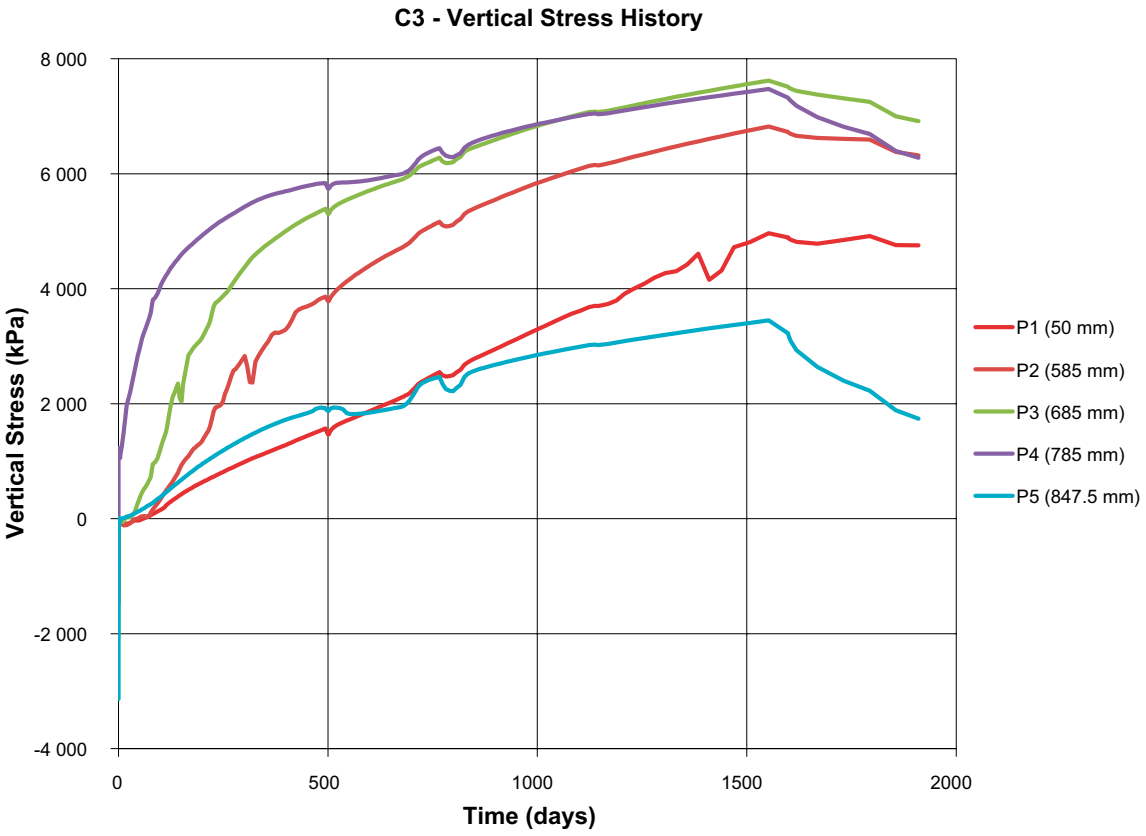
C3 - Vertical Stress History
Vertical Stress (kPa)
8 000
6 000
4 000
2 000
0
-2 000
-4 000
0
500
1000
1500
2000
Time (days)
P1 (50 mm)
P2 (585 mm)
P3 (685 mm)
P4 (785 mm)
P5 (847.5 mm)

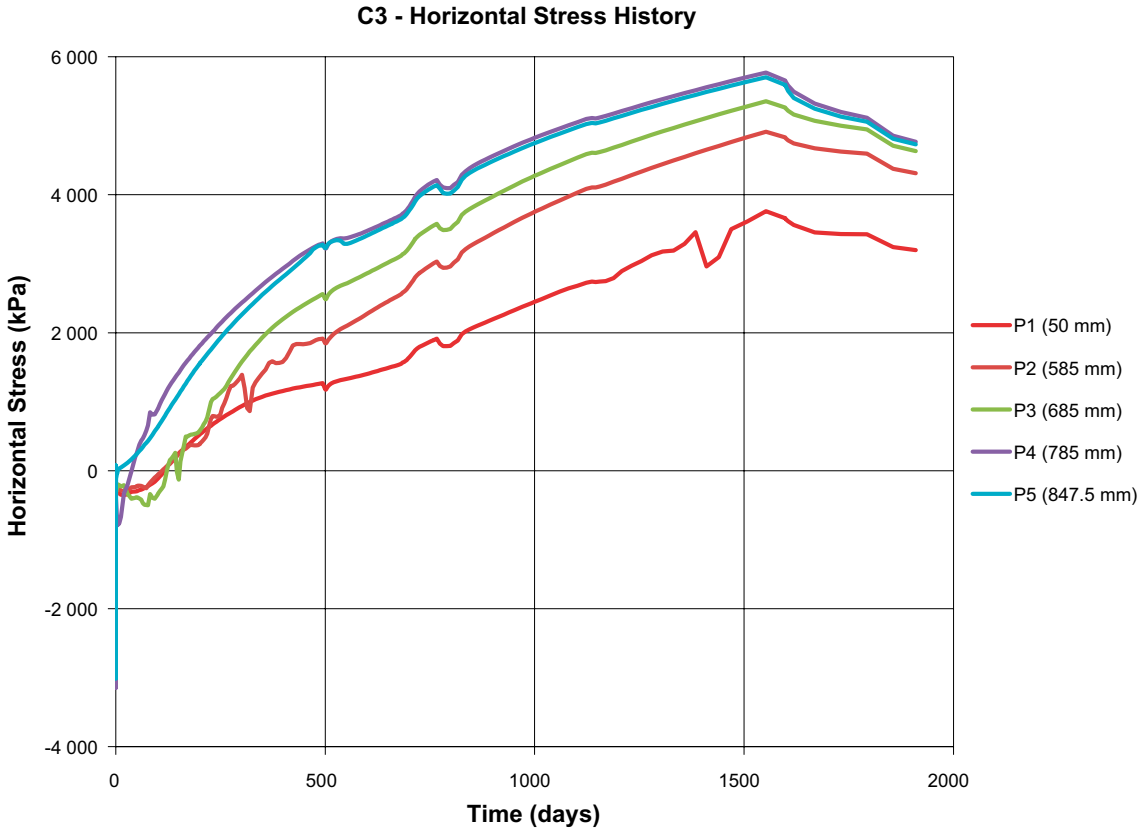
C3 - Horizontal Stress History
Horizontal Stress (kPa)
6 000
4 000
2 000
0
-2 000
-4 000
0
500
1000
1500
2000
Time (days)
P1 (50 mm)
P2 (585 mm)
P3 (685 mm)
P4 (785 mm)
P5 (847.5 mm)

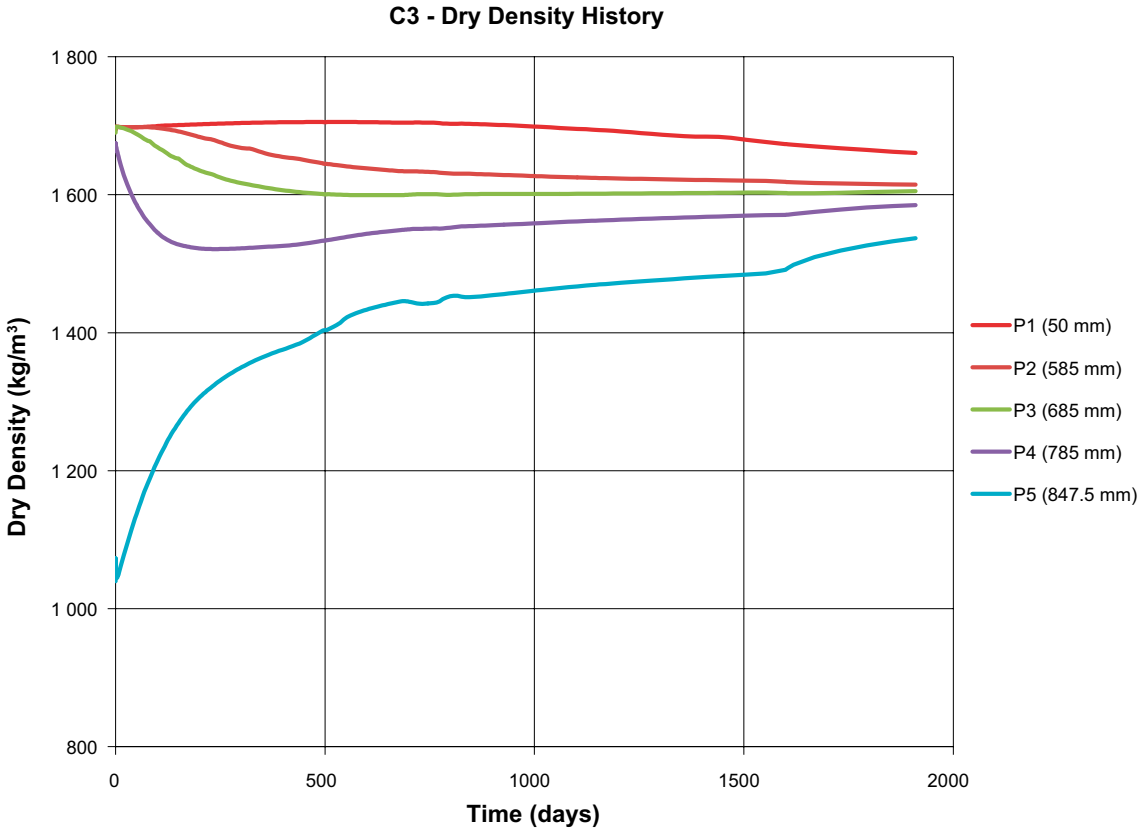
C3 - Dry Density History
1 800
1 600
1 400
1 200
1 000
800
Dry Density (kg/m³)
0
500
1000
1500
2000
Time (days)
P1 (50 mm)
P2 (585 mm)
P3 (685 mm)
P4 (785 mm)
P5 (847.5 mm)

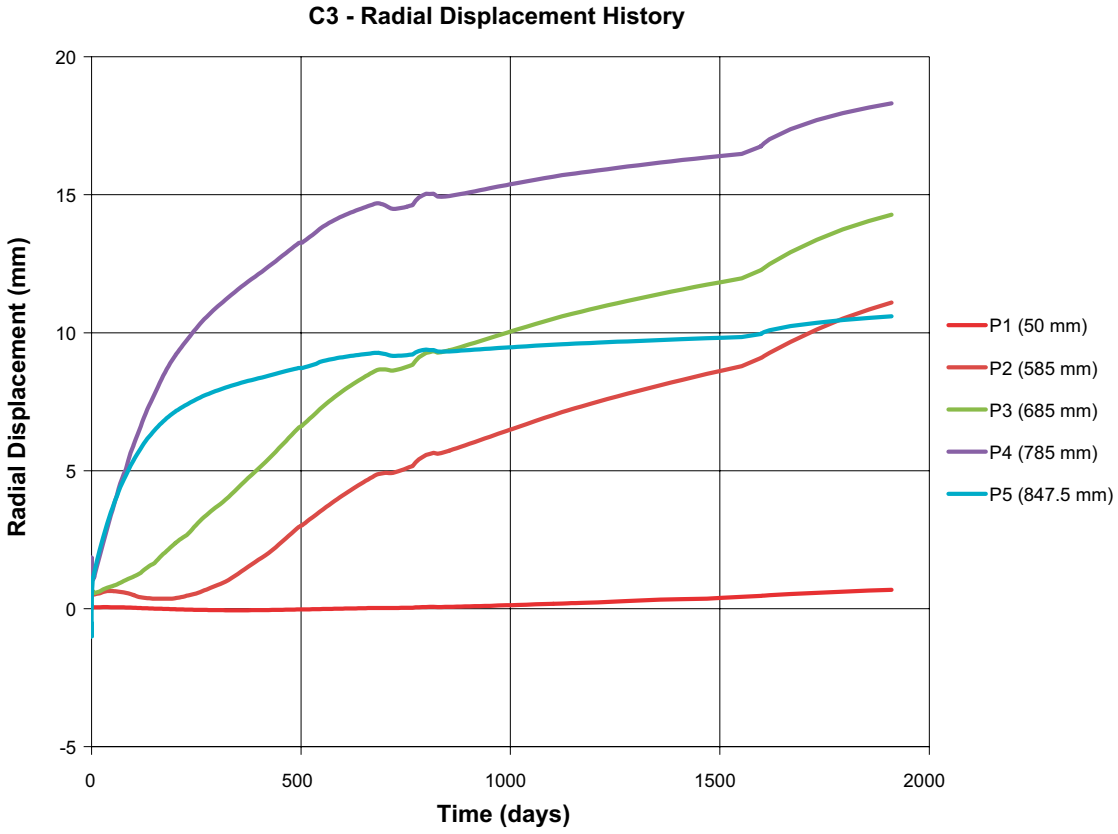
C3 - Radial Displacement History
20
15
10
5
0
-5
Radial Displacement (mm)
0
500
1000
1500
2000
Time (days)
P1 (50 mm)
P2 (585 mm)
P3 (685 mm)
P4 (785 mm)
P5 (847.5 mm)

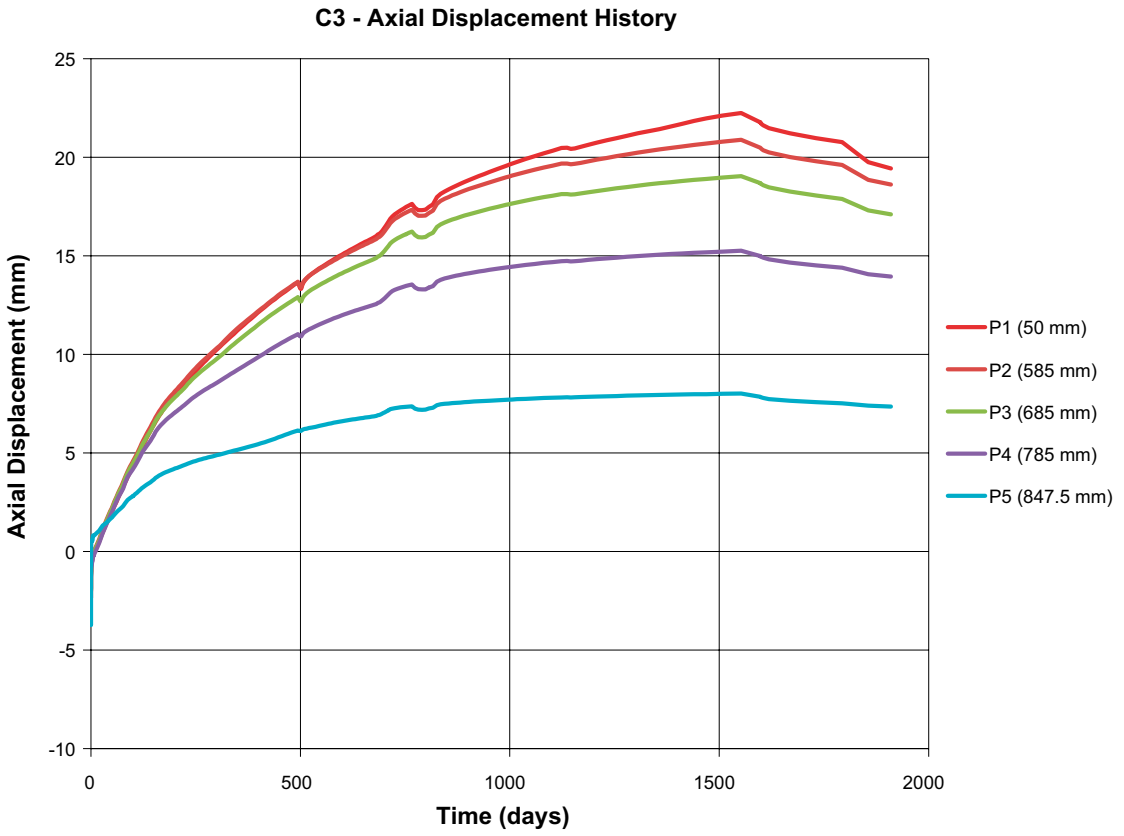
C3 - Axial Displacement History
Axial Displacement (mm)
25
20
15
10
5
0
-5
-10
0
500
1000
1500
2000
Time (days)
P1 (50 mm)
P2 (585 mm)
P3 (685 mm)
P4 (785 mm)
P5 (847.5 mm)

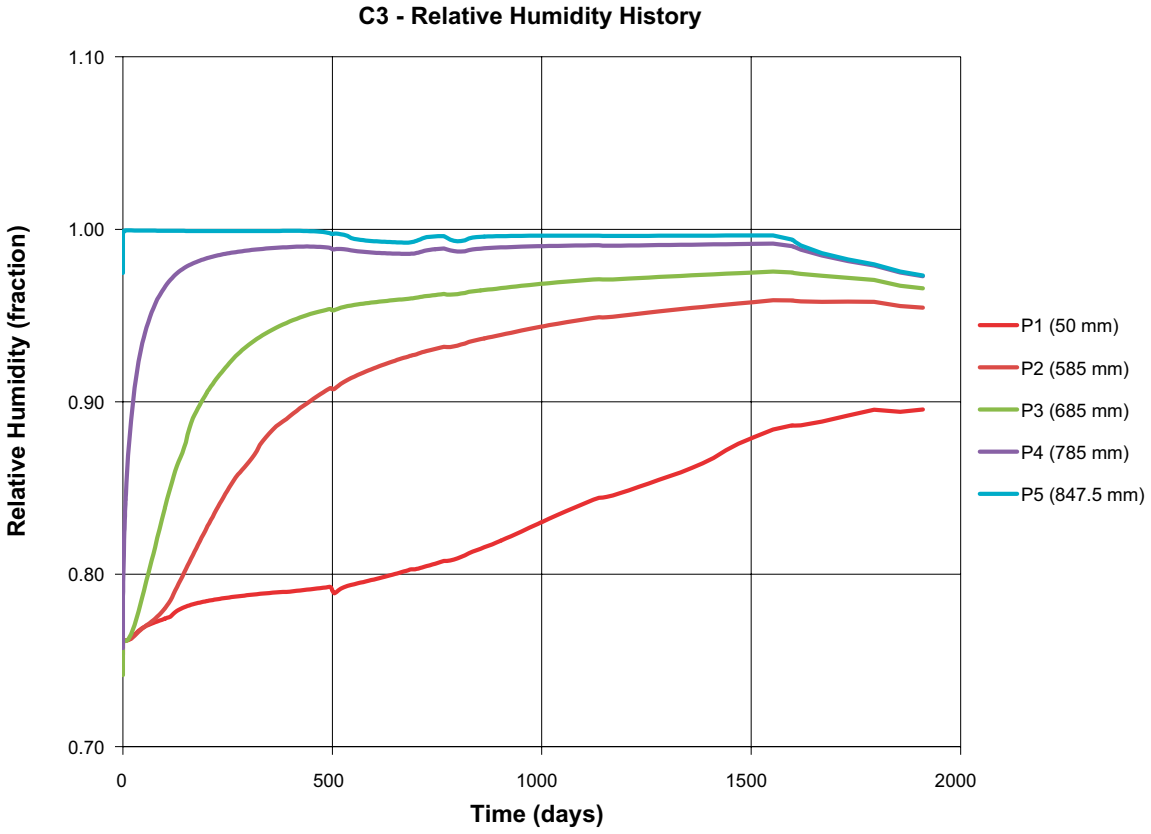
C3 - Relative Humidity History
Relative Humidity (fraction)
1.10
1.00
0.90
0.80
0.70
0
500
1000
1500
2000
Time (days)
P1 (50 mm)
P2 (585 mm)
P3 (685 mm)
P4 (785 mm)
P5 (847.5 mm)

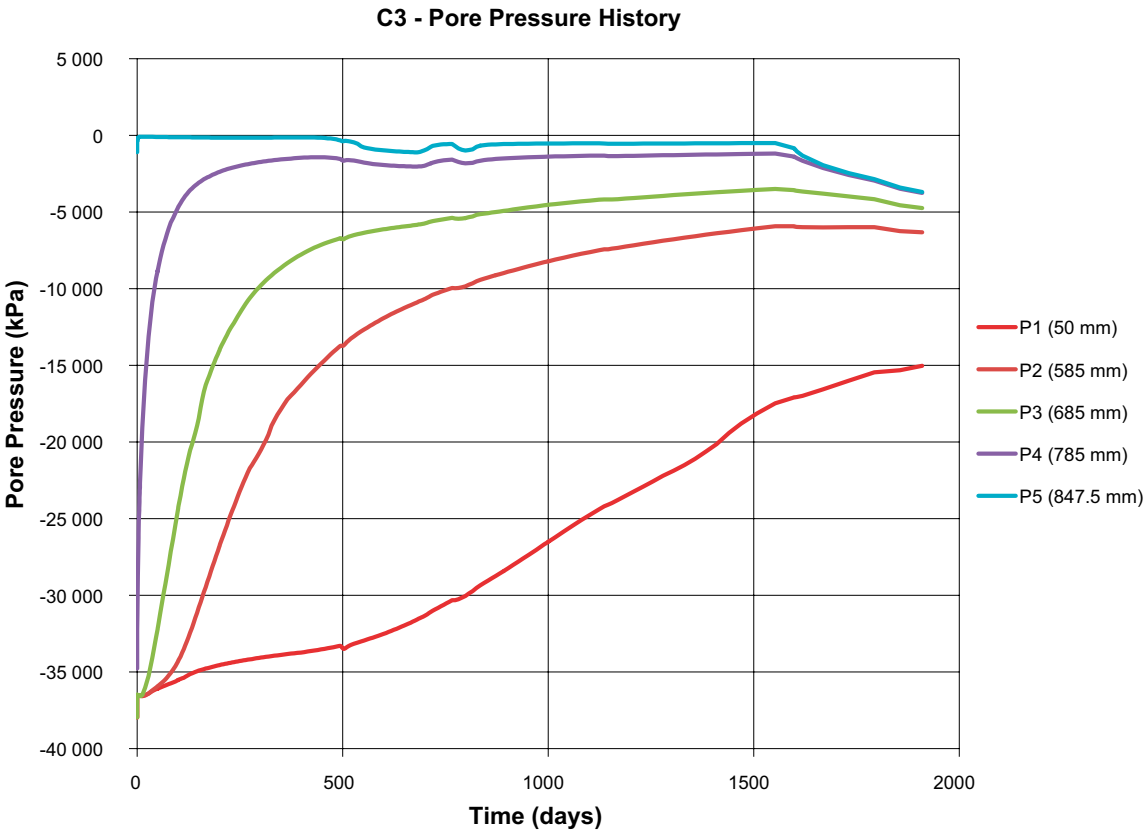
C3 - Pore Pressure History
5 000
0
-5 000
-10 000
-15 000
-20 000
-25 000
-30 000
-35 000
-40 000
Pore Pressure (kPa)
0
500
1000
1500
2000
Time (days)
P1 (50 mm)
P2 (585 mm)
P3 (685 mm)
P4 (785 mm)
P5 (847.5 mm)